# LIMBLESS LOCOMOTION IN COMPLEX TERRESTRIAL TERRAIN

A Dissertation
Presented to
The Academic Faculty

By

Perrin E. Schiebel

In Partial Fulfillment
of the Requirements for the Degree
Doctor of Philosophy in the
School of Physics

Georgia Institute of Technology

May 2019

Copyright © Perrin E. Schiebel 2019

**LIMBLESS LOCOMOTION IN COMPLEX TERRESTRIAL TERRAIN**

Approved by:

Dr. Daniel I. Goldman, Advisor
School of Physics
*Georgia Institute of Technology*

Dr. David Hu
School of Mechanical Engineering
*Georgia Institute of Technology*

Dr. Simon Sponberg
School of Physics
*Georgia Institute of Technology*

Dr. Jennifer Curtis
School of Physics
*Georgia Institute of Technology*

Dr. D. Zeb Rocklin
School of Physics
*Georgia Institute of Technology*

Date Approved: December 18, 2018

Family and friends.

Carolyn Jones and Harriet Schiebel.

Valmi and Roxy Tangerine.

## ACKNOWLEDGEMENTS

My parents Edward Schiebel and Robin Jones are greatly responsible for my success. Throughout my life if I expressed interest in trying something the answer was always yes. They taught my that with work I was capable of doing anything. My sister Madeline taught me to always strive to better understand myself and my role in the world around me. She and Laura Cotton inspire me to not only continually develop my personal morality and values but to stand by them through my actions. There are too many people to list here, but the support and love of my entire family means more than I know how to say. Harriet Schiebel and Carolyn Jones, you both taught me I can be curious and driven while remaining caring and, of course, fabulous. I hope I can touch a fraction of the lives each of you did.

Cheasequah Blevins is both an incredible friend and one of the most tenacious, talented researchers I know. Agreeing to take some boy from another school to prom was one of the best choices I ever made because I ended up meeting her. I also owe thanks to all of the friends I met during my time at Georgia Tech, who kept including me in things even when I disappeared for months.

Everyone in the CRABlab past and present are deserving of thanks. The research of the students that came before has been a continuously consulted divining rod. Prof. Gravish's desk and poster are constant reminders to keep working and I have been influenced and motivated by continued discussions with Prof. Chen Li. Special thanks to Dr. Sarah Sharpe who helped me set up my first animal experiments and whose papers I have read countless times. Dr. Jennifer Rieser has been immensely helpful as both a mentor and a research partner. And lastly, Will Savoie, who has more miscellaneous pieces of information than any person should and never let me take myself too seriously.

Thank you to the vets, farriers, barn owners and managers, trainers, and friends that kept me and Valmi going.

Lastly, thank you to my advisor Dan Goldman. His guidance helped me grow as a scientist, a communicator, and a person. I am grateful for both the insights and suggestions which improved my work as well as the the opportunity to think and develop my research independently.

## TABLE OF CONTENTS

## LIST OF TABLES

## LIST OF FIGURES

## SUMMARY

Limbless locomotion is used by animals ranging from micro to macroscopic to move in a wide variety of terrains. Snakes in particular use their elongate bodies to swim in water, climb trees, burrow into sand and soil, crawl across terrestrial terrain from jungle to desert, and glide through the air. The versatility of limbless locomotion makes it suitable for situations that challenge legged or wheeled platforms, and for this reason snake-like robots are an attractive solution for engineering problems like movement in the confined, unstable rubble of a collapsed building. There are several gaits used by limbless organisms. Of these, lateral undulation is the most broadly used. During lateral undulation, posteriorly propagating body bends interact with heterogeneity in the surroundings, pushing the snake opposite the direction of wave propagation. Despite its ubiquity in limbless organisms, principles of movement using lateral undulation in complex terrestrial terrains are lacking.

Many terrestrial materials can permanently deform under stresses applied by the animals' body bends. Strategies used by limbless organisms to manage hysteretic substrates are unknown. In this dissertation I used a granular material as a model for yielding substrates and studied the desert-specialist snake *C. occipitalis* using lateral undulation to move at the surface. The animals moved quickly using a stereotyped waveform which was well-described by a sinusoidal wave of curvature, a "serpenoid curve" [1]. Granular drag experiments for a partially intruded plate revealed that the ratio of thrust to drag forces was independent of depth or speed over a range relevant to the snake. This anisotropy curve appears to be a general feature of surface drag; measurements in three more granular materials (poppy seeds, oolite sand, 6 mm plastic spheres) at varied intrusion depths and speeds yield similar results. Resistive force theory (RFT) calculation of performance was accurate, indicating, in conjunction with the drag experiments, that the system was resistive-force dominated. That is, the snake experiences its environment more like a microscopic bacteria than an eel. Metrics which accounted for performance alone did not explain the stereotyped

shape adopted by the snakes; it was necessary to account for the demands on the muscles which varied as a function of the waveform. I found that the stereotyped wave used by the animals maximized center-of-mass speed given a constraint on peak muscle power. A 10-link robophysical model permitted systematic exploration of the interaction between different waveforms and the substrate. As the RFT calculation did not account for material hysteresis, it over-predicted robot performance for shapes which did not progress enough per gait cycle. These waveforms interacted with previously disturbed material, leading to failure. The animal's waveform was in the regime where motion was like that in a frictional fluid; by limiting material yield the animal avoided contending with the memory-dependent effects that led to robot failure.

Given the benefits and robust appearance of the sand-swimming waveform, I posited this self-deformation pattern was a kinematic target for the neuromechanical system. To explore strategies for contending with obstacles in the environment, I perturbed the snakes with unexpected collisions using a row of equidistant, force-sensitive posts in an otherwise uniform substrate. Combining many trials revealed a non-uniform pattern of trajectory reorientation resulting from interaction with the array. I developed a geometric model using interaction rules based on previously measured snake muscle activation patterns to mimic open-loop control which relied on passive dynamics to solve constraints imposed by the obstacles. This model reproduced the mechanical diffraction pattern observed in the snake trajectories, suggesting that the animals could use a similar strategy which relied on passive physiological properties to handle unexpected contacts without the need for additional input from the nervous system. A robophysical model using exterosensory-open-loop control was similarly diffracted. The reaction forces measured by the force-sensitive posts were most likely perpendicular to the direction of motion in both snake and robot.

Terrestrial terrains often feature a mixture of substrates and obstacles of varying density. I explored strategies for lateral undulation in cluttered terrain by testing the desert-specialist snake in 2D arrays of posts arranged at varying post separation distances and embedded in

both a granular and a hard, low-friction substrate. Comparison with simulation demonstrated that performance moving along the rows of a square lattice was a function of lattice spacing on the hard substrate, with a drop-off at spacing over wavelength of 0.5. The snakes modified their wavelength to remain below this point. In the usable granular substrate the performance and wave parameters were independent of lattice spacing, suggesting that the animals did not change strategy from the sand-swimming waveform to use the rigid obstacles. Similar performance was recapitulated in a robophysical model using open-loop control with a torque-limit on the motors to introduce flexibility. A generalist snake did not out-perform the specialist in lattices on level ground, but was able to effectively ascend inclined lattices independent of lattice spacing whereas the specialist's performance decreased as the spacing between posts increased. Observation of a fast-running desert-dwelling lizard navigating spherical boulders placed on a granular substrate suggest a strategy similar to that used by the desert snake in which the animal makes no attempt to avoid collisions with obstacles.

I used granular drag measurements and observation of snake kinematics during interaction with complex terrain to advance our understanding of the bio and neuromechanics of undulatory motion in terrestrial environments. The snakes were a useful model system; there are many species with a variety of morphologies and habitats, they were easy to manipulate, the experimental terrains were straightforward to build, and I found they had stereotyped locomotive behaviors.

# CHAPTER 1
# INTRODUCTION AND BACKGROUND

## 1.1 Overview

Movement is integral to the survival of many organisms. Locomotion via waves of *self-deformation*, in which activation of internal motors like muscles causes body shape changes, appears in animals across scales and is adaptable to a wide range of terrains and habitat.

The nematode *Caenorhabditis elegans*, length $O(mm)$ lives in a variety of rotting plant matter [2]. In the laboratory *C. elegans* can undulate through fluids of viscosity encompassing $> 5$ orders of magnitude [3], non-Newtonian fluid [4], and rigid post arrays of varying post sizes and densities [5, 6, 7].

Larger animals like eels (length $O(m)$) not only swim, but can burrow in mud [8, 9] and crawl across land [10]. Snakes from a few centimeters to meters in length swim in water [11], crawl through tunnels [12], burrow in sand and soil [13, 14], climb trees [15], glide through the air [16], and traverse a range of terrestrial terrains [17, 18, 19, 20, 21].

In addition to being highly adaptable and suitable to a wide range of conditions, movement via propagating undulatory waves in the trunk is also morphologically simple. Organisms that move in this manner typically have bodies specialized into repeated segments [17]. The combination of simple morphology and versatility make undulatory locomotion an attractive solution for robots used in, e.g., search and rescue in cluttered terrains [22] and extra-terrestrial investigation where the substrate is potentially highly deformable and difficult to predict *a priori*.

Progress has been made in understanding undulatory swimming of organisms in fluids. Researchers combined animal experiments with computation of the body-fluid interaction made possible by the Navier-Stokes equations (see e.g. [23, 24, 25] and references therein).

However, principles of undulatory locomotion on the surface of terrestrial terrains remain largely unknown. In such environments, unlike in fluids, materials may yield and permanently deform in response to the locomotor interaction.

A few challenges have slowed progress in this subject. First, while our understanding of the movement of animals on hard ground (mediated by normal and frictional forces [26]) and in fluids like water and air is facilitated by the existence of terrain models; the physics of most terrestrial materials like muds and mixtures of soils, leaves, rotting plant matter, etc. are poorly understood. .

Further, while snakes are useful model organisms because they are easy to manipulate in the lab, display a wide variety of morphology and behavior, and have an ecology which is well-known for many species [27], their neurological system is not as well studied as in other model organisms (e.g. *C. elegans* [28], lamprey [29]).

While little is known about most terrestrial materials, granular resistive force theory (RFT) provides a model for interaction with granular matter (GM) in the frictional fluid regime where the grain-grain and grain-animal frictional forces of the flowing matter are responsible for the forces [30]. GM will yield and flow under stress [31], making it a useful model for a broader class of deformable materials. Additionally, studying the kinematics of animals interacting with with complex environments has been illuminating in understanding the neuromechanics in other systems [32, 33].

In this dissertation, we study in the laboratory snakes moving through simplified models of complex terrain–combinations of granular matter and hard substrates and obstacles of varying densities. The overarching goal of this research program is to understand how self-deformation patterns interact with the terrain to enable effective locomotion of limbless systems and, given a desired shape, how the many degree-of-freedom body is coordinated to actualize it. Furthermore, such a study indicates possible improvements in the performance and capability of snake-like robots in deformable, multi-modal terrains.

## 1.2 Limbless locomotion

### 1.2.1 Propulsion via waves of self-deformation

The use of undulatory waving of some or all of the body to produce motion appears in organisms ranging in size over many orders of magnitude.

Microscopic organisms like spermatazoa [34] and motile bacteria [35] use one or several flagella to propel themselves. The flagella are rotated at the point of attachment to the body, resulting in a helical wave which propagates away from the body [35]. These animals are very small so the resistance of the fluid to flagellar movement provides the thrust for the animal rather than inertial contributions from accelerating the fluid.

Similarly, the microscopic *Caenorhabtitis elegans* (Fig. 1.1) uses traveling waves to propel itself. The amplitude and speed of waving depends on the properties of the surrounding materials. In highly viscous fluid or agar the animal "crawls"–the body appears to move in a tube–and the amplitude is high, while when swimming in low-viscosity fluid (like water) the worm "swims" using low amplitude waves and experiencing substantial slip lateral to the direction of motion [36]. As viscosity varies from high to low the nematode's kinematics vary congruently [37] (Fig. 1.1 *bottom*).

Like the bacteria, *C. elegans* is a low-Reynolds (low-Re) number swimmer, that is, its motion is characterized by the dominance of forces which resist the motion of the animal through the material. In fluids the resistive force arises from the viscosity and is proportional to the velocity of the body relative to the fluids [34]. For a body moving sufficiently fast or fluid with sufficiently low viscosity forces are reactive, arising from acceleration of the fluid [39]. The Reynolds number is the ratio of reactive to resistive forces in a system. Animals at low-Re (Re$< 1$) rely on the resistance of the surrounding fluid to the motion of their body and/or appendages to provide thrust. Inertia in such systems is negligible and such animals will stop moving if they stop deforming. Furthermore, at low Reynolds number, because the time-dependent reactive terms are negligible, body deformations must be

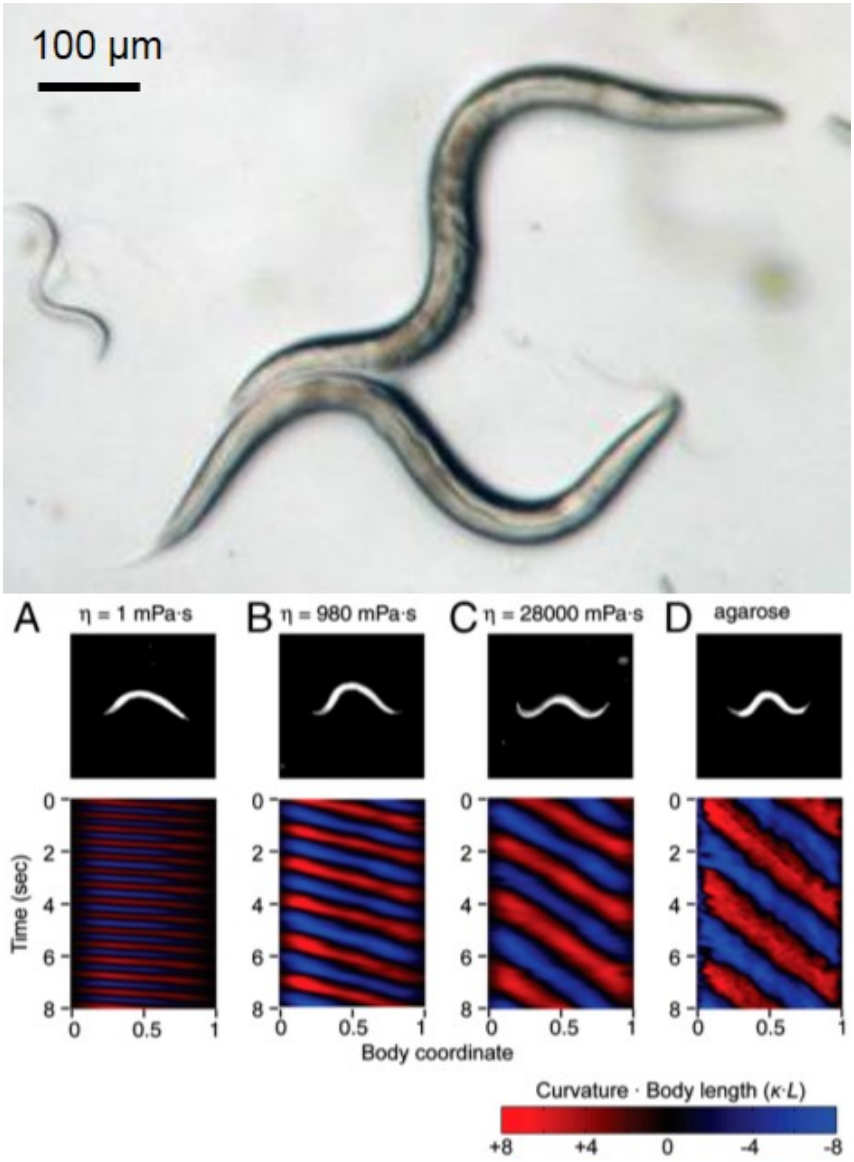


Figure 1.1: The nematode *Caenorhabditis elegans*. (*top*) Microscope image of *C. elegans*. Two worms are in the foreground. Note that, unlike the snake, the worm bends its body in the dorsal-ventral plane. Image courtesy [38]. (*bottom*) *C. elegans* locomotion in fluid of varying viscosity and agar. Figure and following caption reproduced from [3]. Dark field images and time-dependent curvature patterns of adult worms (A) swimming in NGM buffer with viscosity 1 mPas, (B) in dextran solutions with viscosity 980 mPa·s, (C) in dextran solution with viscosity 28,000 mPa·s, (D) crawling on 2% agarose surface. The worm head is to the left in all images. Body curvature as a function of time (in seconds) and normalized body coordinate (varying from 0 at the head to 1 at the tail). Body curvature is represented using the nondimensional product of curvature (the inverse of radius of curvature) and body length.

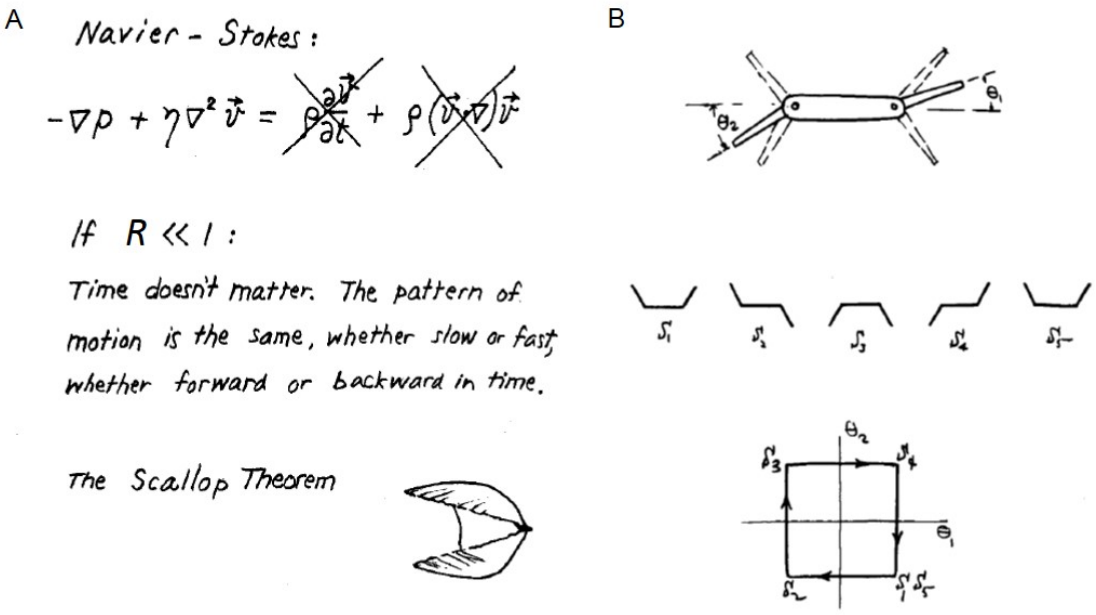


Figure 1.2: Low-Reynolds swimming requires asymmetric gaits. (*A*) A scallop at high-Re can swim by slowly opening then quickly shutting the shell. During the closing motion water is accelerated, propelling the scallop. If the Reynolds number, $Re = \frac{\rho l v}{\eta}$ (where $\rho$ is the fluid density, $l$ the length scale, $v$ the velocity of the body relative to the fluid, and $\eta$ the fluid viscosity), is small, those terms in Navier-Stokes relating to reactive forces ($m\frac{dv}{dt}$) are negligible. In this limit, symmetric self-deformations such as the opening and closing of a scallop's shell will not result in net translation because the flow in and out of the shell is exactly equivalent, regardless of how quickly or slowly (within the low-Re limit) the shell's joint-angle is changed. (*B*) Time-independence at low-Re means the simplest shape which can move has two degrees-of-freedom such that, unlike the scallop, it can create asymmetric, non-reciprocal gaits. Purcell [40] proposed the three-link swimmer which can generate the illustrated asymmetric "square gait". Figure reproduced from [40].

asymmetric for the animal to move [40]. The uni-directional traveling waves of the flagella or body provide this asymmetric motion (see [40, 41] for further detail).

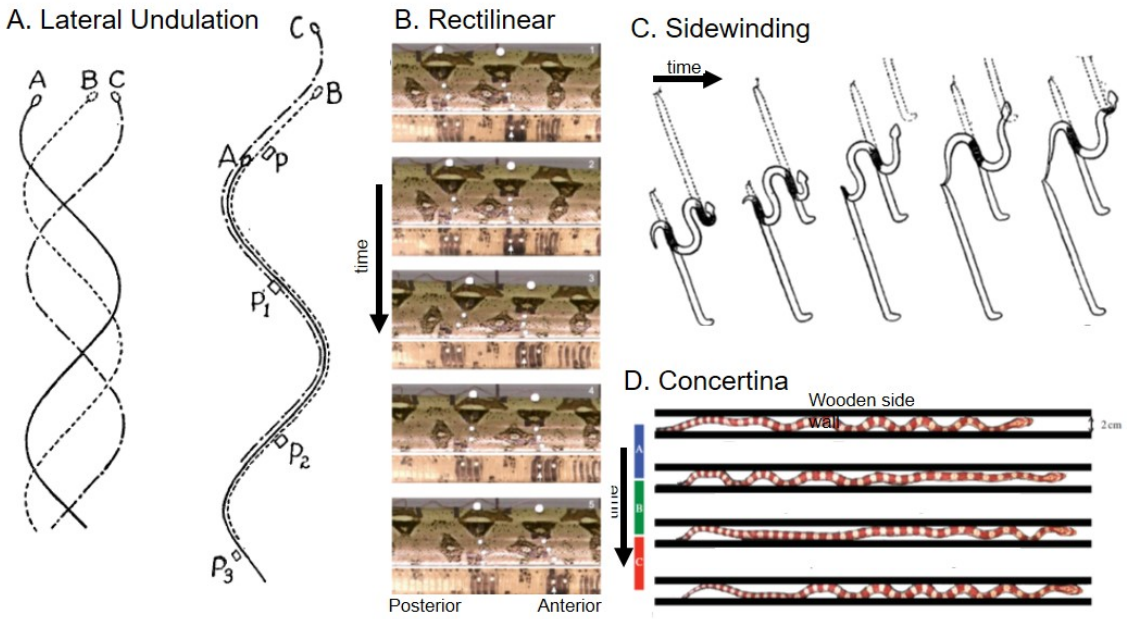


Figure 1.3: Examples of common snake gaits, note this is not an exhaustive list. (*A*) Diagrammatic sketches of lateral undulation. *left* is an example of motion on a low-friction substrate. Time progresses from A to C. Without anisotropy to overcome drag on the ventral surface no progress can by made. *right* illustrates lateral undulation when the body can press against push-points p1, p2, and p3. The body braces laterally against the push-points so that as the wave is propagated backward, the snake translates in the opposite direction. Reproduced from [17] (*B*) Snapshots of a snake performing rectilinear motion. White dots outline points on the integument of the animal. The direction of advancing time in all plots is shown by the black arrow. The snake places portions of the ventral skin in static contact with the substrate and then moves the skin posteriorly relative to the skeleton. The static segment of skin is then pulled up toward the spine, reducing or eliminating friction with the ground, and moved forward relative to the vertebrae. This process is repeated both along the body and through time, resulting in forward motion of the animal. Adapted from [42] (*C*) Diagrammatic sketches of sidewinder locomotion. The snake generates a flattened helical coil on the body using a vertical wave of lifting superimposed on a horizontal wave of lateral bends [43]. The snake "steps" across the substrate on static contacts. Reproduced from [17]. (*D*) Concertina locomotion of a snake in a channel. Black lines denote vertical (coming out of the page) wooden walls. This gait consists of three phases. A, where the posterior part of the body is pressed against the sides of the channel via lateral bends and, using the force developed by these bends pushing against the wall, the head is extended. In phase B the head has reached forward and begins creating bends to anchor the anterior part of the body against the channel walls. Lastly in phase C the posterior part of the snake is drawn forward, returning the snake to its initial kinematic configuration but translated forward in the tunnel. Adapted from [44]

Macroscopic elongate terrestrial organisms also move by passing waves down the body, the most common being snakes. The limbless morphology of terrestrial vertebrates evolved independently numerous times from limbed ancestors [45], suggesting this scheme is generally advantageous. Further evidence for the robustness of the limbless snake lies in the ubiquity of snakes across the planet; they successfully inhabit almost every place on earth which is not too cold for exotherms [46] (notable exceptions include Ireland and New Zealand) such that they successfully move through a wide range of habitats.

In traversing terrestrial habitats, snakes have a number of gaits they can utilize (Fig. 1.3). The most common, and the only gait also observed in all of the limbless reptiles, is lateral undulation (sometimes referred to as serpentine) [45].

In lateral undulation, propulsion is provided by waves of body bending which are propagated posteriorly along the body. Because all points on the animal glide forward at a constant velocity, the only forces acting tangent to the body are retarding frictional forces. To overcome this drag the body must generate lateral propulsive forces using the heterogeneity inherent in natural environments. The wave will interact with "push-points" in the terrain which serve to resist the backwards-slipping of the snake, causing the body to move forward opposite the direction of wave propagation [19]. These push-points may be by discrete obstacles [47] such as rocks or twigs, those created and subsequently used by the body bends like piles of sand [48], or frictional anisotropy introduced by the structure of the integument [49].

The waves of body-bending are primarily in the plane parallel to the substrate, although a vertical wave of twice the spatial frequency and lower amplitude may be superposed on the horizontal wave. This serves to reduce or remove frictional contact with the substrate of the high-curvature portions of the horizontal wave ([49], chapter 2) because these segments are often parallel to the desired direction of motion and thus not providing propulsive force.

Despite some similarity in appearance, lateral undulation is distinct from the anguilliform swimming of elongate fishes like lamprey and eels [52] and snakes moving through

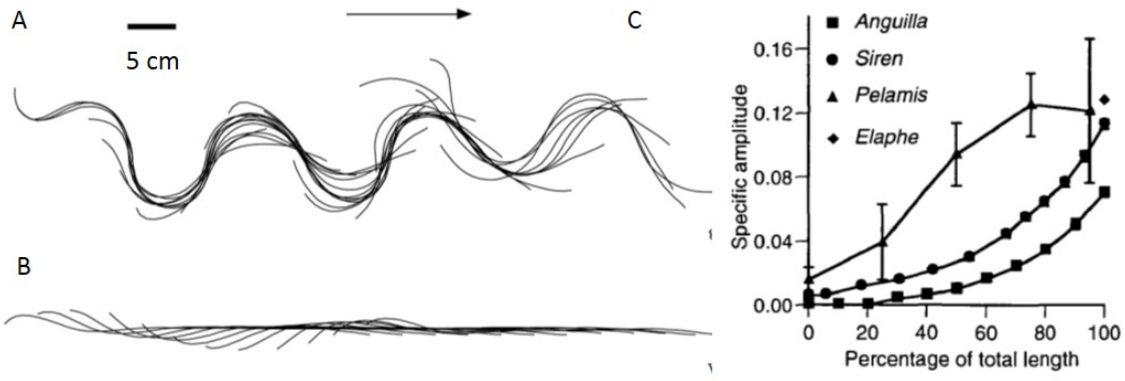


Figure 1.4: Anguilliform swimming amplitude increases monotonically from head to tail. (*A*) A series of midlines of the American eel *Anguilla rostrata* moving in a terrestrial environment and (*B*) and aquatic environment. Reproduced from [10] (*C*) Figure and following caption reproduced from [50]. Undulatory amplitude (measured as a proportion of total length) as a function of longitudinal position (0 = tip of snout, 100 = tip of tail) in a number of similarly sized elongate vertebrates swimming at comparable speeds. Amplitude is measured as half the lateral displacement between successive maximum excursions. Note that for *Elaphe*, data were based upon regression statistics (amplitude was regressed vs. distance along axis of forward motion, rather than distance along body), so only 1 data point is present, showing amplitude at the tip of the tail. Data from eels (*Anguilla*) are from Gillis (unpublished data) using 34—35 cm individuals swimming at 0.5 $Ls^{-1}$. Data from sirenid salamanders (*Siren*) are from Gillis (unpublished data) using 33-38 cm individuals swimming at 0.6 $Ls^{-1}$. Data from sea snakes (*Pelamis*) are from [51] using a 51 cm individual swimming at 0.63 $Ls^{-1}$. Data from colubrid snakes (*Elaphe*) are from [11] using a 33.5 cm individual swimming at 0.55 $Ls^{-1}$.

fluid environments [11]. Like lateral undulation, the anguilliform gait uses head-to-tail waves of body bending to generate propulsion using the surrounding fluid. However, this gait is characterized by the amplitude of the bends, which increases monotonically from head to tail (Fig. 1.4). In contrast, during lateral undulation the bend passes with the amplitude more or less unchanged as a function of position on the body. The increasing amplitude of the anguilliform wave is designed to use impulsive forces generated by fluid inertia [25] whereas the use of body bends in lateral undulation is primarily resistive force based.

Previous researchers modeled the heterogeneity in terrestrial terrain as rigid posts affixed in a hard, featureless substrate [19, 53, 21, 20]. In these experiments, snakes made

forward progress using a single peg, and used multiple pegs to balance lateral and torsional forces which can cause movement of the body axis away from the direction of the desired momentum vector [19].

Studies have also explored the relationship between push-point density and locomotive

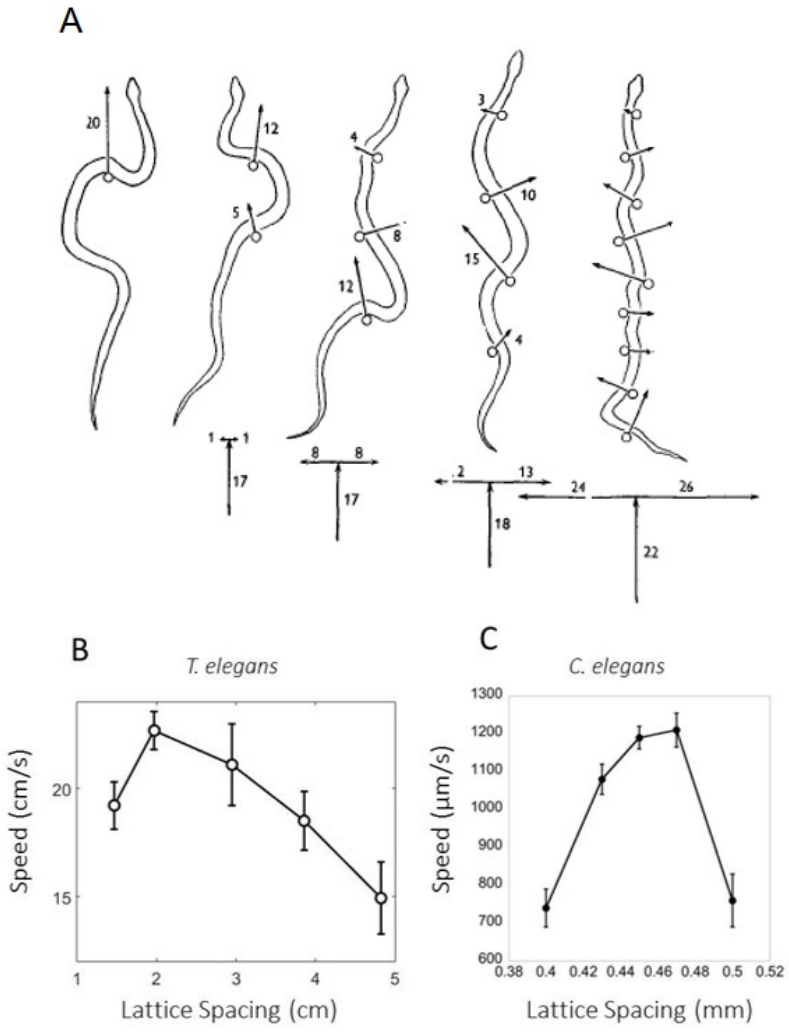


Figure 1.5: Movement through posts as a simplified model for terrestrial terrain. (*A*) Snapshots of the generalist grass snake moving through a row of posts. Post density increases from left to right. Arrows indicate the direction and magnitude of the reaction forces. Reproduced from [19]. (*B*) Center-of-mass speed of the garter snake *Thamnophis elegans* as a function of 2D square lattice spacing. Spacing is the distance between nearest-neighbor posts. Posts were 0.64 cm diameter rigid wooden pegs affixed to a hard, featureless substrate. Adapted from [21]. (*C*) Center-of-mass speed of the nematode *C. elegans* as a function of 2D square lattice spacing. Posts were 300 $\mu$m diameter and made of agar. The lattice was filled with buffer. Adapted from [6].

performance by varying the distance between nearest-neighbor pegs [53, 20, 21] (Fig. 1.5*A*). The connection between terrain parameters and performance in undulatory locomotion is not restricted to snakes. Studies of the nematode *Caenorhabditis elegans* moving in post arrays have also found similar associations between the lattice and worm speed [6, 5](Fig. 1.5*B*).

### 1.2.2 Snake physiology

The number of vertebrae in snakes is variable, even among individuals of the same species, and 200 or more vertebrae are common [27, 20, 21](Fig. 1.6 *top*). Snake vertebrae are designed to limit torsional movement to 1-2° [54] such that flexion is primarily in the lateral and dorsal/ventral planes (Fig. 1.6,*bottom*). Furthermore, lateral flexion of the joints is greater than the longitudinal flexion, with an angle of $\approx 25^\circ$ between vertebrae possible in the lateral plane, an $\approx 13^\circ$ ventral angle, and from $12-18^\circ$ maximum dorsal angle. ([17, 27].

Each vertebra has an associated set of muscles which act as a coherent unit to produce flexions (Fig. 1.7) such that there are as many of these muscles as there are vertebrae. However, these overlapping epaxial muscle groups span a number of vertebrae, anywhere from 9 to over 40 depending on the species [17, 57, 11], meaning that not all vertebral number and angle combinations are available, e.g. step or delta-function type waves cannot be generated by this musculature. Only smoothly-varying waves which are smoothly differentiable are expected. Extended muscle linking is postulated to simplify control [17], and snakes which move quickly using long body bends have fewer vertebrae and therefore longer muscle segments than the constrictors which specialize in strong, low curvature bends [57].

In this work we primarily use the non-constricting desert snake *Chionactis occipitalis*. We perform a preliminary comparative study to the constrictor *Panterophis guttatus*. We restrict our focus in this work to gross differences between the specialist and generalist

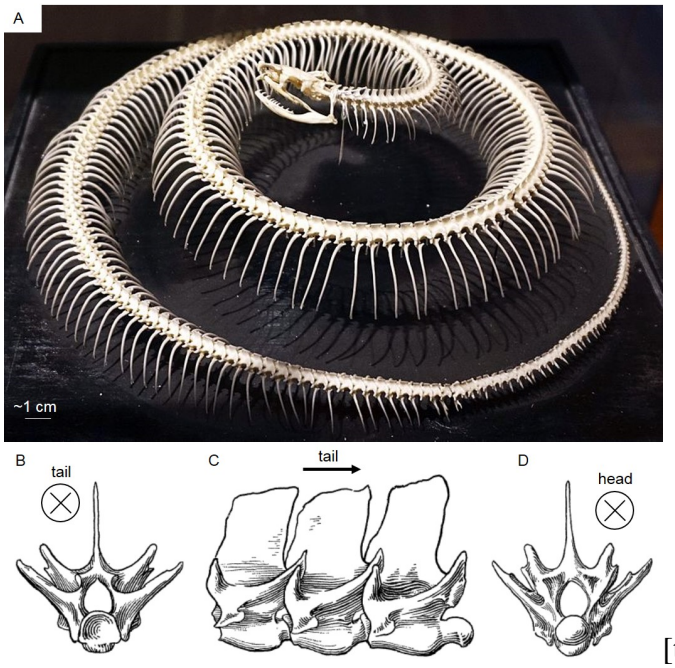


[t!]

Figure 1.6: Snake skeletal structure. (*A*) Example snake skeleton. Most of the body is an elongated ribcage. Ribs are connected only at the top to the vertebrae, allowing articulation and expansion of the ribs. Photo courtesy [55]. (*bottom*) Drawing of a trunk vertebrae as viewed from (*B*) the front (*C*) the side, and (*D*) the back. The club-like structures articulate with the neighboring vertebrae, limiting torsional motion. Reproduced from [56]

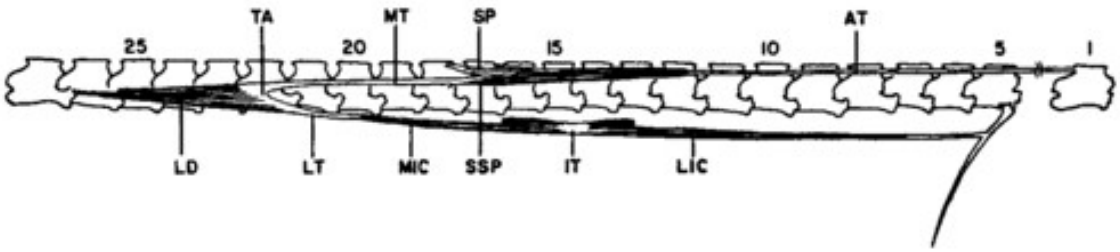


Figure 1.7: Snake locomotor musculoskeletal structure. Figure and caption reproduced from [58]. Simplified right lateral view of the major epaxial muscle segments of *Elaphe obsoleta quadrivitata*. Anterior is to the right. SP and SSP, respectively, indicate the spinalis and semispinalis portions of the M. semispinalis-spinalis, and AT is the anterior tendon of the SSP-SP. LD represents the M. longissimus dorsi, and MT, TA, and LT are the medial tendon, tendinous arch, and lateral tendon of LD. MIC and LIC, respectively, are the medial and lateral heads of the M. iliocastalis, and IT is its intermediate tendon.

snakes.

## 1.3 Neuromechanics

Neuromechanics is the study of how movement arises from the interaction between physiology, neurology, and terrain physics [59]. Deformation of the body can be either actively actuated, e.g. by muscle contractions, or passively arise as a result of stresses applied by the surroundings. It then seems natural that feedback from the surroundings is important to ensure successful locomotion during interactions with complex and unexpected terrain

Typically, feedback is classified as being either neural or mechanical in nature (Fig. 1.8). Neural feedback involves the nervous system and integrates information gathered from the environment by senses like vision and touch and/or information on the internal state of the animal collected using proprioceptive sensors like the inner ear and muscle spindles. An example of neural feedback is the wall-following of a cockroach, in which the animal uses its antennae to sense the relationship between itself and a wall and uses this information to follow bends [60]. In contrast, mechanical feedback acting at the level of the musculoskeletal system uses appropriately designed mechanics and gaits which conspire to create stable locomotion without the input of the nervous system [61, 62]. Rapidly running cockroaches

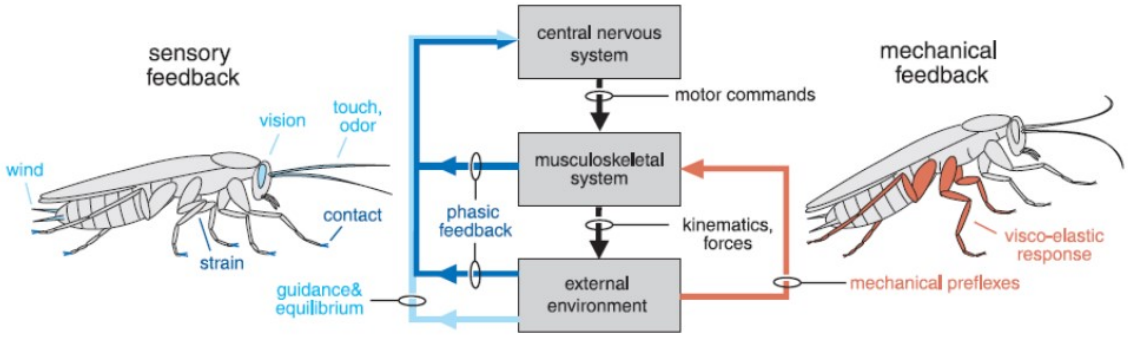


Figure 1.8: Neural and mechanical feedback in moving animals. Figure and caption reproduced from [67]. Both neural and mechanical feedback play roles in controlling locomotion. Although depicted here for a cockroach (shown running slowly on the left, running fast on the right), the diagram represents a general model for locomotor control. The central nervous system generates motor commands that activate the musculoskeletal system of the animal. The musculoskeletal system, in turn, acts on the external environment. The external environment is sensed by multiple modalities and fed back to the central nervous system. Sensory feedback may be divided into three broad categories: guidance and equilibrium from a variety of different modalities (shown combined as light blue) and rapid phasic feedback from mechanosensors (dark blue). The nervous system processes the sensory feedback and modifies the motor commands. In parallel, ic mechanical preflexes (red) act rapidly to resist perturbations.

can rely on mechanical properties of the limbs and gait design to remain stable without input from the nervous system [63, 32]. Carefully designed two-legged walkers can walk down a slope without any motor or control using only the energy provided by gravity [64]. Arthropods can run quickly across complex surfaces by using passive mechanical mechanisms, spines on the limbs which grip onto heterogeneity, without carefully planned foot placement [65].The passive dynamics of a newly deceased trout body results in upstream swimming under the influence of vortices shed from an obstacle [66]

Snake robots, generally consisting of a series of linked motors each responsible for the entire actuation of the related joint, are difficult to control due to the many degrees-of-freedom (DoF) body [68]. Typically, movement in robots relies on precise control of all joint angles, whether to avoid or utilize obstacles, to ensure the body remains coordinated [69]. Effective control strategies have required either tactile [69] or proprioceptive [70] sensing of the environment, and subsequent determination of control targets based on this

information This is in contrast to robots which used other means to generate anisotropy (wheels) did not require rigid obstacles for propulsion and instead sensed them and controlled the body to mitigate their effect [71, 1].

A possible simplification to the challenge of coordinating the many DoF is the repetitive nature of the segments (Fig. 1.7). Undulatory locomotion arises from muscle activation which occurs at constant phase offsets in different body segments [72]. There is evidence that undulatory vertebrates like lamprey have central pattern generators (CPGs) [73, 29]. CPGs are neuronal circuits which generate rhythmic motor patterns from a non-rhythmic input [74]. For example, the lamprey spinal cord exhibits undulatory motion when immersed in a chemical bath, that is, it exhibits a cyclic motor behavior given the non-phasic input of the chemicals in the bath [73, 29]. *C. elegans* is not believed to have CPGs, but research indicates the undulatory motion is coordinated by local excitatory and inhibitory stretch-sensitive neurons which control activation of the muscles based on the local state of the body, namely, the length changes measured at off-axis body positions [75]. Local coordination mechanisms like CPGs and stretch-activation neurons can ensure the successful propagation of body waves without the direct intervention of the central nervous system.

The snake neuromechanical system is not known as well as, e.g. the lamprey or *C. elegans*. Still, there have been previous efforts; some studies performed electromyographic (EMG) measurements of snake muscle activation in freely moving snakes. The coordination of muscle activity with the relative position on the body of external obstacle/s suggests that these snakes are sensing the environment and actuating muscles to create the appropriate waveform response. Generalist snakes using a single post for propulsion utilized a precise pattern of muscle activation to enable effective forward motion ([76] using the boid *Python regius*,[77] using the colubrid *Pituophis melanoleucus affinis*). Muscle activity was confined to the area around the post, and [77] observed local manipulation of the body wall shape to create a cam-follower mechanism.

Snakes moving in post arrays of multiple posts used unilateral activation of the epaxial

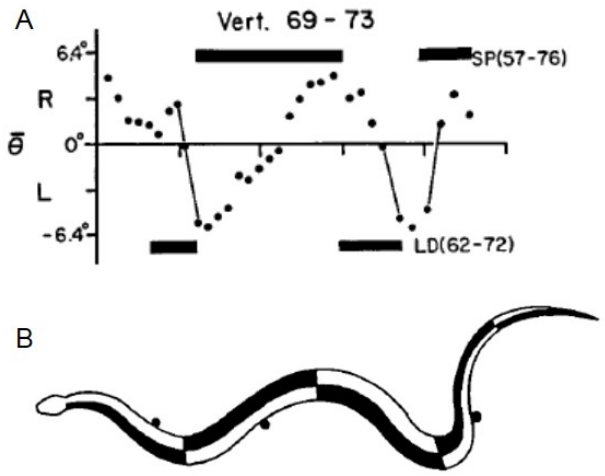


Figure 1.9: Snake muscle activation during terrestrial lateral undulation. (*A*) Simultaneous EMG and kinematic measurements of the colubrid water snake *Nerodia fasciata*. Dots are measurements of the local joint angles at the location of the EMG measurement. The bars indicate when the muscle segments on the right (top) and left (bottom) side of the body were active. (*B*) Diagram of hypothesized pattern of muscle activation in a snake using lateral undulation in terrestrial terrain (modeled as rigid posts affixed to a hard substrate). Black areas indicate active musculature. Figure adapted from [58]

musculature to self-deform (Fig. 1.9)[58]. The change in activation of left side muscles to those on the right side occurs approximately at the apexes of the wave (Fig. 1.9 *B*)[58].

This dissertation will address the lack of knowledge highlighted above by investigating pieces of the snake neuromechanical system. We study the interaction between a laterally undulating snake and a model for deformable terrestrial terrain, granular matter to determine why, within the context of the substrate physics, the animal chooses to use the observed gait. We probe the possible role of passive dynamics in snakes by observing the kinematics as they contend with unexpected collisions with sparse obstacles and compare the results with a model. Lastly we begin exploring the role of sensory feedback in a comparative study of snakes in obstacle arrays.

## 1.4 Movement within and on granular matter

### 1.4.1 Granular matter as a model deformable substrate

Terrestrial terrains are commonly a mixture of materials of different states and properties. For example, moving across the floor of a forest one may encounter soils ranging from loose, dry grains to muds, leaf litter, soft, rotten plant matter, twigs, rocks, and any other number of items in various combinations.

Much progress has been made in understanding undulatory swimming of organisms in fluids using both animal experiments and computation of the body-fluid interaction using the Navier-Stokes equations (see e.g. [23, 24, 25] and references therein). A common feature of many terrestrial environments are flow-able substrates like sand, soil, mud, and leaf litter. A constitutive equation does not exist for these materials, and in general the physics of these materials is unknown.

Granular materials (GM) like sand, however, have been well-studied. Granular materials are collections of discrete, macroscopic particles. While GM can flow like a fluid, the primary difference between the two is that a collection of GM can support shear at rest [78]. The physics of a GM depends on the volume fraction, $\phi$, the ratio of grain-occupied volume to total volume. Under localized forcing material will compact, if $\phi < \phi_c$ and dilate if $\phi > \phi_c$. This dilatancy is another feature that separates GM from fluids. GM can also behave like a gas, however, granular materials are athermal. Grain-grain interactions are dissipative because of the dominance of static friction and inelastic collisions [31]. The granular materials considered in this document are dominated by repulsive forces; grain-grain cohesion is negligible.

### 1.4.2 Granular resistive Force Theory

Resistive force theory for granular media was developed to explore the connection between body deformations and performance in GM [79, 80]. This scheme was originally developed

by Gray and Hancock [34]to predict performance of low-Re swimmers. The calculation uses the assumption that the forces on each body segment $ds$ are independent such that the total force acting on the body is the sum of forces $dF$ acting on each body segment given its motion through the fluid (Fig. 1.10).

Body segments will move through the surroundings given a pattern of self-deformation which determines the orientation and velocity of each segment, $\hat{t}$ and $\vec{v}$ respectively in the lab frame. In viscous fluids the forces acting on a segment can be calculated using Stokes law in which the forces are proportional to the velocity. Lighthill approximated the coefficients for the perpendicular and parallel forces from Navier-Stokes acting on an elongate body with no-slip boundary conditions [81]. The ratio of these coefficients determines how much the body will slip backwards during motion. For example, if the coefficients are equal the body will undulate in place whereas if the ratio becomes large the body will move "in a tube" with every segment following exactly in the path of its anterior neighbor.

There are not constitutive equations for GM that play the role of Navier-Stokes for fluids. Therefore, the force acting on a segment is measured empirically by dragging an object through GM and measuring the resulting forces. By varying the orientation of the intruder one constructs a function describing the forces acting perpendicular, $F_{\perp}$, and parallel, $F||$, to the intruder (Fig. 1.10).

As discussed in more detail in the following section, resistive force theory has proven effective in predicting motion in GM, more so than in the fluids for which it was initially formulated. This method is not accurate in calculation of certain high-Re swimmers as the assumption that forces are hydrodynamically decoupled is violated–there is a flow which moves along the body–and body segments are not interchangeable in that vortex shedding at the tail is an important source of force generation [25]. We note that in some high-Re systems a similar procedure, blade element theory, in which the total force on a surface is assumed to be the sum of the reactive forces on independent, infinitesimal surface elements [82]. RFT was also found to be inaccurate in predicting the forces acting on a helical

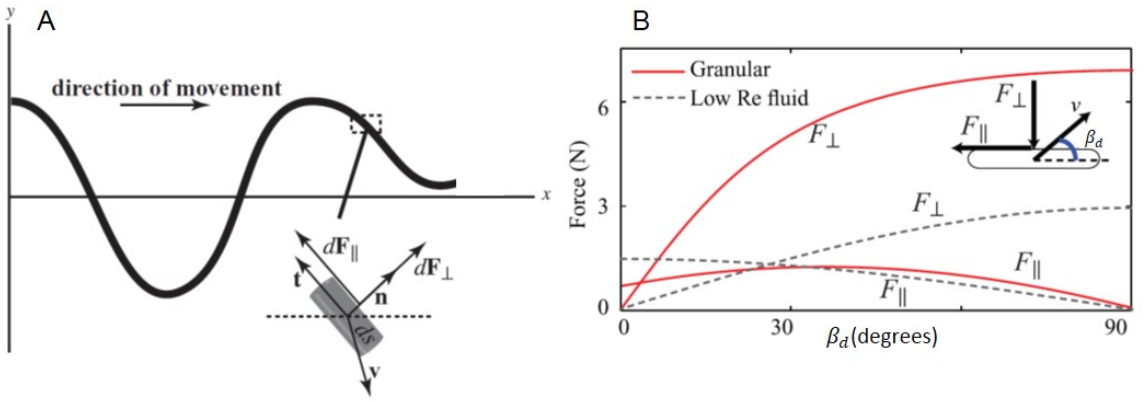


Figure 1.10: Resistive force theory. (*A*) Diagram of undulatory swimmer. Wave propagating right to left, driving the organism left to right. Forces acting on the infinitesimal element $ds$ may be decomposed into those acting normal and tangential to the segment. (*B*) Example force relations. Forces normal and tangential to a segment as a function of the angle between the velocity and tangent vectors. In fluids (dashed line) these are described by Stokes law. In granular matter the forces are empirically determined via drag experiments. Adapted from [30]

flagella at biologically relevant scales [83]. In this case, the coils of the helix are close-enough to each other that the segments are hydrodynamically coupled.

### 1.4.3 Undulatory motion immersed within granular matter

A variety of desert-dwelling reptiles are *subarenaceous*, a term proposed by [84] to apply to animals whose adaptive traits, distinct from those observed in subterranean animals which burrow in firm soil, allow them to not only bury but swim within sand.

The sandfish lizard (*Scincus scincus*, (Fig. 1.11*A*) not only quickly buries into loose GM but also swims for many body lengths while completely immersed. X-ray imaging was used to discover that the sandfish propels itself when immersed within 300 $\mu m$ glass particles by tucking the limbs against the body and using head-to-tail undulations to propel itself [79] (Fig. 1.11*C*) . The motion was dominated by the grain-grain and grain-body frictional forces such that the inertia of both the grains and the animals body is negligible–the system is analogous to swimming in a frictional fluid [79]. Because the system is dominated by these dissipative forces, flow of the GM at one body segment does not change the flow

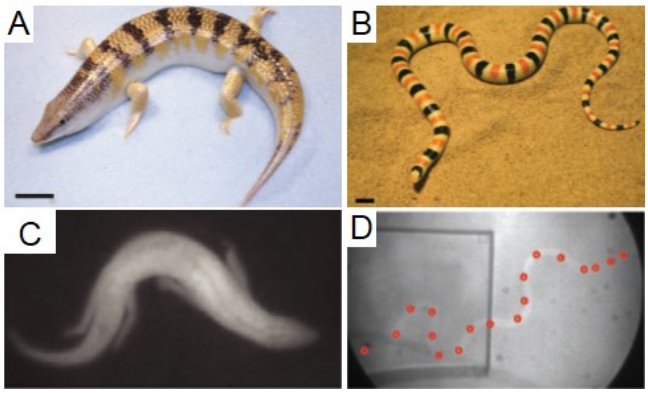


Figure 1.11: Subsurface sand swimmers (*A*) the sand fish skink *Scincus scincus* and (*B*) the shovel-nosed snake *Chionactis occipitalis*. Scale bars in *A* and *B* are 1 cm. (*C*) X-ray image of *S. scincus* and (*D*) *C. occipitalis* swimming immersed within 300 $\mu$m glass particles. Red circles are lead markers affixed to the midline of the snake used for tracking. *A, B* and *D* are adapted from [13] and *C* from [85]

around other parts of the body. Therefore, the total force is the superposition of the forces acting independently on each segment. This property of swimming in GM means resistive force theory (RFT), discussed in further detail below, is an effective method for calculating stresses experienced by the animal and subsequently predicting animal performance as a function of self-deformation pattern.

RFT predicted that the waveform used by the sandfish conferred the benefit of both maximizing the undulation efficiency ($\eta_u$, distance traveled per cycle divided by the arclength of one wave) and minimizing the weight-specific mechanical cost-of-transport (CoT, total power output divided by the forward speed and body weight) [86, 13] (Fig. 1.14 red curves). EMG signals increased as the animal experienced larger external resistance to movement, whether by moving deeper into the material or moving in close versus loose-packed GM, suggesting that the animals were using proprioceptive feedback to execute the desired, beneficial, kinematics [86].

Using RFT Ding et al. [87] predicted the pattern of torques acting on the body of the sandfish and their relationship to the shape of the animal. They found that the pattern of torques, like the curvature of the body, passed from head to tail. However, the torque

lagged behind the curvature. This lag was commensurate with the lag observed in electromyographic (EMG) experiments measuring the timing of muscle activation with respect to the observed animal kinematics and is observed in other systems which use undulatory locomotion, e.g. [10].

The Shovel-nosed snake *Chionactis occipitalis*, like the sandfish, buries into and moves within GM (Fig. 1.11*B,D*). This Colubrid snake is native to the deserts of the Southwestern United States and Northwestern Mexico (Fig. 1.12*top*). This species spends most of its time in the subsurface environment occasionally using pre-existing tunnels but most often moving through loose sand, emerging daily to forage for a total period of time not exceeding five hours [88]. The reason for their fossorial behavior is not definitively known, although it is generally accepted that this species uses the underground environment to escape unfavorable temperatures [88].

*C. occipitalis'* morphology is distinct from the sandfish. It is limbless, and has a larger elongation ratio (length divided by body width) at 33.3±2.5 as compared to *S. scincus'* 7.0±0.4 [13], 1.11*A,B*). The snake also has slick scales which reduce the friction between GM and the integument by a factor of $\approx 2$ (static friction coefficient between ventral scutes and 300 $\mu$m glass particles, animal sliding forward as in usual locomotion $\mu_{snake} = 0.109 \pm 0.016$, $\mu_{skink} = 0.194 \pm 0.022$ [13]).

Sharpe et al. [13] performed a comparative study of *S. scincus* and *C. occipitalis* during subsurface swimming in dry GM. They found that the snake used more waves on the body, wavenumber $\xi$=3.5, than the sandfish, $\xi$=1 The amount the snake's body was slipping perpendicular to the local direction of motion, defined $\beta_s = acos(|\hat{t} \cdot \hat{v}|)$, was $6.9 \pm 1.6^\circ$ versus the sandfish slip of $21.2 \pm 3.5^\circ$ The slip values were well-predicted by RFT calculation for fixed $\xi$ and varying relative curvature $\kappa_m \lambda_s$, a dimensionless variable capturing how sharply bend the body is (Fig. 1.13). $\kappa_m \lambda_s$ is calculated by averaging the product of the maximum curvature and the arclength of each wave along the body and through time.

Using RFT, Sharpe et al. [13] compared the relationship between $\eta_u$, CoT, and $\kappa_m \lambda_s$

Figure 1.12: *C. occipitalis* range and habitat. (*top*) Map indicating the range of *C. occipitalis*. (*bottom*) Example photographs of the snake's natural habitat. Taken by the author. Map compiled by rbrausse with Quantum GIS Map data: Made with Natural Earth. Free vector and raster map data naturalearthdata.com. Range data: Hammerson, G.A., Frost, D.R. Gadsden, H. (2007) Chionactis occipitalis. IUCN 2013. IUCN Red List of Threatened Species. Version 2013.1 Downloaded on 20 October 2013. - own work, based on naturalearthdata.com/downloads (downloaded Oct. 2012) and s3-eu-west-1.amazonaws.com/spatial-data/groups/REPTILES (downloaded Sep. 2013)

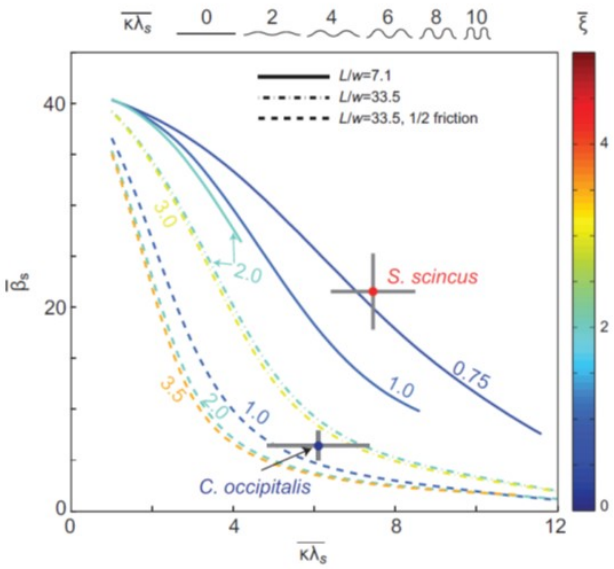


Figure 1.13: RFT prediction of sandfish (red) and snake (blue) average slip value, $\bar{\beta}_s$ for waveforms of different relative curvature $\kappa_m\bar{\lambda}_s$. Curves for different number of waves on the body, $\xi$ are as labeled. Solid lines are for the sandfish L/w=7.1 and body-particle friction $\mu_{skink}$=0.17. Dash-dot curves are for the snake L/w=33.5 and the same friction as the sandfish. Dashed lines are prediction for body-particle friction which is halved, reflected the factor of two difference in body-particle friction between the sandfish and the snake. Figure reproduced from [13]

for the two species. RFT was a good predictor for animal performance, and both species were near the maxima of the $\eta_u$ curves and minima of CoT curves calculated for their given morphology and skin friction (Fig. 1.14). The snake moved with lower slip, lower CoT, and higher $\eta_u$. The long, slender body of the snake allowed it to maintain a high average curvature while increasing the number of waves on the body, that is, its morphology permitted access to a greater number of waveshapes. Further, the reduced friction of its skin appeared advantageous as it reduced the drag on the body.

RFT prediction and the improved performance of *C. occipitalis* as compared to *S. scincus* suggests two (not necessarily independent) routes to improving performance in GM; choosing the correct kinematics for a given body shape and having the "right" morphological features, both by decreasin-g skin friction and increasing L/w to access more effective kinematics [13].

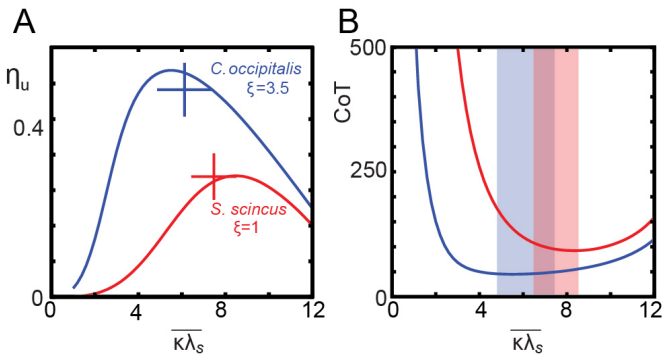


Figure 1.14: RFT prediction of sandfish (red) and snake (blue) performance for waveforms of different relative curvature. Number of waves on the body was fixed at 1 for the sandfish and 3.5 for the snake (*A*) Undulation efficiency, $\eta_u$ is distance traveled in a cycle divided by the arclength of one wave. Crosses are mean and standard deviation of measurements from animal experiments. (*B*) RFT predicted cost-of-transport (CoT). Shaded regions are the kinematics of the animals. Figure adapted from [13]

### 1.4.4 Stepping on the surface

The sidewinder rattlesnake *Crotalus cerastes* shares a habitat with *C. occipitalis*. This animal's elongation ratio is $L/w = 20.0 \pm 4.2$ ($L$ from [89], $w$ measurements made by Henry Astley). This species does not sand-swim, and uses the sidewinding gait (1.2.1) to move across the surface of GM. The sidewinder changes its kinematics when ascending sloped granular matter [89]. The snake increases the length of body in contact with the substrate to decrease the stress applied to the GM and prevent material yield [89].s

Hatchling Loggerhead sea turtles use their flippers, adapted for swimming within water, to move many body lengths across sand to travel from the nest to the water. When moving across sandpaper fixed to a rigid board the turtles kept the limbs fully extended while when moving in GM the wrist would bend, solidifying the GM and facilitating performance that was unchanged from that on a rigid substrate [90].

Mazouchova et al. [91] studied a robophysical model of the sea turtle which revealed that having a mobile wrist minimized disturbance of the substrate. They measured granular resistance as a function of how far from previously disturbed material the intruder was placed and found that both penetration and drag forces decreased as the intruder moved

closer to previous "footprints." By changing the morphology of the robot to having a flexible wrist that solidified the material and increased steplength the robot avoided the locomotor failure which resulted from re-interacting with previously disturbed material.

The mudskipper *Periophthalmus barbarus* is a small fish that uses a crutching motion of the pectoral fins to move on land. When challenged to climb a sandy slope the animals used the tail as an additional appendage [92]. A robophysical muddskipper revealed that use of the tail enabled the robot to maintain large enough step length on the sandy slope to avoid failure from interaction with previous tracks [92]. The addition of the appendage and its appropriate kinematic use allowed robust locomotion when the crutching kinematics or substrate condition were suboptimal.

## 1.5 Organization of the thesis

The remainder of this thesis is organized as follows

- Chapter 2. Study of the connection between gait, terrain physics, and the resulting performance in lateral undulation in deformable substrates using as a model a desert-specialist snake in GM.
- Chapter 3. The role of passive mechanics in contending with unexpected collisions is studied by adding a single row of obstacles to a spatially uniform substrate.
- Chapter 4. Use 2D arrays of posts to examine the relative importance of obstacle density, substrate (usable versus not), and kinematics in multi-modal terrains.
- Chapter 5. Miscellaneous studies: granular drag experiments to understand forces acting on early tetrapods ascending sandy slopes, a torque-limited robot traversing a single row of posts, determination of shape basis function for subsurface sand-swimming animals, and an investigation of lizard running in heterogeneous terrain.

# CHAPTER 2

# SAND SWIMMING

## 2.1 Summary

Elongate, limbless animals move in both fluid and terrestrial habitats using flexural waves of the body. While swimming in fluids is well-studied, little is known about undulatory motion in materials like mud, rotten flora, and granular matter (GM) where the surroundings provide propulsion while yielding but, unlike fluids, may be permanently deformed by the interaction. We studied the desert dwelling snake *Chionactis occipitalis* using lateral undulation to move quickly (2-3 bodylengths/s) across homogeneous GM. The body segment angles of the ten individuals tested were well described by the same sinusoid. Surface drag measurements revealed that the ratio of thrust to drag forces, a determining factor in undulatory performance, did not depend on speed or depth; movement was non-inertial and depended primarily on the animal's shape. Using resistive force theory (RFT) we found that the specific waveform used by the snakes maximized center-of-mass speed given a constraint on peak muscle power. We explored differing waveforms using a robophysical model, a 10-link robot snake, and found that shapes which did not progress enough per gait cycle, such that the robot interacted with previously disturbed material, led to locomotor failure. The animal's waveform was in the regime where motion was like that in a frictional

Drag data was collected by Drs. Jennifer M Rieser and Christian Hubicki. Snake dissection and torque estimation and robot design and build were carried out by Dr. Henry Astley. Robophysical data was collected by Kelimar Diaz Cruz during an REU. Laser line calibration and analysis and data collection was performed by Alex M Hubbard (undergrad, BME). Snake lifting data was collected by Alex Hubbard with the aid of Lillian Chen (undergrad, Bio) and Sarah Bowling (undergrad, Physics). RFT calculation was based on code written by Dr. Tingnan Zhang.

This contents of this chapter are adapted from a manuscript in preparation by Perrin E Schiebel, Jennifer M Rieser, Christian Hubicki, Alex M Hubbard, Henry C Astley, Kelimar Diaz Cruz, and Daniel I Goldman.

fluid; by limiting material yield the animal avoided contending with the memory-dependent effects that led to robot failure.

## 2.2 Introduction

Movement via propagating undulatory waves of the trunk appears in organisms across scales and is adaptable to a wide range of terrains and habitat. The microscopic (length $O(mm)$) nematode *Caenorhabditis elegans* lives in a variety of rotting plant matter [2]. In the laboratory *C. elegans* can undulate through fluids of viscosity encompassing orders of magnitude [3], non-Newtonian fluid [4], and rigid post arrays of varying post sizes and densities [5, 6, 7]. Macroscopic (length $O(dm)$) eels not only swim, but can burrow in mud [8, 9] and crawl across land [10]. Snakes from a few centimeters to meters in length swim in water [11], crawl through tunnels [12], burrow in sand and soil [13, 14], climb trees [15], glide through the air [16], and traverse a range of terrestrial terrains [17, 18, 19, 20, 21].

Much progress has been made in understanding undulatory swimming of organisms in fluids using both animal experiments and computation of the body-fluid interaction using the Navier-Stokes equations (see e.g. [23, 24, 25] and references therein). During swimming in fluids the character of the system is captured by the Reynolds number, the ratio of reactive to resistive forces in the system. For example, *C. elegans* is a low-Reynolds (low-Re) number swimmer–most of its propulsion comes from the resistance of the surrounding material to the motion of the animal. By contrast, eels are at high-Re–propulsion is primarily provided by reactive forces generated by vortices shed by the animal's tail. Low-Re animals cannot "glide" through their surroundings, as soon as self-deformation ceases the viscous surroundings will immediately halt motion (see [40, 41] for review of low-Re swimming).

However, principles of undulatory locomotion on the surface of terrestrial terrains, where materials may yield and permanently deform in response to the locomotor interaction, remain largely unknown.

Granular matter (GM) was previously used as a model for deformable material. While constitutive equations such as Navier-Stokes do not yet exist for GM, resistive force theory (RFT) [34], using empirically obtained equations for the material stress response, can predict the forces experienced by a locomotor in GM [79, 92]. The undulatory motion of organisms completely immersed within GM was found to be like swimming in a frictional fluid [79]; GM re-flows around the animal, ensuring consistent contact with material.

At the GM-air interface, however, the material can be permanently deformed. The presence of "tracks" changes the physics of the substrate. Legged robots using a crutching motion on the surface of GM were negatively impacted when limbs interacted with previously disturbed material; effective forward motion relied on the ability to move far enough per step that the limb was placed in fresh material [91, 92].

How do slithering animals handle memory effects without the option of taking larger steps to avoid their previously-laid tracks? Some species of snakes achieve this by using a specialized sidewinding gait in which loops of the body are placed into static contact with the substrate [17]. The most common mode of locomotion, however, and the only gait shared among all of the elongate, limbless vertebrates, is lateral undulation [45] in which the belly of the animal slides along the substrate driven by posteriorly propagating horizontal waves of the trunk [17].

Similarly to the performance of limbed robots on the surface, a robot failed to translate on poppy seeds when it could not reach undisturbed material after a gait cycle [85]. Failure modes like those observed in the robot on poppy seeds were also seen in several living snake species moving on GM [89].

We chose to study the desert-dwelling *Chionactis occipitalis*, the Shovel-nosed snake (Fig. 2.1*A*), which appears to glide effortlessly across GM. Its body slips little during movement, leaving behind clear tracks (Fig. 2.1*B*). This animal moves many body lengths on the surface using stereotyped, periodic flexions of the trunk which pass from head to tail propelling the animal in the direction opposite wave propagation [48].

In studying this model system, we aimed to determine strategies for effective locomotion on the GM surface using a combination of animal experiments, granular drag measurements incorporated into a surface RFT calculation of performance, and a robophysical model to explore changing waveforms and the limitations of RFT. By studying motion on GM we hope to shed light on strategies for movement in other deformable terrestrial materials like muds, leaf litter, and snow.

## 2.3 Results

### 2.3.1 *C. occipitalis* uses a stereotyped serpenoid waveform

In the laboratory we challenged ten *C. occipitalis* to traverse a model desert substrate with properties similar to that of naturally occurring sands ($270\pm40$ $\mu$m spherical glass particles). An air-fluidized bed prepared the material to an undisturbed, loose-packed state before the animal was introduced to the track way (Appendix 2.5.1). The snakes moved across the surface using alternating left and right bends of the body. Some of the animals moved almost "in a tube" where all segments of the body followed in the path of their rostral neighbors (2.1*C, top*). Others used this strategy only on the anterior portion of the body, appearing to drag the posterior segments in a more or less straight line behind themselves (Fig. 2.1*C, bottom*).

An overhead camera captured kinematics and we tracked the black bands on the snake to determine the body midline positions (Fig. 2.1*C*) using the method described in [13]. The tangent angle, $\theta$ (Fig. 2.1*D*), represented body posture at each instant in time. Space-time plots of $\theta$ (Fig. 2.1*E*) manifested the observed alternating left and right bends.

Principal component analysis (PCA) was a useful tool in revealing a low-dimensional representation of *C. elegans* waveforms [93]. The principal components (PCs) are eigenvectors of the tangent angle covariance matrix which form an orthogonal basis describing the variation of $\theta$ along the body. There were two dominant PCs ($A_1$ and $A_2$) which accounted for $\approx 91\%$ of the variance, meaning most of the snake shapes we measured could

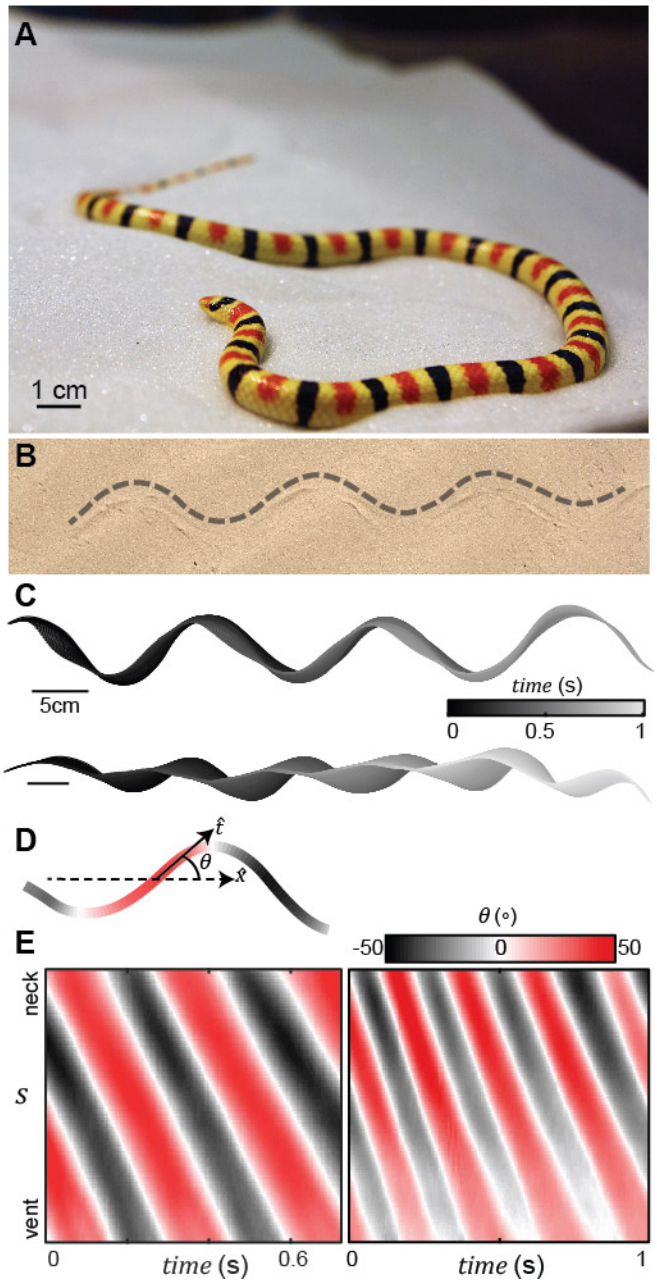


Figure 2.1: **The Colubrid snake *Chionactis occipitalis*** (A) *C. occipitalis* in the lab on glass particles. (B) *C. occipitalis* tracks found in the Mojave desert, Arizona, USA. The animal was moving from left to right as evidenced by the location of the sand "waves" generated by the body during movement. Dashed line is slightly above the tracks to guide the eye. (C) Digitized midlines of two different individuals, 131 (*top*) and 128 (*bottom*). Time indicated by color. (D) Tangent angles of each segment, $\hat{t}$, were calculated using finite differences. $\theta$ was the angle between $\hat{t}$ and the average direction of motion of the animal, $\hat{x}$. (E) Space-time plots of $\theta$ measured from the trials in C. The diagonal bands indicate a posteriorly traveling wave propagated at constant speed.

be represented as $\theta(s,t) \approx \alpha_1(t)A_1(s) + \alpha_2(t)A_2(s)$. We found the coefficients $\alpha_1$ and $\alpha_2$ using $\alpha_i(t) = A_i(s)^T\theta(s,t)$. The PCs were well-fit by sinusoids with phase difference $\pi/2$ (Fig. 2.2*A*) which, when combined with the circle traced by the coefficients through time (Fig. 2.2*B*), yields a traveling sinusoidal tangent angle along the body. Such a wave is called a serpenoid curve, $\theta(s,t) = \theta_m sin(2\pi\xi/L(s + v_{seg}t))$ [94]. The amplitude $\theta_m$ is the maximum value of $\theta$, $\xi$ is the number of waves on the body, and $v_{seg}$ is the wave propagation speed of the segments (the speed of travel if one were riding on the body).

The relationship between $v_{seg}$ and the velocity magnitude of the center-of-mass (CoM) of the animals, $v_{CoM}$ was linear (mean and 95$\%$ confidence intervals of slope=0.81 (0.74, 0.89), y-intercept=0.67 (-4.63 5.94). R-squared=0.94, RMSE=2.88) Fig. 2.2*C*). Previous study of a slow-moving snake on a minimally-deforming surface came to the conclusion that the system could be characterized as low-Re [49]. We posited that the physics governing interaction between the animal and its surroundings was independent of locomotor speed (further supported by the drag experiments in the following (Appendix 2.3.2). The important variables determining performance were therefore those associated with shape of the animal's body, $\theta_m$ and $\xi$.

The range of serpenoid curves which the snakes could physiologically achieve were previously estimated by measuring how sharply the body may be bent under anesthesia [13]. While there was some individual variation, the animals used a limited range of the shapes they were capable of adopting (Fig. 2.2*D*, colored crosses).

The surface waveform was distinct from that used by this species when moving buried within the GM (Fig. 2.2*C*, gray cross [13]). While the angular amplitude was not significantly different (subsurface $\theta_m = 54.7 \pm 11.9^\circ$ compared to the surface value $\theta_m = 48.3 \pm 7.0^\circ$ for all snakes combined, 2-tailed t-test $P = 0.04$), the value of $\xi$ was less for surface swimming ($\xi = 3.53 \pm 0.85$ subsurface versus $\xi = 1.90 \pm 0.14$ at the surface, P$< 0.001$).

There was a slight downward trend in the relationship between $\xi$ and $\theta_m$. We fit a line to

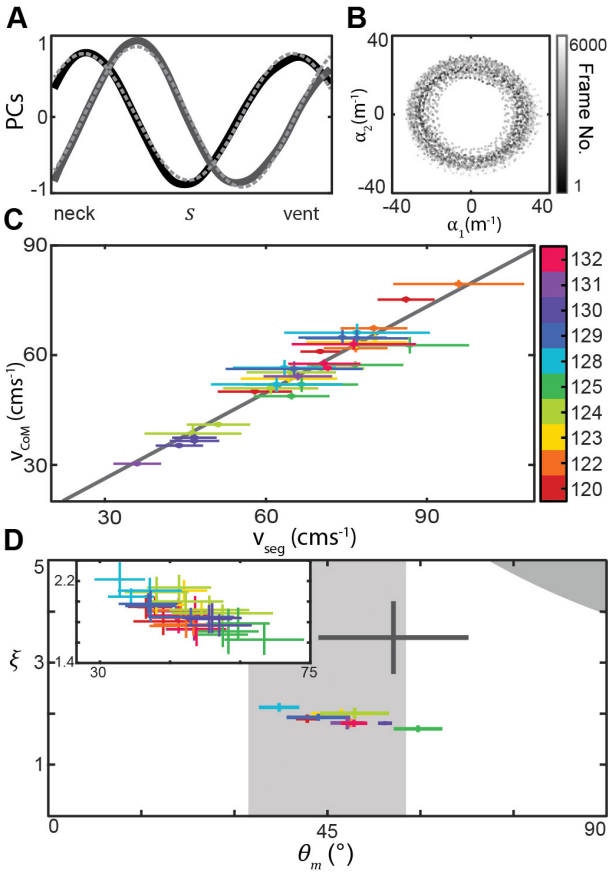


Figure 2.2: **Serpenoid template for sand swimming.** N=10 individuals, 32 trials. (A) The dominant two PCs representing $\theta$. The solid lines are the experimental results, the dashed lines are sine fits to $A_i sin(\xi_i s + \phi_i)$. Coefficients with 95% confidence bounds were $A_1 = 0.83\ (0.82, 0.84), A_2 = 0.92(0.90, 0.94)$, $\xi_1 = 1.44(1.43, 1.45), \xi_2 = 1.40(1.39, 1.41)$, $\phi_1 = 0.05\pi(0.04\pi, 0.06\pi), \phi_2 = -0.41\pi(0.42\pi, 0.39\pi)$. $\phi_1 - \phi_2 = 0.46\pi$. Both vectors were divided by the same maximum value such that the maximum amplitude was one. (B) The amplitudes $\alpha_1$ and $\alpha_2$ associated with the PCs in A. The color corresponds to the data. The trajectories move counterclockwise around the circular structure, indicating a traveling wave. The radius of this circle is the amplitude of the wave of $\theta$. (C) $v_{seg}$ is linearly related to $v_{CoM}$. The mean and range of each trial are plotted separately, colored by individual number. Gray line is the linear fit. (D) Serpenoid parameter space $\theta_m$ and $\xi$. Colored markers are the mean and standard deviation of each individual taken over all trials. Colors correspond to C. The gray cross is the waveform used by *C. occipitalis* when moving subsurface. The light gray rectangle illustrates the range of $\theta_m$ measured from photographs taken of *C. occipitalis* tracks found in the desert. The gray region in the upper right corner are waves which are inaccessible given the flexibility of the snake.

the points displayed in Fig. 2.2*C, inset* (slope -0.016 (-0.020,-0.011) intercept 2.66 (2.42, 2.90), R-square=0.6). Given the weak dependence of $\xi$ on $\theta_m$, which was on the order of experimental error, we decided to combine all of the individual measurements and explore the impact of the average wave, taken as the mean and range across all measurements.

We measured the angle of attack in photographs we collected of tracks in the desert (example Fig. 2.1*B*) and found it was comparable to the $\theta_m$ measured in our laboratory tests ($theta_m = 45.0 \pm 12.7°$, P= $0.31$ Fig. 2.2*D*, gray rectangle).

### 2.3.2 Granular resistance to drag for a partially submerged plate

Movement in sand is facilitated by granular resistance to intrusion and drag. The snake body applied stress which yielded the material, building granular piles on the caudal-facing side of the waveform (Fig. 2.1*B*, Fig. 2.3*A*, Fig. 2.8*B*). We used laser-line measurements of the granular surface to measure track depth (Fig. 2.8Appendix 2.5.3) and found that the snakes intruded at most 5 mm into the material, compared to the average body diameter of $9.2 \pm 0.05$ mm (measured at each black band from immediately behind the head to the vent).

Constitutive equations such as Navier-Stokes for fluids do not yet exist for granular materials. Therefore, we empirically measured the granular stress on a simple model for a snake body segment, an aluminum plate moving at velocity $v_d$ at an angle $\beta_d$ defined relative to the plate face (Fig. 2.3*A,B*). Stresses normal, $\sigma_n$, and tangent, $\sigma_t$, to the plate face were measured as the plate was dragged parallel to the surface for 20 cm at a constant depth, $z$, measured from the intruder's bottom edge (Fig. 2.3*B*). $\beta_d$ was varied from $0°$ (like a blade) to $90°$ (like a plow).

Unlike subsurface drag stresses which developed almost instantaneously to the steady state [79], at the surface, stress monotonically increased over several centimeters before saturating (Fig. 2.3*C*). This is likely due to a pile of sand above the free surface which developed at the front face of the intruder and grew in size over several cm before reaching

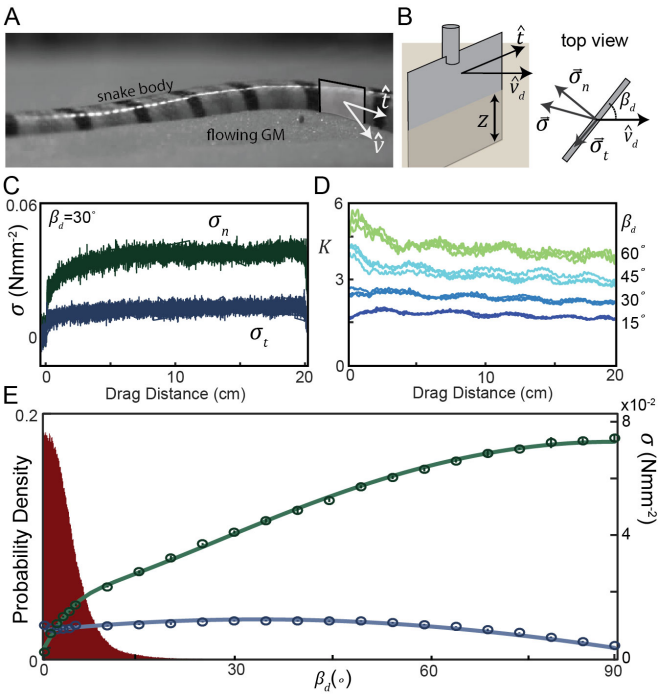


Figure 2.3: **Empirically measured stress on a partially buried intruder.** (A) Side-view of *C. occipitalis* moving on the surface. Snake is moving from left to right. The surface was initially featureless, the piles of sand were generated by the snake. We chose the simplest model of a snake body segment, a flat plate aligned with $\hat{t}$ of the midline moving in direction $\hat{v}$. (B) Aluminum blade model of a snake segment, $3 \times 1.5 \times 0.3$ cm$^3$. *Left*, the plate was kept at a constant depth, $z$, from the undisturbed free surface of the GM to the bottom of the intruder. *Right*, a force transducer decomposed stresses into $\sigma_t$ and $\sigma_n$. (C) Raw drag data collected at $\beta_d = 30°$ and $v_d = 10$ mms$^{-1}$. as a function of drag distance of the plate. The green curve with larger stresses is $\sigma_n$, the blue curve is $\sigma_t$. (D) Stress anisotropy versus drag distance. Since $\sigma_t$ is small, values with noise included can approach zero. As we were interested in force evolutions occurring over several cm (for this drag speed $< 1$ Hz), a low-pass butterworth filter removed fluctuations above 5 Hz. Color corresponds to different $\beta_d$ as labeled to the right of the plot. (E) Average drag force as a function of changing drag angle, vertical axis on the right. Each measurement was calculated by averaging over the last 10 cm of the raw drag data. Each data point is the mean and standard deviation of three trials, note the error bars are smaller than the markers. The solid red region is a pdf of the angles measured on the snake, vertical axis on the left.

an apparent balance. Previous studies of plate drag at the surface (at $\beta_d = 90°$) measured a similar drag-distance-dependent force and observed a wedge-shaped region of moving both horizontally with the plate and with an upward velocity component [95, 96]. We expect that the mass of grains pushed by the plate grows until a balance is reached between the grains which are flowing around the plate edges, new grains being encountered and upwelling within the material, and the mass of grains above the free surface, however, further exploration was being the scope of this study.

At low-Re, the perpendicular and parallel stresses acting on segments of long, slender swimmers in Newtonian fluids are approximated by $\sigma_n = C_n tan(\beta_d)$ and $\sigma_t = C_t tan(\beta_d)$, respectively [34]. The constants $C_n$ and $C_t$ are determined by the geometry of a body segment and the viscosity of the surrounding fluid. The ratio $K_{fluid} = C_n/C_t$ can be used to approximate swimming performance of a given waveform (See [41] for a review of low-Re swimming). We assumed that, like other low-Re swimmers, the performance of the snake was largely a function of the ratio of propulsive to drag stresses, $K = \sigma_n/\sigma_t$. (Note that the $K$ we defined was a function of $\beta_d$ whereas $K_{fluid}$ was a constant. The function $K_{fluid} tan(\beta_d)$ may be seen in Fig. 2.4*C*).

The value of $K$ was largely independent of the drag distance (Fig. 2.3*D*). The slopes of a linear regression fit to the average of three trials as a function of drag distance were $-1.8\times10^{-5}$, $-2.9\times10^{-5}$, $-5.0\times10^{-5}$, and $-6.4\times10^{-5}$ cm$^{-1}$ for $\beta_d = 15, 30, 45$, and $60°$, respectively ($R^2$ = 0.6, 0.8, 0.8, and 0.7). We note there was a periodic fluctuation of $< 1K$ occurring over several cm appearing in all trials. This was likely due to interesting physics in the GM and worthy of further investigation. However, because both these fluctuations as well as the slope of $K$ as a function of drag distance were small, we chose to focus on the larger effect of changing $\beta_s$. Therefore, we took the average of $\sigma_n$ and $\sigma_t$ from 10 to 20 cm drag distance as a function of $\beta_d$ and fit these points to obtain the functions for $\sigma_n(\beta_d)$ and $\sigma_t(\beta_d)$ (Fig. 2.3*E*). $\beta_d$ measured on the snake were small (Fig. 2.3*E*, histogram). This likely reflected the small angles where $\sigma_n$ and $\sigma_t$ were approximately equal.

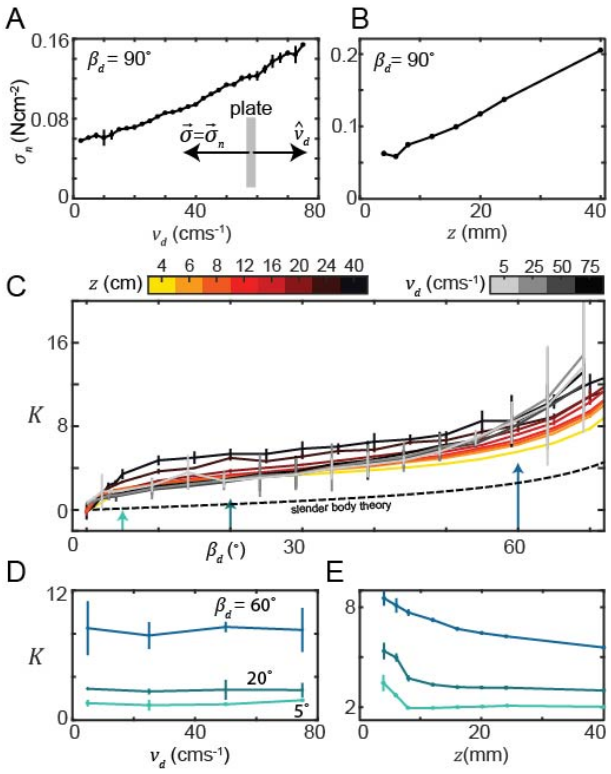


Figure 2.4: **K is independent of drag depth or speed**. (A) Stress normal to the plate face as a function of $v_d$ at a constant depth $z = 8$ mm. $\beta_d = 90°$ for all trials such that the total stress was equal to $\sigma_n$. All data are mean and std of three trials. (B) Stress normal to the plate face as a function of $z$ at $v_d = 10$ mms$^{-1}$. (C) $K$ as a function of $\beta_d$. All depths and speeds are plotted as indicated by color. Anistropy for a low-Re swimmer in Newtonian fluid is the labeled black curve. For a smooth, long, and slender swimmer in a Newtonian fluid, $K_{fluid} \approx 1.5$ (D) $K$ as a function of $v_d$ at the values of $\beta_s$ indicated. Colors correspond to the colored arrows in C. (D) $K$ as a function of $z$. Colors and angles are the same as in D.

Force is dependent on intruder speed for surface drag at the speeds observed on the snakes [97]. To explore whether the balance of thrust and drag forces was similarly dependent on speed we varied $v_d$ from 1 mms$^{-1}$ to 750 mms$^{-1}$, the limit of the robot arm capability, at constant depth $z = 8$ mm.

Stress normal to the intruder increased monotonically with speed (Fig. 2.4*A*). The anisotropy, however, was independent of $v_d$ over the speeds tested (linear regression slope, m, and 95% confidence bounds in parentheses for $\beta_d = 60°$ $m = 0.0016°(-0.0330, 0.0362)$ R-square=0.0203; $\beta_d = 20°$ $m = -0.0006°$ (-0.0108,0.0096) $R^2$=0.0326; $\beta_d = 5°$ $m =$

$0.0041^\circ$ (-0.0119, 0.0201) R-square=0.3765, Fig. 2.3*C,D*). This provides rationale for the low-Re character of the motion; while the force magnitude increased with speed, the increase was proportional over both thrust and drag, suggesting that the physics governing the sand did not change. [49] commented on the non-inertial nature of snakes slithering at low speeds on non-yielding surfaces. This suggests that, even when snakes move at speeds which in fluids would yield reactive force dominated dynamics, they are a non-inertial system.

The intrusion depth of the snakes' trunk into the GM ranged from $0$ (no intrusion) to $\approx 5$ mm (Fig. 2.8). The variation within a run was likely due to the lifting of the apexes of the waveform. Snakes moving on firm surfaces lifted the apexes to reduce drag on these segments which are not responsible for generating propulsion [49]. We found *C. occipitalis* also lifted the apexes such that there was a vertical wave on the body which was twice the spatial and temporal frequency of the horizontal wave (see Appendix 2.5.1, Fig. 2.7). These segments are at a $\beta_d$ around $0^\circ$, where the drag is greater than the thrust (K¡1). Therefore, it is to the snake's benefit to remove these segments from contact with the material.

We explored the effect of intrusion depth on the stresses by varying $z$ from 4 mm, the shallowest depth where force could be resolved, to 40 mm, where the plate was fully submerged with the top edge 10 mm below the surface. $\sigma_n$ increased monotonically with depth (Fig. 2.4*B*). The $K$ versus $\beta_d$ curves overlapped (Fig. 2.4*C*), but there was more of an effect on $K$ than we saw in $v_d$, especially at large $\beta_d$ (Fig. 2.4*E*). At the low angles used by the snake, $K$ decreased twofold as depth increased from $4$ to $8$ mm where it leveled off (Fig. 2.4*E, bottom curve*). The source of this dependence is unknown and beyond the scope of this thesis. However, we note that the stress measurements at $z = 4$ and $6$ mm were noisier than those at $z \geq 8$ mm, likely because the stresses were small.

Our granular drag measurements suggested stress was dominated by frictional interaction between grains over the speeds of wave propagation used by the snakes. Stress acting on a body segment was therefore assumed to originate entirely from resistance of

the surrounding GM to the motion of that segment. Disturbances died out on scales which were small in relation to the size of the animal and its waveform so that stresses acting on different body segments could be assumed independent. Resistive force theory (RFT, see Appendix 2.5.5) was therefore a good candidate for probing the connection between waveform and performance during surface slithering despite memory effects and the inconstant contact of body segments with the substrate due to lifting.

### 2.3.3 Surface RFT calculations

When $\beta_d = 0$, a segment experiences only drag while if $\beta_d = 90°$ the only stress was propulsive. While reducing drag aids movement to an extent, when $\beta_d$ is large segments are not making forward progress as they are moving perpendicular to the desired direction of motion. Therefore, there is a balance between segments sliding forward experiencing drag and laterally generating thrust which leads to effective locomotion [98].

The RFT calculation involved calculating the stress on each segment, $\sigma_i$, as a function of $\beta_{d,i}$, determined by a serpenoid curve of given $\theta_m$, $\xi$, and $v_{seg}$. Summing over $\sigma_i$ yielded the total stress acting on the CoM in $x$ and $y$ and torque about the CoM. MATLAB's lsqnonlin function was used to find the $x$ and $y$ components of $v_{CoM}$ and the angular velocity about the CoM which resulted in zero net stress. That is, we predicted the locomotor velocity when in steady-state (for more information about the RFT algorithm see [34, 79, 13], and Appendix 2.5.5).

We observed that as a body segment pushed laterally against the sand it built a pile similarly to the pile that evolved during drag of the plate. The rostral-facing side of the body, opposite the pile, appeared to be in contact with very little material. Therefore, we chose to model the snake body as a flat plate, representing the caudal-facing side of the body, with an added term to account for drag on the ventral surface. We assumed drag acted on each segment with magnitude $\mu mg/n$ ($\mu = 0.1$ was the coefficient of static friction for the snake's ventral scutes on the glass particles [13], $m$ the average snake mass,

$g = 9.81$ ms$^2$ the gravitational constant, and $n$ the total number of segments) acting in $-\hat{v}_i$. This may not be an unreasonable picture of this species, as the ventral surface is known to be flat or even slightly concave [48]. As the snake held the head slightly raised from the surface we did not include a term accounting for the drag acting against the head as it is pushed through the material.

Further, while shape effects on drag at the surface are not well-known, during subsurface drag the horizontal forces on an object depend primarily on cross-sectional area with very little dependence on the shape of the object, much less than in fluids [99]. While there is a shape-dependence on forces in the vertical direction [80], we assumed that vertical forces acting on the snake were balanced and did not affect the horizontal forces determining performance. Future work could explore the impact of lift forces by modeling the snake body as a three dimensional object and calculating stress on each area element using RFT[80].

Using our surface stress relations, RFT accurately predicted $v_{CoM}$ of the snakes given average $v_{seg}$ (Fig. 2.9*A*). We included lifting by assigning zero stress to those segments whose $\theta$ was in the lowest $20\%$ (equivalent to the wave apexes). This is comparable to the lifting measured on the animal (Appendix 2.5.1, Fig. 2.7). We note that, given the low-friction scales of *C. occipitalis*, including lifting in the calculations did not substantially improve predicted performance (Fig. 2.9*B*). We speculate that these segments may be lifted as a side-effect of the muscle activation responsible for generating the horizontal waveform, that is, the morphology of the trunk means that vertical lifting is a consequence of high-curvature horizontal waves. It may also be that the lifting is intentional and a buffer against deleterious motor program mistakes or changes in the environment, or the small benefit of lifting these segments is greater than the energetic cost.

As the ratio, $K$, of thrust to drag was independent of movement speed we used the drag stresses measured at $v_d = 10$ mm s$^{-1}$. While $K$ was not as clearly independent of intruder depth, we calculated performance using the drag stresses measured at each depth and found

that shape of the curve was independent of depth and the magnitude did not change more than experimental uncertainty (Fig. 2.9). The drag data at 4 and 6 mm was close to the limit of the sensor, so we chose to use the drag relations measured at $z = 8$ mm for the following calculations.

When swimming subsurface *C. occipitalis'* waveform minimized mechanical cost of transport (mCoT), calculated as the mechanical power needed to complete one cycle divided by the product of CoM velocity and mass [13]. We used surface RFT to calculate mCoT as $\theta_m$ and $\xi$ varied (Fig. 2.10*A*). mCoT increased when $\theta_m$ or $\xi$ were small as to achieve zero net stress these shapes required segments to be at larger values of $\beta_s$ therefore yielding more material and requiring greater power. Shapes with high $\theta_m$ also increased mCoT as the body spends more time going "up and down" rather than making forward progress, reducing $v_{CoM}$. There was a large basin of minimal mCoT at intermediate values. The white cross indicates the mean and range for all trials. While was a large range of $\xi$ which minimized mCoT the snake used only a limited subset of these. The animal's $\theta_m$ was also somewhat higher than that which would yield minimal mCoT.

We chose to not include in our calculation the energy required to overcome internal resistance from viscous and/or elastic stresses of the snake body. Ding et al. [87] reported the internal resistance of the sandfish was an order of magnitude less than that of the external resistance of the GM during movement subsurface. The GM stresses at the surface were less than subsurface by an order of magnitude while the snake cross-sectional area is less than that of the sandfish by a factor of $\approx 2$. The torque needed to bend a circular beam is proportional to its radius to the fourth power (see e.g. [100]). We assumed that the internal forces due to the animals physiology were similar for the snake and sandfish so that the Young's modulus of the trunk of these animals is similar and the torque required to bend the snakes' trunk was 16 times less than that required to flex the sandfish. Therefore, we assumed that, similarly to the subsurface case, the forces acting external to the body were about an order of magnitude less than those internal. We chose in this thesis not to directly

measure the bending energy of the snakes' trunk and instead focus on the interaction of the waveform with the external environment. Future study could combine RFT with a model for the internal properties of the animal's body following, e.g., [24].

As the snake in our experiment was performing an escape response we hypothesized that it was targeting maximum speed. We predicted distance traveled per undulation cycle (dimensionless quantity body-lengths per cycle, BLC). Given the linear relationship between $v_{seg}$ and $v_{CoM}$, a waveform which maximized BLC would afford the greatest increase in $v_{CoM}$ per increase of $v_{seg}$. BLC decreased as the number of waves on the body increased ((Fig. 2.10*B*). The body length was fixed, so adding waves on the body shortened "stride length" Changing $\xi$ did not change mCoT as drastically because decreasing the arc length of a single wave (by increasing $\xi$) decreased both power and $v_{CoM}$. The animals appeared to be using a waveform which increased BLC in comparison to the subsurface shape (crosses in (Fig. 2.10*B*), however, BLC was maximized at a lower $\xi$ than used by the animal.

We used RFT to predict the maximum torque, $\tau_{m,RFT}$, experienced by any given body segment over a cycle ((Fig. 2.10*C* see Appendix 2.5.5 for more detail). $\tau_{m,RFT}$ was large at shallow waveforms for the same reason as mCoT; these required larger $\beta_d$ and therefore greater stress magnitudes to balance the forces. There was also an oscillation in torque with changing $\xi$. This appeared to be attributable to unbalanced net torque about the CoM when $\xi$ was at non-integer values.

We endeavored to include physiological limitations of the animal musculature by calculating the maximum $v_{CoM}$ for each waveshape given a maximum peak muscle power. That is, for each shape in the $\theta_m$, $\xi$ space we used RFT to calculate the velocity, $v_{pl}$ where the peak power generated by any given segment over a cycle was equal to a constant. This metric took into consideration both the effort required to achieve a shape given stresses from yielding the material as well as the impact of muscle-shortening-speeds required to achieve each waveform at a given frequency.

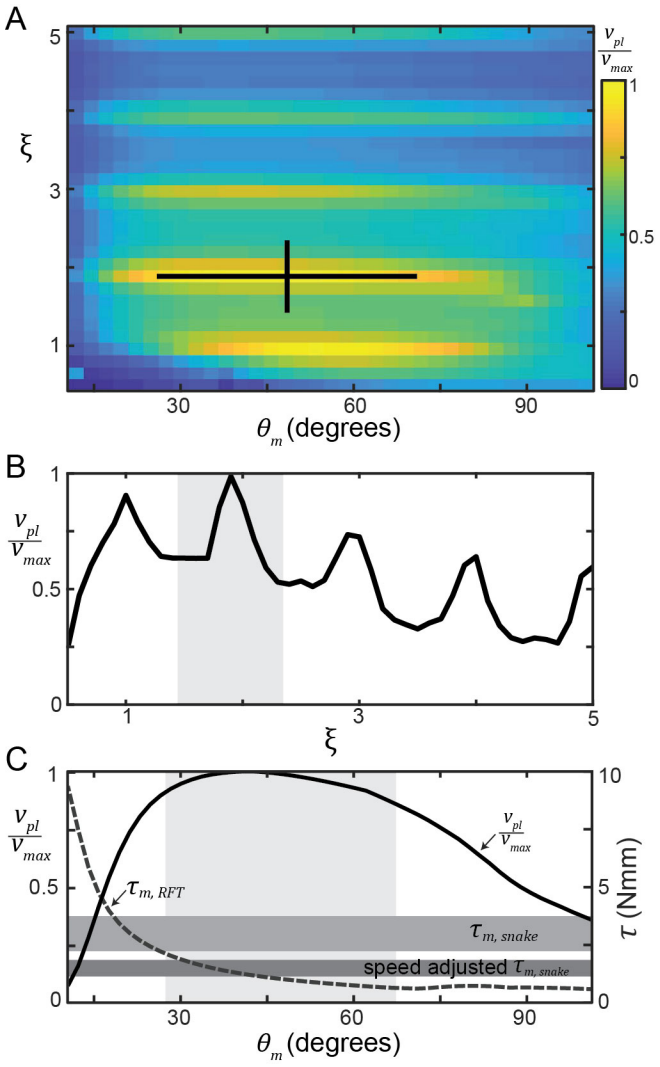


Figure 2.5: **RFT calculation of power-scaled velocity.** Segment-power-limited velocity, $v_{pl}$, divided by $v_{max}$, the largest value of $v_{pl}$ in the $\theta_m$, $\xi$ space. (A) ${}^{v_{pl}}/_{v_{max}}$. Cross is the snake waveform. (B) ${}^{v_{pl}}/_{v_{max}}$ versus $\xi$ for $\theta_m = 48.4$, the average snake value. The gray shaded area is the range of snake values. (C) Solid black curve ${}^{v_{pl}}/_{v_{max}}$ (left vertical axis) and gray dashed curve $\tau_{m,RFT}$ (right vertical axis) versus $\theta_m$ for $\xi = 1.90$, the average snake value. The light gray shaded area is the range of snake $\theta_m$. Horizontal gray bars are the estimated muscle torque capabilities of the snakes (Appendix 2.5.6). The upper bar, $\tau_{m,snake}$ is the estimated maximum muscle torque and the bottom bar, speed adjusted $\tau_{m,snake}$ is the maximum torque reduced to reflect the speed of movement.

The plot of $v_{pl}$ as $\theta_m$ and $\xi$ varied is shown in Fig. 2.5*A*. Similarly to mCoT, small values of $\xi$ and $\theta_m$ did not yield good performance due to power dissipated to the material. Akin to body-lengths per cycle, $v_{pl}$ also decreased as $\xi$ and/or $\theta_m$ became large. Reflecting the oscillations in $\tau$, this metric had maxima near integer values of $\xi$.

This quantity was maximized at the number of waves (Fig. 2.5*B*) as well as at the attack angle (Fig. 2.5*C*) used by the snakes. We estimated the peak torque output of *C. occipitalis*' muscles using dissection of museum specimens (Appendix 2.5.6). The waveform used by the animals lay near the point where $\tau_{m,RFT}$ increased above the capability of *C. occipitalis'* muscle. We report both maximal torque output (Fig. 2.5*C* upper horizontal bar) as well as output scaled for the average contraction velocity (Fig. 2.5*C* lower horizontal bar). It may be that the individual variation in $\theta_m$ reflects differences in peak muscle power capabilities.

### 2.3.4 Robophysical model

We studied a robophysical model, a 10 joint robot moving on the surface of poppy seeds (Fig. 2.6*A*), to gain further insight into the relationship between patterns of self-deformation, GM stress-response, and performance. The number of joints was limited by motor strength; as a result the robot could only achieve $\xi$ between 1 and 1.4 as lower $\xi$ required too much torque and higher were not well-resolved by the number of joints. Both $\xi$ and $\theta_m$ were varied on the robot.

Waveforms with high-enough attack angle, depending on the value of $\xi$, moved with small backward slipping such that the trunk did not interact with previously disturbed material, yielding forward progress (Fig. 2.6*B, left*). Low $\theta_m$ waveforms did not make sufficient forward progress per undulation to reach mostly undisturbed material. In this case the robot swept out a trough in the GM, completely stalling forward progress and sometimes even moving backward as the trunk "rolled" along the trough walls (Fig. 2.6*B, right*). These failures were similar in appearance to those observed in living snakes [89]. Furthermore, increasing the skin friction of the robot by affixing sandpaper to the smooth plastic sur-

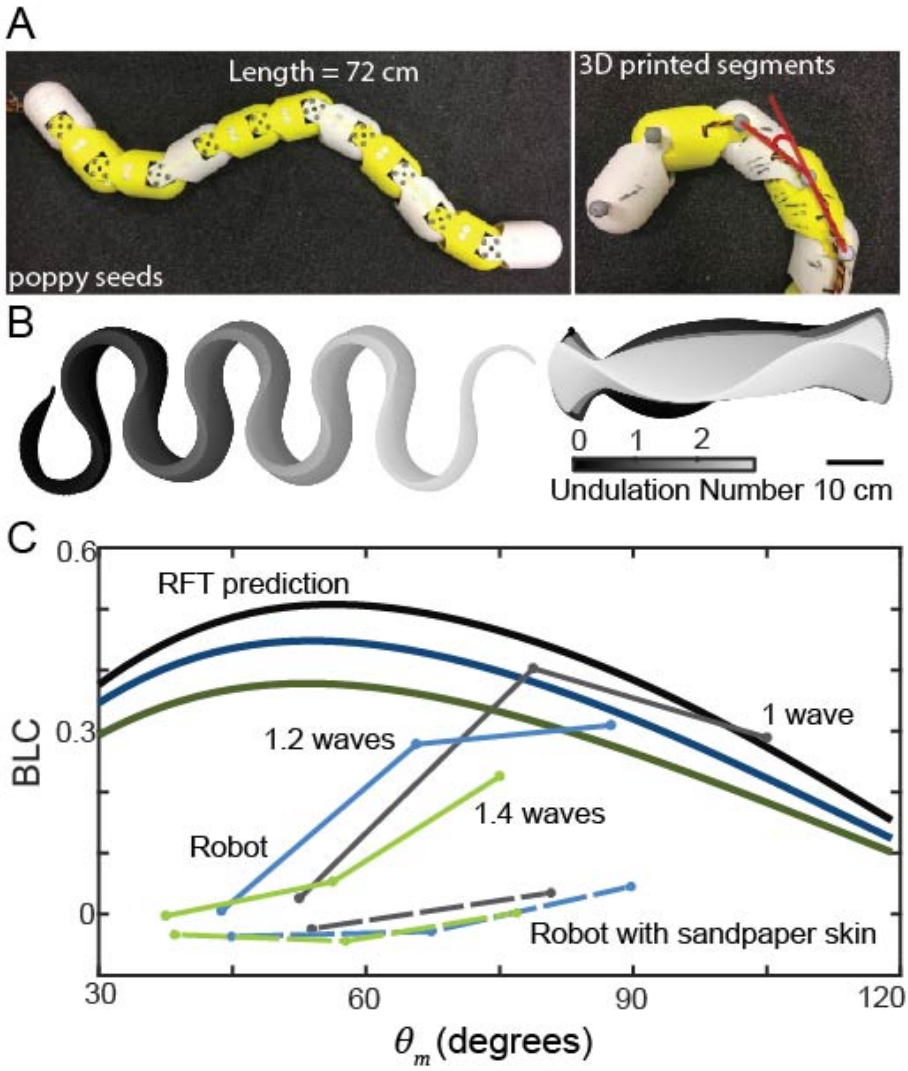


Figure 2.6: **Waveform variation using a robophysical model** (A) (*left*) 10 joint, 11 segment robot on poppy seeds. Shape was controlled by commanded motor positions to vary sinusoidally in time. Each motor was offset from its anterior neighbor by a constant phase set by $\xi$. The period of undulation was 3 seconds and each trial consisted of 3 complete undulations. (*right*) (B) Robot mid-lines for $\xi = 1$ and (*left*) $\theta_m = 105°$ (*right*) $\theta_m = 53°$. Color indicates time in number of undulations. (C) BLC versus $\theta_m$. RFT prediction lines are darker smooth lines, the robot measurements are circles connected by lighter solid lines for the robot with the 3D printed plastic contacting the substrates and dashed lines for sandpaper affixed. Standard deviation is within the markers. $\xi$ is indicated by color as labeled. Black/gray is 1, blue/light blue is 1.2, and green/light green is 1.4.

face would cause previously successful waveforms to fail (Fig. 2.6*C* dashed lines). The increased friction between robot and substrate decreased the anisotropy, increasing $\beta_d$.

We used stress relations measured in poppy seeds [92] to predict robot BLC as a function of $\theta_m$ for each of the $\xi$ tested (Fig. 2.6*C*). RFT was only accurate at the higher attack angles where the robot was not interacting with its own tracks. At lower $\theta_m$ RFT over-predicted the robot performance as it did not take into account the change in physics that occurred when body segments re-encountered material. The highest-speed waveforms predicted by RFT for the robot lay in the region where RFT was no longer accurate due to material hysteresis.

**Discussion**

Stereotypy is common among animals swimming immersed in homogeneous fluids. Elongate swimmers including eels, snakes, and salamanders use a periodic traveling wave to swim; unlike sand-swimming, however, this anguilliform swimming is characterized by a wave which increases in amplitude from head to tail [50]. The head undergoes minimal lateral displacement and the lateral excursion of the body axis increases posteriorly to the tail which makes sweeping excursions. The lateral displacement of *C. elegans* swimming in Newtonian fluids [75, 101] is comparable to *C. occipitalis* sand-swimming rather than anguilliform swimming. This likely reflects the dominance of resistive forces shared by the worm's and snake's motion.

Eels use the anguilliform shape when swimming in fluids and transition to a waveform more like that of *C. occipitalis* (with an approximately constant amplitude of lateral excursions from head to tail) when moving on land [10]. During terrestrial movement, eels recruited anterior muscles to a greater degree than posterior ones [102]. The difference in path following of the tails of different *C. occipitalis* (Fig. 2.1*C*) suggested that the snakes may use a similar pattern of muscle activation. Future EMG studies could confirm this hypothesis. [102] hypothesized that portions of the eels' body are passively pulled or pushed

through the sand groove created by the anterior body segments. This study provided further evidence to this hypothesis in that we observe the mounds of sand being generated primarily by the anterior portions of the body while posterior segments were not observed enlarging the mounds. However, it is unclear whether the posterior was being passively bent by the mounds, or whether the piles simply grew to a steady state where the force applied by the snake was balanced by the material stresses without further flow.

We assumed, based on the linear relationship between $v_{seg}$ and $v_{CoM}$ and the independence of drag anisotropy to $v_d$ that the snake was in a resistive force dominated regime. The accurate prediction of animal performance using RFT calculation provides further evidence that our ansatz that the animal was low-Re was correct and, despite the fast motion of the snakes, the locomotion was resistive force dominated. For example, RFT was not as useful when applied to the swimming of an eel for which reactive forces are not negligible [25].

The robophysical tests revealed our surface RFT was not accurate when the locomotor re-encountered material. The highest-performance shapes predicted by RFT failed to progress in the physical system. It is therefore important to consider hysteresis of the material in designing gaits in limbless robots intended for use in yielding terrestrial terrain.

RFT was also previously found to be less accurate than, e.g., Lighthill slender-body theory when applied to the tight helical motion of a bacterium's flagella [83]. In this system forces on the segments were not independent, an important assumption in the RFT formulation. This suggests that surface RFT will be inaccurate for shapes in which body segments pass close enough to each other that interaction occurs either between a segment and the granular pile generated by another part of the body or between piles. We note, however, that such shapes (which were never observed in *C. occipitalis*) are low-slip and therefore not expected to generate large piles. Some robot shapes had segments which passed relatively close to each other (see for example Fig. 2.6*B, left*) but we did not observe any interaction of the piles.

Failure of the robot, similar to that of some snakes, revealed the challenge of moving at the surface; animals and robots must manage their kinematics to avoid or correct for changes in the material that occur as a result of previous interaction. The memory introduced by the interface is not important to the locomotor given it is successful enough to avoid re-encountering previously disturbed material. *C. occipitalis'* waveform and the robot at higher attack angles moved far enough per undulation that the leading edge of the wave was always encountering new material-the lack of re-flow was in essence unknown to the locomotor and motion was, as during subsurface swimming in GM, like that in a frictional fluid [79]. This strategy was similar to the sufficient step-length gaits in the limbed robots which allowed subsequent steps to land "far enough" from previous tracks to avoid penalizing performance [91, 92].

Strategies which are effective when in a material which will re-flow on timescales shorter than those of the locomotor such as fluids and homogeneous GM may fail in these hysteretic materials. This may explain why the sandfish has stout limbs. This animal swims subsurface in GM using body undulations with the limbs tucked against the trunk [79]. It has a limited range of waveforms given its morphology, so its subsurface waveform interacts with already encountered material. As the GM re-flows, however, this strategy leads to forward motion beneath the surface. Sandfish, however, would likely not be successful on the surface using body undulations as it cannot physiologically use shapes which move far enough per undulation to avoid its own tracks. In this case, retention of the limbs for running on the surface, where it can lift the legs away from the GM and set them down away from previous tracks, may be crucial for the sandfish's movement on the surface.

This points to a possible origin of the unique sidewinding gait evolved separately in two desert specialist viper species. This gait relies on static contacts with the GM, much like those made using limbs, to "step" across the granular surface. *C. occipitalis* was successful by being long and slender, having low friction skin, lifting, and using the right waveform. All of these factors combined buffer this species against failure. For an animal like the

vipers which are short and stout compared to *C. occipitalis* and have higher friction scales laterally undulation on the surface would have been very sensitive to waveshape and potentially impossible when failure due to hysteresis is consider. For these snakes, changing the control of their gait to sidewinding may have been an easier adaptation to the desert habitat than making morphological changes.

Despite the challenges, locomotion on the surface appears to offer advantages over swimming immersed in material. *C. occipitalis*' escape response when startled on the surface is to flee across the GM rather than dive into it [103], suggesting a preference for surface slithering. Drag is reduced by both avoiding forces required to push the head through material and a reduction in frictional drag which is due only to animal mass instead of mass and granular pressure. *C. occipitalis* can also modulate ground contact to further reduce drag forces by lifting segments which are not generating thrust. Power dissipated to the media decreases at the surface as the torques required to achieve the desired shapes decrease. We posit that torque reduction is the reason *C. occipitalis* increased the number of waves as it moved subsurface. This may also be why it moves more slowly–the muscles can generate the higher torques required. This is similar to the strategy used by *C. elegans* contending with materials of increasing viscosity. They decreased the wavelength and frequency of undulation as viscosity increased in order to manage increasing power requirements and maintain the desired angle of attack [3].

## 2.4 Conclusions

*Chionactis occipitalis* slithers quickly across the surface of sand using a stereotyped traveling wave. Using granular drag experiments and RFT calculations we demonstrated that this specific shape confers the benefit of maximum speed given the limits of animal physiology. *C. occipitalis* is a useful model for studying locomotion and control in complex terrestrial terrains. The highly stereotyped shape makes changes to the waveform easier to measure. The low-Re motion also opens the door to comparison with the popularly studied

*C. elegans*.

A critical element to the snake's success was the ability to avoid its own tracks, as illustrated by a robophysical model. The findings here may be applicable more broadly to motion in a range of deformable terrestrial materials. A similar independence of thrust to drag forces was found for a larger intruder in poppy seeds and oolite sand. $K$ was the same for both materials and independent of depth and speed [92]. The comprehensive appearance of this curve suggests it may be a more general feature of deformable materials.

We therefore hypothesize that non-inertial slithering locomotion is general to a range of terrestrial habitats and similar performance considerations will be important. Namely, balancing speed with the power needed to yield the substrate and generate propulsive stress as well as choosing a waveform which minimizes yield to avoid interacting with previously disturbed material.

## 2.5 Appendix

### 2.5.1 *Chionactis occipitalis* experiments

Snakes were collected in the Mojave desert in Yuma, Arizona, USA under scientific collection permits (SP790952, SP625775, SP666119) approved by the Arizona Game and Fish Department. Neither the sex nor the age of the animals was determined; gender and age dependent effects were beyond the scope of this study. For the 10 individuals used in this study snout-tail-length $L = 38.4 \pm 2.3$ cm and mass $21 \pm 3$ g (mean$\pm$ s.d. of 10 individuals).

The glass-oxide particles (Ballotini Impact Beads, Potters Industries Inc.) filled an air-fluidized trackway of area $152 \times 53$ cm$^2$ to a depth of 4.5 cm. The bottom cavity of the trackway was connected to a blower (Dayton 10 5/8" wheel diameter) which forced air through a layer of Al honeycomb (Plascore, Zeeland, MI USA. PAMG-XR1-8.1-1/8-002-N-5052-B09) and porous plastic (Interstate Specialty Products, Sutton, MA USA. 0.2" thick 50-90 $\mu$m pore size) which both supported the sand and acted as a flow distributer. We fluidized the GM between each trial to erase tracks and reset the substrate to a featureless,

loose-packed state; air flow was turned off during trials. The temperature in the track way and snake holding area was measured prior to each trial. Lamps were used to ensure the temperature in both remained at $26 \pm 1$ °C, within the active range for *C. occipitalis* [104]. The heat lamps on the track way were turned off during data collection and LED lights were used for illumination.

An overhead high-speed camera (AOS Technologies X-PRI or S-Motion, Baden Daettwil, Switzerland) captured the motion of the snakes at 250 frames-per-second. The animals would often immediately flee across the surface upon introduction to the track way; otherwise a light tail tap would illicit an escape response. Snakes were tested at most every other day with a maximum of two successful trials collected per day. A run was included if the snake performed at least four complete undulations moving along a straight trajectory at apparently constant speed. All experimental procedures were conducted in accordance with the Georgia Institute of Technology IACUC protocols A14066 and A14067.

Animal midlines were digitized by tracking the black bands (Fig. 2.1*A*) from neck to vent using a custom MATLAB code as described in [13]. The number of tracked points depended on the number of bands on an individual. To facilitate comparison between snakes of different lengths, a cubic spline was fit to the tracked data such that each snake was evenly divided into 100 segments from neck to vent.

$\theta$ was calculated using finite differences to estimate the x and y values for each segment's tangent vector. We generated sample serpenoid waveforms of known parameters and used these to determine that the most accurate measurement of the tangent vector was obtained by subtracting the average position of the segment in question and three segments anterior from the average of the segment and the next three posterior segments. This method helped buffer against noise while still providing an accurate measurement. We found the maximum angle on the body at each time step and then averaged over all times in a trial in the to obtain $\theta_{max}$. To measure $\xi$ we found the points of zero curvature–corresponding to the inflection points of the waveform. We then measured the arclength

between these two points for the first half-wave on the body, multiplied by 2 to get the arclength of one full wave, and divided the individual's length by the result.

### 2.5.2 Lifting measurement

An OptiTrack motion capture system (4 Prime 17W cameras) captured 3D kinematics of the animals moving in the track way. OptiTrack's Motive program calculated the x,y, (horizontal plane) and z (vertical distance above the GM surface) coordinates of IR-reflective markers 3 mm in diameter placed at 1.5 cm intervals along the animal's mid-line starting between the eyes and continuing to the vent. The markers were small enough we did not observe any difference in the snakes behavior or movement after application.

We calibrated the origin of the Optitrack coordinate system using the provided calibration square. We placed the square so that the top surface was level with the free surface of the GM and used a level to ensure the square was horizontal. The error in placing the square was difficult to determine but we estimate it was within $3^\circ$ in any direction. Because the calibration was imperfect we rotated the z-coordinates of the snake by fitting a line to the average position of the snake in y and z at each moment in time, finding the angle between y and z given the slope of this line, and using a rotation matrix to rotate the z coordinates.

Space-time plots of $\theta$ (the horizontal wave on the body which is clearly seen by eye) and z (the vertical wave of lifting) show traveling waves in both, although the wave of lifting in z appeared to be double the spatial and temporal frequency (Fig. 2.7*A,B*). We fit the function $a_s sin(\xi s) + b_s cos(\xi s)$ to each time step in $\theta$ and z, separately. Fig. 2.7*C* is the probability density of the $\xi$ associated with the best fit of the function. We included only those values for which R-squared$\geq 0.70$. The median value of $\xi$ for the horizontal wave was $1.6 \pm 0.2$ and for the vertical wave $3.4 \pm 0.5$. The ratio of vertical to horizontal waves was 2.1, that is, the snake lifted the body segments twice for every one wave passed down the body. Note that $\xi$ of the horizontal wave is less than that reported in the text for the animals. This was because in measuring the $\xi$ of the animals we divided the total length of

the animal by the arclength of the first complete wave. In contrast, here we are fitting the data points which do not represent the entirety of the snakes body as some amount is lost in averaging to calculate $\theta$ and the posterior points were frequently missing as sand would flow over the tail..

We fit the function $a_t sin(\omega t) + b_t cos(\omega s)$ to the trajectory of each point through time for $\theta$ and z, separately. We found the wave phase by converting the amplitudes $a_t$ and $b_t$ to polar coordinates and taking the polar angle. A plot of the phase of $\theta$ compared to that of $z$ reveals two linear bands (Fig. 2.7*D*), indicating the propagation of the waves is linearly related. The wave of lifting occurred twice as fast as the horizontal wave. Further, we note that the wave of lifting is in turns in phase and $\pi$ out of phase with the horizontal wave. Peaks of the lifting wave align with $\theta = 0$ (the highest-curvature portions of the wave).

Given uncertainty in the surface we could not determine whether the animal was in contact with the surface or not. However, we assumed that lifted segments are applying less load to the material.

### 2.5.3 Laser line measurements of the free surface

We characterized the tracks created by *C. occipitalis* using a laser-line apparatus. An off-axis webcam (Logitech-C920 Pro) captured images of the laser line. Both the laser and camera were affixed to a linear bearing and moved using a linear actuator (Firgelli). We used MATLAB to move the actuator and collect an image every mm, verified using a ruler placed in view of the camera. The location of bright pixels in the images was used to reconstruct the surface (Fig. 2.8*A*).

### 2.5.4 Granular drag measurements

The same glass particles used in the snake experiments filled an air-fluidized bed of area $32.5 \times 28 \times 15$ cm$^2$. The bottom cavity of the bed was fluidized by two shop vacs controlled by a proportional relay. The fluidization mechanism was the same as in the snake trials,

and again the material was fluidized before each trial and the air was turned off and all grain movement ceased before a trial began. An aluminum rod attached the Al plate to a force transducer (ATI nano43) accurate to 2 mN. This apparatus was located on the end effector of a six degree-of-freedom robot arm (Denso VS087A2-AV6-NNN-NNN) which controlled intruder movement. The robot arm first rotated the plate to $\beta_s$, then submerged it to depth $z$, next dragged the plate parallel to the surface at constant speed for 20 cm, and lastly stopped and extracted it.

### 2.5.5 RFT formulation

We approximated the shape of the snake using 100 segments at 70 points in time divided evenly over one full undulation cycle. We calculated the wave shape using $\theta(s_s, t_j) = \theta_m sin(^{2\pi\xi}/_L(s_i + v_{seg}t_j))$ for each combination of parameters $\theta_m$ and $\xi$.

Previous research [49] found that the ventral scutes are anisotropic such that gliding directly forward produces less drag than sliding laterally and both forward and lateral motion results in less frictional drag than moving directly backwards. The coefficient of static friction of C. occipitalis' scales is low ($0.109 \pm 0.016$ ventral forward and $0.137 \pm 0.018$ backward [13]). The lateral coefficient of friction for *C. occipitalis* scales is not known, however, given [49] results we assumed that it was bounded between 0.10 and 0.14 such that the difference between frictional forces acting parallel and perpendicular to segments was negligible compared to the larger plate-drag forces. Therefore, we chose not to include the frictional anisotropy in our RFT calculation. We approximated the frictional force acting on the ventral scutes as $F_{friction} = mg\mu$ where $\mu = 0.1$. We previously found the coefficient of static friction between Aluminum and the glass particles is approximately 0.2 [79]. Therefore, in predicting the performance of *C. occipitalis* we scaled the $\sigma_t$ function measured using the Aluminum plate by $^1/_2$.

We did not re-distribute ventral drag forces to account for lifting.

### 2.5.6 Dissection and torque estimation

As part of a different study, four adult Chionactis (SVL $33.0 \pm 3.7$ cm, mass $16.4 \pm 3.4$ g) which had preserved in formalin and stored in ethanol were skinned and the body (from the posterior margin of the quadrates to the cloaca) was cut into 10 equal length segments, which were then weighed intact. Segments were then eviscerated and the epaxial muscle mass (consisting of the largest muscles, the m. multifidus, m. semispinalis-spinalis, m.longissimus dorsi, and m. iliocostalis [58]) was removed, and the viscera, muscle, and remaining body tissue were weighed. All tissues were kept moist in $70\%$ ethanol and dabbed dry before weighing. Snakes were an average of $22.1 \pm 3.8\%$ muscle by mass, but this proportion varied regionally due to uneven total segment masses and viscera masses; absolute muscle mass was highest at midbody and decreased anteriorly and posteriorly, though the highest muscle mass was only $27.0 \pm 3.8\%$ higher than the average.

Because of postmortem and preservation distortion of body shape (facilitated by the mobile ribs of snakes), average body radius was computed from SVL and mass by treating the snake as a uniform cylinder with a tissue density of 1.05 g/cm3 (typical for vertebrate tissues). As the muscular lever arms for lateral flexion are unknown for any snake, we estimated the maximum lever arm as 1/2 the radius of the body; while some epaxial muscles may have larger lever arms (m. iliocostalis), others likely have much lower lever arms (m. multifidus and semispinalis-spinalis). Similarly, muscular PSCA for the entire epaxial muscle group was computed as a cylinder based on SVL and total muscle mass; while snake epaxial musculature is highly complex, none of the muscles show strong pennation. Peak isometric muscle force was estimated based on the standard 30 $\text{Ncm}^2$ value seen in most vertebrate muscles, and divided by two to account for unilateral activation [58]. Although the maximal shortening speed and shape of the force-velocity relationship is unknown in snakes, we assumed that during lateral undulation, snakes would be operating near their peak isotonic power, and thus with a force of half the peak isometric muscle force; as activation/deactivation kinetics and length tension properties are also unknown

in snakes, we did not attempt to account for these. Peak torque was computed as this force divided by estimated lever arms. Although many crucial properties are unknown, this value represents a charitably high estimate of peak torque; this value would be depressed by steeper force-velocity curves, departure from the plateau of the length-tension curve, incomplete activation during the work loop, or lower muscle lever arms, while the higher muscle mass at midbody and slightly larger vertebrae would increase the peak torque.

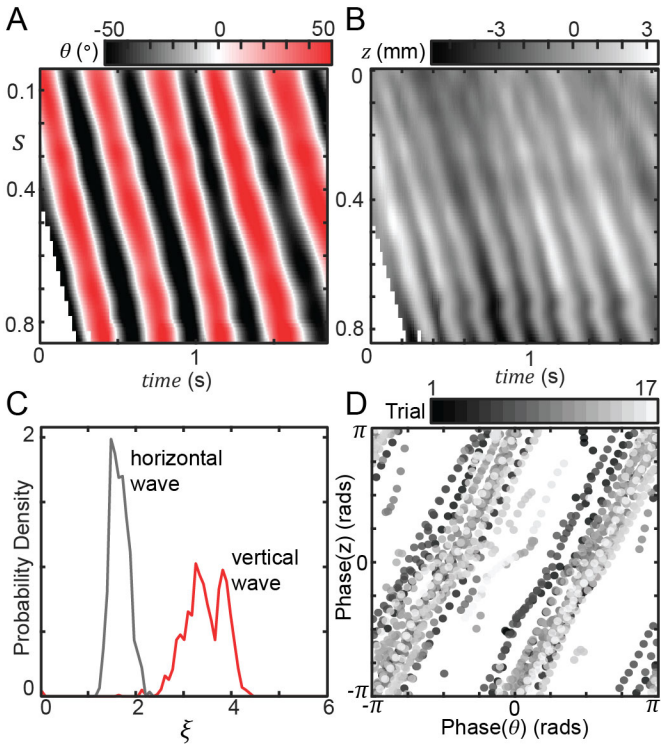


Figure 2.7: Measurement of the vertical wave of lifting. (*A*) Space-time plot of $\theta$. $s$ is the fractional arclength from the neck at $s = 0$ to the vent at $s = 1$. (*B*) Space-time plot of the vertical position of the belly of the snake measured relative to the free surface. Axes are as in *A*. (*C*) Probability density of the wavenumber of the horizontal wave (gray) and vertical wave (red). The ratio of the median values of the two curves is 2.1, indicating that the spatial frequency of the wave of lifting is twice that of the wave in the horizontal plane. (*D*) The phase of the wave in $z$ versus the wave in $\theta$. The wave in $z$ is traveling at twice the frequency of that in $\theta$. The result is that the peaks of the wave in $z$ align with the extrema in $\theta$, that is, the apexes of the horizontal wave are lifted off of the substrate. Ratio of the median values of each curve is 2.1

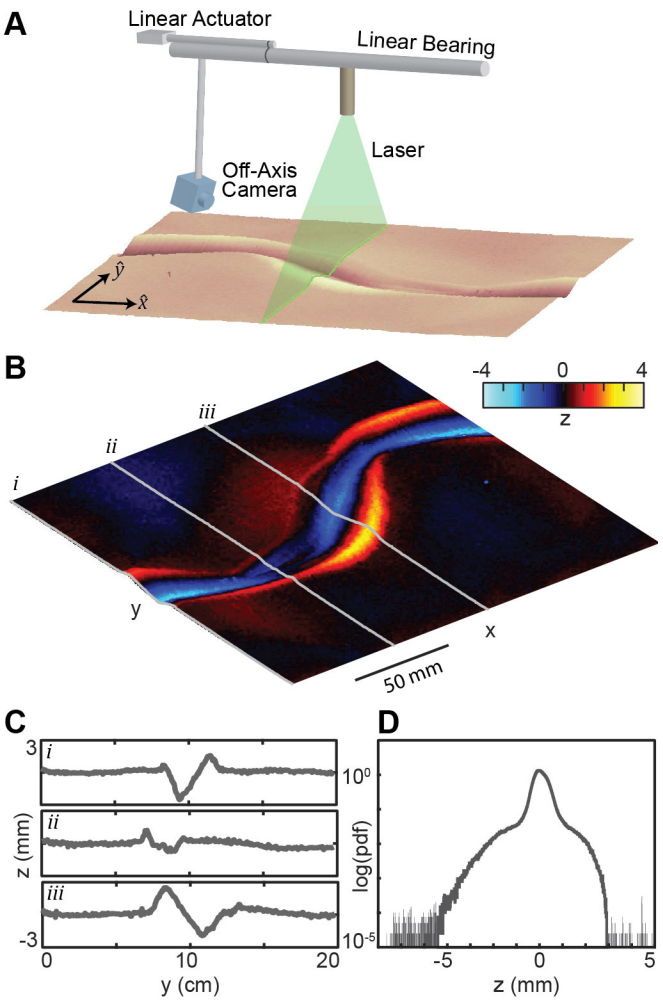


Figure 2.8: *C. occipitalis* tracks (left) Laser-line apparatus. A laser sheet spans the sand-fluidized bed. The off-axis camera detects changes in the height of the line. The linear bearing allows the laser and camera to move in x and reconstruct the snake tracks in 3D (D) Buildup of a granular pile on the front face of the intruder at y = 90o. (right) Track in the GM remaining after a trial. Warm colors indicate the piles formed rising above the free surface. The snake travelled in the direction indicated. The body intrudes beneath the free surface and yields the material, creating piles on the anterior edges of the path like those described by Mosauer and seen in the tracks observed in the field.

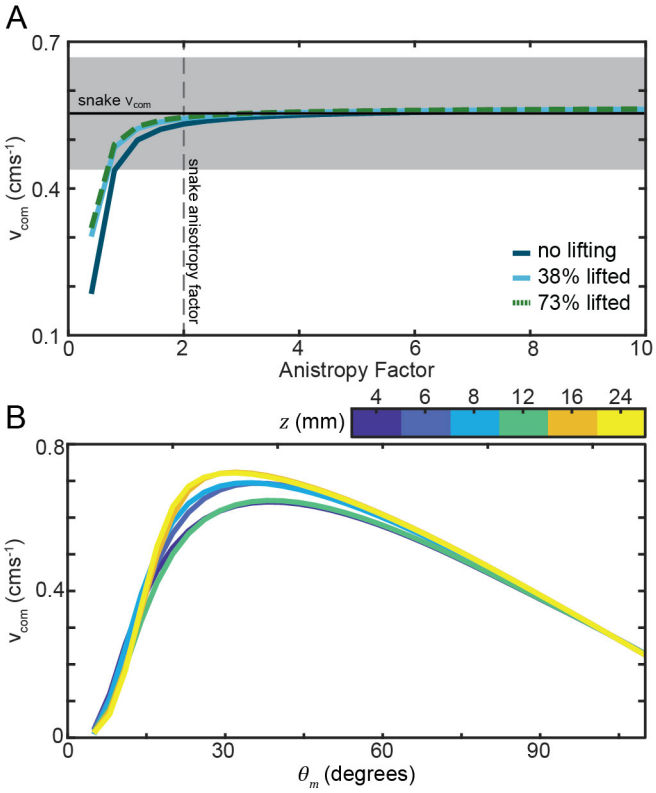


Figure 2.9: Comparison of RFT results with snake performance and impact of changing parameters. (*A*) $v_{CoM}$ as a function of the anisotropy factor–an overall multiplier on the perpendicular forces. An anisotropy factor of two corresponds to the animal, as the low-friction scales of the snake reduces the friction by a factor of two as compared to the Aluminum plate used in the drag measurements. The blue line is RFT calculation for the snake parameters without any lifting, light blue calculated for lifting of segments which are in the top $38\%$ of curvatures, and green dashed for in the top $73\%$. The black line and gray bar is average and range of $v_{CoM}$ calculated from experiment. The RFT prediction and animal measurements come into agreement at an anisotropy factor of two, as expected. We also see that lifting does not greatly impact $v_{CoM}$, nor does decreasing friction (thereby increasing the anisotropy factor) beyond the value achieved by the snake. (*B*) RFT calculation of $v_{CoM}$ as a function of $\theta$. The different colors indicate force relations obtained by fitting data taken at the noted depths. We find that the RFT prediction was relatively insensitive to depth which we expected given the depth independence of $K$. Further, the peak of the curves does not depend on depth. Therefore, we use in the calculations force relations measured at a depth of 8 mm.

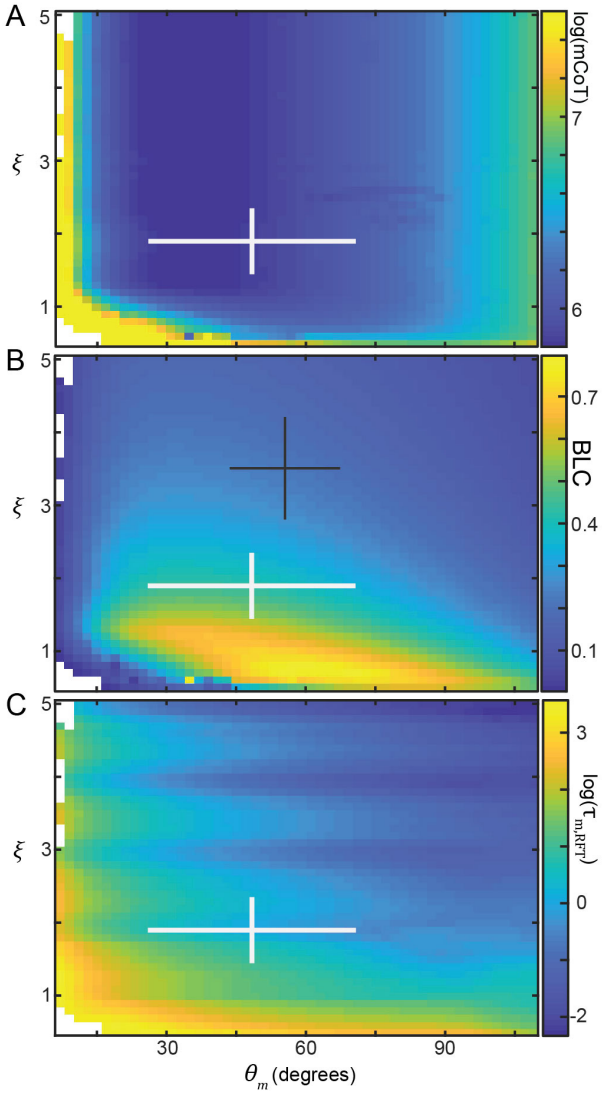


Figure 2.10: **Surface RFT results for mCoT, BLC, and $\tau_{m,RFT}$.** The horizontal axis of all plots is $\theta_m$. Moving from left to right increases how sharply bent the body wave is. The vertical axis is $\xi$, the number of waves on the body increases from bottom to top of each plot. Crosses are average $\pm$ range of values measured in 32 snake trials (N=10 individuals). (A) Mechanical cost of transport, mCoT, calculated for each pair of $\theta_m$ and $\xi$. The color corresponds to log(mCoT). (B) Bodylengths traveled per cycle, BLC. (C) Maximum segment torque, $\tau_{m,RFT}$, predicted within a full cycle.

# CHAPTER 3

# SCATTERING

## 3.1 Summary

Limbless animals like snakes inhabit most terrestrial environments, typically generating thrust to overcome drag on the elongate body via contacts with environmental heterogeneities. The complex body postures adopted by some snakes and the unknown physics of most terrestrial materials frustrates understanding of strategies for effective locomotion. As a result, little is known about how limbless animals contend with unplanned obstacle contacts. We studied a desert snake, ***C. occipitalis***, which uses a stereotyped head-to-tail traveling wave to move quickly on homogeneous sand. In laboratory experiments, we challenged snakes to move across a uniform substrate and through a regular array of force-sensitive posts. The snakes were re-oriented by the array in a manner reminiscent of the matter-wave diffraction of subatomic particles. Force patterns indicated the animals did not change their self-deformation pattern to either avoid the posts or grab them. A model using open-loop control incorporating previously described snake muscle activation patterns and body-buckling dynamics reproduced the observed patterns, suggesting a similar control strategy may be employed by the animals.Our results reveal how passive dynamics can benefit limbless locomotors by allowing robust transit in heterogeneous environments with minimal sensing.

The ray model was developed by Prof. D. Zeb Rocklin. Force-sensitive posts were developed by Alex M. Hubbard (undergraduate, BME) Snake experiments and tracking were carried out by Alex M. Hubbard and Lillian Chen (undergraduate, Bio). The contents of this chapter are adapted from a manuscript accepted for publication by Perrin E Schiebel, Jennifer M Rieser, Alex M Hubbard, Lillian Chen, D. Zeb Rocklin, and Daniel I Goldman.

## 3.2 Introduction

Disentangling the roles of environmental mechanics, physiology, and neurology to discover principles of movement in natural environments requires integrating insights from disciplines including neurobiology, biomechanics, control theory, and soft matter physics [105, 106, 107, 108, 109]. While progress in such integration has been made in locomotion in homogeneous environments (open fluids, flat hard ground, dry sand [110, 111, 109, 112]), understanding movement in heterogeneous terrain remains a frontier in locomotion studies across scales [113, 6, 5, 114, 115]. This is in part because interactions in these environments can change discontinuously and unexpectedly, making it unclear how biological control schemes and bodyplans accommodate unplanned collisions.

In organismal neuromechanics [59], locomotion control is classified on a spectrum between closed and open loop [116], each dealing with heterogeneities in different ways. We will consider these defined as the relationship between information about the surrounding terrain and consequent determination of the self-deformation pattern. During the former (typically associated with careful, deliberate movements) the animal uses sensory input to collect information about the terrain and self-deforms in response to novel interactions [117, 118]. In contrast, rapidly moving animals [119, 120, 121, 122] can rely on the passive dynamics of mechanical structures to rapidly reject unexpected perturbations without additional input from the nervous system.

While the strategies used by limbed animals to contend with collisions have been carefully studied [123, 115, 60], little is known about how body-undulating locomotors like nematode worms, eels, and snakes handle unplanned interactions (e.g. turbulence, obstacles) [6, 124, 125]. Understanding movement strategies in heterogeneous environments is particularly difficult in terrestrial undulatory locomotors like snakes which often rely on complex terrain heterogeneities to propel themselves. The only gait shared by all limbless, elongate vertebrates, is lateral undulation [45] in which primarily planar curves of

the trunk press against heterogeneities–whether discrete obstacles [47], those created and subsequently used by the body bends such as piles of sand [48], or frictional anisotropy introduced by the structure of the integument [49]–to generate propulsion.

Coordinating interaction between the many degree-of-freedom trunk and complex terrain is a nontrivial task as evidenced by the failure of snakes challenged to move in a novel terrain [89]. It is unclear how limbless organisms contend with unexpected collisions and whether passive dynamics could facilitate robust transit as in limbed systems. Previous studies of generalist snakes (those with a diverse geographical range encompassing a variety of habitats) found that the waveform was related to the density of heterogeneities [19, 21], and subtle, local deformation was precipitated to utilize obstacles [125]. These complex shapes confound understanding of the relationship between terrain, shape change, and performance.

Here, we take a first step to understanding the neuromechanics of laterally undulating snakes in heterogeneous environments by working with a relatively simple system, a desert-dwelling snake that relies on a stereotyped self-deformation pattern to move within its habitat, composed largely of homogeneous sand but containing sparse obstacles (Fig. 3.8). In the absence of the ability to interrogate the motor control system in freely moving snakes (unlike the increasing number of tools in microscopic swimmers, e.g. [75]), we explored the animals' response to unexpected terrain interactions using a "scattering" approach [126]–studying the kinematic and dynamic outcomes of collisions with heterogeneities. Determining principles of body coordination in complex terrains will help simplify control and improve mobility in snake-like robots [89, 43].

## 3.3 Results and Discussion

### 3.3.1 Biological model

The shovel-nosed snake *C. occipitalis* (Fig. 3.1*A*), transits open desert between the cover of larger flora to forage or escape threats [48]. This intervening terrain consists of a

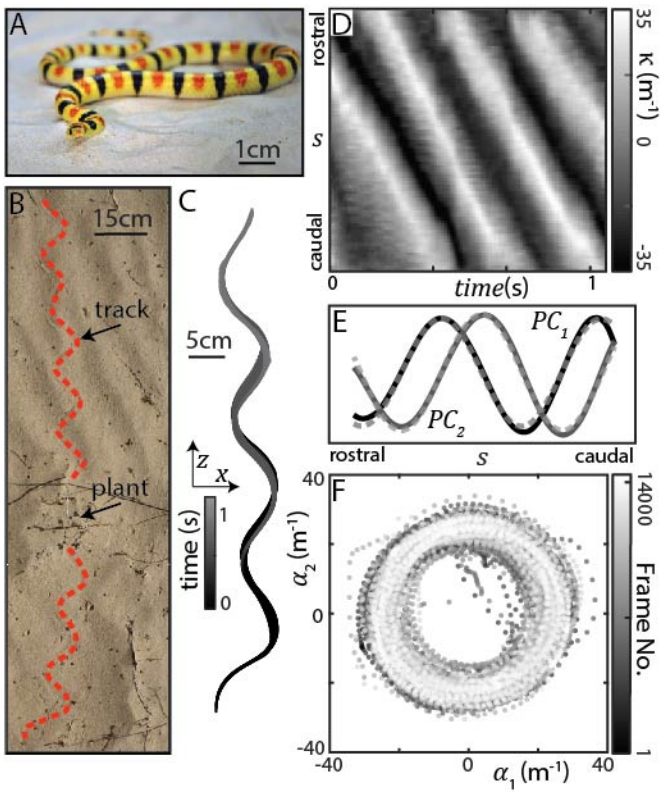


Figure 3.1: Stereotyped waveform of a desert snake. (*A*) *Chionactis occipitalis*, the Shovel-nosed snake at rest on sand. Total length $L = 37.3 \pm 1.9$ cm, mass $19 \pm 3$ g, total average body width $0.80 \pm 0.04$ cm, average of first half $0.96 \pm 0.03$ cm (mean$\pm$ s.d. of 8 individuals). (*B*) Picture of desert terrain with *C. occipitalis* tracks. The dashed line lies to the right of the sinuous track in the sand left by the snake. This snake was moving from bottom to top, changing direction as it encountered plant matter. (*C*) Example snake midlines, described by 100 x,z coordinates along the body, colored by time. Snake was moving on the sand-mimic substrate in the lab with no obstacles present. (*D*) Space-time plot of curvature, $\kappa$ (Fig. 3.5.9), of the trajectory in *C*. Horizontal axis is the arclength along the midline, **s**. Included are data from the neck to the vent. Diagonal bands are indicative of a traveling wave initiated near the head and passed posteriorly with limited variation. (*E*) PCA of $\kappa$ measured in 47 trials (N=7 individuals, 90 equidistant measurements along $s$ (Fig. 3.5.9), 15398 frames) on the sand-mimic substrate without posts. The first two components, $PC_1$ and $PC_2$, captured $86\%$ of the variance (Fig. 3.9*D*) and were well-fit by sinusoids (dashed gray lines, $PC_1$ R-squared=0.98 $PC_2$ R-squared=0.99) approximately $\frac{\pi}{2}$ out of phase ($0.45\pi \pm 0.04\pi$). (*F*) $\kappa$ can be approximated by $\kappa(s,t) \approx \alpha_1(t)PC_1(s) + \alpha_2(t)PC_2(s)$. A plot of $\alpha_1(t)$ vs. $\alpha_2(t)$, colored by frame number, revealed trajectories moved clockwise along a circular path which, combined with the sinusoidal PCs, produced a traveling wave of constant amplitude and wavenumber.

sand substrate interspersed with sparse heterogeneities such as small plants and twigs (Fig. 3.1*B*). This desert-dwelling species uses a stereotyped traveling wave when mov-

ing quickly ($30 - 80$ cms$^{-1}$, $0.8 - 2.1$ Ls$^{-1}$) on the surface of sand [48]). We previously found that this specific waveform confers maximum speed given a joint-level-power limit chapter 2, providing rationale for the conserved appearance of the waveform between individuals and trials.

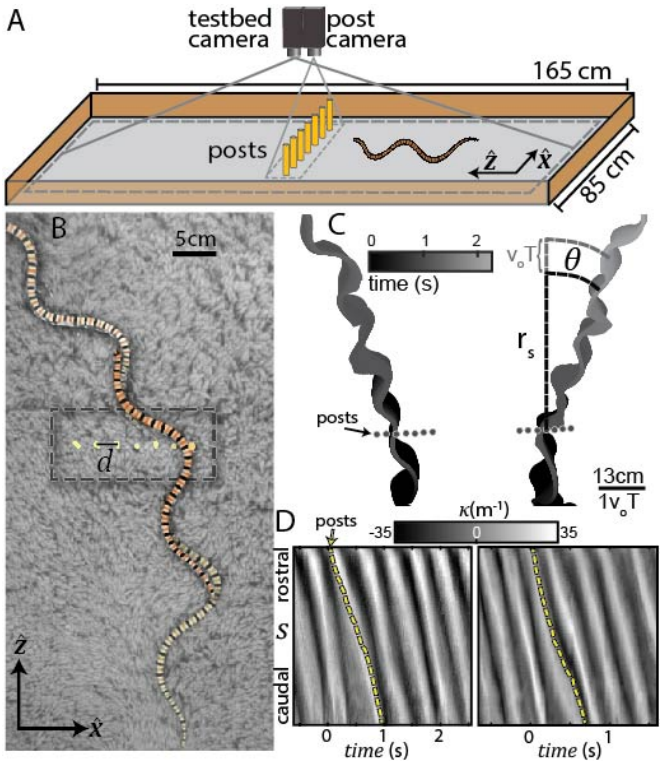


Figure 3.2: Interaction with model multi-component terrain. (*A*) Diagram of the laboratory model for desert terrain. Six force-sensitive posts radius $r_{post} = 3.2$ mm and one rigid fiducial were rigidly affixed to the experimental track–high pile carpet glued to a flat wood board. Two overhead cameras (AOS) captured video at 200 fps. Snake kinematics were obtained from the testbed camera while forces were calculated from post deflections captured by the post camera (Appendix 3.5.3). Note diagram is not to scale. (*B*) Snapshots $\approx 60$ ms apart of a snake moving from bottom to top and passing through the posts. Gray substrate is the high-pile carpet. Within the dashed rectangle are the equidistant posts placed in a straight line along $\hat{x}$ at a center-to-center distance $d = 23$ mm. (*C*) Example digitized snake trajectories (Appendix 3.5.8) from two individuals (120 and 124). 100 data points tracing the mid-lines of the snake from head to tail are plotted at each instant with color denoting time. Posts are gray circles. Scattering angle, $\theta$, was characterized by averaging the polar angle, measured with respect to the central post, of all data points in each trial found between a radial distance $r_s$ and $r_s + \text{v}_\text{o}\text{T}$. $\text{v}_\text{o}\text{T}$ is a dimensionless unit of distance equal to the average distance traveled in a single undulation. (*D*) Space-time plots of $\kappa$ for the trials in *C*. The dashed yellow line indicates the location on the body of the row of posts.

Fig. 3.1*C* is an archetypal example of the sinuous waveform used by this species when moving on spatially uniform and yielding substrates like sand or the sand-mimic substrate, high-pile carpet, used in this study to increase the rate of data collection (Appendix 3.5.6). This traveling wave initiates near the head and passes posteriorly with little variation along the arclength, $s$, of either maximum curvature, $\kappa_{\mathrm{m}}$, or wavelength (Fig. 3.1*D*). Principal component analysis (PCA) (inspired by [93]) is a method of dimensionality reduction in which one calculates the eigenvectors of the curvature covariance matrix. The resulting principal components (PCs) form an orthogonal basis describing the variation of $\kappa$ along the body. PCA revealed that $\kappa$ was well-approximated by a *serpenoid curve*[1] [94], $\kappa(s,t) \approx \kappa_{\mathrm{m}} sin(\frac{2\pi}{L}\xi s + \omega t)$ with $\kappa_m = 25.2 \pm 3.0$ m$^{-1}$ and wavenumber $\xi = 2.0 \pm 0.3$ (Fig. 3.1*E,F*).

We modeled the sand and sparse heterogeneities of the desert terrain as a row of 6 rigid, force-sensitive posts (Appendix 3.5.3) embedded in the carpet substrate, (Fig. 3.2*A,B*). Given both the robust appearance of this waveform across individuals and the advantages of using this shape to slither across sand, an omnipresent substrate in *C. occipitalis'* natural habitat, we endeavored to discover the snakes' strategy for contending with unexpected collisions. Namely, whether the animal would change strategy upon contact by altering the waveform to either avoid or grab the post, or if passive mechanics could allow transit without apparent change to the self-deformation program.

We challenged *C. occipitalis* (N=8) to travel across the substrate and through the post array. High-speed video captured kinematics and custom MATLAB software digitized the snake midlines for analysis (Appendix 3.5.8. We obscured the spectacle scales of the snakes using non-toxic face paint (Snazaroo Classic, Appendix 3.5.5) to focus on control modalities where the animal reacted to collisions rather than avoiding them. This behavior is likely relevant to this species as they do not appear to rely on vision during fast movement, supported by the wall-collision experiment discussed later. This also prevented reaction of the animal to cues external to the experiment, e.g. movement of the researchers.

[1]The waveform changes in time according to $\omega t$. However, because in our system inertia is dominated by damping, we will not include $\omega$ in analysis and $\omega = 1$ in all models.

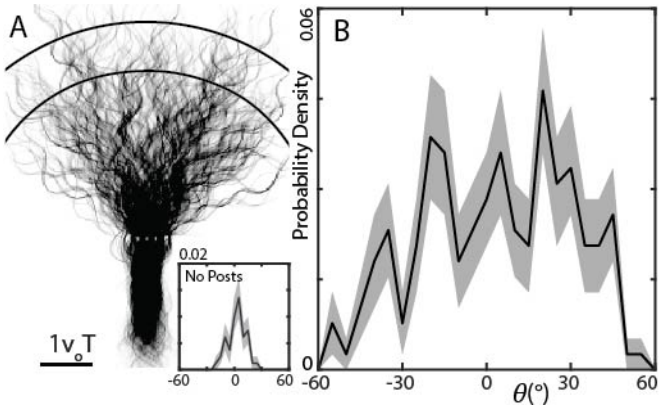


Figure 3.3: Mechanical diffraction pattern. (*A*) 253 trajectories collected using eight individuals. Data were shifted so the center of mass of each individual's trajectory before the array was within $^{d}/_{2}$ of the central post. We calculated the average value of $\theta$ for each trial using all data points within the arc shown. In *A* and *B* the solid curve is the normalized probability density (such that the integral under the curve is one) of $\theta$. The shaded area illustrates the $15.9^{th}$ and $84.1^{th}$ quantile estimated from a 10000 iteration bootstrapping using resampling with replacement. (*B*) Probability density of $\theta$ measured when no posts were present. Trials were shifted such that the average direction of motion of the first third of all trials aligned with $\hat{z}$. The last two thirds were used to calculate $\theta$ as in the array trials ($n = 44$ trials, $N = 8$ individuals) (*C*) $\theta$ probability density from the array experiment ($n = 194$, $N = 8$). Only trials with $\geq 50$ data points within the arc were included.

We focused our analysis on trials in which the snake initially traveled parallel to $\hat{z}$, passed through the array placed along $\hat{x}$, then continued along a straight line (Fig. 3.2*B,C*, Appendix 3.5.10). The pattern of alternating body bends was preserved throughout (Fig. 3.2*C,D*). We measured an average decrease in speed of $84\% \pm 27\%$ from before initial contact to once the snake was entirely clear of the array (Fig. 3.11*A,B*). While significant ($P \ll 0.001$ Wilcoxon signed rank test), the decrease was similar to that measured when no posts were present ($83\% \pm 19\%$, $P \ll 0.001$) and the animals were never observed stopping or turning back after contact.

After transiting the array, many snakes were deflected away from their original heading (Fig. 3.3*A*). We characterized the pattern of reorientations by finding the angle with respect to $\hat{z}$, $\theta$, of each trajectory (Fig. 3.2*C*) and calculating the probability density of all trials combined.

When there were no posts present, $\theta$ was at most 25° (Fig. 3.3*B*). In contrast, trajecto-

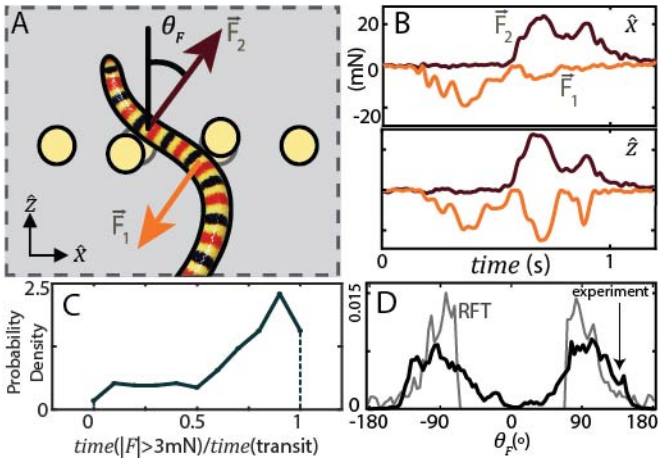


Figure 3.4: Pattern of forces during transit through array. (*A*) $\theta_F$ is the angle between $F_{\text{post}}$ and $\hat{z}$. Reaction forces $\vec{F}_{1,2}$ were measured using post deflections (Appendix 3.5.3). Diagram is not to scale. (*B*) Example post forces in $\hat{x}$ (*top*) and $\hat{z}$ (*bottom*). The animal in this trial contacted a post on both its right (orange, $\vec{F}_1$) and left (red, $\vec{F}_2$). (*C*) Compare to the force contact time–the sum of all frames in a trial that the force magnitude $|F|$ is measured above a threshold of 3mN–to the transit time–the time between when the first tracked point first reaches the array to the last tracked point exiting (n=233, N=8). A value of one indicates the snake experienced force $> 3$ mN for the duration of the time it was passing the posts, values ¡1 indicate the fraction of time the snake was passing the posts that $|F| > 3$ mN. (*C*) PDF of angle $\theta_F$ measured in experiment (black) and predicted by RFT (gray). (n=194, N=8, 28497 total measurements)

ries which passed through the posts were spread over $-57.2°$ to $56.1°$; the animals were diffracted by the interaction like fluid waves passing through narrow apertures (Fig. 3.3*C*). We observed three central peaks in the distribution, reminiscent of the interference pattern observed in matter-wave diffraction. The appearance of these peaks was robust to the measurement method (3.12) and these feature were present in $79.8\%$ of bootstrapping-predicted distributions (Appendix 3.5.2).

Reaction forces from the posts, $F_{\text{post}}$ (Fig. 3.4*A,B*), persisted over timescales comparable to the time it took *C. occipitalis* to transit the array (Fig. 3.4*B,C*, P=0.29 signed rank test comparing $70\%$ of the snake transit time to the total time forces above 3 mN were measured, Fig. 3.14*D*).

We predicted the forces experienced by *C. occipitalis* body segments during movement across sand using resistive force theory [79](RFT, Appendix 3.5.12). The median force

measured by the posts was 5.2 times that calculated from RFT, which is similar to the ratio, 4.9, of drag force in the sand-mimic versus sand (Fig. 3.14textitB,C). The forces from post were non-negligible compared to those used for locomotion, implying that the snake did not change its self-deformation pattern upon detecting a collision to avoid the obstacle.

Measurement of the force orientation angle, $\theta_F$ (Fig. 3.4*A*), revealed $F_{\text{post}}$ was most often oriented perpendicular to $\hat{z}$, that is, the snake pushed "left/right" rather than "forward/back" (Fig. 3.4*D*). As the snakes were not observed to change kinematics to "grab" the posts nor did we measure forces which were anti-aligned with the direction of motion at contact (i.e. $\theta_F = \pm 180$), we concluded that the animals did not change strategy upon collision to propel themselves forward using primarily the post. Interestingly, RFT calculation predicted a similar distribution of $\theta_F$ arising from interaction with a sand substrate (Fig. 3.4*D*). While further study of the forces acting between the animal and the sand-mimic substrate would be necessary to make a definitive statement, this pattern of transverse forces is consistent with non-inertial undulatory propulsion, suggesting that the animal interacts with the posts in the same way they push against piles of sand.

We hypothesized that forcing from the posts caused passive shape changes which broke the symmetry of the forward wave causing reorientation of the snake [127]. However, changes to the waveform during interaction with the post array were subtle (Fig. 3.2*B,C*). Therefore, to understand how the body deformed during interactions with obstacles, we elicited large deformation by replacing the post-array with a solid wall. Vision was not obscured during these trials and snakes made no observable effort to avoid the collision, providing further evidence that these snakes do not rely on visual path planning during movement.

Upon collision with the wall the body "buckled" at the nearest area of maximal curvature until the head traveled parallel to the board, at which point the animal changed strategy to attempt to bypass the obstacle (Fig. 3.5*A*). This pulse of high curvature, appearing as a red band in the $\kappa$ space-time plot (Fig. 3.5*B*), was spatially localized; $\kappa_m$ of the next ex-

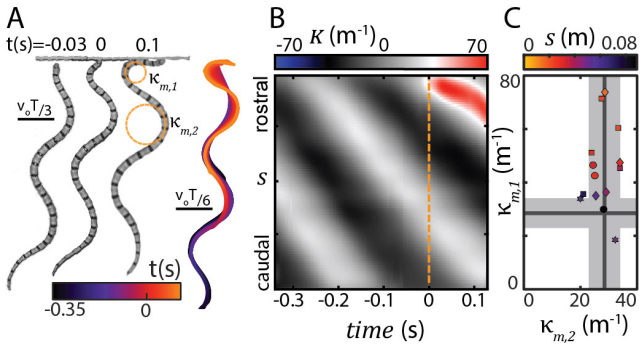


Figure 3.5: Localized deformations arose from collisions. (*A*) Three snapshots from experiment at the times indicated and the digitized midlines at all times, indicated by color. Dashed orange circles indicate where $\kappa_{m,1}$ and $\kappa_{m,2}$ in *C* were measured. (*B*) Space-time plot of $\kappa$ for the trial in *A*. The snout first contacts the wall at time t=0 indicated by the dashed orange line. (*C*) Maximum curvature of the bend closest to the wall, $\kappa_{m,1}$, versus that of the second closest, $\kappa_{m,2}$. Lines and gray area are the mean and standard deviation of the nominal $\kappa_m$ measured when the snake is not in contact with the wall. $\kappa_{m,1}$ increased above the average value during contact with the obstacle to a value related to $s$ measured at first contact, indicated by color (Appendix 3.5.9).

.

trema, measured simultaneously (see diagram Fig. 3.5*A*), was unchanged (Fig. 3.5*C*).

### 3.3.2 Slithering and Buckling Model

We previously observed "mechanical diffraction" patterns in an open-loop snake-robot which was rigidly rotated to certain $\theta$ during interaction with posts [128, 129]section 5.2. We hypothesized that mechanical diffraction in the animals could similarly arise from adherence to a serpenoid self-deformation pattern which passively buckled in response to external forcing by the posts.

We developed a model to explore the outcome of our hypothesized strategy. Previous models of elongate, undulatory animals calculated the acceleration of body segments using internal forces, such as muscle activation and viscosity of the viscera, and external forces, like friction of the scales, discrete posts, or fluids [49, 130, 25, 24]. Rather than use a dynamical model of our system, we chose to develop a purely geometric model which allowed us to focus on the contribution and consequences of the hypothesized strategy.

We bypassed the complexity of the interaction between the spatially extended body, the

substrate, and the post by assuming forces between the body and the substrate were such that the snake propagated with minimal slip (Appendix 3.5.4) and the body was buckled by the post the minimum amount necessary to prevent overlap. The position of each segment was prescribed at each time based on these assumptions (see Appendix 3.5.13 for details).

Snakes performing terrestrial lateral undulation use waves of unilateral activation of the epaxial muscles to self-deform [58]. Therefore, we assumed passive body buckling would occur at those locations on the waveform where the shape change would only further shorten already active muscle segments [131]. To mimic this waveform-dependent compliance, we dictated that $\kappa$ changed at a "preferred buckling" location, $s_{\text{buckle}}$, determined by the muscle activation pattern (Fig. 3.6*A*) and dependent on wave phase and post contact location (Fig. 3.15*B,C*).

When the model snake contacted a post, curvature at $s_{\text{buckle}}$ was set to the predetermined absolute maximum value of $\kappa_{\text{abs}} = 50\ \text{m}^{-1}$ (the nominal amplitude was $\kappa_{\text{m}} = 25\ \text{m}^{-1}$) over as many segments necessary to solve the constraint, leading to a pulse of high-curvature like that observed in the snake wall-collision trials (Fig. 3.6*B*). Given the assumption that the body was passively deformed by external forces, the modified waveform was passed down the body at the wave speed.

Like *C. occipitalis*, the model trajectories were spread by the array interaction (Fig. 3.6*C*), either continuing approximately along $\hat{z}$ or at an angle $\theta = \pm 22.0 \pm 7.0^\circ$ (Fig. 3.6*D*).

The location and relative prominence of the peaks depended on the geometric parameters. We defined $R_{\text{buckle}} = (\kappa_{\text{abs}} r_{\text{post}})^{-1}$ and $D_{\text{buckle}} = s_{\text{max}} r_{\text{post}}^{-1}$, where $s_{\text{max}} = {}^{L}/_{2\xi}$ was the largest possible value of $s_{\text{buckle}}$. In the model we used the same $d = 23$ mm as in the snake experiment but increased post radius to $r_{\text{post}} = 10$ mm as, because the model is infinitesimally thin, using the same dimensional parameters as in the snake resulted in fewer post collisions (Fig. 3.17*A*). We used $R_{\text{buckle}} = 4.1$ and $D_{\text{buckle}} = 20$ in the model. These parameters were comparable to the average snake values of $R_{\text{buckle}} = 3.5 \pm 0.4$ (mean and range estimated using both the the wall trials and an anesthetized snake [13])

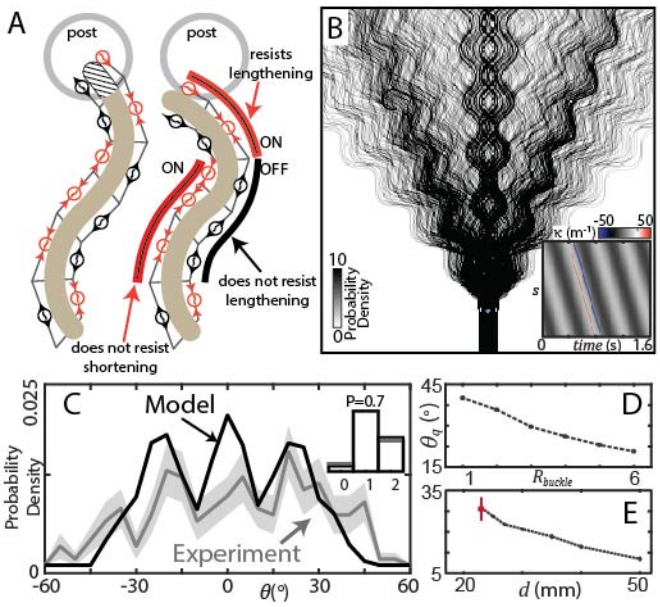


Figure 3.6: Mechanical diffraction arises from open-loop control and passive dynamics. (*A*) Cartoon diagram of snake muscle activation. Red units are actively shortening while black are passively lengthening, as indicated by the arrows on the units. (*left*) Example of a nominal shape which violates the post constraint, indicated by the hashed area. (*right*) The model solution which moved the head out of the post by increasing curvature at the red muscle units which would not resist shortening. (*B*) Space-time plot of $\kappa$ for an example trial in which the model snake contacted two posts. White bands are the large $\kappa$ buckling occurring at post contact. (*C*) Probability density of model trajectories. (*D*) Probability density of $\theta$ measured from experiment (gray curve, n=194, N=8) and model (black curve, n=700) in the arc $r_s = 3.3 - 4.3$. Filled areas are standard deviation estimated using bootstrapping. Standard deviation of the model is $\approx$1 line width. (*E*) $\theta_q$ as a function of $R_{\text{buckle}}$, $d$ fixed. $\theta_q$ is the average of the 15th and 85th quantiles of the scattering distribution. Vertical bars are the standard deviation of these two values. The deviation is small, reflecting the symmetry of the distributions. (*F*) $\theta_q$ versus $d$, $R_{\text{buckle}}$ fixed. Black circles and dashed lines are from the model, red marker is from experiment (n=194, N=8).

and $D_{\text{buckle}} = 31.8 \pm 3.1$ and yielded the same distribution of post contacts as in the animal (Fig. 3.6*D, inset*).

Inspired by the effect of slit width on diffraction patterns, we used the model to examine $\theta_q$, the spread of the trajectories (the "diffraction"), as $R_{\text{buckle}}$ and $d$ varied. Increasing $R_{\text{buckle}}$ meant that to bypass the post more segments were involved in buckling, shifting the average location of the bend further away from the post. The further from the post buckling occurred, the less angular deflection of the trajectory was needed to bypass it (as seen below in Fig. 3.7*C*), so as $R_{\text{buckle}}$ increased $\theta_q$ decreased (Fig. 3.6*E*).

Although our system is highly deterministic (Fig. 3.15*D,E*) $\theta_q$ decreased $d$ increased as in diffraction of fluids or subatomic particles (for constant wavelength, Fig. 3.6*F*). When freely moving, the maximum angle the body made relative to $\hat{z}$ was $\phi_o = 45.6°$. At $d =$ 23 mm the maximum angle the body could make between the posts was $\phi_p = 29.6°$ and $\theta$ was determined primarily by the wave phase at contact (Fig. 3.15*D,top*). In contrast, when $d = 50$ mm $\phi_m = 66°$, the model never contacted more than one post in a trial, and the impact location on the post was influential (Fig. 3.15*D,bottom*). We rationalized that for small spacings there was a greater probability the body had to reorient to match $\phi_m$ for the trajectory to pass between the posts, regardless of the initial contact location. As $\phi_m$ became larger than $\phi_o$ the wave always "fit between" the posts and $\theta$ were dominated by how far the trajectory must deflect to bypass the initially contacted post. Further, as $d$ increased more trials transited the posts without contact, increasing the signal at $\theta = 0$ and moving $\theta_q$ inward.

### 3.3.3 Ray Model

To gain insight into the fundamental interactions behind snake re-orientation we developed a further simplified analytical description. We represented the snake as a ray, that is, the limiting case of the serpenoid curve (sinusoidally varying curvature [94]) as $\kappa_m \to 0$. This simplification, reducing a traveling wave to a ray which interacts with its surroundings

following rules set by the properties of the full system, aides in the calculation of, for example, the specular scattering of light (see e.g. [132]).

For the current study, we focused on understanding interactions with a single post. While we were not able to perform the snake experiments for a single post due to the low probability of the animal contacting an obstacle, using the slithering model we noted that the width and peak locations in the distribution of $\theta$ were comparable to the multi-post case (Fig. 3.16*C*). The most noticeable difference was the higher central peak relative to the side lobes, likely because the addition of multiple posts remapped trajectories that would have had small-scatter collisions with the single post to collisions which resulted in larger angles [128].

We calculated the distribution of scattering angles for rays initially parallel to $\hat{z}$ which bent to $\kappa_{\text{abs}}$ at location $s_{\text{buckle}}$ to solve the post constraint (Fig. 3.7*A, B*). The predicted distribution agreed well with that calculated using the slithering model for a single post (Fig. 3.7*C*). Scattering angles from head-buckle ($s_{\text{buckle}} = 0$, Fig. 3.7*A*) trajectories rose from zero probability at $\theta = 0$ to a maximum value set by $\theta_{\text{max}} = \cos^{-1}\left(\kappa_{\text{abs}}^{-1}/(\kappa_{\text{abs}}^{-1} + r_{post})\right)$ (Appendix 3.5.14) before dropping off, yielding the secondary peaks. The central peak was primarily trajectories which buckled at locations $s_{\text{buckle}} > 0$ (Fig. 3.7*B*).

The agreement between the ray model and the more complicated slithering model suggested that the periodic undulation of the body was not as important in determining the features of the scattering pattern as was the constraints on motion imposed by the unilateral muscle activation and the spatially extended body which limited how sharply the direction of motion could be changed. Future work could include extending the ray model to include multiple posts.

## 3.4 Conclusions

Our surprising discovery of a mechanical diffraction pattern arising from interaction between a sand-specialist snake and multi-component terrain revealed the benefit of pas-

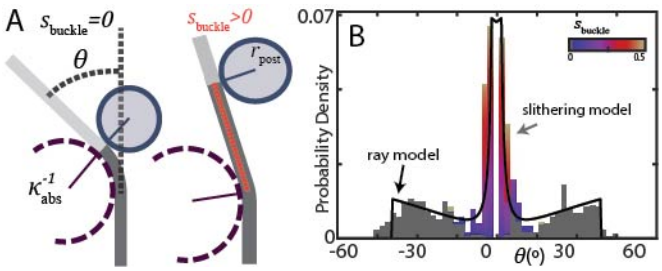


Figure 3.7: Ray model reproduces single-post scattering pattern. (*A*) A ray bends at $s_{\text{buckle}}$ to avoid overlapping the post (solid circle). $\kappa_{\text{abs}}$ is the maximum radius of curvature and $r_{post}$ is the post radius. $s_{\text{buckle}} = 0$ in $50\%$ of trajectories; the ray buckles at the point of post contact ("the head" in the slithering model). (*B*) The other $50\%$ of trajectories have a value of $s_{\text{buckle}}$ which is equally distributed on the interval $(0, s_{\text{max}}]$ (Fig. 3.16*D, inset*). (*C*) PDF of $\theta$ calculated for a single post using the ray model prediction (black curve) and the slithering model (colored bars, n=579). The colors represent the buckling location $s_{\text{buckle}}$ in the trial which scattered to that angle. $R_{\text{buckle}} = 3.5$ and $D_{\text{buckle}} = 31.8$ in both models. The slithering model algorithm limited the smallest possible scattering angle to $\pm 1.3°$, resulting in the gap around $\theta = 0°$ (Appendix 3.5.13).

sive mechanics in negotiating collisions in limbless systems. We used a geometric model to show that the reorientation pattern was reproduced by an open-loop control strategy wherein the motor program continued unaltered during unexpected collision with the posts while unilateral muscle activation allowed the body to passively buckle around obstacles. A ray model provided insight into the fundamental mechanisms behind the diffraction, implicating that the existence of preferred buckling locations on an extended body, engendered in our case by the unilateral muscle activity pattern, caused trajectories to scatter non-uniformly off of a post.

The paradigm in snakes [125] and snake-like robots [68] is closed-loop control of joint trajectories which ensures the many joints remain coordinated in using complex terrains to generate propulsive forces. Our work provides a starting point for disentangling the role of mechanics and active control; testing hypotheses for neuromechanical control in a frame as suggested by [133] would be illuminating in this regard. The use of mechanical structure to supplement open-loop control has been largely studied in rapidly-moving legged animals [119, 120, 121, 122] and used to simplify control in bipedal and sprawled-posture robots [134, 135]. This work suggests that passive mechanisms are more general in nature,

and a similar strategy could be useful in the next generation of limbless robots. However, future work is needed to determine when this strategy is not appropriate, e.g., terrains with more dense obstacles or even certain waveform/obstacle combinations.

Finally, we comment on our results in the context of the emerging field of active matter and non-momentum conserving collisions [136]. Our biological mechanical diffraction mimics phenomena found in subatomic systems; this is part of a growing realization that active collisions are a fertile source of interesting dynamics, from mechanical diffraction in a robot [128], the scattering of microorganisms off walls [137, 138], to shape-induced reorientation of a cockroach [114]. We posit that a framework which takes inspiration and uses tools from diverse systems could help develop broader understanding of principles of heterogeneous interaction of self-propelled systems across scales.

## 3.5 Appendix

### 3.5.1 Snake experiments

All *Chionactis occipitalis* were collected in accordance with scientific collection permits (nos. SP790952, SP625775, SP666119) approved by the Arizona Game and Fish Department. All snake experiments were conducted under the Georgia Institute of Technology IACUC protocols A14066 and A14067. Snakes were set in the arena and once they began moving were not contacted during a trial. We used trials where the snake approached perpendicular to the row of pegs and continued moving straight for at least three full undulations (Appendix 3.5.10). Temperature in the testing and holding area was maintained at $27.2 \pm 0.6^{\circ}$ C. Note that all reported values are mean$\pm$ standard deviation unless otherwise indicated.

### 3.5.2 Bootstrapping

We used bootstrapping to estimate the importance of the features observed in the $\theta$ histograms. Using $\theta$ measured in 194 trials we generated 10000 distributions using random

resampling with replacement. We counted how many times the three central peaks and two central valleys were present in the distribution by searching for features of prominence at least 0.004 (smallest prominence in the real distribution=0.0052) occurring on the interval between its neighboring features, measured from the distribution in Fig. 3.3*C*. Peak locations were $[-30, 10)^\circ$, $(-10, 15)^\circ$, and $(15, 35]^\circ$ and valleys were $(-20, 5)^\circ$ and $(5, 20)^\circ$.

### 3.5.3 Force-sensitive posts

The theoretical prediction for force, $F$, as a function of peg tip deflection, $\delta$, is $F = \frac{3E\pi r_{post}^4}{2a^3(9\frac{L_{post}}{a}-5)}\delta$. $L_{post} = 7$ cm, $a = 2.81$ cm is the height of applied force measured from base, Young's modulus $E = 5.7 \pm 0.6$ MPa, and peg tip deflection $\delta$ measured from the high-speed video (Fig. 3.2*A*. Post deformations were small compared to snake length scales (3 mm deflection at tip for a load of $0.050$ N at $a = 2.7$ cm). Uncertainty due to variation in $a$ was $< 10\%$ (Fig. 3.10*C*, Appendix 3.5.11). The signal from the rigid fiducial was subtracted to account for relative movement between the arena and the camera.

### 3.5.4 Geometric model

*C. occipitalis* experiences low but nonzero slip when moving on carpet (Appendix 3.5.6) so that the body could slide into contact with the posts at locations other than the head. Because such contacts were minimal we dictated the model moved with no slip. We initiated the model trajectories at 700 locations representing a uniform sampling of combinations of wave phase and peg contact location (Fig. 3.15*A*). In both the models and the biological snake the interactions with each post were independent as the lattice spacing was large enough that deformations caused by a post would not involve enough of the arc length to reach locations in contact with other posts.

### 3.5.5 Snake"Blindfolding"

Instead of eyelids to protect the eye, snakes' have a specialized spectacle scale which is continuous with the surrounding skin. To prevent visual path planning, we obscured the snakes' spectacle scales using black water-based face paint (Snazaroo classic face paint) prior to data acquisition with a clean sponge brush. Upon completion of a day's data collection, the paint was gently removed with a different wet sponge brush.

### 3.5.6 Sand-mimic substrate

Collecting a successful run (see criteria in Run Sorting section below) involved several unsuccessful trials. We found that data collection using a granular matter (GM) substrate was an impediment to the study due to the need to fluidize the GM and reset the post array multiple times to capture a single successful trial. Therefore, we endeavored to find a sand mimic on which the animals used the sand-swimming waveform which also allowed rapid repetition of trials.

To this end we tested a number of materials including artificial turf and several types of carpet. We found a high pile (¿1 inch) carpet (Room Essentials, Style E363, gray color, 100 nylon (latex backing)) on which *C. occipitalis* used a waveform comparable to that measured on GM. To verify this we collected 47 trials (N=7 snakes) on the sand-mimic substrate without any pegs present and compared to those collected on homogeneous $297 \pm 40$ $\mu$m glass particles (N=9 snakes, 32 trials). On carpet (mean$\pm$s.d.) $\kappa_m = 25.2 \pm 3.0$ m$^{-1}$ and $\xi = 2.0 \pm 0.3$ compared to the similar GM values $\kappa_m = 25.6 \pm 3.6$ m$^{-1}$ and $\xi = 1.9 \pm 0.2$. PCA of both datasets revealed the same two dominant, sinusoidal $PC$s with a periodic, circular relationship between $\alpha_1$ and $\alpha_2$ (Fig. 3.1*E,F* for shag and Fig. 3.9*A,B* for sand). The normalized eigenvalues and variance squared on each substrate were similar (3.9*C,D*).

Movement on carpet was higher-slip than on GM, measured using the slip value, $\beta_s = \sum_{i=1}^{N} acos(|\hat{t}_i \cdot \hat{v}_i)$ [13], where $\hat{t}_i$ and $\hat{v}_i$ are the tangent and velocity unit vectors for each

segment $i$ of $N$ total body segments ($N = 100$ for this calculation). This is a measure of how well each segment follows in the path of the preceding segment, e.g. $\beta_s = 0$ is a snake moving "in a tube". On carpet $\beta_s = 7 \pm 6^\circ$ while on GM $\beta_s = 3.7 \pm 1.5^\circ$. From these results we concluded that the carpet was an acceptable sand mimic for the purpose of our study.

### 3.5.7 Selection of array layout

We performed exploratory studies using a few combinations of post sizes and center-to-center distances. We tested in the snakes in the 0.64 cm diameter posts used in the study at spacings of 2.3 cm and 8.8 cm and 2.54 cm diameter posts spaced at 5.01 cm.

We decided against using the larger diameter posts because the smaller posts allowed us to measure forces. The smaller posts also had a radius of curvature which was much greater than that of the snake such that we assumed the impact of the post curvature was negligible.

We chose to use the smaller spacing because at the larger spacing the snakes rarely contacted an obstacle.

### 3.5.8 Snake Tracking

The arena was filmed with two AOS high-speed cameras at 200 frames per second. The two cameras (one X-PRI, one S-Motion, AOS Technologies, Switzerland) were mounted above the arena with the approximate fields-of-view as shown in Fig. 3.2*A*. The setup was such that we did not need to correct the digitized data to account for lens distortion. Video from the full-bed-view camera (1280×696 px$^2$=151.5×82.4 cm$^2$), was digitized using custom MATLAB code.

We first imported the images to MATLAB as matrices of grayscale values. We used the MATLAB function *imfindcircles* to find the posts in the first frame then created a binary image of the posts using the position and radius of the circles and the MATLAB function

*impolygon*. To track the snake we subtracted subsequent frames and subtracted the binary image of the posts from the resulting matrix. The snakes' dark/light banding meant the body stood out in the difference between successive images. The background was thresholded to changes which were less than expected for a moving snake and the MATLAB function *medfilt2* was used to further reduce noise. Next we performed image dilation of the remaining pixels using MATLAB *imdilate* with a disk size of 25 pixels, converted to a binary image, and reduced pixels to a line using MATLAB *bwmorph, 'thin'* with n=inf. *regionprops* listed all pixels in each continuous line and any line length less than minThresh = 100 or greater than maxThresh = 600 was deleted to removes objects which are too small or large to be a snake, e.g. dark areas at the edges of the arena or researcher arms/hands. Lastly we found the linear indices corresponding to the remaining points, these were our (x,z) snake midline coordinates.

At each time a smoothing spline of length 200 was fit to the the midline coordinates then downsampled to 100 points.

### 3.5.9 Wave Measurements

For all space-time plots of animal data $\kappa$ was calculated from the digitized data. To reduce noise, $\kappa(s_i, t_j)$ was calculated using the points $\pm 0.05s$ anterior and posterior to $s_i$ at time $t_j$ so that roughly the neck to the vent of the midline was reported and the number of data points was reduced from 100 to 90. In the wall collision trials we were unable to robustly track the snake when it was in contact with the wall. Therefore, to measure the curvature, ImageJ was used to manually fit circles to the images. The arclength was measured from the nose to the point of maximum curvature at the instant of contact with the wall. The curvatures $\kappa_{m,1}$ and $\kappa_{m,2}$ were measured at the same instant in time once the head of the snake was parallel to the wall.

We note that in the slithering and buckling model (see below Slithering and Buckling Model section) $\kappa_{\text{abs}}$ is a constant, as defined. However, in the wall collision trials, when we

measured on the snake by hand it was a function of arc length from contact. This may be because the hand measurements were averaging the effect of $\kappa_{\text{abs}}$ appearing over a number of segments. The number of segments recruited is a function of how far the head must move which depends on how close the extrema is on contact.

We saved images from the model started at different initial conditions and colliding with a wall then measured $\kappa_{m,1}$ and $\kappa_{m,2}$ from using the same ImageJ method as in the animal trials. This resulted in a distribution which had some dependence on the arclength at impact as in the snake (Fig. 3.17*B*), suggesting that the hand measurements report a value which is related to the number of segments involved in the buckling. This also gives an idea of the uncertainty introduced by the hand measurement. $\kappa_{m,2} = 25$ m$^{-1}$ in all of the trials. The error in hand measurement was (mean$\pm$s.d.) $1.6 \pm 3.9$ m$^{-1}$. The largest reported error was $9.8$ m$^{-1}$ which is less than the difference $\kappa_{m,1} - \kappa_{m,2} = 18.9 \pm 4.8$ m$^{-1}$ in the model or in the snake, $\kappa_{m,1} - \kappa_{m,2} = 20.0 \pm 16.7$ m$^{-1}$.

We also note that the internal viscous damping and the overlap of many muscle segments means that in the animal the change in curvature is not as localized in the model.

$v_o T$ was measured in each trial (without posts present) by calculating it at for each of the hundred points along the body then taking the average. At each point we find the inflection points in $\kappa$. These occur every half of a complete undulation. Using these locations we then pinpoint the location in the lab frame of a known point on the waveform and calculate the Euclidean distance between these. We use as a unit of measurement the average across all trials. We chose $v_o T$ over wavelength $\lambda$ because the animal experiences some slipping of the body, as discussed in the above **Sand-mimic substrate** section. The context for the distances we measured was understanding how far the snake was moving, rather than the waveshape. For example, in calculating $\theta$ we wanted to average over an undulation.

### 3.5.10 Run Sorting

The snake did not always travel perpendicular to the posts before contacting the array nor continue along a straight trajectory after the array. We were interested in first understanding the impact of the posts on a snake whose original heading was perpendicular to the array. Therefore, we accepted only trials where the heading of the snake prior to the array was $< 15^\circ$ with respect to $\hat{z}$. Heading was measured by fitting a line to the maxima/minima of the trajectory of each point through time and averaging the slopes.

We also wanted to understand the emergent behavior of the snake in response to the posts as opposed to secondary behaviors such as stopping or turning which we believe were elicited by outside factors such as movement of the researcher. To remove these behaviors, we accepted only runs where the radius of the osculating circle, measured by picking out three maxima and/or minima pairs and fitting a circle to them, describing the trajectory of the snake after exiting the array was greater than 15 cm. This is larger than the typical maximum radius of curvature of the snake waveform ($\approx 3$ cm).

### 3.5.11 Force-Sensitive Posts

The posts were made from $6.4$ mm diameter polyurethane rods (Shore 60A durometer, semi-clear amber color, McMaster-Carr) cut to a length of $7 \pm 0.1$ cm. They were affixed via interference fits in the plywood and protruded through small holes in the rug. Six of the pegs were force-sensitive and rigid peg at the end of the row was used as a fiducial. The pegs were coated with a light dusting of baby powder to reduce friction.

We measured snake-post contact height, $a$ (Fig. 3.10*B*), from 23 total trials among three individuals. The snakes transited posts with ruler markings added and a mirror was used to collect simultaneous top and side view video (Fig. 3.10*A*). All other conditions were the same as in the scattering experiment. We estimated the snakes contacted the post at $a = 28.1 \pm 1.6$ mm.

To verify that the relationship between tip deflection and force was valid for the con-

ditions in the experiment we characterized the peg reaction forces using a 6-axis industrial robot arm (Denso VS087A2-AV6-NNN-NNN) to quasi-statically deform pegs a set distance (1 mm) at different $a$. A 6-axis force-torque transducer (NANO 43, ATI Industrial Automation. Apex, NC, USA) measured the reaction force. A 3D printed plastic part attached to the force-torque transducer was used to contact the peg. The peg was firmly clamped, and $a$ was measured from where the peg emerged from the clamp. We compared these measurements to those predicted by the theory and found they were in good agreement for $a \leq 8$, which was much less that the snake contact heights (Fig. 3.10*C*).

### 3.5.12 Resistive force theory calculation

Resistive force theory (RFT) was used to estimate the reaction forces experienced by the snake during movement. As the pattern of self-deformation and resulting performance on granular matter was comparable to that on the sand-mimic, we calculated forces acting on the body using the surface drag relations for homogeneous $297 \pm 40$ $\mu$m diameter glass particles (chapter 2, similar grain size to the sand in *C. occipitalis'* natural habitat).

We used the nominal sand-swimming template as the self-deformation pattern and calculated horizontal-plane-forces $\vec{F}_x$ and $\vec{F}_z$ as well as torque about the center-of-mass. At 70 equally spaced points in time over a single undulation cycle we used the MATLAB *fminsearch* function to find the center-of-mass velocity which minimized the sum over all segments of each of these three quantities.

The force angle was calculated using $\arctan\left(\vec{F}_z(s,t)/\vec{F}_x(s,t)\right)$. The histogram in Fig. 3.4*C* was calculated using this value over all $s$ and $t$. Force magnitudes were calculated $\sqrt{|\vec{F}_{z(s,t)}|^2 + |\vec{F}_{x(s,t)}|^2}$ and Fig. 3.15*B* included this value for all $s$ and $t$.

For more information about RFT see [34, 139].

### 3.5.13 Slithering and Buckling Model

Snake muscle activation during terrestrial slithering is unilateral. This can be represented as a condition on $\kappa$

$$\text{if } \frac{d\kappa}{ds} < 0 \text{ then left side active} \rightarrow \kappa \text{ increasing}$$

$$\text{if } \frac{d\kappa}{ds} > 0 \text{ then right side active} \rightarrow \kappa \text{ decreasing}$$

The head will move either clockwise or counterclockwise around the post, whichever direction minimizes the angle between the head and post tangent vector, illustrated in Fig. 3.15*B*. The location where buckling begins is therefore determined by the first segment on the body where the condition on $\kappa$ moves the head in the desired direction. Once the buckling location is determined the curvature of the segment at that location is set to $\pm\kappa_{\text{abs}}$ with sign determined by transit direction. The new shape is then calculated by integrating the new $\kappa$ and the post overlap condition checked again. If the head is still in the post, the next posterior segment is assigned to $\pm\kappa_{\text{abs}}$ and so on until the head is no longer in the post.

Once the head is no longer violating the post constraint the model moves to the next timestep by passing the current shape down one segment and assigning to the head the pre-calculated $\kappa$ for the new time. The number of segments is chosen based on wavespeed such that at each time step a segment takes the place of its anterior neighbor. The no-slip condition is enforced by using MATLAB's *fminsearch* function to find $v_{CoM}$ which minimizes the the sum of all $\beta_s$.

### 3.5.14 Ray Model

Here, we present details of the analytic derivation of the scattering probabilities of a snake scattering off a single post in the limit of zero slithering amplitude. Remarkably, this single approximation leads to an exact solution which recovers and explicates key features of the

scattering distributions of the experimental and simulation trajectories.

In this model, a snake initially contacts the post (in units such that $r_{\text{post}} = 1$) at some position to the left of its midpoint a distance $0 \leq \bar{x} \leq 1$ (with all such distances having equal likelihoods), leading ultimately to some scattering to the left by an angle of amplitude $\theta$. By symmetry, trajectories impacting the same distance to the right of the post's midpoint scatter by the same amplitude to the right.

Upon contact with the post, the snake begins to buckle with radius of curvature $r_{\text{min}}^{-1} = \kappa_{\text{abs}}$. Although the slithering amplitude is zero, we retain the slithering *wavelength*, such that depending on where the snake is in its cycle this buckling begins a point $s_{\text{buckle}}$ at either the head (with $50\%$ likelihood), or at some point uniformly distributed between the head and some distance $s_{\text{max}}$ back along the snake's body (see Fig. 3.16*A* for distribution of $s_{\text{buckle}}$ measured in the slithering simulation). This is a good but imperfect approximation to the true snake buckling behavior.

After buckling, the snake's head continues along the post, eventually rotating until it can continue onward at scattered angle $\theta$, as shown in Fig. 3.7*A,B*. Where the snake buckles, it follows a section osculating circle of radius $r_{\text{min}}$. In between, the snake undergoes free-space propagation for a distance $s_{\text{buckle}}$, which in this case is a straight line (see diagram Fig. 3.16*B*).

Remarkably, this behavior leads to a simple geometric relation between the parameters of the trajectory, $(\bar{x}, s_{\text{buckle}})$ (Fig. 3.16*B*) and the scattering angle. The lateral distance, $\bar{x} + r_{\text{min}}$ can be calculated two different ways, leading to

$$\bar{x} + r_{\text{min}} = (1 + r_{\text{min}})\cos(\theta) - s_{\text{buckle}}\sin(\theta).$$

For fixed $s_{\text{buckle}}$, the probability $P(\theta)$ that the scattering angle falls within a range $(\theta, \theta + d\theta)$ can be related to the probability $P_x(\bar{x})$ that the contact point $\bar{x}$ falls within some range $(\bar{x}, \bar{x} + d\bar{x})$ via $P(\theta)|d\theta| = P_x(\bar{x})|d\bar{x}|$. Since $\theta(\bar{x})$ is monotonic in this range (larger offsets lead to larger scattering angles, this leads to $P(\theta|s_{\text{buckle}}) = \frac{d\theta}{d\bar{x}} P_x(\bar{x})$. Since the

snake is equally likely to encounter the post with any lateral displacement, this leads to the unnormalized probability distribution

$$P(\theta|s_{\text{buckle}}) = (1 + r_{\text{min}}) \sin\theta + s_{\text{buckle}} \cos\theta.$$

To obtain the full distribution of scattering angles, $P(\theta)$, we need only integrate the above expression over all possible buckling positions. To do so, it will prove necessary to determine the maximum scattering angle possible for a given buckling position. General trigonometry reveals that this occurs at $\bar{x} = 0$, and be equal to

$$\theta_{\text{max}}(s_{\text{buckle}}, r_{\text{min}}) = \arccos\left(\frac{r_{\text{min}}}{\sqrt{(1 + r_{\text{min}})^2 + s_{\text{buckle}}^2}}\right) - \arccos\left(\frac{1 + r_{\text{min}}}{\sqrt{(1 + r_{\text{min}})^2 + s_{\text{buckle}}^2}}\right).$$

In the event that the scattering angle $\theta$ considered is less than the maximum scattering angle allowed at $s_{\text{max}}$, our integral of $P(\theta|s_{\text{buckle}})$ simply ranges from $s_{\text{buckle}} = 0$ to $s_{\text{buckle}} = s_{\text{max}}$. However, as the scattering angle increases, it eventually assumes values such that even at $\bar{x} = 0$ only certain buckling positions can lead to such angles. Thus, the buckling integral in this case should cut off at

$$s_m(\theta) = \left[(1 + r_{\text{min}}) \cos\theta - r_{\text{min}}\right] / \sin\theta.$$

Because of the simplicity of the snake's distributions (in this non-slithering approximation), each of these cases may be performed separately, resulting in the full scattering distribution

$$P(\theta) = \begin{cases} 2(1+r_{\text{min}})s_{\text{max}}\sin\theta + (1/2)s_{\text{max}}^2\cos\theta & 0 \leq \theta < \theta_{\text{max}}(s_{\text{max}}) \\ (1+r_{\text{min}})(s_{\text{max}} + s_m(\theta))\sin\theta + (1/2)s_m^2(\theta)\cos\theta & \theta_{\text{max}}(s_{\text{max}}) \leq \theta \leq \theta_{\text{max}}(0) \\ 0 & \theta_{\text{max}}(0) \leq \theta \\ P(-\theta) & \theta \leq 0. \end{cases}$$

This distribution, as shown in Fig. 3.7*C* (as well as Fig. 3.16*C*), captures in a single model the peak of low-scattering angle trajectories with buckling occurring far from the head and peaks at finite scattering angle associated with head-buckling.

Table 3.1: Number of trials per individual.

| Individual | No. total trials | No. trials in main text plots |
|---|---|---|
| 120 | 17 | 13 |
| 121 | 21 | 20 |
| 122 | 54 | 50 |
| 124 | 40 | 33 |
| 125 | 35 | 32 |
| 129 | 16 | 11 |
| 131 | 18 | 15 |
| 132 | 32 | 28 |

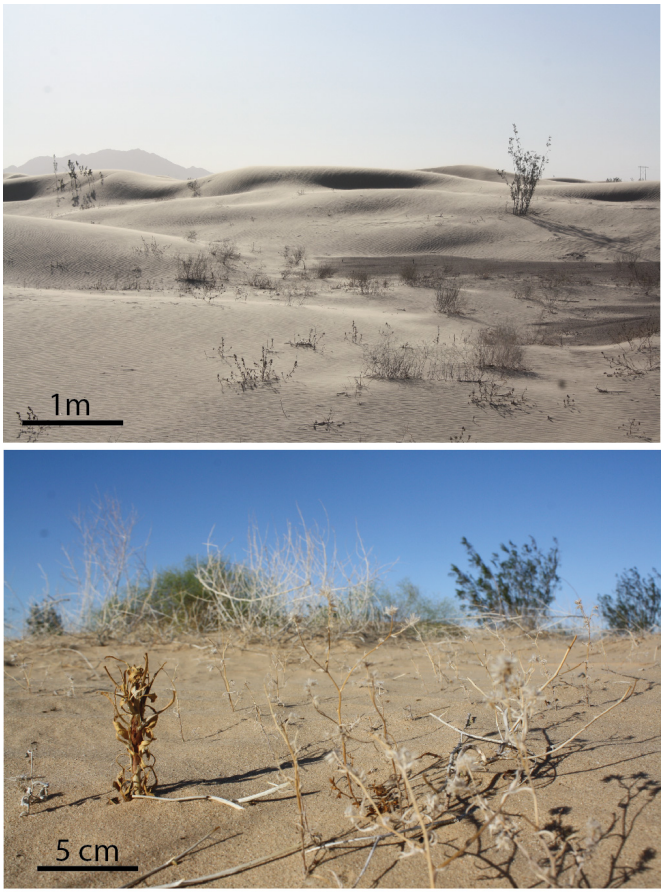


Figure 3.8: Examples of *C. occipitalis'* desert habitat. The granular substrate is omnipresent and interspersed with obstacles at varying spacings. Photographs taken in Yuma, Arizona, USA.

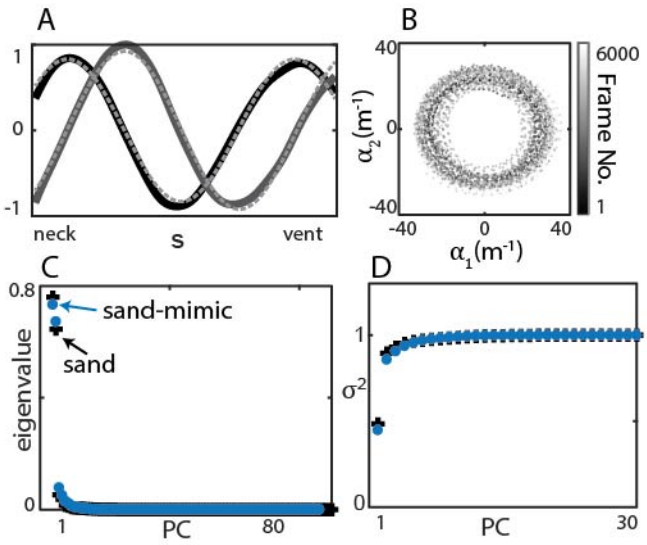


Figure 3.9: PCA comparison of GM and sand-mimic data for 8 and 7 individuals, respectively, moving on the substrate with no posts present. (*A*) First two PCs calculated from 32 trials on homogeneous GM (6604 frames, 94 measurements along the body). Dashed lines are sinusoidal fits. (*B*) Coefficients $\alpha_1$ and $\alpha_2$ associated with the PCs in *A*. Color denotes frame number. (*C*) Normalized eigenvalues for all $PC$s. GM calculation in black crosses, sand-mimic in blue circles. (*D*) The amount of squared variance captured by including additional $PC$s up to $PC_{30}$ and beginning with $PC_1$. GM calculation in black crosses, sand-mimic in blue circles.

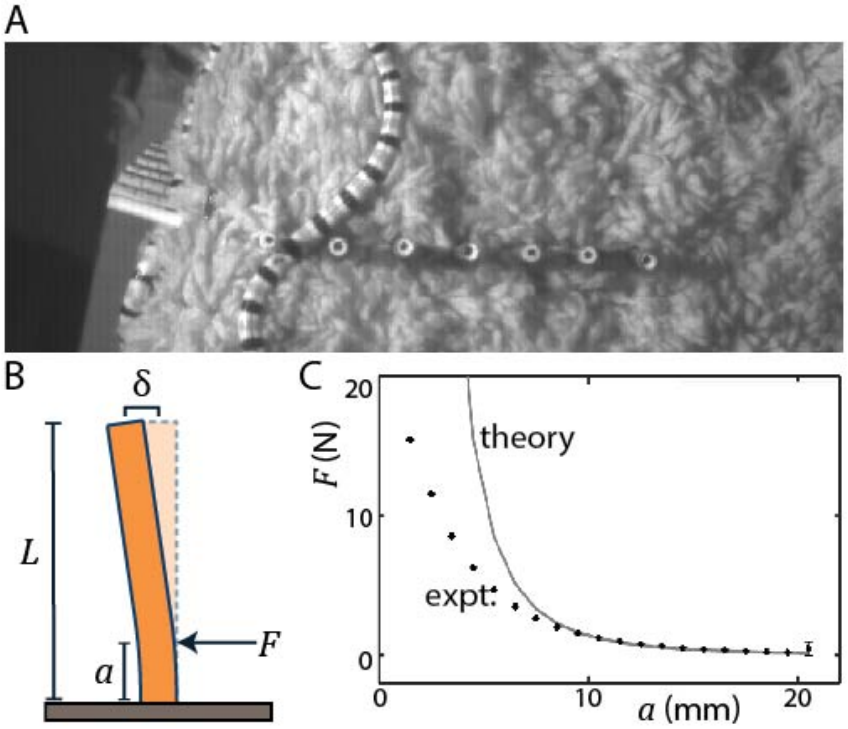


Figure 3.10: Post characterization. (*A*) Snapshots from experiment to determine height of post contact. The posts were wrapped in a printed ruler and a mirror used to capture simultaneous top and side views. We collected 27 trials. The mean $\pm$ s.d. contact height was $28.1 \pm 1.6$ mm. (*B*) Post schematic. The base of the post was rigidly affixed. Force was applied at some height above the base, causing the tip of the peg to deflect a distance $\delta$. (*C*) Black circles are experimentally measured reaction forces due to the robot arm pushing a distance of 1 mm at different $a$. Each point is mean $\pm$s.d. of three trials. The theoretical prediction is the solid gray line. The experimental and theoretical values converged at a height of approximately 8 mm above the base.

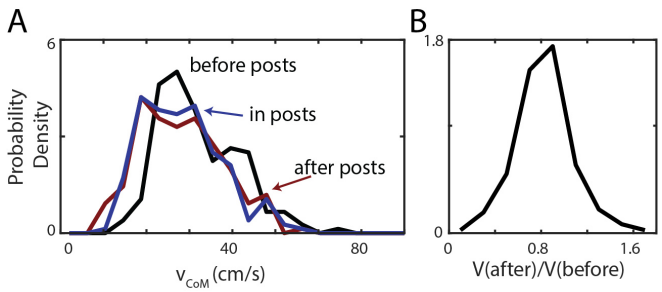


Figure 3.11: Snake performance during post transit. (n=233 trials, N=8 individuals) (*A*) Distribution of center-of-mass speed ($v_{com}$) measured in each run. Average was taken from the start of the run to the instant the head first crosses the array (before posts, black), from the head's first crossing to the tails last (in posts, blue), and after the tail crosses the array until the end of the trial (after posts, red). (*B*) Probability density of the ratio of speed after exiting the array over speed before contact. Average speeds before and after were computed and the ratio taken on a run-by-run basis.

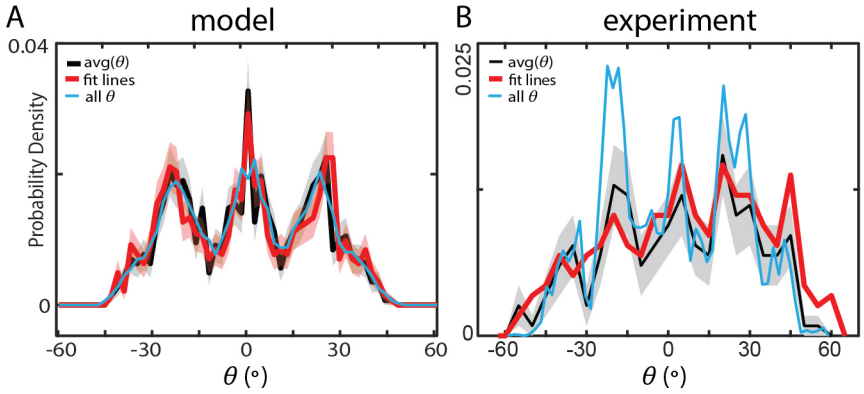


Figure 3.12: Comparison of scattering angle measurement methods (*A*) For the model we calculate $\theta$ measured by averaging all points passing through the arc from $r_s = 3.3 - 4.3$ as in the main text (black curve) as well as by fitting a line to the trajectory after it was clear of the array (red curve). Bootstrapping was used to estimate the standard deviation (filled areas). Bin widths were $2^\circ$ (n=700). (*B*) For the experimental trials we calculate the same average $\theta$ as in *A* and the main text (black curve, filled area is the standard deviation estimated from a 10000 iteration bootstrapping) as well as angles from lines fit to the trajectories (red curve). The blue curve is the probability density of all data points used to calculate the average $\theta$ per trial (1789094 data points). Bin widths were $5^\circ$ for the average $\theta$ and the fit lines and $2^\circ$ for all $\theta$. $N = 8$ individuals, $n = 196$ trials.

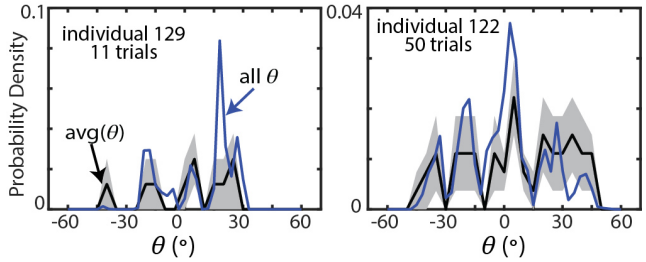


Figure 3.13: Scattering histograms for individual snakes. Black curves are histograms of the average $\theta$ as in the main text with gray standard deviation estimated using bootstrapping. Blue curves are histograms using all data points within the arc. (*left*) Distributions using only the snake with the fewest number of successful trials, individual 129 (n=11 trials, 33496 total data points in the arc), and (*right*) the snake with the greatest number of successful trials, individual 122 (n=50 trials, 19.697 total data points in the arc).

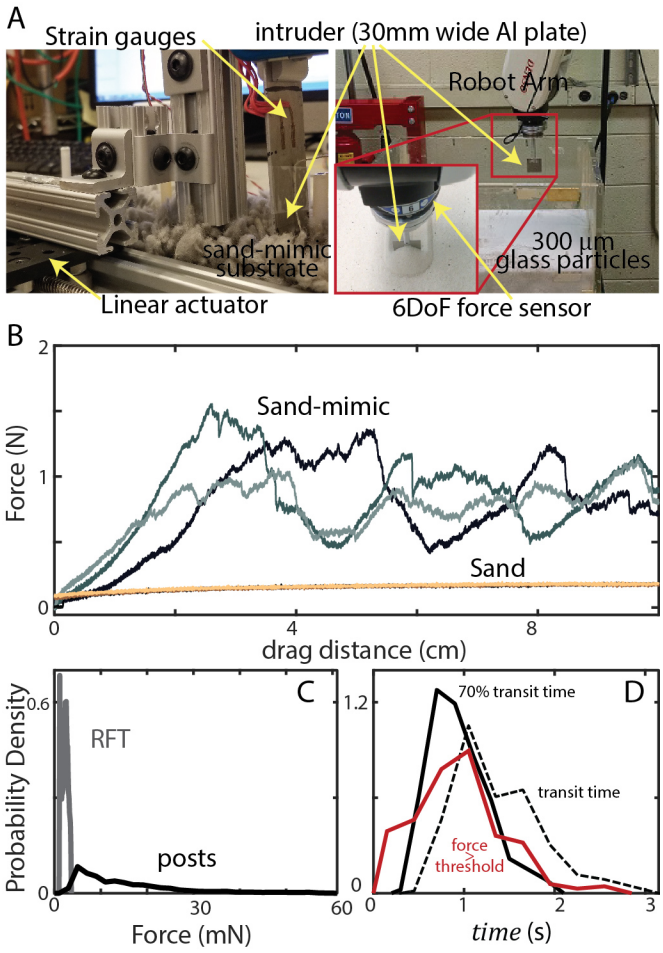


Figure 3.14: (Caption next page.)

Figure 3.14: (Previous page) Force magnitude is greater during motion on sand-mimic than predicted for sand (*A*) Experimental setup. A 30mm wide aluminum plate was dragged at a constant speed of 10 $\text{mms}^{-1}$ and constant depth of 8 mm measured from the free surface to the bottom edge of the intruder. Free surface of the carpet was approximated by eye as the height of the fibers was variable. For the sand-mimic the intruder was moved by a linear actuator and forces measured using strain gauges in a full Wheatstone bridge configuration (*left*). The intruder was moved through the 300 $\mu$m glass particles using a robot arm (Denso) and forces were measured with a 6DoF force-torque sensor (ATI). (*B*) Raw drag forces from three trials measured in the sand-mimic (gray curves) and glass particles (brown curves). Forces in the carpet were highly variable as the fibers were of a size comparable to that of the intruder (see picture in *A*). The ratio of average steady-state (mean forces from a drag distance of 2 to 10 cm) carpet to GM drag forces was 4.9. The minimum and maximum ratios, using the absolute minimum and maximum forces measured on the carpet, were 2.5 and 8.7. (*C*) Distribution of the reaction force magnitude measured using the posts in experiment (black) and estimated using granular resistive force theory (RFT, gray). The ratio of the median force measured by the posts to that predicted by RFT was 5.2. This is similar to the average ratio of the drag forces and bounded by the minimum and maximum ratios. This difference in the force magnitudes between the sand-mimic and sand was likely responsible for the larger forces measured by the posts as compared to those predicted by RFT. (*D*) Transit time (dashed black curve) is measured for each trial (n=233, N=8) as the time between when the first tracked point first reaches the array to the last tracked point exiting. Force contact times are the sum of all frames in a trial that a force is measured above a threshold of 3mN. We found that these distributions were statistically similar ($P \ll 0.001$) when comparing the force times to 70$\%$ of the transit time.

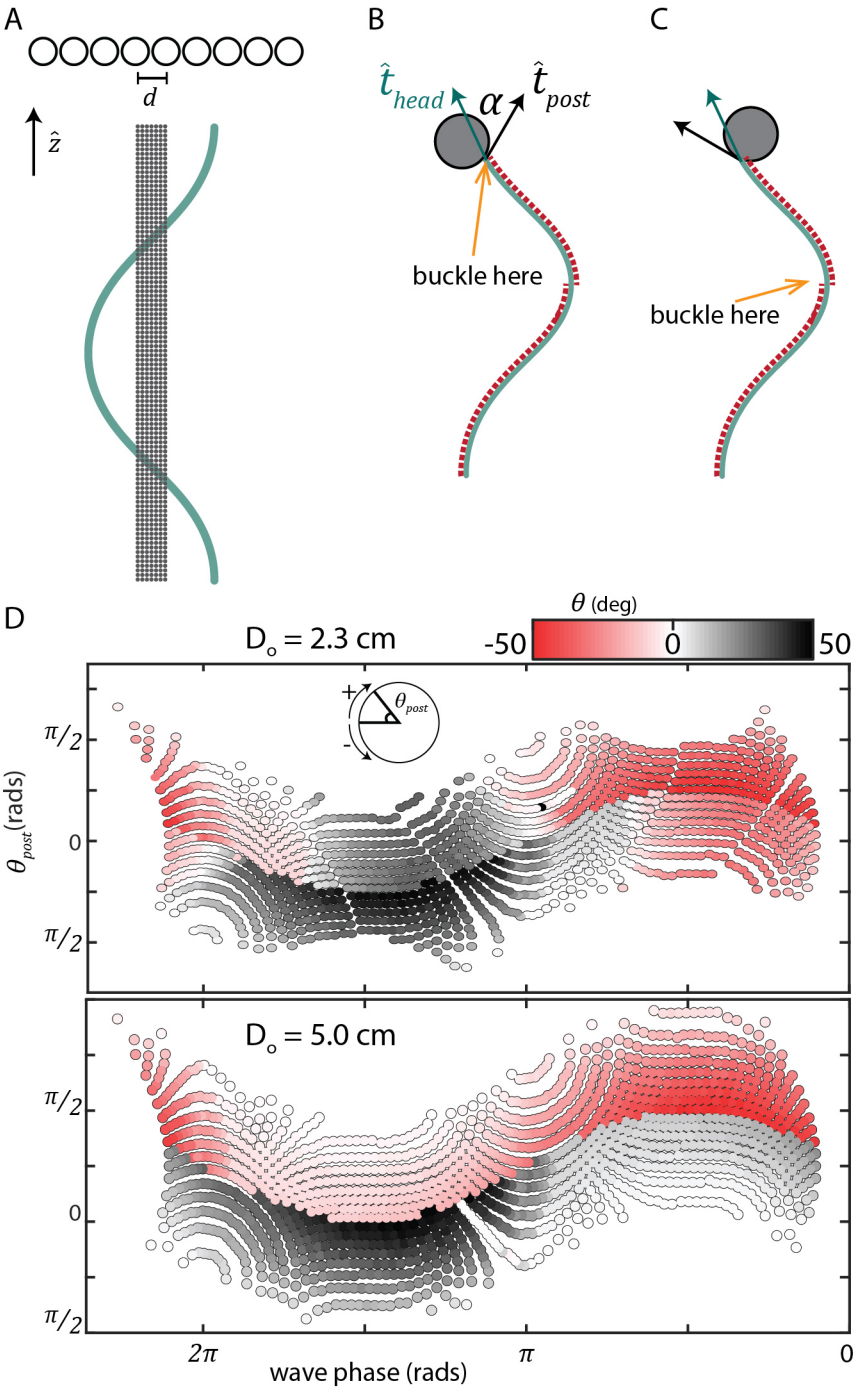


Figure 3.15: (Caption next page.)

Figure 3.15: (Previous page.) Slithering and buckling model details. (*A*) Model initial conditions. Each dot in the rectangular grid is a starting point for the center-of-mass of the model snake. An example model snake shape is shown in green. The length of the box is one wavelength and the width is equal to the center-to-center spacing between posts. This collection of starting points will sample the range of snake-post collisions. We used 700 initial conditions in the multi-post case. For the single post the box was expanded to the peak-to-peak amplitude of the waveform and 2700 initial conditions were used. (*B*) the direction the model will pass the post is chosen to minimize the angle $\alpha$ calculated as the angle between the peg tangent vector, $\hat{t}_{head}$, and the snake head tangent vector, $\hat{t}_{head}$, at the moment of impact. Two cases are shown, *B*, in which the model snake passed counter-clockwise around the post and buckled at the head and (*C*), in which the model snake passed clockwise and the muscle activation pattern dictated buckling occurred at the first extrema as indicated. Note that the buckling location was chosen based on the activation pattern *and* the direction of transit. (*D*) Scattering angle as a function of the wave phase at time of first contact and the location on the post the head first touches as measured in the slithering model, $\theta_{post}$ as illustrated in the inset diagram. The snake in this case is approaching the post from the left. Wave phases of zero and $2\pi$ are the waveshape shown in *A*. A phase of $\pi$ is as shown in *B* and *C*. The apparent relationship between these system parameters and the scattering angle, such that the resultant trajectory could be predicted by knowing these values, suggests the system is deterministic. (*top*) is for a spacing $d = 23$ mm. In this case the angle changes more as wave phase changes than post contact location. In contrast (*bottom*) is the same plot made using simulation data from $d$=50 mm. In this case the simulated snake only ever contacts a single post and the scattering angle is more strongly dependent on the contact location with the post..

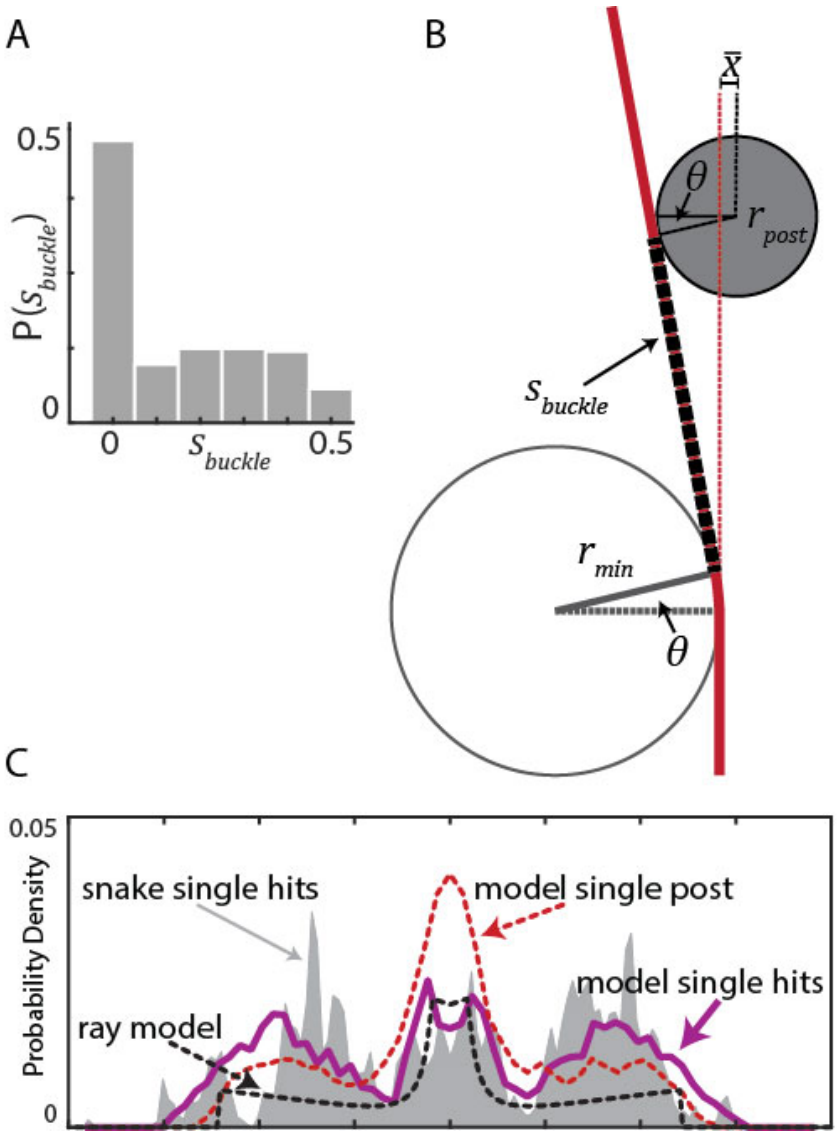


Figure 3.16: Ray model details. (*A*) The distribution of $s_{\text{buckle}}$ from the slithering and buckling model. In the ray model we assume half of the trajectories buckle at the head, $s_{\text{buckle}} = 0$ and the other half are evenly distributed on the interval $s_{\text{buckle}} = (0, s_{\text{max}}]$. (*B*) Ray model diagram. The ray, the thick solid red line, buckled at a distance $s_{\text{buckle}}$, indicated by the thick black dashed line. The distance from the center of the post to the ray's "nominal trajectory", indicated by the thin dashed red line, is $\bar{x}$. (*C*) The live snake (filled gray curve) and slithering model (solid purple curve) multi-post scattering angles calculated using trajectories which collided with one and only one post. In comparison, the dashed lines are calculated from the slithering model (red) and using the ray model (black) in the single post case. The primary and secondary peaks for both cases are similar, however, in the single-post case the primary peak at $\theta = 0$ is larger.

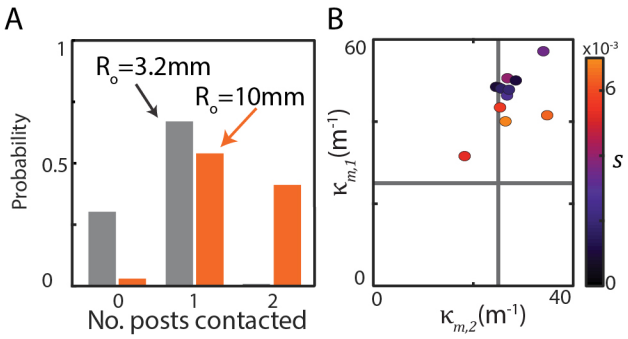


Figure 3.17: Compare details of the slithering model and the snake. (*A*) Probability to contact a given number of posts in the slithering model for $r_{\text{post}} = 32$ mm (used in snake experiment) and $r_{\text{post}} = 100$ mm (used in multi-post model). (*B*) $\kappa_{m,1}$ vs $\kappa_{m,2}$, analogous to Fig. 3.5*C*), measured in ImageJ from slithering model images. Color corresponds to the arclength along the midline from $s = 0$ to the location of $\kappa_{m,1}$ at the instant of impact. We know from the model algorithm that $\kappa_{m,1} = 50$ m$^{-1}$ and $\kappa_{m,2} = 25$ m$^{-1}$. We posit that the hand-measurement acts to average $\kappa$ over several segments so hat when the first curve is further from the wall, such that fewer segments are recruited into the changed curvature, the hand measured curvature is lower than $\kappa_{\text{abs}}$. This measurement method also introduces some error as seen in the spread in $\kappa_{m,2}$.

# CHAPTER 4
# USE OF MULTI-MODAL TERRAINS

## 4.1 Introduction

The most general gait used by limbless organisms is lateral undulation in which waves of curvature are passed from head to tail down the body [17]. Despite the apparent specialization of the limbless state, the passage of traveling waves down the body is effective in habitats ranging from aquatic to arboreal, and, most commonly, the surface of terrestrial terrains. Snakes in particular demonstrate its high adaptability–they are found in nearly every habitat which is not too cold [46].

While undulatory locomotion in fluids has been well-studied [110, 142, 83], a similar depth of understanding is lacking for slithering motion in terrestrial habitats. A challenge to understanding is the complex nature of most terrains which are frequently a multi-component mixture of substrates like soils, muds, and sands with discrete materials like plants and rocks embedded within them at varying densities.

Lateral undulation relies on the use of "push-points" in the surroundings to generate propulsion. These push-points may be discrete obstacles [19], heterogeneity introduced to a yielding substrate by the motion of the trunk (chapter 2), even frictional anisotropy of the ventral scutes [49]. Previously, we studied the desert-specialist Shovel-nosed snake, *Chionactis occipitalis*, moving on the surface of homogeneous granular matter (GM). This species uses a stereotyped waveform to move across GM like the sand of its natural habitat

All simulation work was done by Tingnan Zhang, further details may be found in his dissertation [140]. The snake-like robot was developed by Prof. Howie Choset's Biorobotics Lab at Carnegie Mellon University's Robotics Institute [141]. Robot experiments and analysis were carried out by Chaohui Gong and Jin Dai at Carnegie Mellon. The shape-based controller was developed by Matt Travers and is published in [70].

[48]. We discovered that this waveform provides the benefit of both moving at a maximum speed given a constraint on peak muscle power, as well as prevents the trunk from sliding into previously disturbed material (chapter 2). We rationalized that the GM allowed the snake to generate push-points at will by yielding the material, permitting the use of the stereotyped waveform. Most terrestrial terrains, however, are not spatially uniform.

Prior research on the kinematics of snakes modeled the push-points of terrestrial terrain as symmetric arrays of rigid posts affixed to a hard, featureless substrate and found that the snakes kinematics [19] and performance [21] were a function of the spacing between posts. A similar result was found in the microscopic nematode *Caenorhabditis elegans* using traveling waves to move through arrays of posts [5, 6]. We endeavored to explore the capability of *C. occipitalis* when challenged with different multi-modal terrain and use as a comparison a generalist snake like those previously studied. As a model for multi-modal terrain we added pegs in symmetric, rigid arrays to the sandy substrate such that snakes could use either the substrate, the posts, or a combination to move. We also tested the snakes on a hard, low-friction whiteboard substrate both with and without the rigid arrays.

## 4.2 *C. occipitalis in obstacle arrays*

We chose whiteboard as a rigid substrate. Snakes do not move effectively using lateral undulation on the low-friction surface. While they can make some progress via the frictional anisotropy of the scales [49], the surface is slick enough that the body experiences high lateral slipping. To affix the posts we drilled holes in the whiteboard which held small wooden dowels using an interference fit. Onto these dowels we could then affix 3D printed sleeves. For the current work we used cylindrical posts 0.64 cm in diameter, but the system was designed so that arbitrary shapes could be printed and put onto the lattice.

Lattices were constructed in two configurations, square and hexagonal. The square lattice provides the snake with straight, unobstructed rows while the hexagonal lattice has the benefit that a post is equidistant to all of its neighbors. We characterize lattice spacing

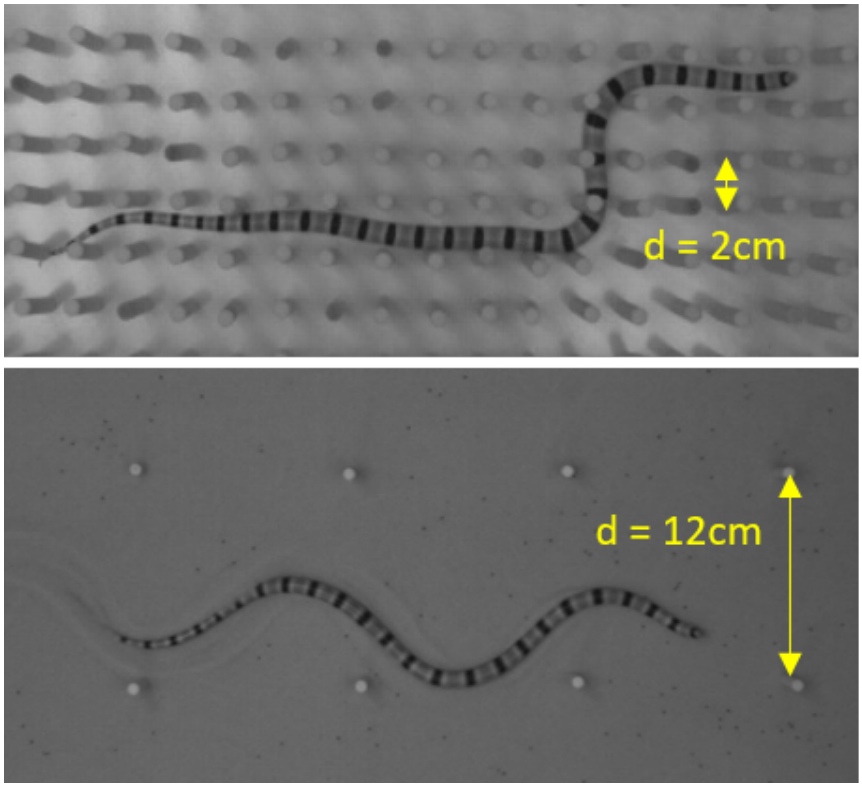


Figure 4.1: *C. occipitalis* in square lattices of different $d$ on the whiteboard substrate (*top*) and GM (*bottom*).

using $d$, the nearest-neighbor distance between posts (Fig. 4.1).

To control the initial state of the GM using the fluidized bed we designed a lattice which would allow the air to pass through it. Posts which fit in the holes in sheet of Aluminum honeycomb were designed. The posts were placed in the sheet, then pushed down into the GM during fluidization. When the air was turned off the GM would settle around the posts in a loose-packed state (Fig. 4.2). The Aluminum honeycomb was completely buried beneath the GM at a depth of several centimeters, well below the depth the animal's trunk would intrude (at most $\approx 5$ mm chapter 2).

The waves of undulation were primarily in the horizontal plane. Snakes may superimpose a vertical wave as well to improve performance ([49], chapter 2), however, thrust is generated primarily by the action of the horizontal wave, so we chose to focus the current study on kinematics in this plane.

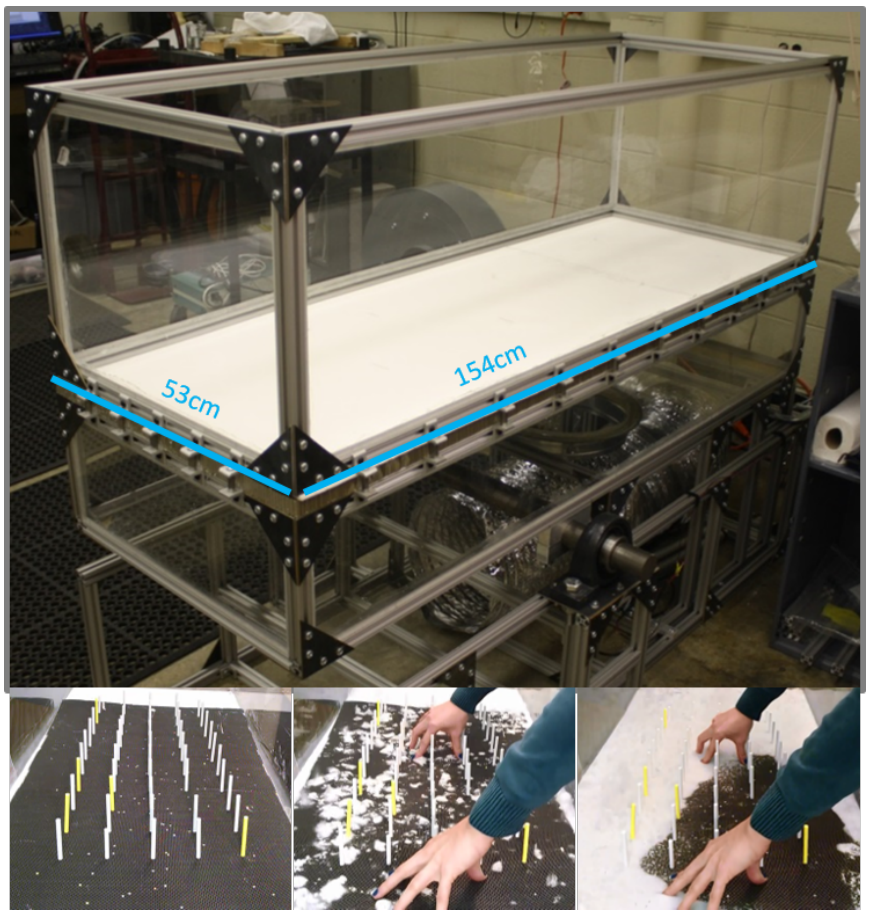


Figure 4.2: Design of lattices for use in fluidized bed. (*top*) Fluidized bed apparatus. (bottom, *left*) 3D printed posts were placed in the desired array in a sheet of Aluminum honeycomb. (*middle*) Particles are fluidized and the honeycomb is pushed down into the material. (*right*) The GM flows through the Al honeycomb and fills in around the posts, when air is turned off the GM settles into a loose-packed state around the posts.

We tested three individual *C. occipitalis* in seven lattice spacings in both square and hexagonal lattices and collected a minimum of three runs per individual per run. The videos were digitized by tracking the animals natural black bands using MATLAB and the tracking algorithm described in [13].

### 4.2.1 Movement along a row: geometry-dominated performance

We began with a simple case, *C. occipitalis* moving parallel to rows in the square lattice. Using ImageJ we measured the wave efficiency, $\eta$, defined as the distance traveled per undulation cycle divided by the wavelength as a function of post spacing over the wavelength, $d_\lambda$. When the lattice was placed in the GM substrate $\eta$ was independent of $d_\lambda$ and equal to that measured on the homogeneous GM (Fig. 4.3). When traveling in the lattice on whiteboard performance was similar to that in GM up until a drop-off occurring past $0.5d_\lambda$ (Fig. 4.3).

The snake performance when the GM substrate was added was independent of the lattice dimensions and $d_\lambda$ increased monotonically with lattice spacing, as expected for a constant wavelength (Fig. 4.3). We conjectured that the presence of GM decoupled snake performance from lattice geometry. The snakes' $\eta$ was close to unity in the homogeneous GM, so using the posts was not necessary for effective movement. In contrast, on whiteboard $\eta < 1$ without the posts. Apparently, addition of the push-points facilitated performance similar to that on GM, but only for small-enough $d_\lambda$.

Tingnan Zhang developed two simulations to explore the origin of the drop-off in $\eta$ as $d_\lambda$ increased on the whiteboard (see [140] for more information). A 1D simulation in which the model snake was constrained to move down a row of posts and a 2D dynamical simulation using the open-source Project Chrono for a snake of similar morphology and waveshape as *C. occipitalis*[143] (Fig. 4.4). The 1D simulation exhibited a stepping behavior; the (constant) wavelength of the snake would match the (changing) spacing such that it would move without slip only at terms in the geometric series $\frac{1}{2}^2$. Between these values

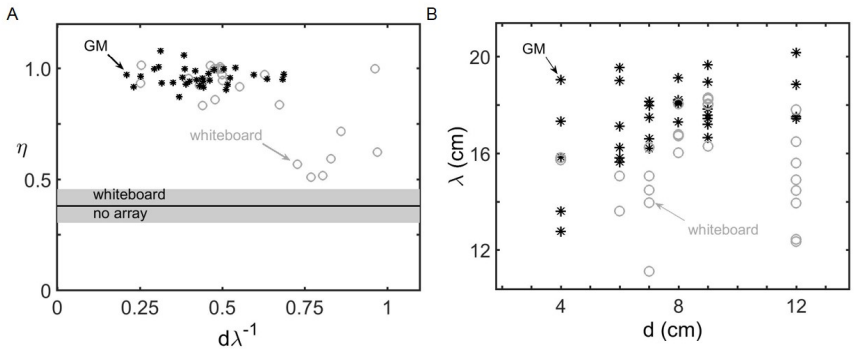


Figure 4.3: *C. occipitalis* performance moving along rows in a square lattice. Marks are measurements from ImageJ. (*A*) Wave efficiency, $\eta$ is the distance traveled per undulation cycle divided by the wavelength, $\lambda$ versus lattice spacing over wavelength, $d\lambda^{-1}$. Black stars are performance on GM and gray circles are on whiteboard. (*B*) Wavelength versus spacing.

the snake slipped backward at each undulation until contacting a post such that $\eta$ decreased as $d_\lambda$ decreased toward the next term in the series. This picture captured a drop-off at 0.5, although for most data points between 0.5 and 1 it over-predicted snake performance (Fi.g 4.5*A*).

The 2D model revealed the challenge in moving at large $d_\lambda$ which was not captured by the 1D model, causing it to generally over-predict snake $\eta$. The finite-length snake had 2 waves on its body. Therefore, for $d_\lambda$ larger than 0.5 a body moving down the row would rarely contact more than a single post at a time. As a result there was a net torque on the body which rotated the snake, causing it to move into the space between rows (Fig. 4.4).

The snake data was in agreement with the average performance of the models at $d_\lambda < 0.5$ (Fig. 4.5*A*). It did not degrade as quickly past this point, and was roughly bounded between the 2D and 1D model predictions at $d_\lambda > 0.5$. We hypothesized this was because the model executed the serpenoid waveform exactly whereas the snake is certainly capable of adjusting its shape whether to completely change the basis functions of the waveform or, as supported by observation and further measurements below, it changes the serpenoid parameters, whether passively or actively, to match the lattice geometry.

There was a group of snake data at $d_\lambda$ just below the drop-off at 0.5. We plotted the

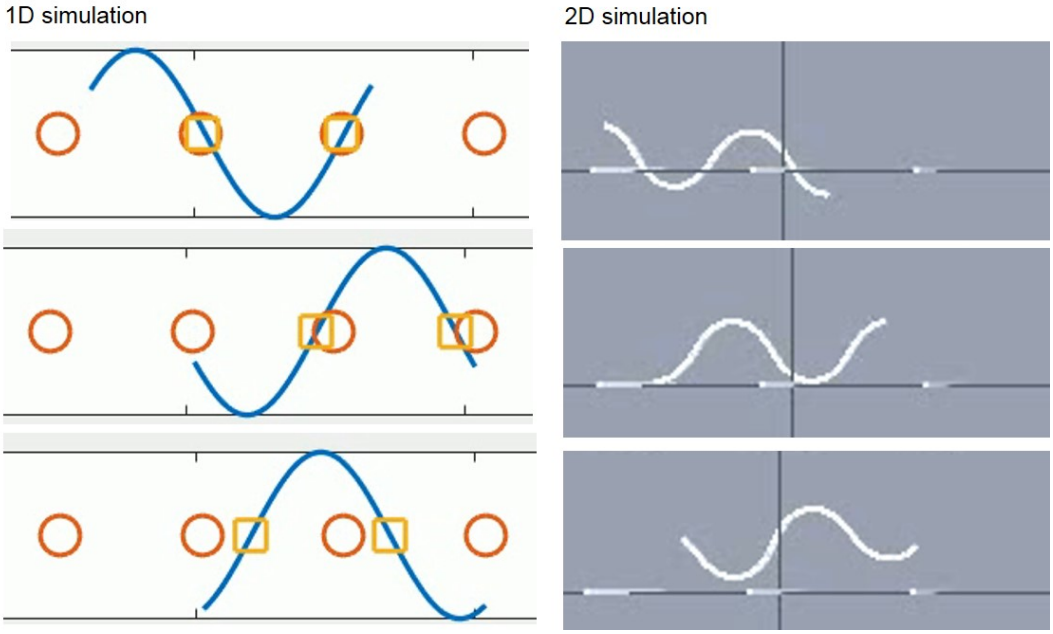


Figure 4.4: 1D and 2D snake simulations. Figure adapted from work by Tingnan Zhang (unpublished).

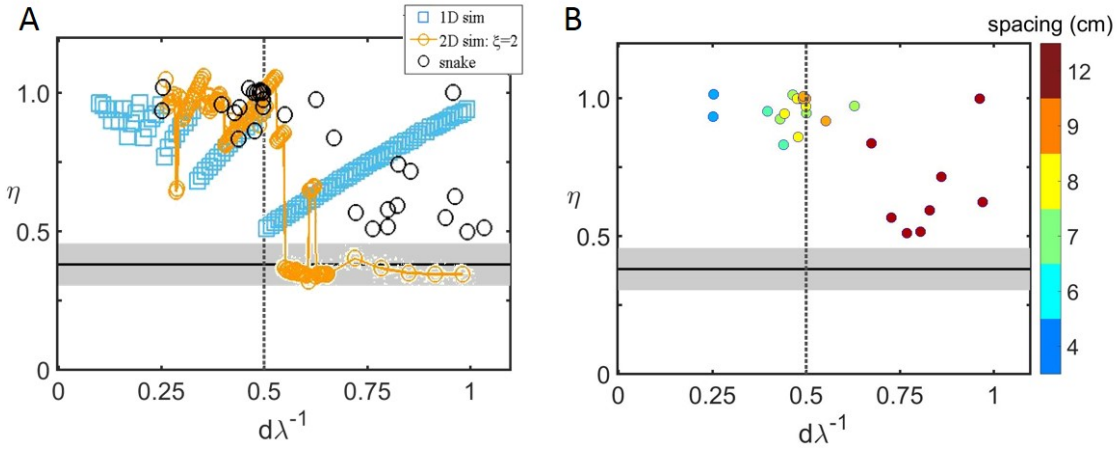


Figure 4.5: 1D and 2D simulation results. (*A*) Wave efficiency measured in the 1D simulation (blue squares) 2D simulation (orange circles), and snake experiments (black circles). Plot adapted from work by Tingnan Zhang (unpublished). (*B*) $\eta$ versus $d_\lambda$ measured in experiment, colored by post spacing in the lab frame. Only whiteboard is shown. Vertical dashed line is at $d_\lambda = 0.5$, the location of the performance drop-off seen in the simulation.

snake data and colored the points by the post spacing in the lab frame (Fig. 4.5*B*). This revealed that, rather than the data for each spacing being evenly distributed in $d_\lambda$ as is the case if wavelength is kept constant (and as is the case for the snake moving in GM Fig. 4.3), at intermediate post spacings the wavelength of the snake was increasing to maintain $d_\lambda < 0.5$.

We next used a robophysical model to investigate whether this waveform change could occur passively. We commanded joint angles of the Series Elastic Actuator (SEA) snake (Fig. 4.6*A*[141]) using the serpenoid function

$$\zeta(s,t) = \zeta_m sin(\xi s - \omega t)$$

. We tested the robot in square lattices constructed on a varnished wood board using posts made of PVC pipe (Fig. 4.6*B*).

The robot used only mechanical feedback–the "internal loop" of the robot was always closed–the joint positions were known and a PID controller was used to track the commanded $\zeta$ (Fig. 4.6*C*). We found that the motors were strong enough that the robot would frequently become completely stuck in the array. Therefore, we added passive compliance by limiting the motor current available to the motors such that the robot could be bent away from the desired $\zeta$ when experiencing torques beyond what the motors were permitted to provide. The addition of this very simple passivity resulted in greater ability to traverse the array.

The robot $\eta$ was less than unity when in homogeneous GM (6mm diameter plastic BBs). Therefore, the robot performance was improved by the addition of the array in both GM and whiteboard (Fig. 4.7*B*). For both substrates as $d_\lambda$ increased past 0.5 $\eta$ dropped off, eventually converging on the homogeneous substrate performance. The wavelength of the robot was passively changed by the lattice, however, it was not obvious that the change mimicked that seen in *C. occipitalis*. Further study could illuminate whether the change

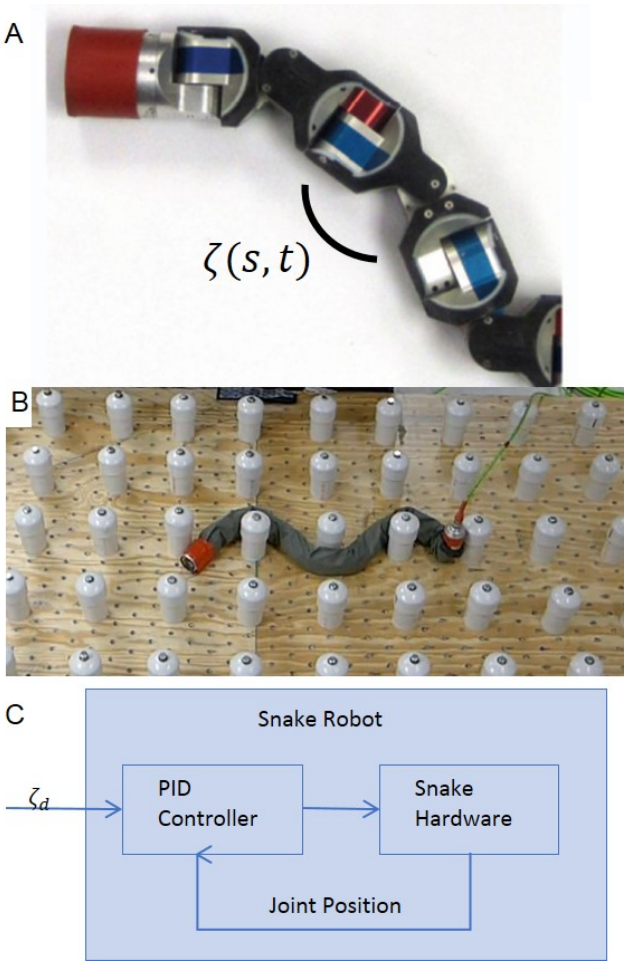


Figure 4.6: SEA snake robot. (*A*) Photograph of the robot. Joint angles $\zeta$ are commanded to execute a serpenoid curve. (*B*) Photographs of the robot in the post array. (*C*) Robot control. Onboard PID control tracks joing trajectories $\zeta_d$. When the torque of the motors is limited they are not always able to reach $\zeta)d$ when in the lattice.

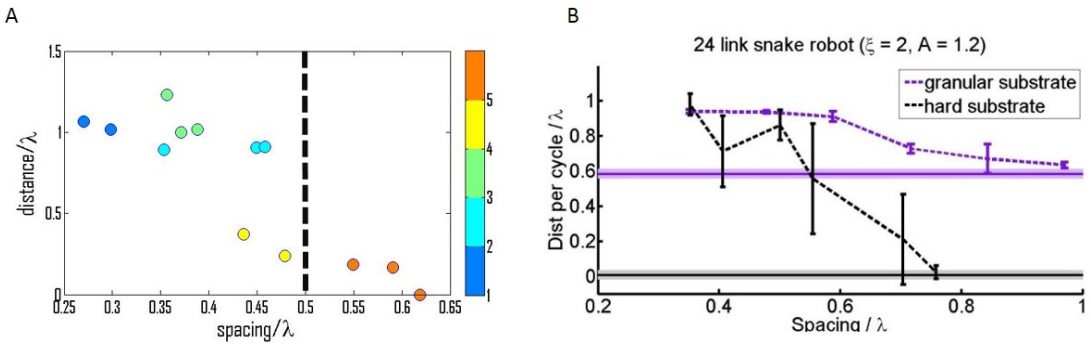


Figure 4.7: Robot in a square lattice. The robot has only information about joint angles. A torque limit on the motors means it can be passively bent away from the serpenoid curve, but it is not sensing or using the terrain. Purple data is the robot in a GM (6 mm diameter plastic BBS) and black is on the hard substrate.

can be explained by purely passive mechanisms or if the snake must exert neural control to actively change the wavelength.

We previously found that performance in GM depends sensitively on the waveform (chapter 2). These results indicate that on the whiteboard locomotion is coupled to lattice geometry. *C. occipitalis* reduced sensitivity to the lattice geometry by modulating its wave parameters. We hypothesize that the ability to adjust wave parameters to utilize the geometry of the environment is important in complex terrain, and that an ability to modulate the parameters to an even greater extent than observed in *Chionactis* would allow locomotors to further decrease sensitivity and overcome more challenging heterogeneous terrains

### 4.2.2 *C. occipitalis* in 2D lattices

The snakes were unable to make effective progress on the whiteboard alone (Fig. 4.8), but always successfully transited the trackway when posts were present. At the smallest spacing (d=2 cm) the lattice was close to the width of the snake body (≈1 cm) and the waveform in the lattice both in sand in the whiteboard was unlike that used to move on homogeneous GM (Fig. 4.8). For all other lattice spacings, however, the waveform was comparable to that in GM. Performance did not appear to depend on lattice layout, therefore, we chose to simplify by combining results from square and hexagonal lattices of the same spacing.

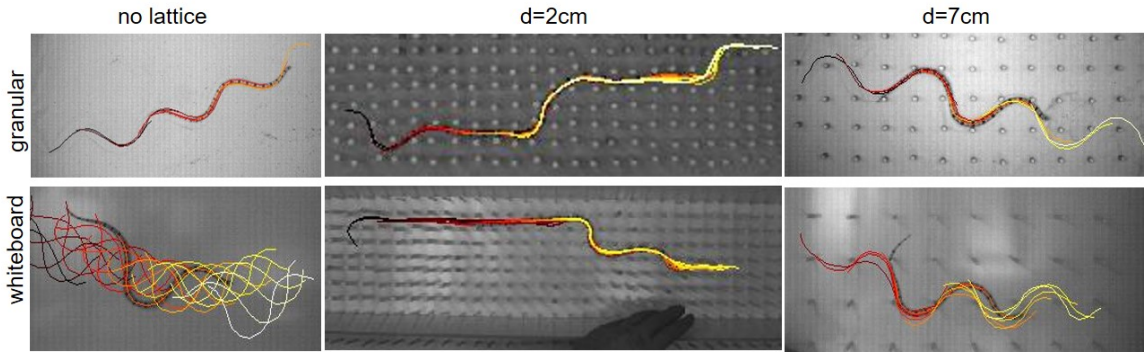


Figure 4.8: *C. occipitalis* kinematics in multi-modal terrain.

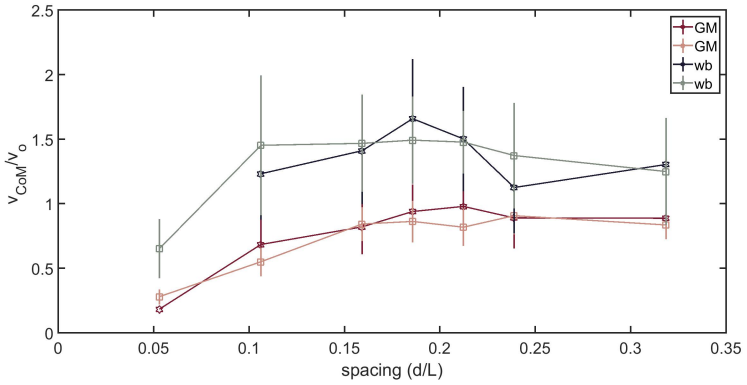


Figure 4.9: Speed in the lattices relative to speed on the homogeneous substrate. Mean and standard deviation of all snakes and trials on the whiteboard (gray) and in GM (red). Square markers are trials in the square lattice and stars are hexagonal lattice. Note there is no data for movement in the 2 cm spacing hexagonal lattice on whiteboard

We measured center-of-mass velocity of the snake ($v_{CoM}$) and normalized it by the average $v_{CoM}$ of the animals moving on the relevant substrate when no posts were present. *C. occipitalis'* did not increase speed on the GM when posts were present (Fig. 4.9, gray curve). In contrast, adding the lattice to the whiteboard resulted in increased performance (Fig. 4.9, gray curve). The animals pushed against the rigid obstacles when on the whiteboard substrate to propel themselves.

It was not apparent a priori that adding posts to the GM would not increase animal performance. The posts are completely rigid; presumably the animal could take advantage of them to push itself forward in a manner which was not supported by the deformable GM. However, this did not appear to be the case. As further demonstrated below, the waveform

was not dramatically changed in any of the lattices, and the animals did not perform better in GM with posts added in any of the metrics we used.

## 4.3 Specialist and generalist snakes

### 4.3.1 Species comparison in 2D post arrays

We acquired two juvenile corn snake *Pantherophis guttatus* through the pet trade. *P. guttatus* (Fig. 4.10*top,right*) is a habitat generalist. Its range covers an area which consists of a variety of terrains such as wetlands, forests, man-manipulated areas, and, as a semi-arboreal species, they can climb trees (Fig. 4.10*top, left*). This species will therefore encounter many materials including water, muds, sand, gravel, dirt, and leaf litter with any number of objects like rocks, twigs, and plants in them (Fig. 4.10*bottom*). The experimental procedures were the same as those for *C. occipitalis* with the exception that black marks were painted along the spine of *P. guttatus*. This line was used to digitize the midline of the snakes using MATLAB image processing functionality. We tested *P. guttatus* only in the whiteboard post arrays in order to compare the ability of the specialist *C. occipitalis* to use singular push-points to that of a generalist.

We measured the average slip angle, $\bar{\beta}_s$, calculated by finding the angle between the velocity and tangent unit vectors of all segments through time and average, e.g. $|\hat{v}\cdot\hat{t}|$. This value tells us how much the animal is moving as if it were "in a tube" such that if every segment on the body follows exactly the path of its anterior neighbor $\bar{\beta}_s = 0$.

The slip angle was larger when *C. occipitalis* was on the homogeneous whiteboard, $\bar{\beta}_s = 26.7 \pm 3.3°$ as compared to GM $\bar{\beta}_s = 4.7 \pm 1.3°$. In the GM substrate, the addition of the lattice did not appreciably change the slip angle (Fig. 4.11). Adding the lattice to the whiteboard, however, decreased $\bar{\beta}_s$, although $\bar{\beta}_s$ never reached the GM values. $\bar{\beta}_s$ was dependent on lattice spacing on the whiteboard; as spacing between the posts increased the slip angle increased. This result was somewhat intuitive, in that the limit as $d \to \inf$ becomes again the homogeneous substrate, and in practice, assuming the system is non-


Figure 4.10: (*top left*) The Corn snake *Pantherophis guttatus*. Photo courtesy [144](*top right*) Range of *P. guttatus*. Map courtesy [145]. (*bottom*) Examples of habitats in *P. guttatus'* range. Photos courtesy [146].

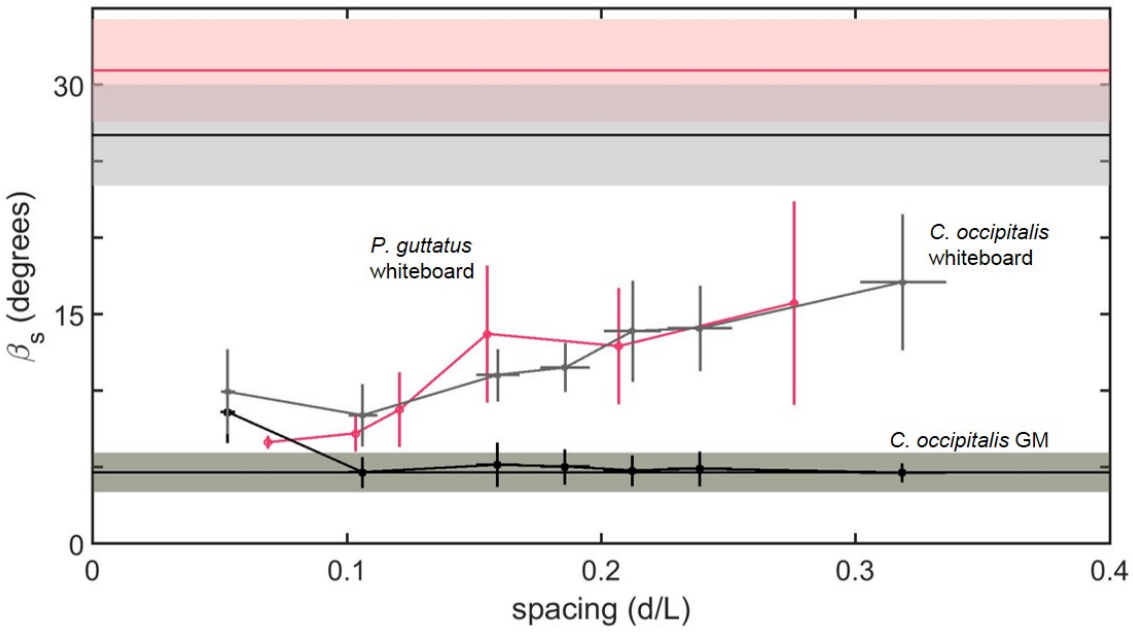


Figure 4.11: Slip versus lattice spacing over snake length for *C. occipitalis* and *P. guttatus*

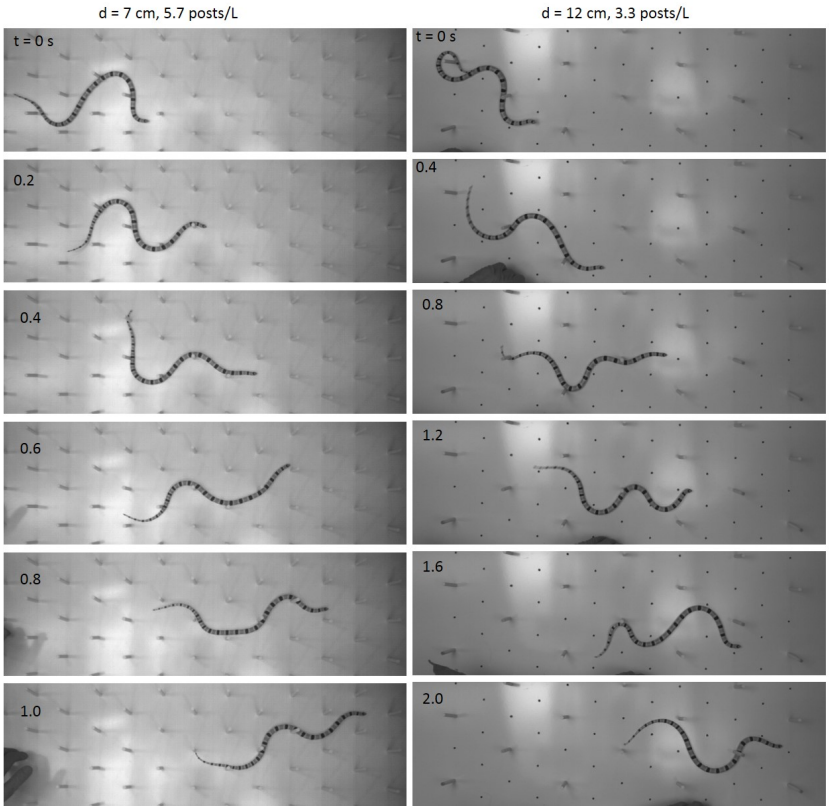


Figure 4.12: *C. occipitalis* moving through 2D arrays on whiteboard. Time is as indicated on each still.

inertial such that the animal cannot "hop" between posts, as $d$ becomes large relative to the snake length we may expect performance to be negatively impacted. However, it was not obvious that the animal could not adopt different postures depending on lattice spacing. For example, increasing wavelength to reach posts which were farther apart.

Based on our observations and the previous research [19, 21], we expected the generalist snake would out-perform *C. occipitalis* in the post arrays on whiteboard. textitP. guttatus used what appeared to be more variable waveforms, (Fig. 4.12 vs Fig. 4.13), and gave the impression of greater competence. However, contrary to our expectations, *P. guttatus* had slip very like that of *C. occipitalis* and slipped more as lattice spacing increased (Fig. 4.11).

We used principal component analysis (PCA) to search for low-dimensional representations of the snakes' waveforms. The first two PCs captured $78.6\%$ of the variance for *C. occipitalis* in lattices in GM and $72.6\%$ when it was in lattices on whiteboard. These

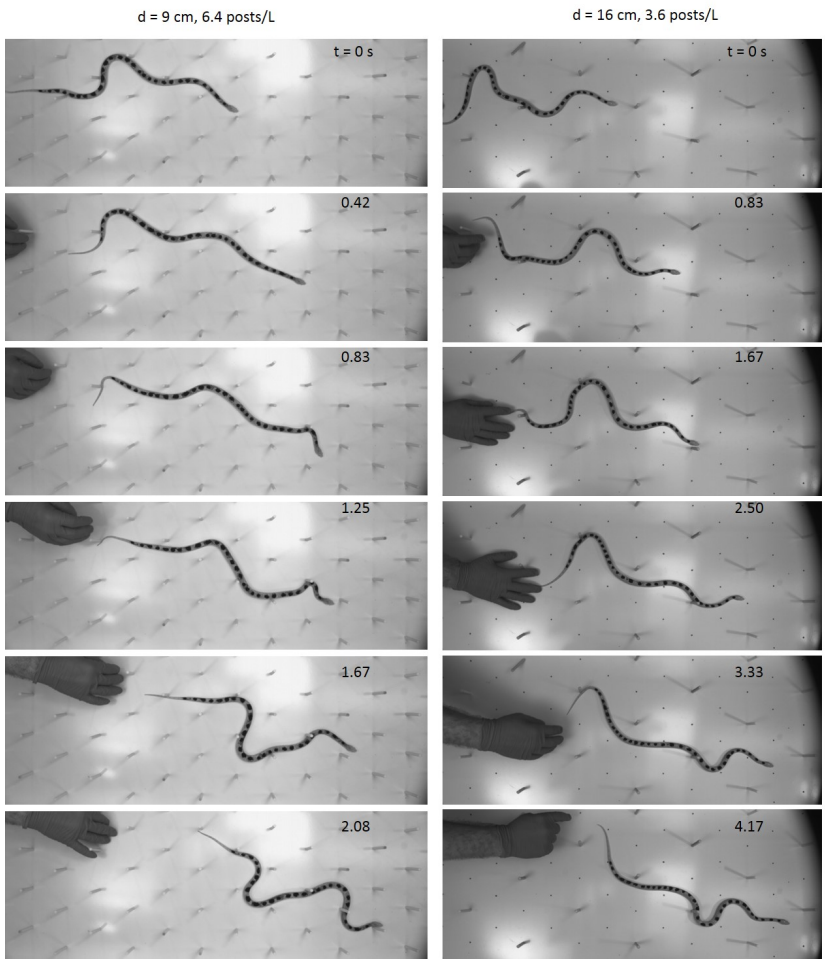


Figure 4.13: *P. guttatus* moving through 2D arrays on whiteboard. Time is as indicated on each still.

PCs are less dominant than when the desert specialist is moving on homogeneous GM ($\approx 91\%$, see chapter 2 for more details), but more so than for *P. guttatus* for which they capture $47.3\%$. This likely reflects the qualitative differences in the waveforms; *C. occipitalis* appears to use a shape which is more often like that observed during movement on homogeneous GM (Fig. 4.12) while *P. guttatus* make waveforms which varied widely in amplitude and arclengh (Fig. 4.13).

The two most dominant PCs were similar for *C. occipitalis* on GM and the whiteboard (Fig. 4.14*A,B*). Similarly to when they were on homogeneous GM, the amplitudes associated with these PCs traced out a circle through time (Fig. 4.14*D,E*). We note that the radius of the circle in $\alpha_1, \alpha_2$ is larger for the whiteboard substrate. This was in line with our measurements of the snakes' amplitude, which increased when on the hard surface.

*P. guttatus'* two most dominant PCs were also sinusoidal in appearance, but the amplitude increased posteriorly. The amplitudes were also less stereotyped. This likely reflects the more complex shapes we observed the snake using. This analysis suggested that while both species made using of traveling sinusoidal curvatures to propel themselves, the strategies were different.

The number of PCs needed to capture $95\%$ of the variance were similar across the three data sets. *C. occipitalis* in GM needed 11, on the whiteboard 9, and *P. guttatus* needed 10. This is contrary to what we guessed a priori, that *P. guttatus* would require more PCs to reconstruct the shapes given its more complicated appearing waveforms and less dominant first two modes. It is unclear why our guess was incorrect. It may be a limitation of the tracking such that looking at $95\%$ of the variance is including noise. It is also possible that the temporal integration of PCA is obscuring important differences. In this analysis we also chose to group data from all lattice spacings to discover if there were underlying kinematics which were preserved across environments. It may be that kinematic differences are dependent on lattice spacing. In the future we aim to explore further options for capturing the underlying kinematics.

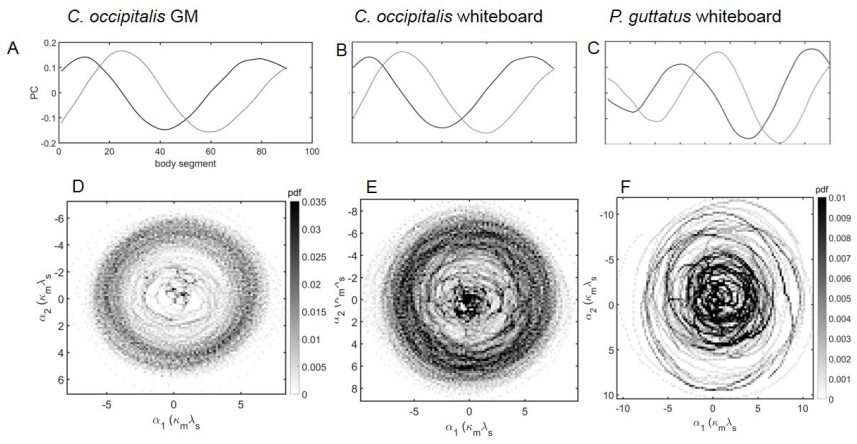


Figure 4.14: Preserved kinematics in post arrays. (*A,B,C*) are the first two PCs and (*D,E,F*) the associated amplitudes. PCA was performed on the entire data set including all lattice layouts and spacings for the indicated species and substrate.

In observing the videos we noticed that the snakes would frequently slide parts of the body perpendicular to the overall direction of motion, causing large $\beta_s$. This slipping, however, did not appear to negatively impact the ability of the snake to make effective forward progress. Unlike *C. occipitalis* which experienced large slip when it was not contacting enough posts and appeared to move in a manner similar to that on the homogeneous whiteboard, *P. guttatus* was moving smoothly forward with the portions of the body in contact with the posts and allowing, for example, posterior portions which were not contacting posts, to move freely. Such slipping is low-cost energetically as little energy is dissipated to sliding across the low-friction whiteboard. Therefore, we further challenged the snakes by placing the lattice on an incline and chasing the snakes up against gravity.

We hypothesized that climbing would both penalize parts of the body which were freely swinging, since the body is of finite length, swinging a portion to the side would result in a component of the velocity moving uphill, as well as challenge the animal by asking it to not just overcome the small drag on the whiteboard but lift a portion of its body weight using the posts.

The results of these experiments are preliminary, we tested one *P. guttatus* and two *C. occipitalis* and collected only one trial per individual for most lattice spacing and slope

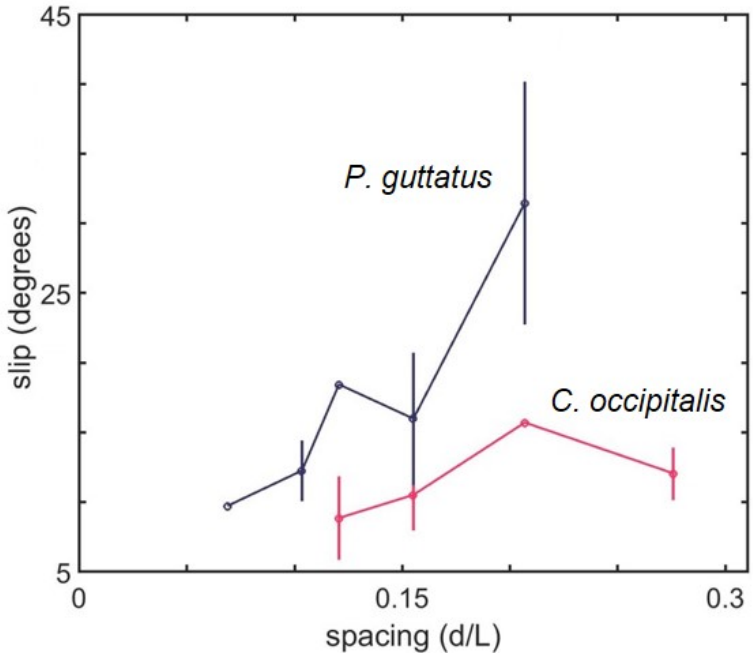


Figure 4.15: Slip versus lattice spacing for *C. occipitalis* and *P. guttatus* on inclines

pairs. We chose to combine the results for each species for all slopes tested (15, 20, and 30°) as a function of lattice spacing. When challenged with the slope *P. guttatus'* slip was less than that of *C. occipitalis* (Fig. 4.11). The generalist snake was able to effectively use the posts to move uphill, and it appears that slip is reduced from the flat ground case, although more data is needed.

In observing the snakes we note a qualitative difference in the way they interact with the posts. *P. guttatus* appears to bend the body and "grab" each post it contacts and continue to maintain contact (Fig. 4.16). In contrast, *C. occipitalis* would make and break contacts with posts, sometimes even falling backwards down the incline (Fig. 4.17).

The failure of the snakes to use the pegs to increase speed when moving on the granular substrate may be explained by the wave efficiency, the distance traveled in one undulation cycle divided by the wavelength. The assumption behind the hypothesis that the snakes would move more quickly using the pegs in GM was that the pegs provide rigid points for force generation as compared to the yielding sand. However, the snakes are able to achieve

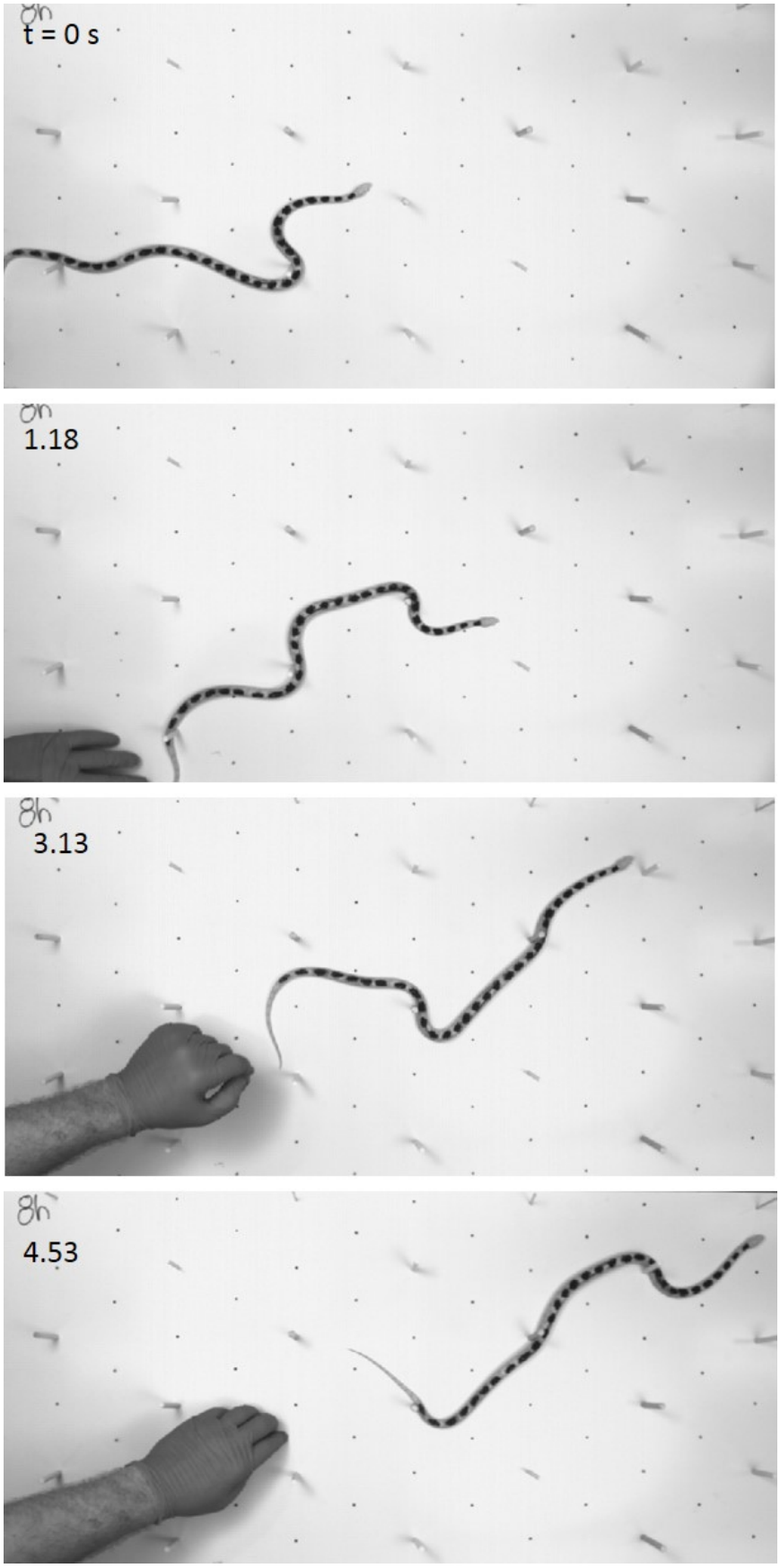


Figure 4.16: *P. guttatus* ascending 30° incline. Post density was 3.61 posts per bodylength.

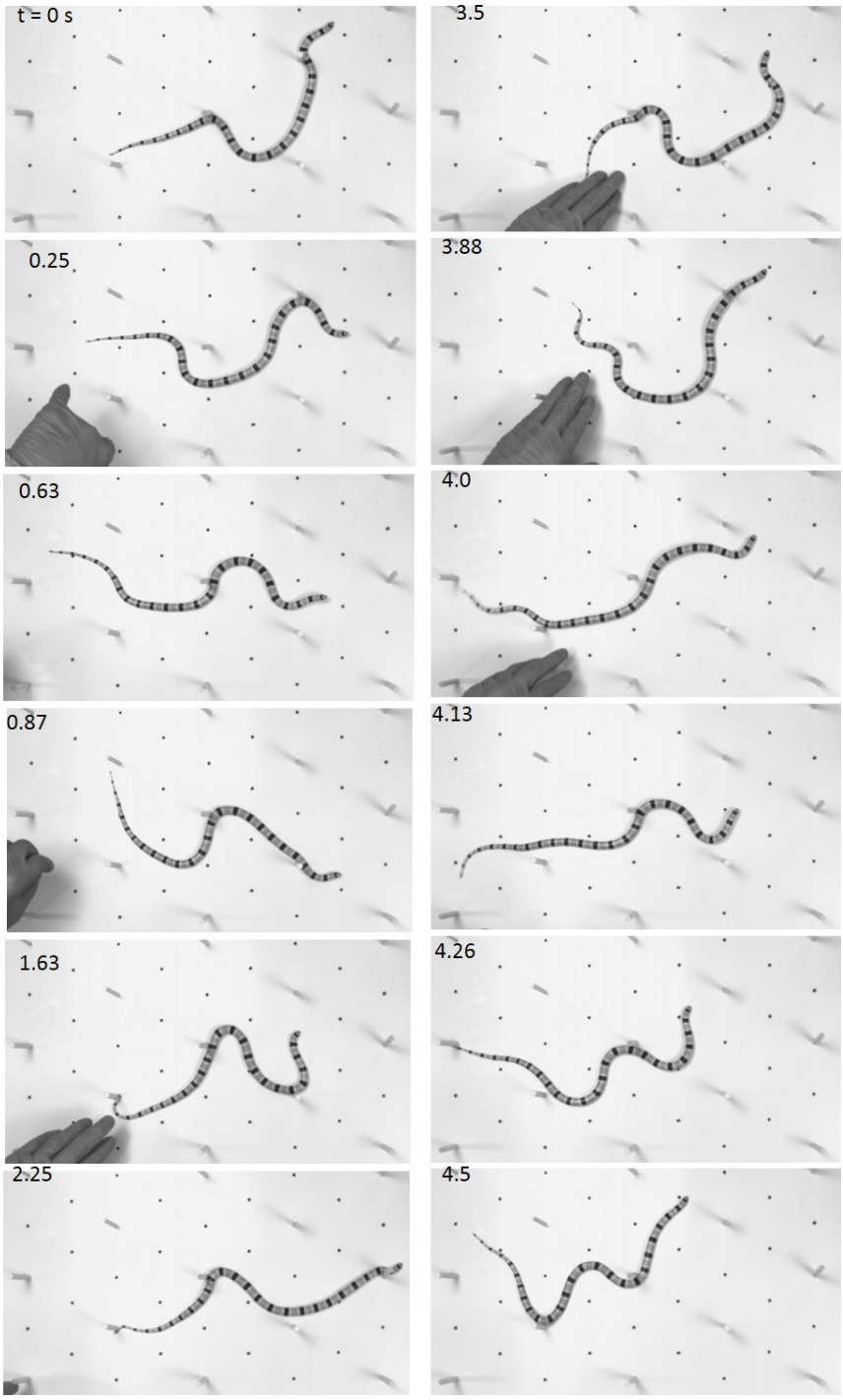


Figure 4.17: *C. occipitalis* ascending 20° incline. Post density was 3.34 posts per bodylength.

a wave efficiency of nearly unity (no backwards slipping) when moving in homogeneous granular media. Therefore, they cannot improve performance through the use of pegs without the changing the underlying kinematic template and so appear to be using the granular substrate and ignoring the obstacles.

Based on these results we developed a new type of controller for snake-like robots which uses serpenoid shapes as basis functions, thereby simplifying the task of coordinating the many joints, but allows the set points of the serpenoid curves (the amplitude $\zeta_m$ and the wavenumber $\xi$) to adapt to the surroundings. These set points were assigned their own dynamics which were modeled as a damped spring-mass,

$$M_d(\ddot{q_d} - \ddot{q_o}) + B_d(\dot{q_d} - \dot{q_o}) + K_d(q_d - q_o) = \tau_{ext}$$

,

where $q_o$ are the set points (maximum joint angle $\zeta_o$ and number of waves $\xi_o$) of the nominal waveform and the $q_d$ are the commanded set points ($\zeta_d$ and $\xi_d$) which can change based on the torque experienced by the motors ($\tau_{ext}$), measured using the current (Fig. 4.6*C*). This controller would therefore actively command the waveshape to match motor load to that expected when using the nominal waveshape on the hard ground without posts. This controller led to successful autonomous transit of unknown, rigid terrains. For more information on this controller see [70].

## 4.4 Conclusion

By propagating waves from head to tail, limbless organisms like snakes can traverse terrain composed of rocks, foliage, soil and sand. Previous research elucidated how rigid obstacles influence snake locomotion by studying a model terrain-symmetric lattices of pegs placed in hard ground. Many terrains are comprised of a mixture of substrates and discrete obstacle. We explored how different substrate-body interaction modes affect performance

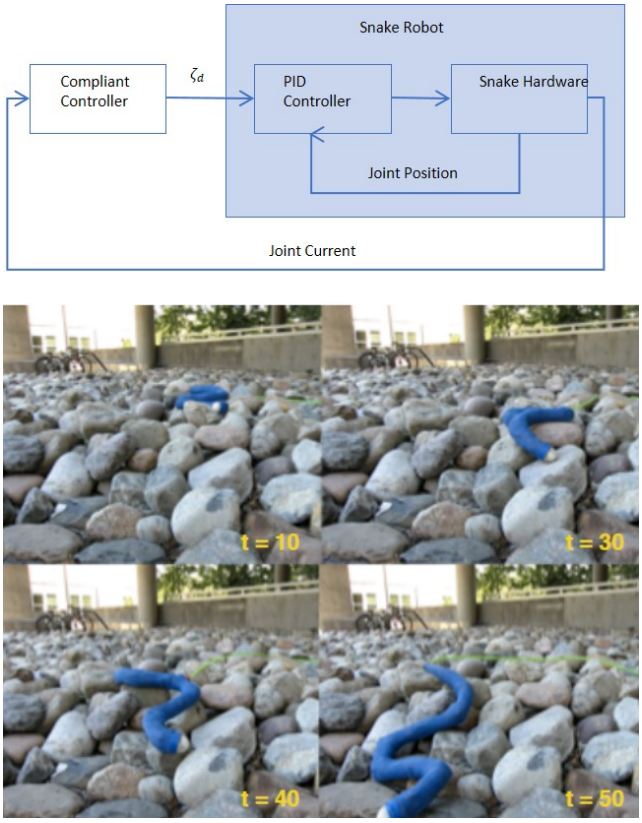


Figure 4.18: SEA snake robot moving autonomously over an unknown rock pile using the shape-based compliance control in 3 dimensions. Reproduced from [70].

of both a desert specialist snake and generalist snakes. We challenged snakes to traverse two laboratory treatments: lattices of 0.64 cm diameter obstacles arrayed on both a hard, slick substrate and in a GM of 0.3 mm diameter glass particles. Simulation of *C. occipitalis* moving along lattice rows on the whiteboard substrate suggested that performance was dominated by the geometry of the lattice relative to that of the waveform. A robotic snake using open-loop control with a joint torque limit exhibited similar performance.

The addition of posts to the whiteboard increased snake speed relative to moving on homogeneous whiteboard but speed on GM was not increased by the addition of the rigid push-points. Performance characterized by the amount of lateral slipping of the body was similarly unchanged in GM with the addition of posts and improved by the addition of obstacles to the whiteboard. The amount of slip on the whiteboard was a function of the lattice spacing, with slip increasing as spacing increased. Unexpectedly, we measured the same relationship for the generalist snakes, despite the qualitatively different waveform and apparent performance. When challenged to ascend an incline, however, preliminary data suggests that *C. occipitalis* is unable to robustly utilize the posts, leading to large slip as spacing increases as compared to *P. guttatus* which was relatively insensitive to spacing and performs similarly as on level ground. These results inspired a shape-based compliance control which adjust the serpenoid wave parameters based on torques imposed by the surrounding terrain. This control enabled a snake-like robot to move robustly through unknown terrain made of rigid materials. Future work will involve combining our findings for movement on yielding materials (chapter 2) with tests of snakes in non-rigid obstacles to develop control for use of materials which can yield under forces produced by the organism/robot.

# CHAPTER 5

# MISCELLANEOUS EXPERIMENTS

## 5.1 Partially buried intruders in different granular materials.

### 5.1.1 Introduction

In the evolutionary transition from aquatic to terrestrial terrain early tetrapods were challenged with traversing near-shore habitats [147]. They were therefore likely challenged with ascending deformable substrates like sand. We hypothesized that the tail played an important role in making early tetrapod locomotion robust to unexpected terrain interactions and kinematic mistakes. We studied a biological model which moves terrestrially using the pectoral fins, the mudskipper fish *Piriophthalmus barbarus*, and found that when ascending sandy slopes it prevented performance degradation due to yielding of the material by also using the tail for propulsion (Fig. 5.1*A,B*). A robophysical model revealed that use of the tail was not greatly beneficial when on flat GM, but using the tail on inclined GM made allowed locomotion over a range of limb kinematics which otherwise would fail.

We wanted to better understand the interaction between limbs, tail, and material. We carried out geometric mechanics calculations to explore the connection between self deformation patterns and the resulting motion in the lab frame[148]. This required an understanding of the forces acting between the appendages and the material. Therefore, we carried out a series of granular drag experiments on partially submerged intruders.

This work is published in [92]. The study of tail use in early tetrapods was designed by Benjamin McInroe. The robophysical experiments were carried out by Benjamin McInroe and analysis performed by McInroe and Henry Astley. Mudskipper experiments and analysis were performed by Sandy M. Kawano and Richard W. Blob. Geometric mechanics calculations were done by Chaohui Gong and Howie Choset.

Granular drag experiments using the robot arm were performed by Jennifer M. Rieser, who developed the automated system allowing rapid data collection.

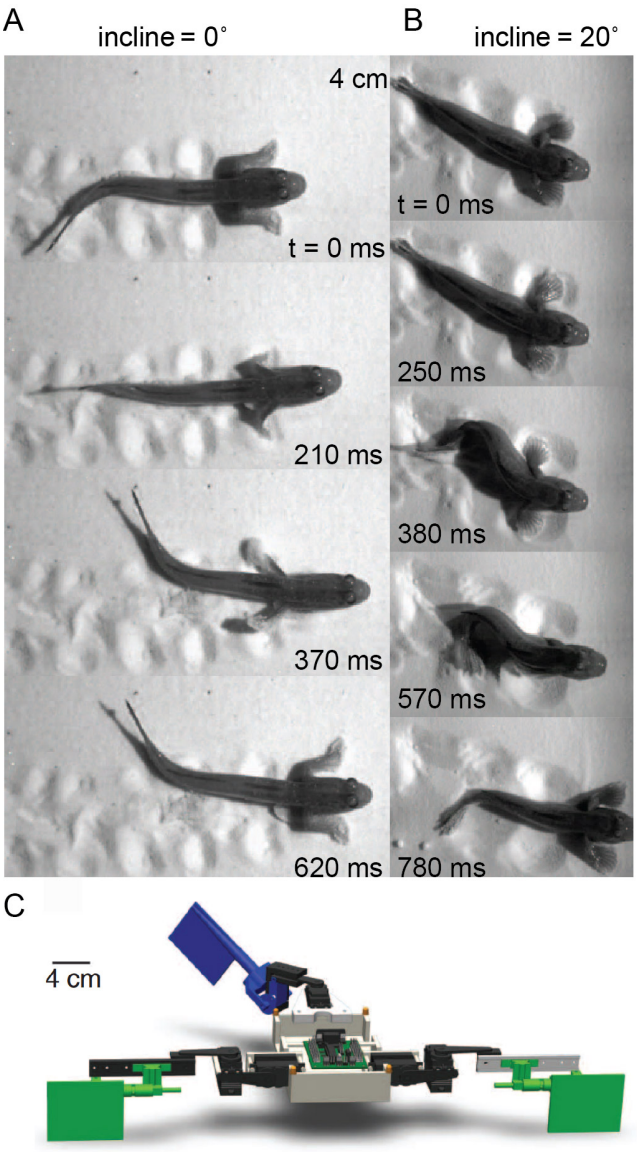


Figure 5.1: Mudskipper fish and robophysical model. (*A*)Mudskippers use a crutching motion of the pectoral fins to move in terrestrial environments. (*B*)When challenged to ascend inclined granular matter (oolite sand) the mudkipper uses the tail as an additional appendage. When the tail was not used the step length decreased significantly as compared to the level GM treatment. (*C*) Robophysical model of the mudskipper. The robot moved in poppy seeds and 6 mm diameter plastic spheres (BBs) as the oolite sand would damage the motors. The limb flippers are green and the tail is blue. Adapted from [92].

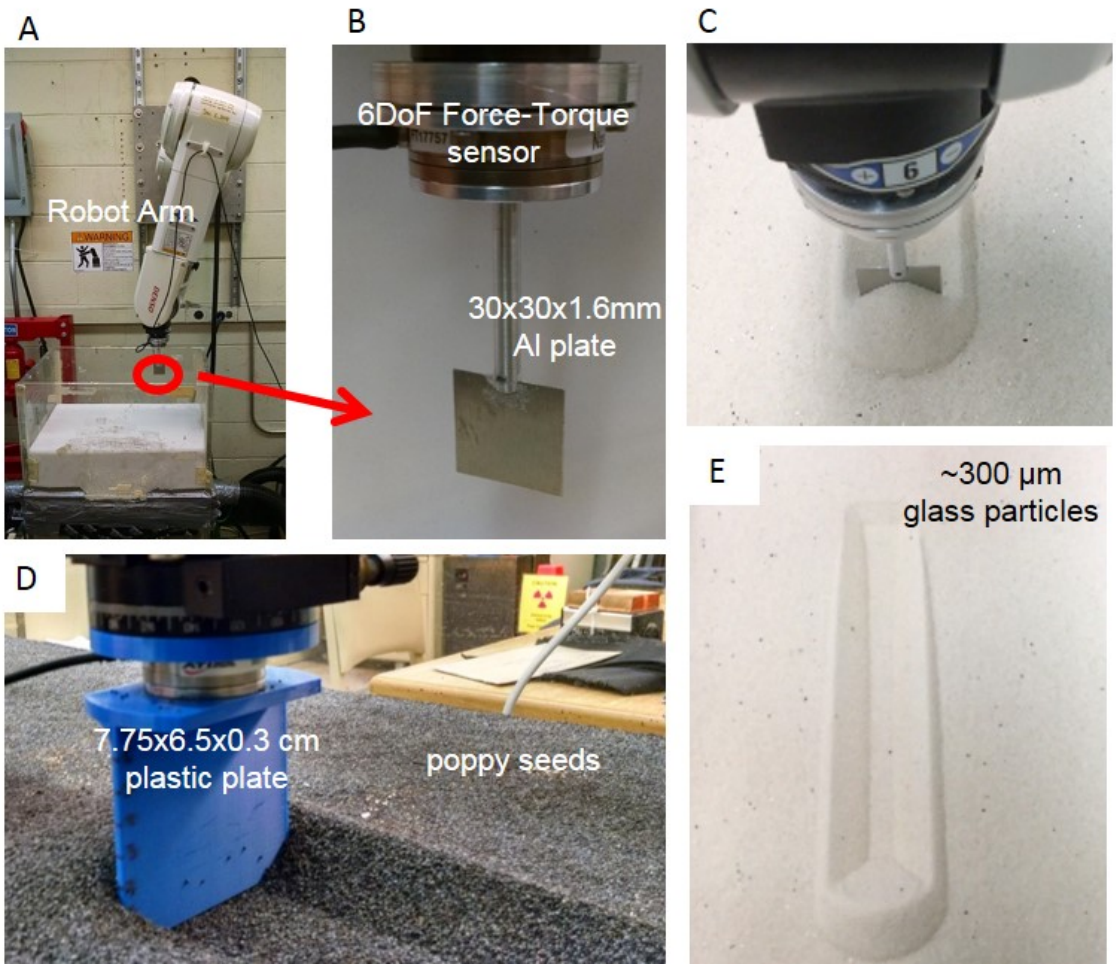


Figure 5.2: Experimental setup for granular drag on partially intruded plates. (*A*) Robot arm moves the force-torque transducer and intruder plate through the material. (*B*) Close-up of the force sensor and Aluminum plate. (*C*) Example of the Al plate moving partially submerged in the oolite sand. (*D*) Example of the plastic plate moving through poppy seeds. (*E*) Track in the GM left by the intruder.

### 5.1.2 Granular drag experiments

Granular drag measurements were performed using a 3D printed plastic flat plate $7.75 \times 6.5$ cm$^2$ (Fig. 5.2*D*, same material and dimensions as the blue/green limbs in Fig. 5.1*C*). The plate was partially submerged into the granular media, with intrusion depth measured from undisturbed granular surface to the bottom edge of the limb. In these experiments, the limb was moved through loose-packed poppy seeds a distance of 21.5 cm at a speed of 1 cms$^{-1}$ for intrusion depths of both 1 and 3 cm. All tests were performed in both level

granular media and 20° media incline, both uphill and downhill. The forces normal and tangential to the plate in the direction of motion were measured as a function of drag angle $\gamma$, defined as the angle between the tangent vector to the limb face and the direction of displacement. An air fluidized bed of 152 cm length and 53 cm width was used to control the initial state of the media. The poppy seeds filled the bed to a depth of 8 cm, sufficient to prevent boundary effects acting between the floor and the intruder. Before each trial, air was passed through the porous rigid floor of the bed to fluidize the poppy seed grains, allowing them to behave like a fluid and thereby erase prior deformations due to yielding. Airflow was then turned off and the grains allowed to settle into a loosely packed state. For trials on the 20° slopes, two linear actuators (Firgelli Automation FA-200-L-12) were used to slowly change bed angle once the media had settled. A rotation stage (Newport 481-A) was used to manually adjust the angle of the intruder relative to the direction of motion (drag angle, $\gamma$) from 0° to 90° in 10° increments. The granular drag forces acting on the limb were measured using a 6-axis force/torque sensor (Mini40, ATI industrial) mounted between the intruder and the rotation stage. Data were collected at 1000Hz and the sensor resolved the force measurement into components parallel, $F_{||}$ , and perpendicular, $F_{\perp}$ , to the limb face. Intruder displacement was achieved using a Copley linear actuator (Copley Controls) attached to a linear stage (Igus DryLin) on which the intruder, rotation stage, and force sensor were mounted ((Fig. 5.3*A*) see subsection 6.2.4 for Copley motor setup).

We used the following previously suggested empirical functions to fit the data [149, 91]:

$$F_{\perp}(\gamma) = C\sin(\gamma)$$

$$F_{||}(\gamma) = A\cos(\gamma) + B(1 - \sin(\gamma)) + F_o))$$

Using MATLAB lsqnonlin function we found values for the fitting parameters (with 95% confidence intervals) for a limb intruded 1 cm in level media to be:

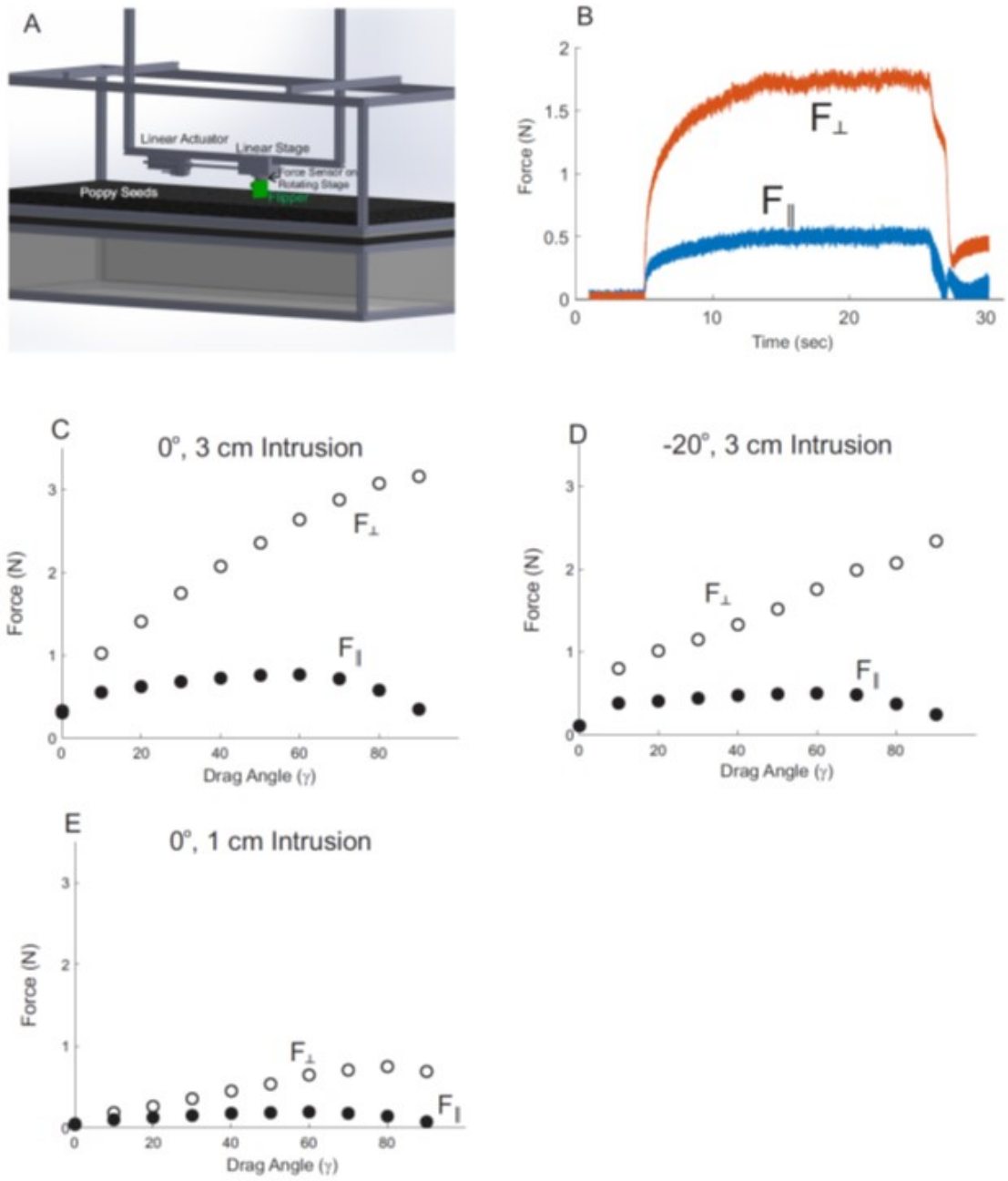


Figure 5.3: Perpendicular and parallel forces during drag experiments in poppy seeds. (A) Experimental setup for drag characterization. (B) Parallel and perpendicular forces over time in an example trial (insertion depth = 3 cm, bed angle = 20° downhill, limb angle = 60° ). (C) Forces (perpendicular = hollow, parallel = solid) for various drag angles at a 3 cm insertion depth and 0° bed angle. (D) Forces (perpendicular = hollow, parallel = solid) for various drag angles at a 3 cm insertion depth and 20° downhill bed angle. (E) Forces (perpendicular = hollow, parallel = solid) for various drag angles at a 1 cm insertion depth and 0° bed angle.

$$C = .066.0(64.0, 69)N$$

$$A = 0.27(20.0, 33)N$$

$$B = 0.320(-0.38, -0.26)N$$

$$F_o = 0.09(0.07, 0212)N$$

In the locomotion experiments the substrate was smoothed by hand rather than using a fluidized bed as in the drag experiments. To assess the effect of hand smoothing on the properties of the poppy seeds we used a 6- axis robotic arm (Denso VS087A2-AV6-NNN-NNN) to drag the 3D printed plastic muddybot limb over a distance of 20 cm at 1 cm$s^{-1}$. Forces were resolved using a 6-axis force/torque 5 sensor (Nano43, ATI Industrial). The poppy seeds were filled to a depth of approximately 15 cm in an air-fluidized bed 44 cm in length and 29 cm in width, large enough to prevent boundary effects due to the walls or floor of the bed. We used both fluidization-prepared loose-packed poppy seeds–the same preparation technique as used in the above drag experiments–as well as hand-smoothed poppy seeds–the preparation technique used in the muddybot robot trials. We collected three trials each at drag angles of 90° (plate face perpendicular to the direction of motion) and 45° for a total of 12 trials (6 fluidized and 6 hand-smoothed). We found that hand-smoothing did not affect the material response to drag, and the anisotropy (ratio of perpendicular to parallel force) of the manually reset trials agreed with that of the fluidized trials (Fig. 5.5).

To determine the nature of the material response to drag for the different granular media used in our locomotion experiments, we used the same setup and dragged the intruder 20 cm at a speed of 1 cms$^{-1}$. Drag angle was varied from 0-90° in 10° increments, similar to the motion used to determine the empirical functions. We tested the spherical plastic particles used in the robot trials using the muddybot flipper intruder and the oolite sand used in the mudskipper trials using a$3 \times 3 \times 0.01$ cm$^3$ Aluminum plate. This Al plate

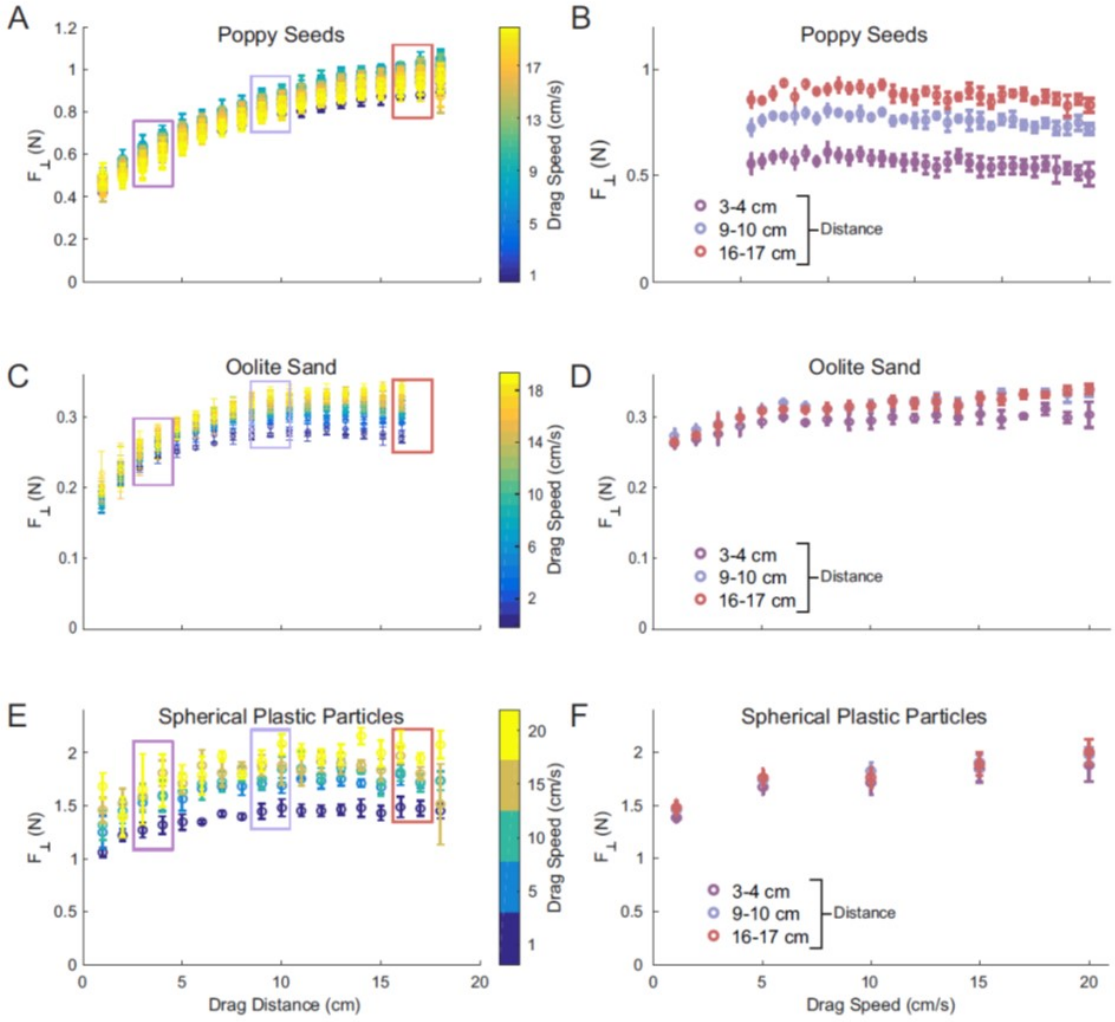


Figure 5.4: Drag experiments across media types and speeds. Perpendicular force as a function of distance (A, C, E) and speed (B, D, F) of intruder movement in three materials: (A, B) poppy seeds (prepared by fluidization), (C, D) oolite sand (prepared by fluidization), and (E, F) spherical plastic particles (prepared by hand-smoothing). Boxes in A,C, E indicate the distance intervals used in B, D, F, with corresponding colors.

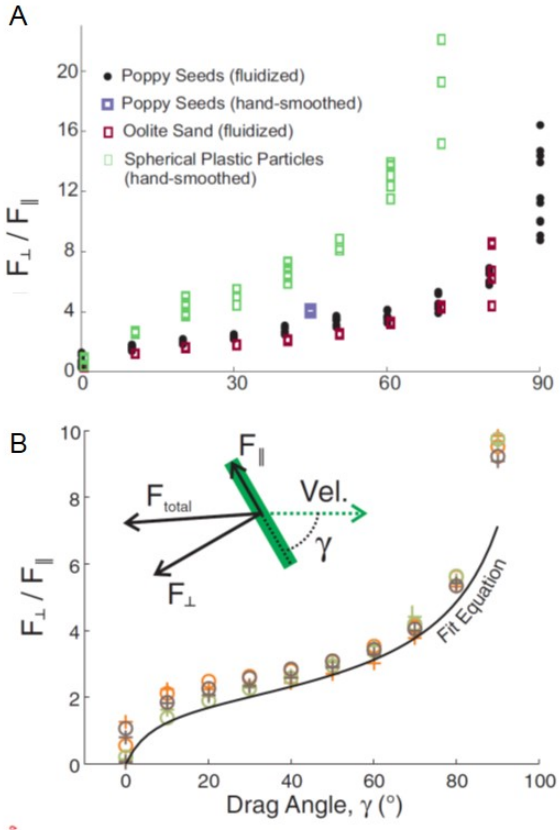


Figure 5.5: (*A*)Drag experiments across media types and preparation techniques. The ratio of perpendicular and parallel forces for poppy seeds prepared via fluidization, hand-smoothed poppy seeds, oolite sand, and spherical plastic particles. The plastic particles depart from the curve, due to low parallel forces as a consequence of low friction between the particles and flipper. Values at high drag angles are not plotted for all media as the parallel forces near zero. (*B*) The ratio of forces parallel and perpendicular to the limb surface during poppy seed drag experiments at various drag angles to the direction of motion, insertion depths, and substrate slopes. Intrusion depths are 1 cm (crosses) and 3 cm (circles),with q = 0° (brown), 20° uphill (orange), and 20° downhill (green).The black line represents the ratio of perpendicular and parallel equations.

is comparable in scale with the mudskipper (anterior-posterior length 10.5±3.9 cm). The oolite sand was prepared using fluidization while the plastic particles, which could not be fluidized using the current setup, were hand-smoothed between trials. In the plastic particles, the drag angle was varied from 0-90° in 10° increments at an intrusion depth of 3 cm. We chose this intrusion as 3 cm intrusion is in line with the intrusion depths observed in muddybot trials. We also collected trials at approximately 1 cm depth for 20°, 40°, 60°, and 80° drag angles and find that the force anisotropies for the two intrusions are equivalent (Fig. 5.5). In the oolite sand, the drag angle was varied from 0-90° in 10° increments at an intrusion depth of 5 mm. This agrees with the limb intrusions observed in the mudskipper experiments. As with the plastic particles, we also tested the four drag angles (20°, 40°, 60°, and 80°) at 1 cm intrusion to confirm that the anisotropy is independent of depth at these ranges and find good agreement both with the anisotropy of oolite sand intruded to 5 mm as well as with the anisotropy of the poppy seeds. The relationship between anisotropy and drag angle of the spherical plastic particles has a similar shape to that of the poppy seeds and oolite sand, however the magnitude of the anisotropy increases more quickly as the angle increases. We believe this can be attributed to the low friction between the plastic flipper and plastic beads as compared to that between the flipper and poppy seeds or Al plate and oolite sand.

We also verified that the granular response to drag is insensitive to velocity. The yielding media speeds encountered by the robot and mudskipper were ≈5-10 cms$^{-1}$. The poppy seeds and spherical plastic particles were again tested with the flipper intruder and the oolite sand using the $3 \times 3 \times 0.01$ cm$^3$ Al plate. Material was prepared the same way as in the material response trials. The flipper was intruded to a depth of 1cm in the poppy seeds, 3 cm in the plastic particles, and 5 mm in the oolite sand. In poppy seeds and oolite sand, perpendicular forces were measured for intruder speeds from 1 to 20 cms$^{-1}$ in 1 cms$^{-1}$ increments and at 0.5 cms$^{-1}$. In plastic particles, the forces were measured at speeds of 5, 10, 15, and 20 cms$^{-1}$. We find that force is insensitive to speed for speeds relevant to

the locomotion tested (Fig. 5.4). Calculations of maximum yielding sand movement speed based on the robot movements ((21 cm $\pi$/3 )/ (2 sec) = 11 cms$^{-1}$) and digitizing the interface between yielding sand and both the pectoral and tail fins ($\approx$5-10 cms$^{-1}$) yielded similar speeds for the granular media in high-yield 6 cases, and both were well within the range of speeds for which force is speed-insensitive in all media (Fig. 5.4).

## 5.2 Mechanical diffraction in open-loop control of a robophysical model

Snakes can utilize obstacles to move through complex terrain, but the development of robots with similar capabilities is hindered by our understanding of how snakes manage the forces arising from interactions with heterogeneities. We previously studied a desert-dwelling snake, C. occipitalis, in a model terrestrial terrain—a single row of vertical posts. Interaction with the post array resulted in reorientation of trajectories away from the initial heading. Combining trajectories from multiple trials revealed an emergent mechanical diffraction pattern in the final heading. We explored the relationship between flexibility of the serpenoid waveform and the resulting mechanical diffraction using a robophysical model, a 12-link snake-like robot. The robot snake using open-loop control which accurately tracked the commanded waveform demonstrated a pattern similar to the snake, despite a different scattering mechanism. The pattern persisted when we changed the maximum torque output of the robot motors from 1.5 N-m to 0.38 N-m in which case local deformation of the robot from the serpenoid curve appears during interaction with the posts. This suggests the emergent collisional diffraction pattern is a general feature of these systems. We posit that open-loop control of the serpenoid template in sparse terrains is a simple and effective means to progress, but if adherence to a heading is desired more sophisticated control is needed.

Robot design and build by Zachary Goddard This section is adapted from [129].

### 5.2.1 Introduction

Principles governing movement in heterogeneous terrains remain largely undiscovered. During terrestrial locomotion, contacts with the surroundings are often intermittent and can lead to unexpected emergent behavior [150]. Snakes are remarkable in their ability to use a seemingly simple morphology—a limbless, elongate trunk—to navigate many habitats including a wide range of terrestrial environments. Previous research on terrestrial snake locomotion focused on so-called generalist snakes which encounter a variety of terrain (forest, grassland, wetland, etc.) consisting of many different materials. These snakes use posteriorly-propagating body bends to push the trunk laterally against obstacles and generate the forces needed for forward movement [19, 21]. The versatility and simplicity of this scheme makes it an attractive model for robots [151]. However, the challenge of controlling the many degrees of freedom to effectively manage interaction with obstacles can stymie robotic implementation of slithering locomotion.

Locomotor templates [152] can simplify control and aid understanding. We previously found the desert-dwelling sand-specialist Mojave Shovel-nosed snake (Chionactis occipitalis Fig.1a) uses a highly-stereotyped waveform which adheres to a sinusoidal curvature in both time and arclength along the body (a "serpenoid" curve [94], Eq.1) when moving on the surface of homogeneous sand. Given the observed stereotypy of the waveform both between individuals and trials, we hypothesized that C. occipitalis uses open-loop control, where the muscle activation is not modified in response to perturbation from the terrain.

Therefore, to begin a systematic search for principles of slithering movement in terrestrial environments, we previously studied C. occipitalis navigating a model terrestrial terrain – a single row of vertical, rigid posts embedded in a homogeneous substrate – inspired by the omnipresent sand substrate and sparse obstacles in their natural habitat. We compared the performance of the living snake to a multi-link snake robot in a similar model terrain ([**FIGrobotdiagram**]). The robophysical model provided the benefit of behaving in a controlled way which facilitated understanding both of the control strategy of the animal

as well as the benefits and drawbacks of using the simple open-loop serpenoid template scheme in multi-modal terrain.

We constructed a robophysical model [153] of the snake from 13 rigid, 3D printed segments actuated by 12 servo motors (Dynamixel AX-12A) (Fig. 5.6).The robot moved on rubber mats and LEGO wheels on the underside of the robot facilitated low-slip locomotion comparable to that of C. occipitalis in granular media. A row of five rigid 4.5 cm diameter posts with a 5.7 cm opening between posts was placed perpendicular to the direction of travel of the robot. The force applied to the posts was measured via strain gauges bonded to the square Aluminum-rod base.

Interaction with the array was dependent on the phase and position of the robot when it contacted the posts. Therefore, to explore all possible initial conditions, we varied the initial placement of the center-of-mass (CoM) of the robot within a rectangle whose width was set by the periodicity of the posts and length by the wavelength of the waveform. The x and z coordinates of each segment were captured at 120 Hz by a system of four OptiTrack cameras (Flex 13, Natural Point) tracking infrared reflective markers on the robot. The robot was controlled using a Robotis CM-700 controller and powered using an external supply. The actuator positions were determined by the equation for a serpenoid curve (Eq.1).

$\zeta_i = \zeta_M sin(ks_i + 2\pi ft)$ (1)

$\zeta_i$ is the angular position of actuator i =[1,. . . ,12] with a set maximum angular excursion $\zeta_m = 0.62$rads, spatial frequency k = 1, and temporal frequency f=0.15 Hz. The waveform seen on the robot in Fig. 5.6 is this serpenoid curve at time t=0. The control signal sent to the robot was open-loop such that these parameters were not changed at any point in any of the trials and the control signals would continue to be sent as a function of time and position on the body regardless of external forces or tracking accuracy of the actuators.

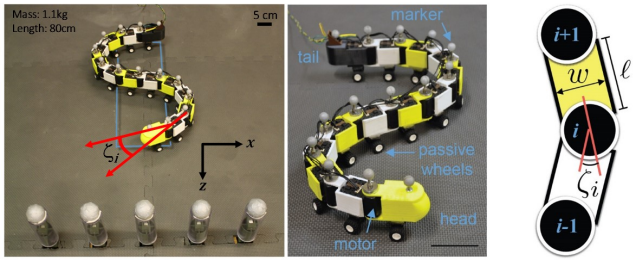


Figure 5.6: Robophysical model for *C. occipitalis*

### 5.2.2 Robot experiment

We tested two versions of this control on the robot. The first case was high-torque (HT). In this case the maximum torque each actuator could produce was 1.5 N-m. The HT robot could accurately track the desired waveform in most cases. We verified the tracked robot positions using the OptiTrack data and found the tracking error was $< 5\%$.

For the limited-torque (LT) case we kept all other aspects of the robot and controller the same but limited the torque output of each actuator to $25\%$ of the overall maximum (0.38 N-m). For reference, the largest torque measured in the robot moving on the rubber mats alone was $20\%$ max, or 0.3 N-m (Fig. 5.7). In the LT case the actuator would track the commanded trajectory up until the torque exceeded 0.38 N-m. At this point the motor continued attempting to track the commanded angles but did not exert more than 0.38 N-m of torque. The motor resumed successful tracking of the commanded trajectory once this was possible with $\leq$ 0.38 Nm of torque. The inability of one actuator to achieve the desired position did not change the commands to it nor to the other actuators. The observed result of the LT condition was that local deformations from the serpenoid curve appeared during interaction with the post array (Fig. 5.8). The distribution of tracking error during interaction with the posts had a similar mean to the HT case but the tails of the distribution were longer and asymmetric with a greater number of large positive errors (maximum tracking error measured was $34\%$) than seen in the HT case. This reflects the observed local deviations from the commanded angles. We compared the kinematics of the

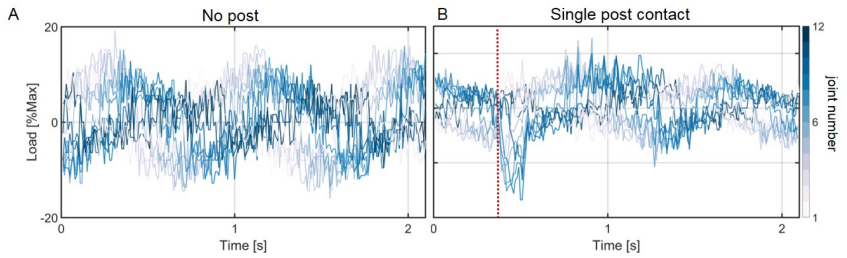


Figure 5.7: Torque measured by robot motors.

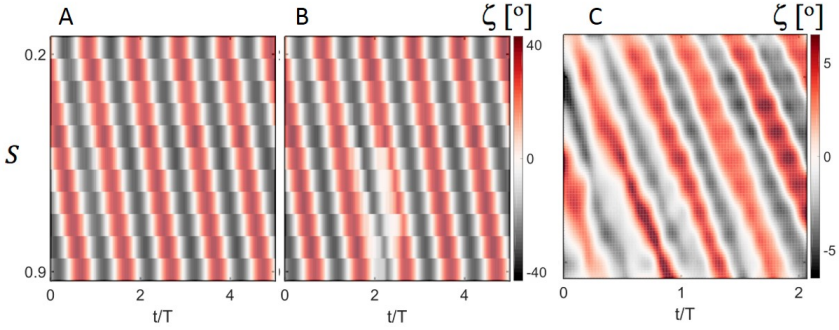


Figure 5.8: Spacetime plots of $\zeta$ for the robot and animal (A) Local joint angle $\zeta$ calculated from the tracked experimental data for the rigid robot (no torque limit) transiting the 5.7 cm spacing array. (B) $\zeta$ calculated from the tracked experimental data for the torque-limited robot (torque limit at 25% maximum torque capacity) transiting the 5.7 cm spacing array. (C) $\zeta$ calculated from tracked experimental data for C. occipitalis transiting the 2.3 cm spacing array. The smaller $\zeta$ values for the snake arises from the greater spatial resolution of the snake morphology—the snake has significantly more "segments" than the robot (roughly 200 vertebrae). We splined the snake body using 100 points as compared to the 14 points which describe the robot shape.

HT to the LT case for the robot moving in a steady state with no pegs present to verify that decreasing the maximum torque available to the actuators did not otherwise change their behavior.

The compliance introduced by the torque limit is be illustrated in spacetime plots of the joint angles. Fig. 5.8*A* is a spacetime plot for the rigid robot, and Fig. 5.8*B* is a spacetime plot for the torque-limited robot. The local deformation of the torque-limited robot can be seen in the lower left hand quadrant of Fig. 5.8*B* where the alternating red and black bands are deformed. For comparison Fig. 5.8*C* is a spacetime plot of a snake trial.

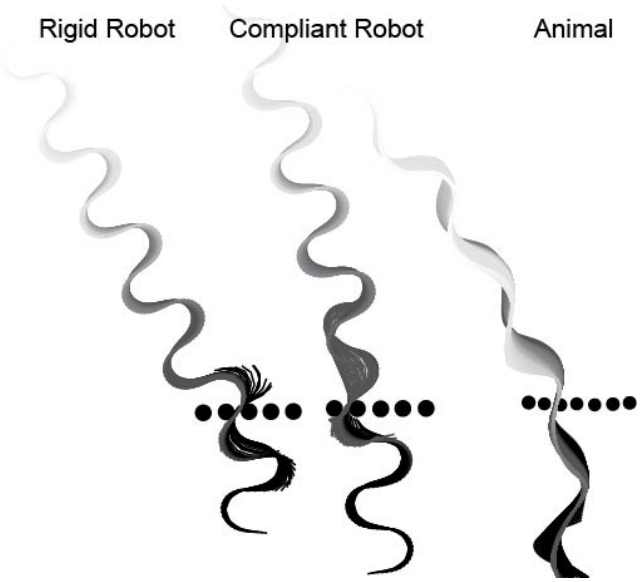


Figure 5.9: Snake and robot trajectories. Each was moving vertically up the page before interacting with the posts (black circles) then continuing up the page at an angle. Color from black to white indicates advancing time.

### 5.2.3 Results

The array acts to scatter the snakes and robot alike Fig. 5.9. The action of the array is best illustrated when all trajectories from all trials are combined as in Fig. 5.10. The snakes move from bottom to top, in the direction of positive z. The units are normalized by voT, the average CoM velocity times the period of the motion, i.e., the average distance travelled in one undulation. The trajectories are colored according to the scattering angle $\theta$. To calculate $\theta$ we averaged the polar angle of the trajectory with respect to the z-axis as it passed through a band between three and four voT from the array.

The trajectories of the LT and HT robot trials are shown in Fig. 5.10*e* and *f* respectively. The trajectories are colored by scattering angle as before, and as in the trials with C. occipitalis some trajectories were deflected away from the z-axis by the interaction with the array. The LT robot generally scattered at smaller angles than the HT robot. We note that the largest scattering angles of *C. occipitalis* were greater than those of the robot, but we cannot say whether this is of any significance. During these trials we found that the scat-

tering angle was sensitive to a number of factors related to the various dimensions of the system, and it is as of yet unclear which of these drove the differences between C. occipitalis and the robot, or if it was to a greater degree due to differences in the neuromechanical systems (e.g. the use of bilateral muscle versus a single servo to actuate the trunk).

The emergent pattern of the trajectory re-orientations was further illustrated in a histogram of the scattering angle. These histograms are above their corresponding trajectory maps in Fig. 5.10. It is clear that both the living and robotic snakes are more likely to travel in certain directions than others upon exiting the array, and this pattern is qualitatively similar for the three systems tested.

The forces applied to the obstacles revealed a similar emergent pattern. The angle $\theta_F$ is the angle between the force vector and the positive z-axis, i.e. atan(Fx/Fz). The bottom row of Fig. 5.10 shows histograms of $\theta_F$ for all trials. We find that both the living and robotic systems are more likely to push left/right against the array. It seemed reasonable to expect that $\theta_F$ and $\theta$ would be correlated. However, we did not find any relationship between the two. This may be attributed to the complexity of the interactions acting simultaneously between the posts, the body, and the substrate; perhaps in combination with the highly dissipative nature of the surroundings.

### 5.2.4 Discussion

This study highlights the benefits and repercussions of using an open-loop serpenoid curve during limbless locomotion in multi-modal terrain. Control of the serpenoid template was easy to implement, and we note that it was exceedingly rare ($\approx 1\%$ of trials) for the rigid robot to become wedged in the array, while the compliant robot and living snake always transited the array. We therefore argue open-loop control of the serpenoid template is an effective strategy for transit of sparse terrain which requires no external sensors, with the caution that the pattern of trajectory reorientation appears to be a general feature of these systems. A more sophisticated control scheme which can correct the heading changes

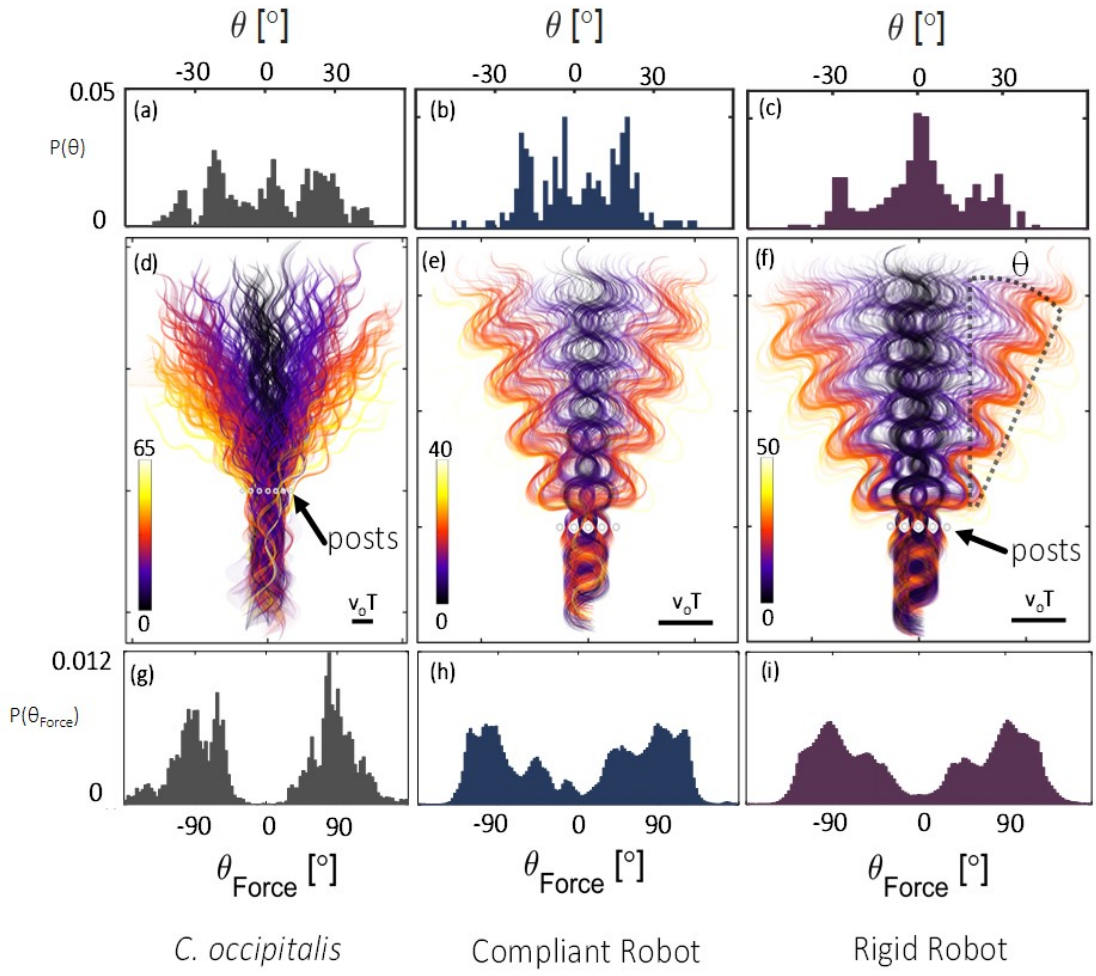


Figure 5.10: Mechanical diffraction pattern in a snake and snake-like robot. (a-c) Scattering angle $\theta$ for the snake (181 trials), limited-torque (LT) robot (216 trials), and maximum-torque (HT) robot (366 trials), respectively (left to right). Snake scattering angles are calculated as the mean polar angle of a trajectory when it is a distance between 7 and 8 voT from the center of the post array (see diagram in Fig.1d and discussion in Section 2). As the robot waveform has less natural variation, scattering angle is calculated by fitting a line to the maxima/minima of the trajectory for all body segments and calculating the angle between these lines and the vertical. $\theta$ is taken to be the average of all of these values. (d-f) Trajectories for the snake, LT robot, and HT robot, respectively (left to right). To help differentiate trajectories each run is colored according to the absolute value of its scattering angle. Light gray circles indicate the position of the posts. Prior to the posts the group of trajectories is "collimated" whereas after interacting with the array some trajectories deflect away from the vertical z-axis. (g-i) Force orientation angle $\theta$Force for the snake, LT robot, and HT robot, respectively (left to right). $\theta$Force is calculated for each contacted post throughout each run by finding the angle between the force vector and the z-axis. A value of zero corresponds to the snake pushing directly forward (+z) while 180° is the snake pushing directly opposite the direction of motion (-z). The peaks in the distributions occur around $\pm 90°$, meaning the snakes are most likely to push left/right on the posts.

caused by collision with obstacles may be necessary if a specific trajectory is desired

## 5.3 Low-dimensional templates for suburface sand-swimming in *Scincus scincus* and *C. occipitalis*

Geometric mechanics is a frame work which is used to calculate the connection between an animal (or robot) self-deformations and the resulting translations and rotations in the lab frame [148]. Recent advances in geometric mechanics allowed for the use of a *shape basis* to describe kinematics [154]. The shape basis is a low-dimensional representation of a locomotor's kinematics. For example, the serpenoid curve which describes the self-deformation pattern of *C. occipitalis* moving on the surface (chapter 2). Using such a basis one can prescribe kinematics using, as in the previous example, a list of amplitudes through time rather than assigning a numerical value to the position of each joint.

To use this framework to explore the motion of animals, however, it was necessary to determine such a basis. Our aim was to use geometric mechanics to explore the subsurface sand swimming of the sandfish *Scincus scincus* and the Shovel-nosed snake *Chionactis occipitalis* (chapter 1).

### 5.3.1 Subsurface swimming kinematics

Previously, data on both the sandfish and *C. occipitalis* swimming subsurface in 270$\pm$0.04 $\mu$m glass particles was collected using x-ray imaging. Lead markers were glued to the midline of the animal and tracked using MATLAB. Trials were conducted in both loose (packing fraction $\phi$ =volume of grains/total occupied volume = 0.635$\pm$0.013) and close packed ($\phi$= 0.58) states, but as the kinematics were not influenced by $\phi$ [13] the data from both loose and close packed trials was combined for the following analysis.

We up-sampled the sandfish data from 8-10 to 50 points using a cubic spline interpolant

Sandfish and snake data were collected and tracked by Ryan Maladen and Sarah Sharpe, respectively.

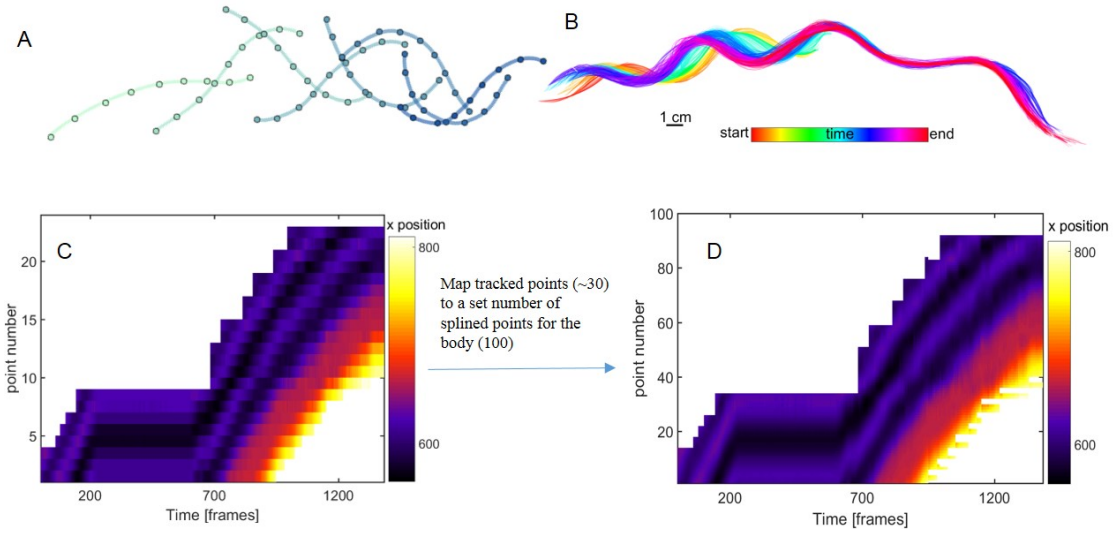


Figure 5.11: Splining of sandfish and snake data to standardize position along the arclength (*A*) 8-10 lead markers on sandfish up-sampled to 50 points using a cubic spline interpolant. (*B*) Example snake tracks. The snake was long enough that it was common for only a subset of the ≈30 markers to be in view at any given time. (*C*) Example of the x position of each marker (vertical axis) as a function of time (horizontal axis) to illustrate the inconstant number of markers in view. (*D*) The fraction of the number of visible points to total points was mapped to an equivalent fraction of a 100 point cubic spline interpolant.

(Fig. 5.11*A*). The snake was long enough that often portions of the snake were out of view of the x-ray imager. Therefore, we mapped however many of the the ≈30 tracked points in each run to an equivalent fraction of 100 splined points (Fig. 5.11). Example kinematics of *S. scincus* and *C. occipitalis* may be seen in Fig. 5.12*A* and *B* respectively.

We represented the sandfish shapes using the tangent angle, $\theta$, (Fig. 5.13). The snake shapes were often more convoluted so we used curvature, $\kappa$ (Fig. 5.13). Similarly to *C. occipitalis* moving on the surface, both animals passed alternating left and right bends from head to tail with relatively little variation in the amplitude.

We used PCA to find a low-dimensional representation of the sandfish kinematics from 27 trials collected using 6 animals. The first two PCs accounted for $\approx 92\%$ of the variance and were well-fit by sinusoids approximately $\pi/2$ out of phase ($0.56\pm0.02$ rads, Fig. 5.14).

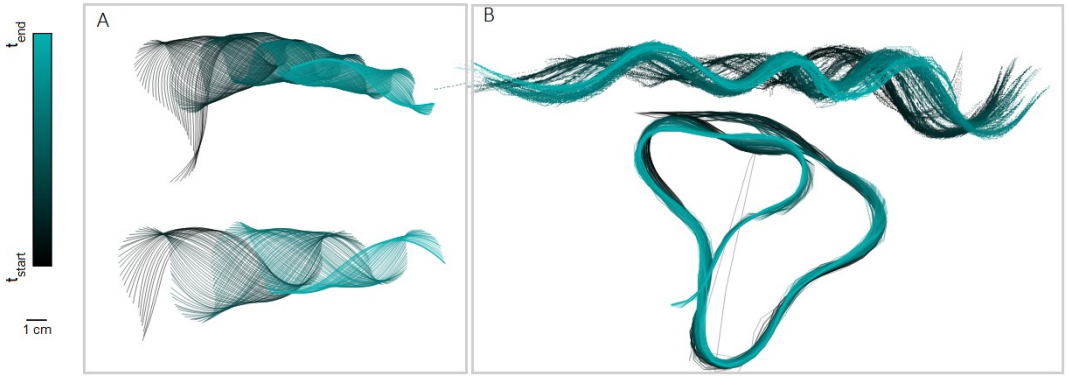


Figure 5.12: Example kinematics of *S. scincus* and *C. occipitalis* swimming subsurface. (*A*) Two sandfish trials. Color corresponds to time as indicated to the left. (*B*) Two snake trials.

The amplitudes associated with the first two PCs travel around a circle, indicating a traveling wave as was qualitatively observed (Fig. 5.14*B*).

PCA was not as illuminating for the snake as for the sandfish. In part because there was less data and in part because the number of waves on the body used by the animals in different trials was more variable (e.g. Fig. 5.12): PCA was effective in the sandfish because they all used about one wave one the body, so a sinusoid of the same wavenumber was present in all trials. We instead decided to make the ansatz that the shape could be described by sinusoidal curvature of the form

$$\kappa(s,t) = a_0 + a_1 \sin(\xi s) + a_2 \cos(\xi s)$$

, where $a_1, a_2$ and $a_3$ are amplitudes of the same units as $\kappa$ (inverse pixels, $\text{px}^{-1}$) and $\xi$ is the spatial frequency of the wave–by allowing $\xi$ to be a fit parameter this method was

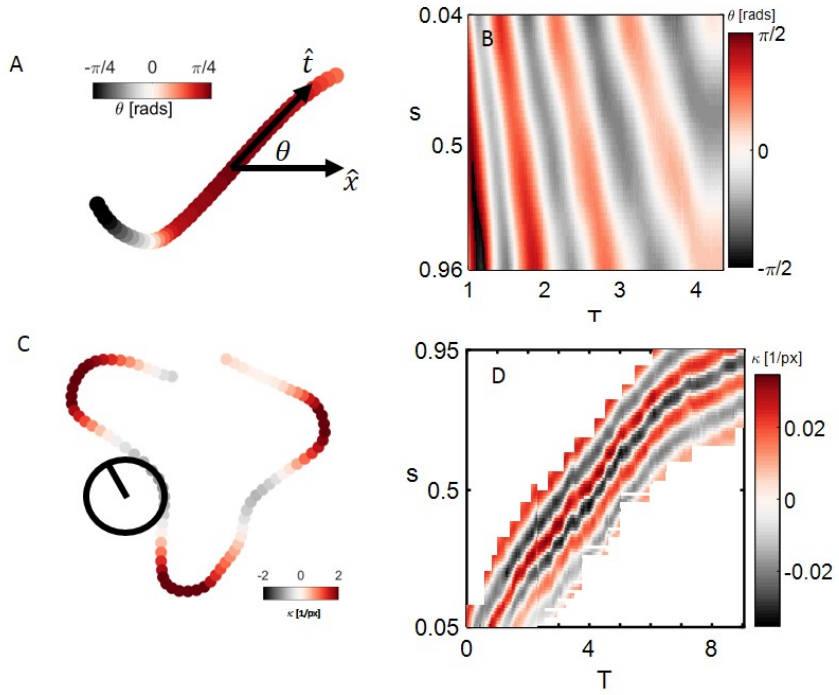


Figure 5.13: Animal-frame waveform measurements. (*A*) The sandfish tended to travel along a straight line using a shape which was clearly stereotyped. Therefore we measured the tangent angle, $\theta$, along the body. (*B*) Space-time plot of $\theta$ calculated from a single trial. $s$ is the arclength along the curve with $s = 0$ being the head and $s = 1$ being halfway between the vent and tail tip. Horizontal axis is time divided by the average undulation period. (*C*) Example *C. occipitalis* shape. Because the snake would commonly make such convoluted shapes we characterized the waveform using curvature, $\kappa = 1/r$, where r is the radius of the osculating circle as drawn. (*D*) Space-time plot of $\kappa$. Convention is as in *B* with the exception that $s = 1$ is the vent.

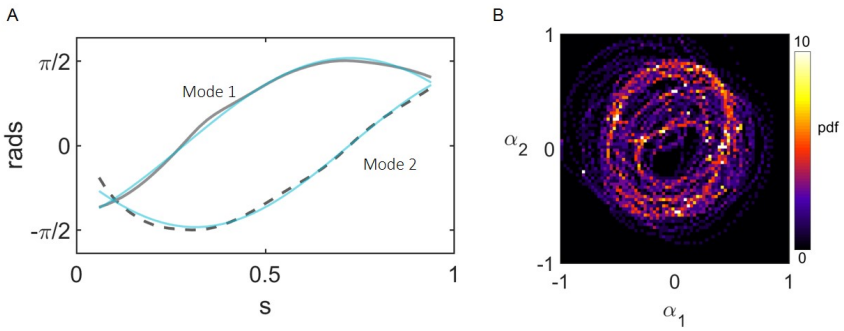


Figure 5.14: *S. scincus* PCs and amplitudes. (*A*) First two PCs, normalized to a maximum of $\pi/2$ rads. PCs are in gray and sine fits in teal. Fits to $asin(bs+c)$ were (95% confidence interval in parentheses) a=1.62(1.595, 1.644), b=0.50(0.49,0.51), c=-0.80(-0.83,-0.78) and a=1.52 (1.49, 1.55), b=0.54 (0.53, 0.55), c=-2.55 (-2.60,-2.50) for modes 1 and 2, respectively. (*B*) Probability density function of the amplitudes associated with the first two PCs.

better able to determine the applicability of a sinusoidal description to the kinematics. We used nonlinear least square fitting (MATLAB lsqnonlin) to fit each time step in all of the 15 snake trials using 3 animals.

Like the sandfish amplitudes, the snake amplitude values traced out a circle through time. We used the non-dimensional unit $\kappa_m \lambda_s$ to characterize the amplitude. The median percent error calculated from all trials and frames for this fit was $32\%$ (Fig. 5.15*B*). This indicates that over half of the kinematics are accurately captured by the sinusoidal curvature. It is not surprising that a two-function basis is not as accurate for *C. occipitalis* given its often tortuous shapes. However, we found it interesting that the majority of the shapes were described by this low-dimensional basis. This suggests that, despite the complex appearance of *C. occipitalis'* kinematics, it may result from relatively minor variation superimposed on the serpenoid curve. This provides evidence that there may be a similar template description for limbless locomotion as exists for limbed walking and running [61].

We further explored the accuracy of this fit using histograms of the mean and confidence intervals of the fit variable and comparing these to the experimentally measured values. We characterized the amplitude of the wave by finding the radial location of each point in the $a_1, a_2$ space, $R$. The values of $R$ and the upper and lower $95\%$ confidence bounds calculated from the fit were comparable to the $\kappa_m \lambda_s$ calculated programatically from the data (Fig. 5.15*C*). Similarly, the fit values for $\xi$ were in good agreement with those measured (Fig. 5.15*D*)

## 5.4 Lizard locomotion in heterogeneous granular matter

Locomotion strategies in heterogeneous granular environments (common substrates in deserts), are relatively unexplored. The zebra-tailed lizard (*C. draconoides*) is a useful model organism for such studies owing to its exceptional ability to navigate a variety of desert habitats at impressive speed (up to 50 body-lengths per second) using both quadrapedal and bidepal gaits. In laboratory experiments, we challenge the lizards to run across a field of boulders

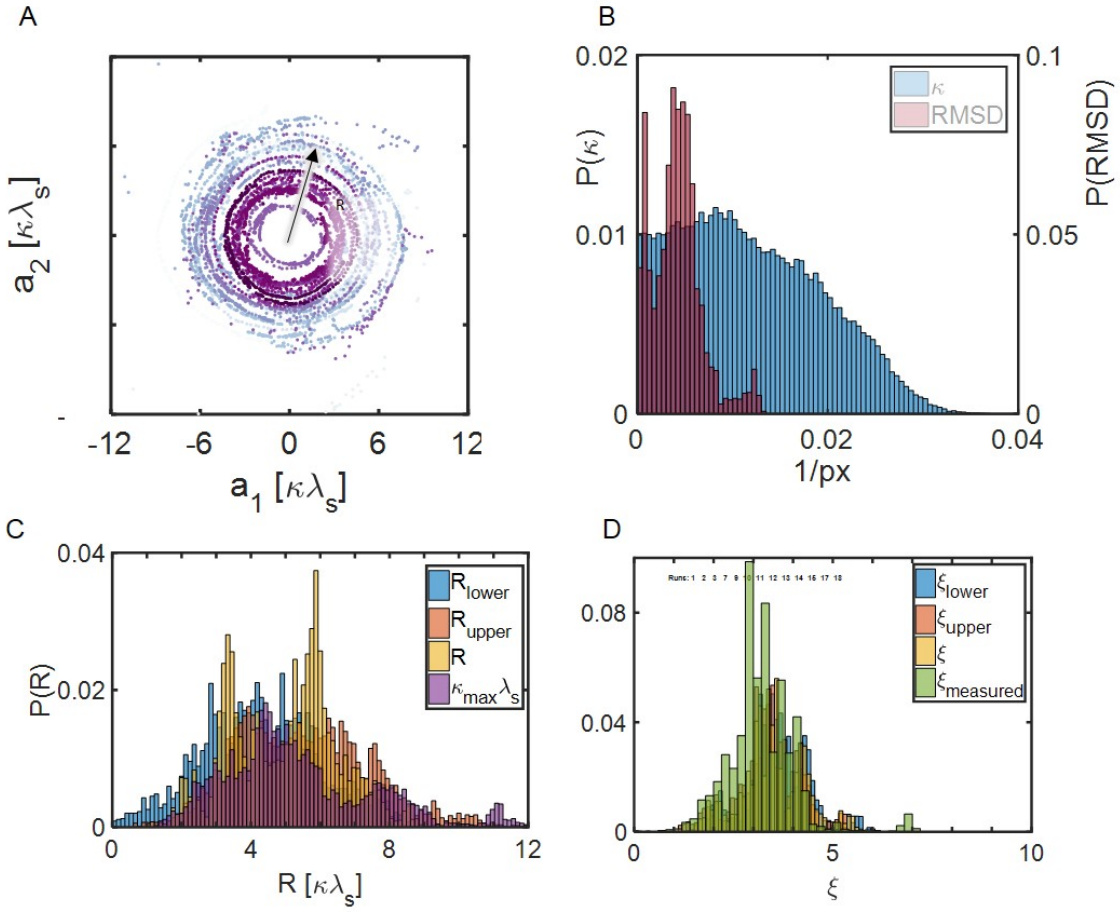


Figure 5.15: Sinusoidal fit to subsurface snake curvatures. (*A*) The amplitudes $a_1$ and $a_2$ from the fit, converted to dimensionless units of $\kappa_m \lambda_s$. Color indicates time progressing from light to dark. All data is included. The arrow indicates how $R$ was measured. (*B*) Probability density function of $\kappa$ in units of inverse pixels, $\text{px}^{-1}$ in blue. In red is the root mean square deviation of the fit to $\kappa$ as a function of arclength at each time step. (*C*) Probability density functions of the curvature amplitude calculated as the radius in $a_1, a_2$ space from the fit ($R$, yellow) and the upper and lower bounds from the 95% confidence intervals (blue and red). Purple curve is measured directly from the data. (*D*) pdf of $\xi$ as in *C*.

(2.54 cm diameter glass spheres or 3.8 cm 3D printed spheres) placed in a lattice pattern and embedded in a loosely packed granular medium of 0.3 mm diameter glass particles. Locomotion kinematics of the lizard are recorded using high speed cameras, with and without the scatterers. Preliminary data suggests that, unlike the typical quadrupedal locomotion using a diagonal gait, when scatterers are present the lizard tends to use a bipedal gait, with a raised center of mass (CoM). We propose that the kinematics of bipedal running, in conjunction with the highly compliant hind foot of the zebra-tailed lizard [155], are the keys to this lizard's successful locomotion in the presence of such obstacles.

### 5.4.1 Introduction

Robots can be used to great effect in many situations which are dangerous or impossible for humans. From bomb diffusion to extraterrestrial exploration, robots have been deployed with success. However, there are many environments which are still closed to robotic application due to inaccessibility to vehicles with wheels or tracks. The study of legged animals suggests that robust navigation through a great variety of complex and challenging terrain is possible, and that the use of legs in these situations may be the best choice. However, the complexity of organisms makes it prohibitively difficult to exactly copy every aspect of successful natural systems. It is rather better to search out the underlying principles of the organism which are most applicable to the problem at hand [61].

*Callisaurus draconoides*, the zebra-tailed lizard, is a useful model organism for study. This lizard is a desert generalist which successfully thrives in a variety of habitats containing multiple substrates [156, 157, 158]. In addition, *C. draconoides* is the fastest-running desert lizard among those of similar size, with a sprint speed of over 50 body lengths per second [159], and whose speed is not effected greatly by changes in the substrate [160, 158]. These lizards may employ both a quadrupedal trotting gait as well as a kinematically distinct bipedal gait [159] where the front limbs are held stationary off of the ground and the hind limbs alone are used.

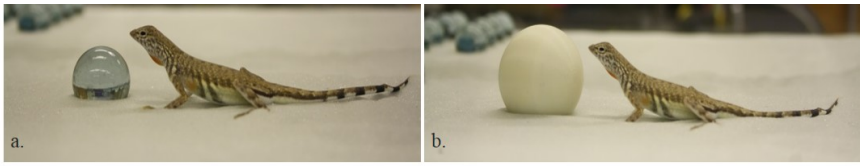


Figure 5.16: *C. draconoides* at rest next to obstacles used in the study. a) 2.54 cm diameter glass sphere and b) 3.81 cm printed plastic sphere.

### 5.4.2 *C. draconoides* in boulder fields

We challenged the zebra-tailed lizard (*Callisaurus draconoides*) running on a granular bed of slightly polydisperse, 0.3 mm diameter glass particles. Larger particles ( 2.54 cm diameter glass spheres or 3.8 cm 3D printed spheres) are placed on top of the bed. These are comparable to the size of the lizard (Fig. 5.16) such that interaction may force a deviation from the steady-state gait used when traversing homogeneous terrain. The obstacles were placed in a variety of configurations both at random and in regular lattice patterns of various spacing and row angles (Fig. 5.17). The locomotion kinematics of the lizard are recorded with and without the scatterers at 500 frames-per-second.

The ambient temperature was maintained at approximately 35 °C for all runs. The temporary enclosures where the lizards were held when data was not being taken were maintained between 31 °C and 38 °C. The lizards were observed successfully navigating the terrain (success defined as maintaining an approximately constant velocity) even when faced with many obstacles and/or large obstacles. We observed three broad categories of kinematics applied by the lizards:

Low CoM quadrupedal running. In this mode the lizard travels quadrupedally, with a diagonal gait and a sprawled limb posture. The CoM of the lizard is not significantly raised above the substrate. This method was the least successful. It often resulted in interactions between the body or upper limbs and the spheres. The spheres are heavy enough (20 g for the glass spheres, 18 g for the plastic) that the lizard's momentum (average mass 10 g, average speed on the order of 1 $ms^{-1}$ is not such that the boulders will significantly yield

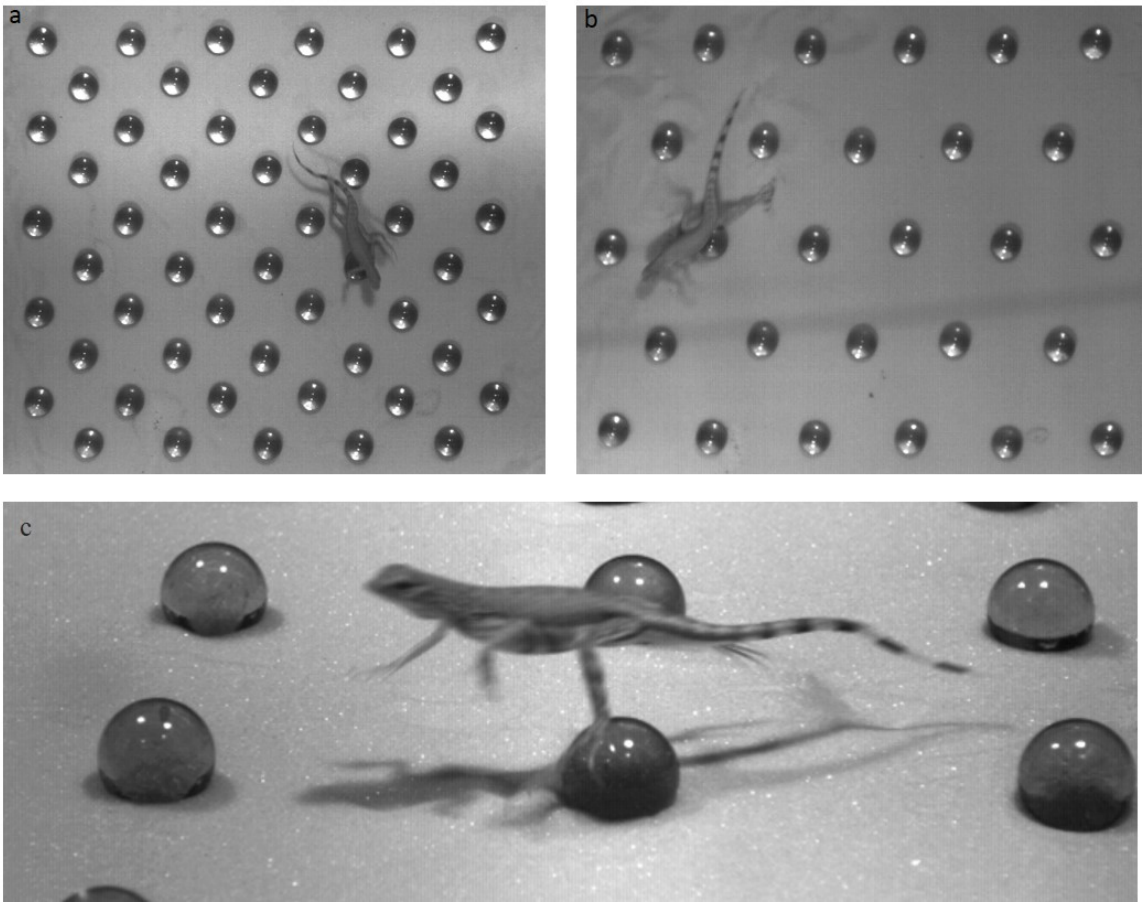


Figure 5.17: Examples of boulder fields. 2.54 cm glass spheres in a) 45° lattice and b) 60° lattice. c) Bipedally running lizard interacting with 2.54 cm glass sphere in a lattice.

to the animal. *C. draconoides* was observed clambering over the obstacle in the case of proximal impact, resulting in a loss of speed even to the point of stopping, or, for more distal impacts, the animal would experience roll in the body which was quickly corrected and often resulted in a change in heading.

High CoM quadrupedal running. The lizard employs a quadrupedal gait with the CoM raised above the substrate. Using this gait the body of the lizard was generally high enough to pass over the glass spheres. In this mode most interactions are between the feet or legs and the spheres.

Bipedal running. *C. draconoides* is also capable of travelling bipedally. This gait is kinematically distinct from quadrupedal running [159]. The forelimbs are held stationary and the torso is generally at some angle above the horizontal, resulting in the CoM being higher and further toward the pelvis as viewed in the frontal plane. This places the CoM above the smaller spheres, and increased stride length often resulted in fewer interactions. Callisaurus was able to negotiate more challenging heterogeneity when using the bipedal gait. Successful recovery from more severe perturbation was observed, with the body undergoing and subsequently recovering from more variety in the body variables of roll, pitch, and yaw than seen in either quadrupedal gait.

When running at speeds of approximately 1 $ms^{-1}$ ( 10 body lengths per second) or greater, the lizards were observed interacting with obstacles even when a clear path was present (Fig. 5.18). We hypothesize that as speed increases it is somehow advantageous for the animal's handling of heterogeneity to rely on feedforward preflexive systems and feedback based somatosensory neuromechanical control rather than careful pre-sensing of the environment with the external senses and subsequent path planning.

### 5.4.3 Discussion and future directions

The reasons behind the emergence of bipedalism in lizards are not fully understood [161, 162, 159]. Species with different morphologies exhibit kinematically different bipedal

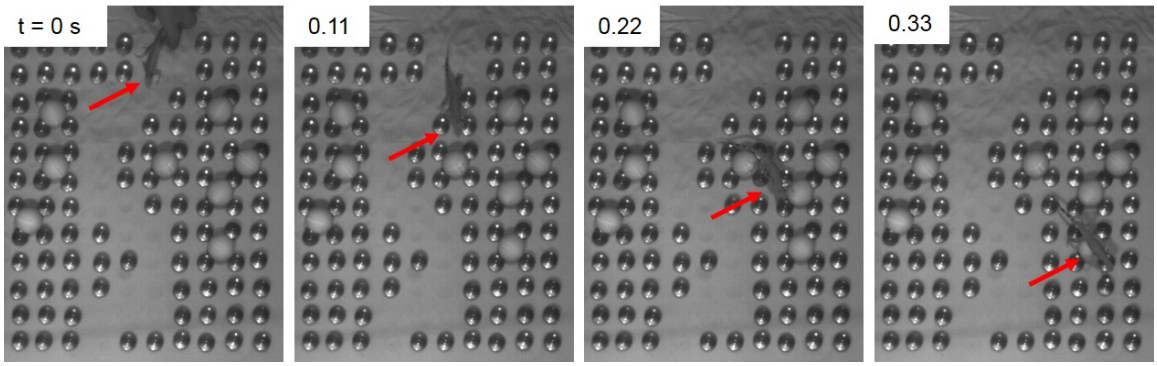


Figure 5.18: *C. draconoides* runs through a boulder field rather than clear path. Red arrow is pointing at the lizard.

gaits, suggesting that bipedality in lizards may have arisen separately in these different species [160]. While bipedalism has been suggested as an adaptation for increased speed [162], certain species exhibit no significant difference in speed between quadrupedal and bipedal running [159], implying that there may be another factor in the gaits persistence. We propose that it is a combination of bipedal gait kinematics and passive mechanical properties of the elongate foot which allow *C. draconoides* to successfully navigate heterogeneity when running at speeds of approximately 1 $ms^{-1}$ or greater.

Our preliminary work with *C. draconoides* captured the lizards travelling between 0.5 $ms^{-1}$ and 2.5 $ms^{-1}$, well below their maximum sprint speed ( 4 $ms^{-1}$ quadrupedally and over 5 $ms^{-1}$ bipedally [159]. Despite traveling well below speeds necessitating bipedal running, the lizards frequently employed the bipedal gait when in the presence of obstacles. Prior studies have shown the lizard *Sceloporus malachiticus* to employ the bipedal gait as a method to tackle obstacles [163]. Furthermore, the lizard *Aspidoscelis sexlineata* was studied negotiating obstacles, and it was found that when running bipedally it did not adjust stride length or kinematics upon approach to an obstacle [164]. [164] postulates that, as bipedalism does not widely confer a higher speed among a variety of lizard species, it may have persisted as a means of obstacle negotiation as the elevated CoM aids in tackling obstacles. The CoM must be raised above the obstacle prior to surmounting it [163] and the CoM of quadrupedally running lizards is comparatively lower.

Our observations of *C. draconoides* navigating both fields of obstacles and single boulders suggest that the lizard is most successful in terms of maintaining both speed and heading when using a bipedal gait. We hypothesize that bipedal running in *Callisaurus* has persisted as a method of disturbance rejection. That not only does the raised CoM allow the body to pass over higher obstacles, but also that the lizard targets a specific periodic oscillation of the CoM which by its nature acts to reject perturbation to the animal's heading and speed. This CoM oscillation will be a neurological control target which relies on proprioceptive feedback upon perturbation of the body and therefore does not demand pre-interaction sensing and path planning, allowing for successfully navigation of heterogeneity with less computational and sensing complexity.

We also hypothesize that the elongate foot plays a crucial role in disturbance rejection. When contacting the solid boulders, the tendons will store elastic energy such as previously studied in hard ground running. When the oscillating kinetic and potential energy system of the CoM is disrupted by interaction with an obstacle, which may be described by a potential, we propose that the great mobility of the appendage allows it to make up for any deficit or overage in CoM energy more quickly than the muscles in the limbs can correct the CoM energy by providing mechanical energy. This foot is a passive, feed-forward system which is able to act more quickly than responses which require neurological control.

This strategy is similar to that proposed for a cockroach running quickly through heterogeneous terrain in which kinetic energy facilitates motion across gaps and the mechanical properties of the legs permit stable running without neural inputs [32].

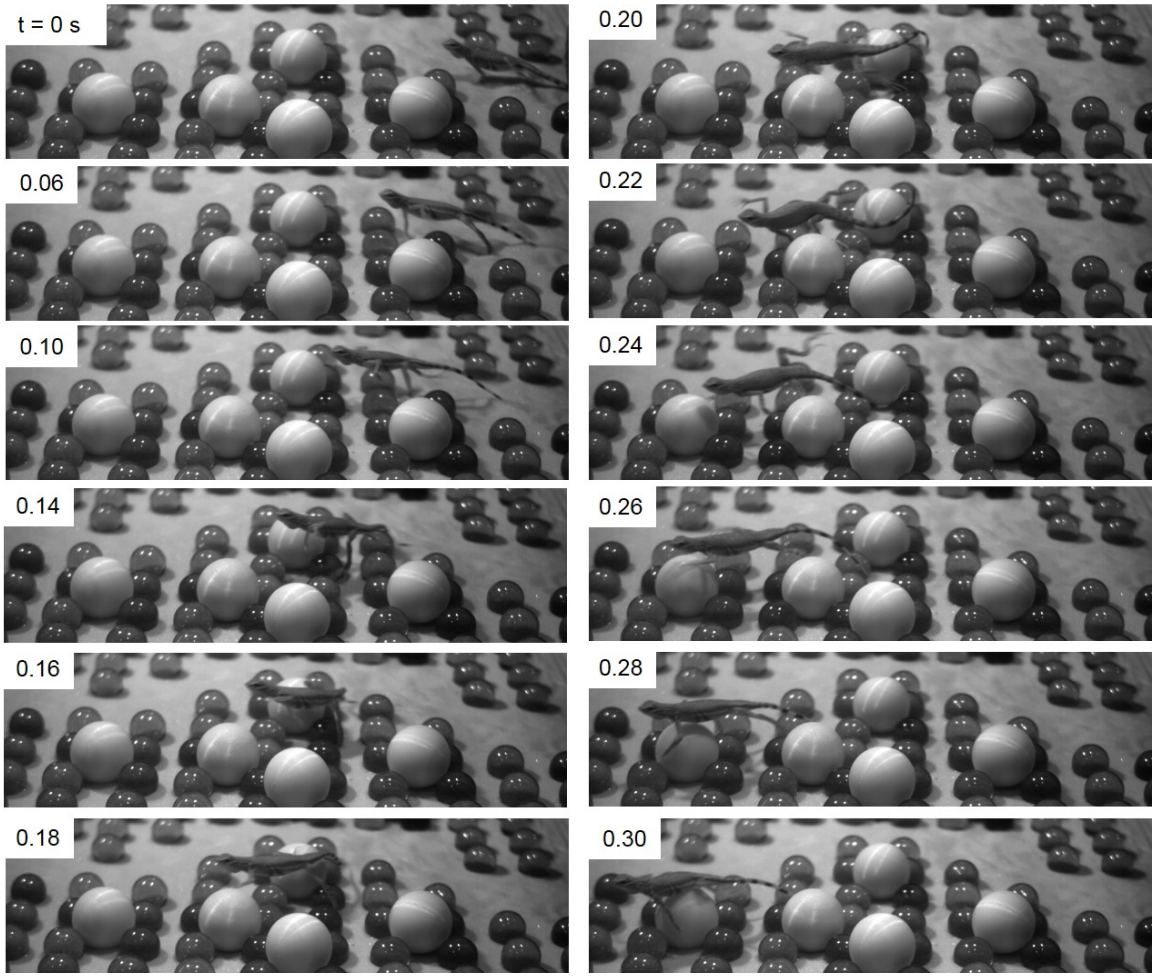


Figure 5.19: Negotiation of large bidisperse obstacles. The lizard is able to recover from large perturbations arising from both colliding with the boulders and foot slips off of the low-friction surface of the obstacles.

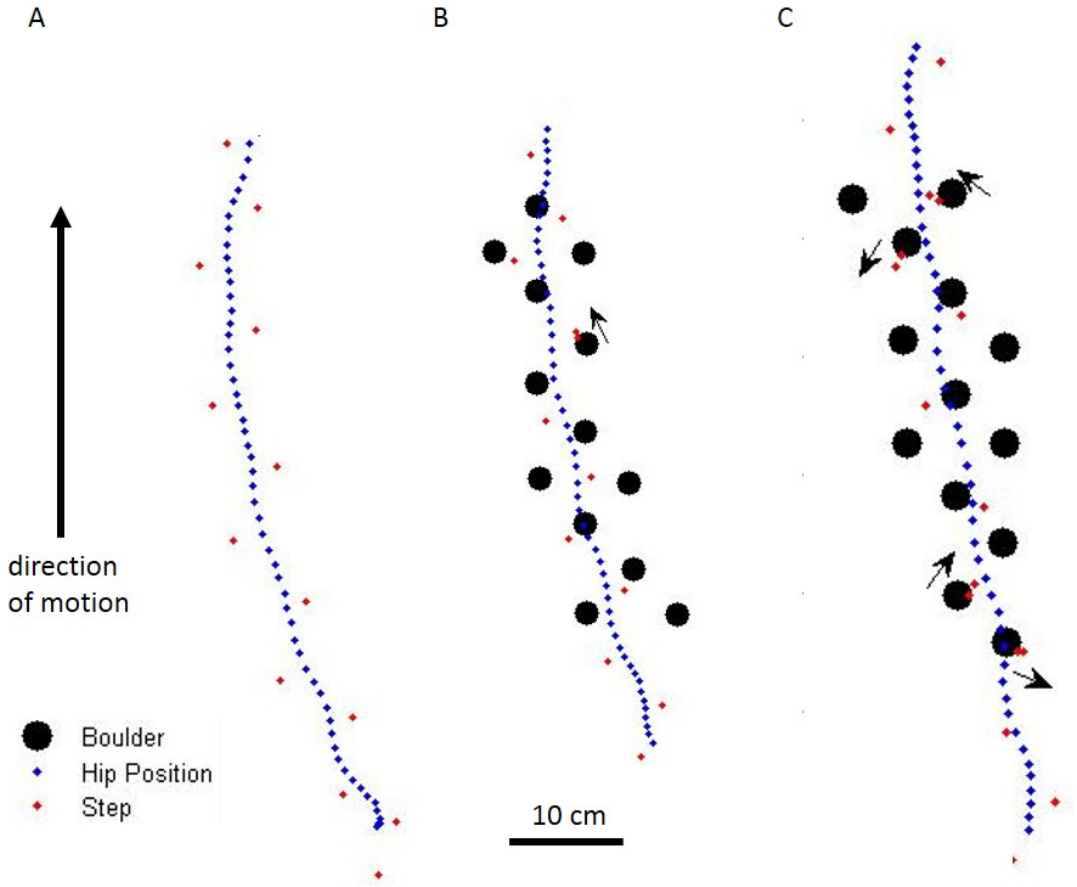


Figure 5.20: Tracked lizard kinematics. (*A*) High CoM, quadrupedal running without obstacles present. The blue dots are the position of the hit and the red dots the step location of the hind limbs. (*B*) High CoM quadrupedal running in a 45° square lattice of 2.54 cm diameter boulders. When an arrow is next to two red points it indicates a step which initially contacted a boulder and then slipped off of the low-friction surface in the direction of the arrow. (*C*) Bipedal running in the same lattice as in *B*

# CHAPTER 6
# CONCLUSIONS AND FUTURE WORK

## 6.1 Conclusions

Limbless locomotors must coordinate the interaction between their high degree-of-freedom trunk and the complex physics of the surrounding terrain in order to move effectively. These systems must both choose appropriate waveforms for the environment and subsequently control the internal deformations to execute the desired shape. In this dissertation I combined insights from a variety of fields to make several advances in understanding undulatory motion in terrestrial terrains.

Combined study of a desert-specialist snake, new surface granular drag measurements in granular resistive force theory, and a robophysical model revealed that while lateral undulation on the surface of granular matter is not sensitive to intrusion depth or movement speed, it is of paramount importance to choose the appropriate waveshape which avoids interaction with previously disturbed material. We probed the role of passive mechanics in contending with unexpected collisions by taking a scattering approach and observing the emergent kinematics of the desert-specialist as it transited a row of posts. Comparison with a computer model indicated that a controller which did not use neural feedback and relied on the passive flexibility of the body to solve constraints imposed by sparse obstacles in the surroundings could explain the mechanical diffraction pattern observed in the animal. The performance of the desert snake in 2D arrays placed in both a usable substrate (GM) and an un-usable one (whiteboard) suggested that the animal often adhered to the sand-swimming waveform, a strategy which was effective when the GM substrate was present, but could lead to degraded performance when it was necessary to use the rigid posts.

## 6.2 Future Work

### 6.2.1 Granular flow around a surface sand swimmer

The robophysical snake revealed the importance of managing the substrate interactions in deformable materials. If an inappropriate self-deformation pattern is used, interaction with previously disturbed material will degrade performance. There is a subtlety here, however, as the posterior portions of the body are following more or less the path traced out by those anterior and are therefore interacting with material disturbed by their head-ward neighbors. We observed that robot failure occurred when the low-curvature, thrust-producing portions of the wave on the anterior part of the waveform slid back into the tracks which were made by the low-curvature portions of the wave half a period prior. The relative role of different portions of the body in producing thrust is unknown, but EMG measurements in eels using lateral undulation terrestrially suggested that the anterior portions are responsible for the majority of force generation [10].

Particle image velocimetry (PIV) is a technique in which images taken of the system at different times are compared to estimate the velocity of features in the image. PIV measurement of the granular flow around both successful and unsuccessful robot waveforms could provide insight into both how flow differs around different body segments (for example, do anterior portions build up piles which the posterior portions utilize or are the piles dynamic throughout) and how interaction between the flow at different parts of the body changes between successful and unsuccessful shapes.

### 6.2.2 Development of a passive compliant snake robot

We presented evidence that passive compliance allowed a snake to transit sparse obstacles without having to change the neural control of the waveform. This hypothesis was challenging to test in a robophysical model because traditionally snake-like robots are actuated by a single motor at each joint which is commanded to move left/right to enact left/right

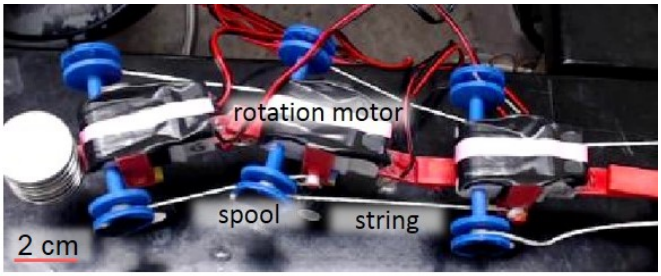


Figure 6.1: Cord-driven robot. Each joint has two motors and spools. Joints are connected by string. The motor can spool the string in, creating tension and decreasing joint angle in that direction, or unspool the string, making it relaxed but cannot change the joint angle. Designed and built by Georgia Tech undergraduates Siddharth Salunkhe (ME) and Richard Newsome (Physics).

bends. This is unlike the unilateral muscle activation in snakes, where different actuators are responsible for bending each way. We have designed a prototype robot which uses spooled string to actuate the joints (Fig. 6.1). The string can only support tension such that a motor/spool/string mechanism can increase joint angle towards the side on which it is situated but cannot actuate the joint in the opposite direction.

Using this robot we can test hypotheses about control and passive compliance in snakes which uses true mechanical passivity rather than attempting to design control which mimics unilateral activation.

### 6.2.3 Control strategies for heterogeneous terrain

In this work we studied the movement of two snake species moving through multi-modal terrain and hypothesized that the performance dependence on both substrate type and lattice spacing was a result of the organisms control strategy. However, we have not yet tested this hypothesis. Understanding what information the animals are gathering from the environment and in turn how they integrate this into their control will both further our knowledge about snake neuromechanics but also advance the capability of robots. Future analysis could use analyses proposed by [165] and [166] as well as ideas from the literature on control of snake-like robots (e.g. [167, 168, 70])

We use two species in this work, the desert snake *Chionactis occipitalis* which is not a constrictor and *Panterophis guttatus* which is. Previous research hypothesized that snakes which move quickly using long body bends have fewer vertebrae and therefore longer muscle segments than the constrictors which specialize in strong, low curvature bends [57]. It may be illuminating to expand on preliminary work we performed with a third species, the garter snake *Thamnophis thamnophis* which is a generalist like *P. guttatus* and a non-constrictor like *C. occipitlias*.

### 6.2.4 Physics of anistropy independence

We report in this dissertation that the ratio of stresses acting perpendicular and parallel to a partially intruded plate moving parallel to the surface of granular matter is independent of depth, speed, and material type. We do not, however, understand the physics of the flow which results in the preservation of the curve across conditions. Future work will use the data collected for the studies presented here to ferret out the underlying mechanism. Recent advances in the modeling of granular materials using plasticity theory [169] and added-mass corrections to RFT [170] will be used in this investigation.

# Appendices

# APPENDIX A

## A.1 Investigation of tracking noise and analysis methods

Surface snake data was tracked using MATLAB. The details of the tracking algorithm may be found in Sharpe 2015. To determine the signal to noise introduced in tracking we created artificial data. Each frame had thirty black points with an area of 36 pixels, comparable to the roughly 45 pixel area of a black band on the snake in the collected trial videos. These points were designed to follow a serpenoid curve such as that used by the snake ($\xi$=2,$\kappa_m\lambda_s$=5) with similar slip. We then tracked this artificial data using the same program. We found that the difference between the known and tracked points was small (Fig. A.1), and appeared to arise from the tracked position lagging behind the known position. Comparing the known and tracked points we estimated a signal-to-noise (SNR) of 50 to 1 introduced by tracking.

We next endeavored to characterize the relationship between splining methods, averaging distances, and error for both $\kappa$ and $\theta$ measurements. Again, artificial data was created which simulated the points measured from experiment-30 points on a serpenoid curve of $\xi$=2,$\kappa_m\lambda_s$=5. This data was then splined using each of two splining methods, cubic spline interpolation (CSI) and ten basis Bezier-splines (B-spline) using functions adapted from code developed by Miguel Moises Serrano. The splines were calculated both from the data as it was defined as well as the points with noise added using the MATLAB awgn function to add white Gaussian noise to each point at a SNR of 50. We then using different increments in the calculation of both $\kappa$ and $\theta$ to explore how this affects the accuracy of the measurement. $\kappa$ and $\theta$ were both calculated using different increments and splining methods. The error was calculated relative to the value of $\kappa$ and $\theta$ known analytically from

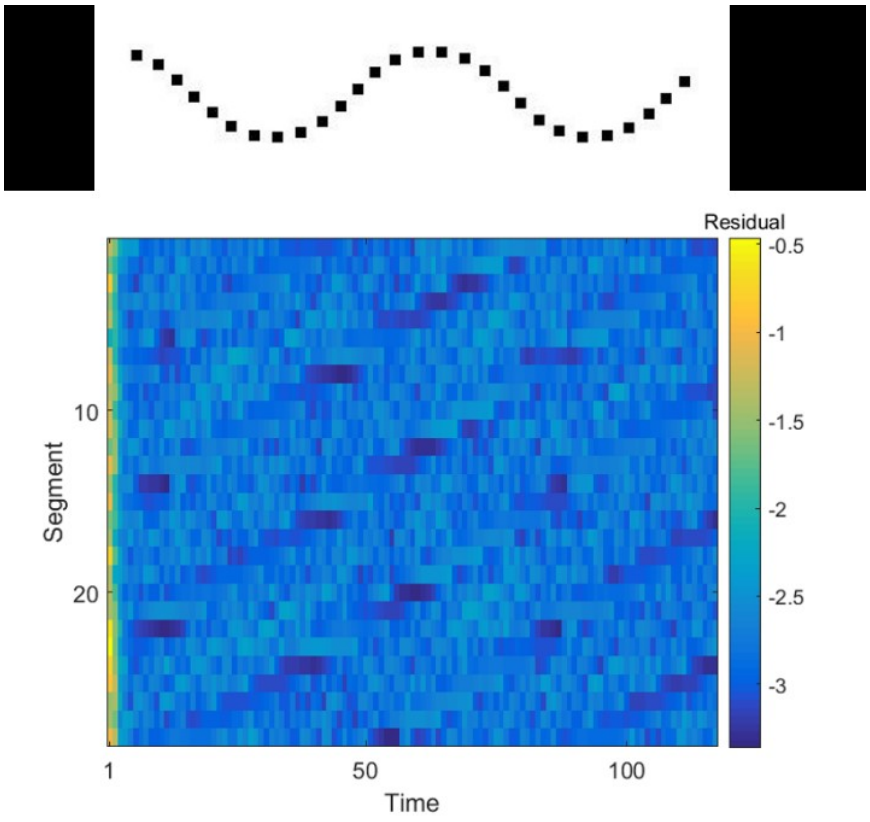


Figure A.1: Artificial data tracking. Top: example of a frame of artificial data. Bottom: Difference between known and measured segment positions.

the serpenoid function. The error at each segment and time step was found and the average over all values plotted in Figure MB.

We found that for noise-less data a small increment was the most accurate. However, when noise is added small increments are sensitive to the noise, especially in the calculation of $\kappa$. The B-spline method yielded better results at small increments for both measures. We believe this is attributable to discontinuities in the second derivative of the CSI (Fig. A.2,*top*). All measurements became equally inaccurate at large increments as the averaging begins to "wash out" the signal of interest. We find that in calculating $\theta$, small increments of three to five are preferable. At this low range the relative error is not highly sensitive to the increment, and little of the data is "lost" in averaging. We found $\kappa$ had a basin around 7-8 increments where the relative error was minimized (Fig. A.2,*bottom*).

## A.2 Principal component analysis artifact

When searching for shape basis functions for the Shovel-nosed snake moving subsurface we initially used principal component analysis (PCA) as was used for *C. occipitalis* on the surface and the sandfish subsurface. We decided to use the sinusoidal ansatz procedure instead for several reasons, one of which being the artifact introduced by the snakes not being entirely in the view of the camera, leading to an envelope on the curvature eigenvectors (Fig. A.3).

We verified that this was the result of the incomplete data sets using artificial data. First we performed PCA on a binary matrix (Fig. A.4*A*). Such a matrix leads to sinusoidal PCs as the band of ones is creating a square wave such that the lowest-order modes are single wavenumber sinusoids(Fig. A.4*D*). We verified this was the cause of the envelope using artificial sinusoidal curvature data (Fig. A.4*F*) and superimposing a traveling band (Fig. A.4*G*).

In the future, seeing as PCA is a time-integrating function, data could be shifted such that the missing data is removed entirely.

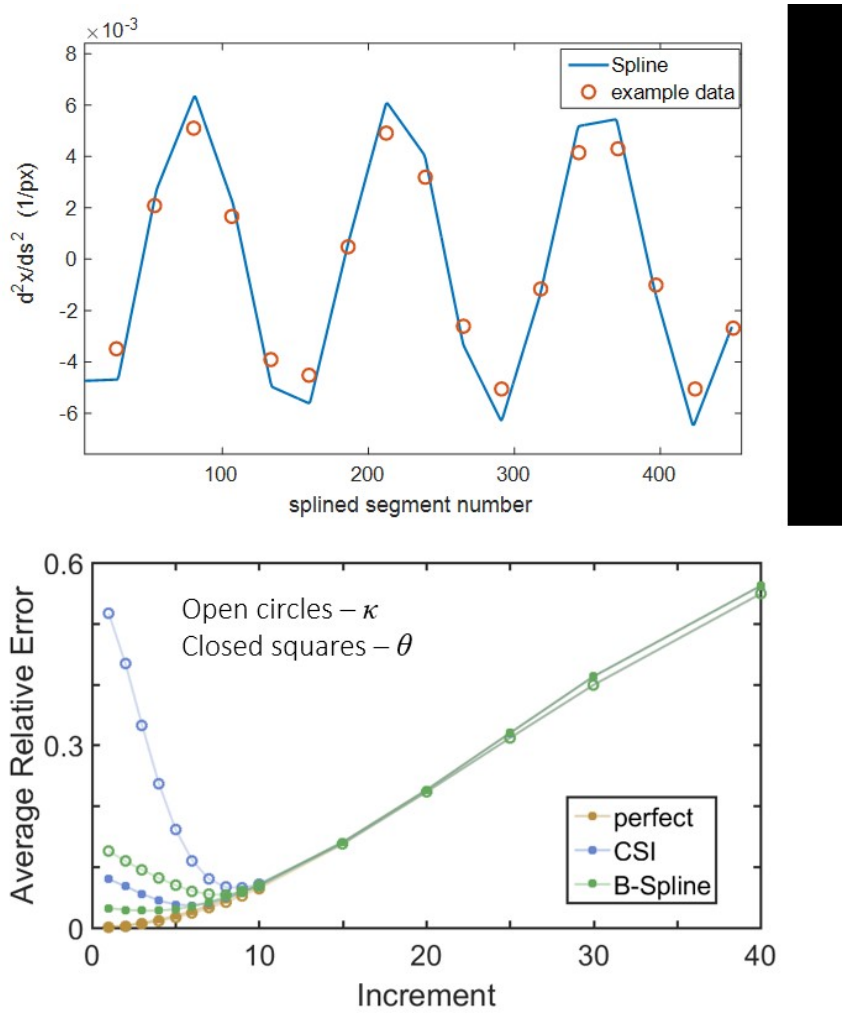


Figure A.2: Relation between measurement error and analysis choices. Calculated from artificial data with a SNR of 50. (*top*) Discontinuity in the second derivative of a cubic-spline interpolant. Bottom: Average relative error as it relates to the increment used in calculating both $\kappa$ and $\theta$. The colors relate to the difference between "perfect" data determined analytically as a serpenoid curve and the two splining methods applied to serpenoid data with white Gaussian noise at a SNR of 50.

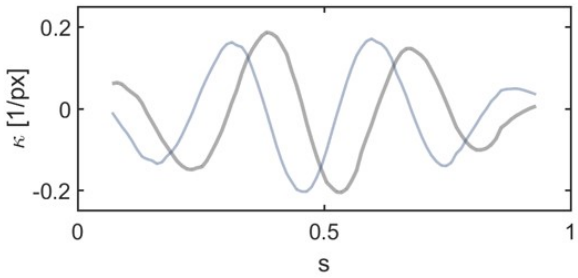


Figure A.3: Subsurface snake modes from PCA. First two modes from 13 trials of *C. occipitalis* moving buried within 270±40 $\mu$m glass particles.

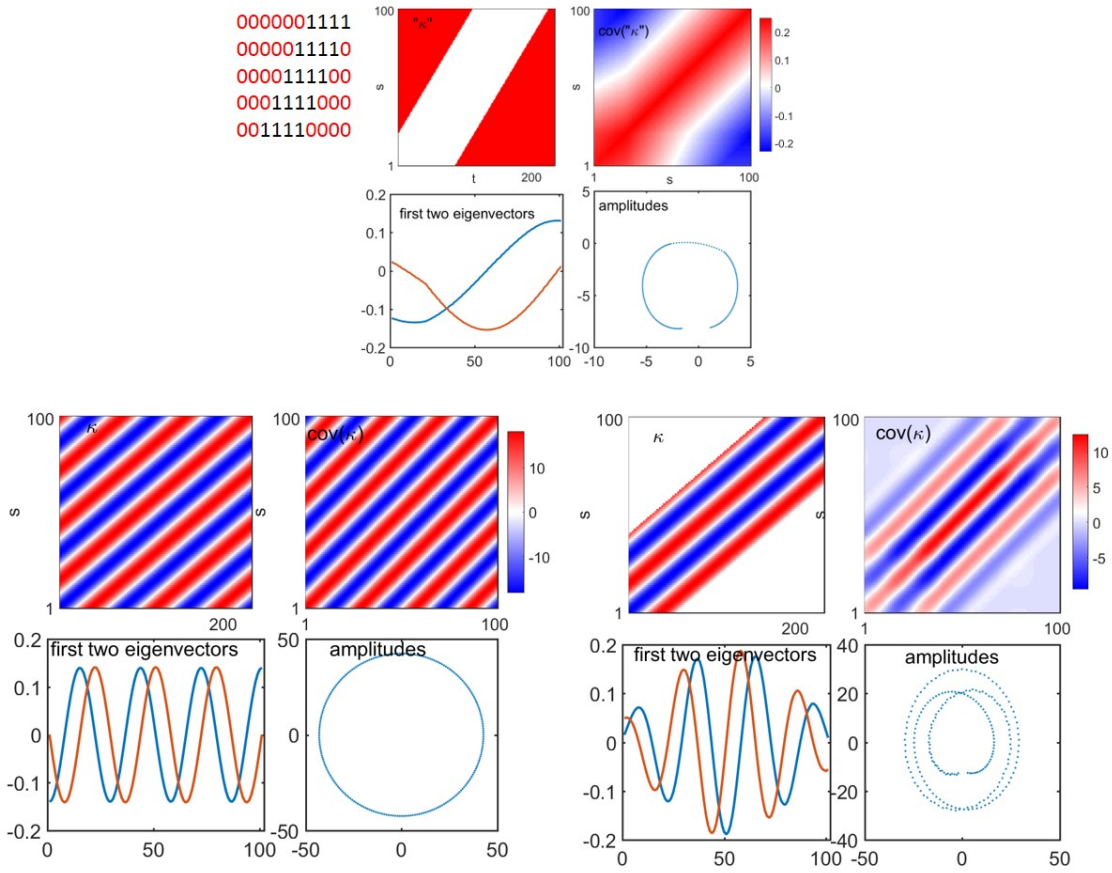


Figure A.4: Artifact introduced to PCA from bands of data. (*A*) Created a matrix of zeros with a traveling band of ones. (*B*) Matrix of ones and zeros illustrated as a heatmap. This is our artificial curvature $\kappa$. (*C*) Covariance matrix of *A*. (*D*) First two eigenvectors (principal components) from a PCA of the matrix illustrated in *C*. (*E*) Amplitudes associated with the first two modes. (*F*) Four plots are the same as *B* through *E*. Artificial data calculated for a serpenoid curve of the average snake subsurface values ($\kappa_m \lambda_s$=6, $\xi$ = 3.5). (*G*) Envelope on the eigenvectors resulting from curvature measurements which pass in and out of the frame.

## A.3 Force-Sensitive Posts

The pegs were constructed using 1.6 cm x 1.6 cm square Al rods (McMaster). A strain gauge (Omega KFH-6-120-C1-11L1M2R) was bonded using Gorilla Super Glue to each of the four faces of the rod with the bottom of the gauge 7 mm from the base and the gauge centered on the face and parallel to the long axis (Fig. A.5textitA,B,C). Opposing pairs of gauges were wired in a half bridge configuration with an INA125 amplifier chip (Burr-Brown Corp. USA) with a gain of 6000. Each half bridge was used to measure the force on that axis of the peg such that forces applied in both x and z (with respect to the coordinate system used throughout) to the pegs were resolved. Each bridge leg was 220 Ohms and a trimmer (Bourns 3296) was included in series with one of the legs and used initially to balance the bridge. Circuits were placed in a small conducting tin (Altoids Smalls) for shielding (Fig. A.5*D*). The output of the amplifier chips was connected to the differential measurement ports on a DAQ (NI USB 6210). A custom Labview (National Instruments, 2015) code collected and saved the signals from the DAQ at 1000 Hz. An IR LED was placed in the view of the cameras and the voltage over the circuit read by the DAQ. This signal was activated by closing the circuit by hand at least once per trial and used to synchronize the kinematic and force data.

The peg plates were bolted to a length of 3.8-cm-wide t-slot aluminum (80-20) which ran parallel to the peg row and between the two 1.2 m square platforms and the two 1.2 x 1.8 m platforms (Fig. A.5*E*). The spacing between the pegs was changed by changing the lateral position of the Al plates on the t-slot. The mats were cut to admit the pegs such that the mats would not contact the pegs.

The pegs were bolted to rectangular Al plates with a square recess to ensure proper alignment (Fig. N*C,E*). A 3D printed sleeve was designed to slide over the solid Aluminum square rod (Fig. N*A*). A 4.5 cm outer diameter (3.2 cm inner diameter) polycarbonate cylinder fit snugly onto the top of the sleeve (Fig. N*B*). This cylinder could not rotate and was

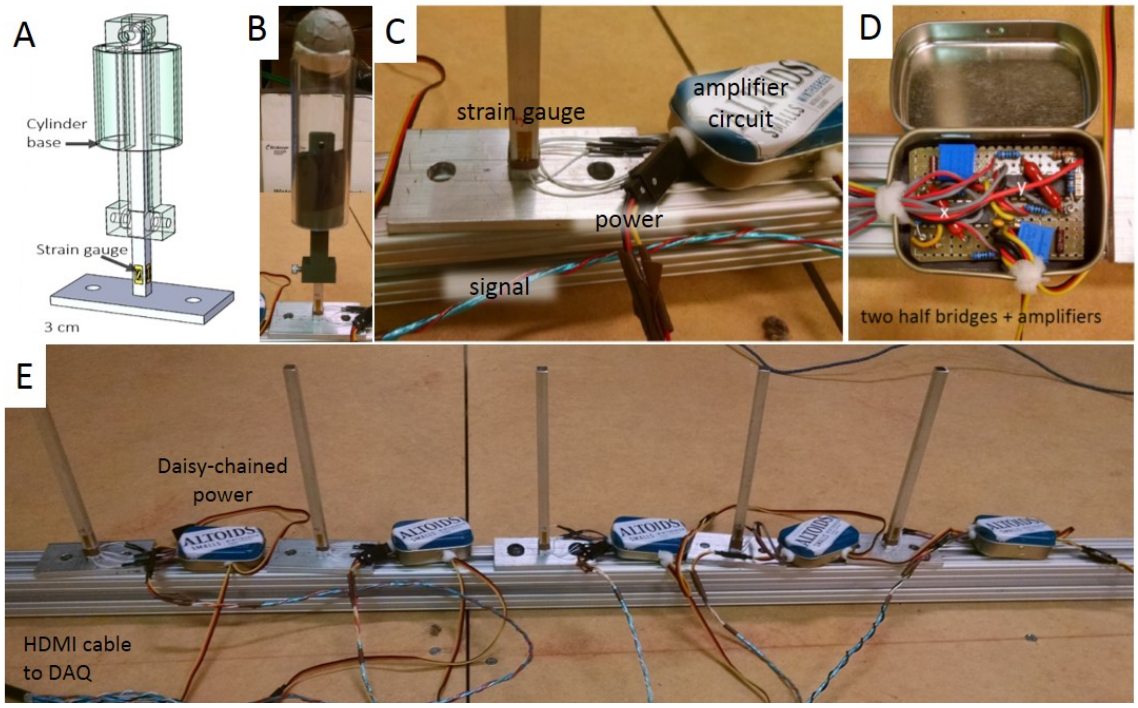


Figure A.5: Force sensitive post design (*A*) Schematic of post design. Strain gauges are bonded to the Aluminum rod. A 3D printed plastic sleeve to support the smooth plastic tube which is in contact with the robot is clamped on. (*B*) Assembled post. Note the bottom part of the assembly is below the mats the robot moves on. The silver sphere on top of the post is covered in IR tape and tracked by the Optitrack system. (*C*) Close up of strain gauge and circuit. (*D*) Amplifier circuit. INA125 (Texas Instruments) used in a half Wheatstone bridge configuration. Each axis has a separate circuit. Blue trimmer potentiometers are used to initially balance the circuit and may be used to balance in the case that the circuit experiences an event which unbalances it. (*E*) Five posts were bolted to a piece of 80-20 which ran underneath the robot arena. The power was provided by an external power supply and daisy chained between the circuits. Connections were designed so that each post could stand alone or be combined in any order. Signal was sent through an HDMI cable which provided shielding to a DAQ.

the surface contacted by the sides of the snake robot. The bottom of the plastic sleeve was 3 cm above the Al plate and held at this height by set screws. The polycarbonate cylinder started 3.5 cm above the mat such that the sides of the plastic motor brackets would touch the polycarbonate cylinder while the wheels would pass freely beneath the cylinder.

To characterize the force response of the pegs and determine the voltage to force conversion we performed systematic tests using known masses hanging under gravity. The peg brackets were mounted to a section of 80-20 which was clamped firmly to a table so that the Al rod extended horizontally from the table top (Fig. A.6*A*). The signal would drift for twenty to forty minutes after power was initially supplied, therefore we would let the device run for at least an hour before taking measurements during characterization as well as robot trials (Fig. A.7*A*). The frequency of noise in the signal was approximately an order of magnitude less than the undulation frequency of the robot ((Fig. A.7*B*)) and cross-talk was negligible (Fig. A.8).

A wire was used to hang a container from the bottom of the cylindrical section (Fig. A.6*A*). For each $F_{applied}$ the relevant masses were gently placed into the hanging container and the measurement was taken once all movement of the container ceased. After the measurement all masses were removed from the container before applying the next load.

I verified that voltage varied linearly with the height of the wire above the base (Fig. A.6*B*), such that using the average value of robot contact is equal to integrating over the total area. Therefore, to calibrate the posts measurements were taken at a distance above the base of 1.5 cm, the average height of robot contact.

$F_{applied}$ was measured at eight values from 0.001 N to 11.890 N for at least two perpendicular axes (e.g. +x and +z). The remaining two axes were tested for at least four values from 0.001 N to 9.908 N. At least three trials were taken for each $F_{applied}$, and for a few values seven trials were taken to verify repeatability. Results are shown in (Fig. A.6*C*). for all pegs. All trials on all axes are included in this plot. We find a conversion of 0.13±0.01 volts per Newton.

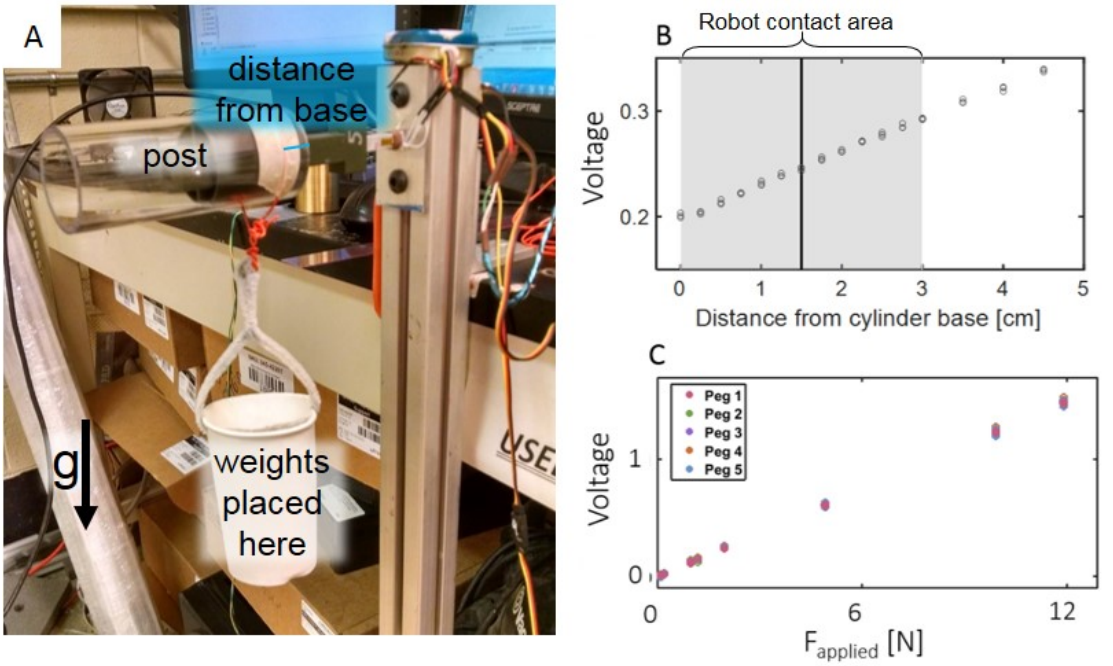


Figure A.6: Measure the conversion from Voltage to Newtons of the posts. (*A*) Setup used to measure forces. the post was affixed so that it was perpendicular to gravity. (*B*) Voltage as a function of the distance between the base of the cylinder and the supporting wire location. The gray area represents where the robot segments are in contact. The black vertical line is the average value of the height of contact of the robot. (*C*) Voltage measured as a function of $F_{applied}$. Masses of known weight were placed in the cup in *A* and the voltage recorded once it reached a steady state. All posts are plotted denoted by color as indicated. The posts were nearly identical such that the points overlap. The slope of the linear regression was of 0.13±0.01 V/N.

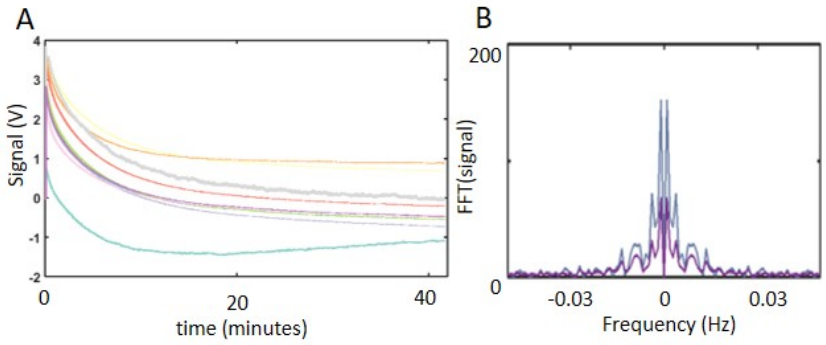


Figure A.7: Signal drift and noise. (*A*) Power was supplied to the posts at time zero and recorded continuously at 60 Hz. (*B*) Example FFT of two signals taken at 10 kHz. The robot undulation frequency is $\approx 0.3$ Hz.

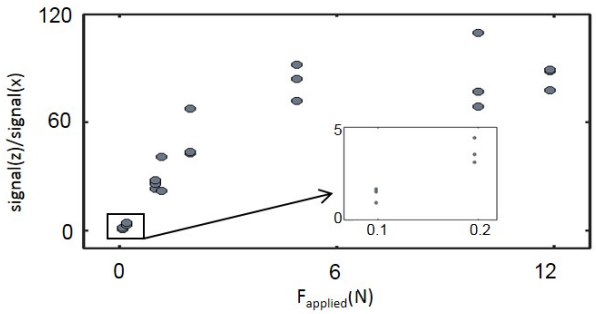


Figure A.8: Cross-talk between the axes is negligible at the force magnitudes of interest ($O(1\ N)$). Signal measured on the z axis divided by that measured simultaneously on the x axis. Inset is the result at 0.1 and 0.2 N.

## A.4 Miscellaneous figures

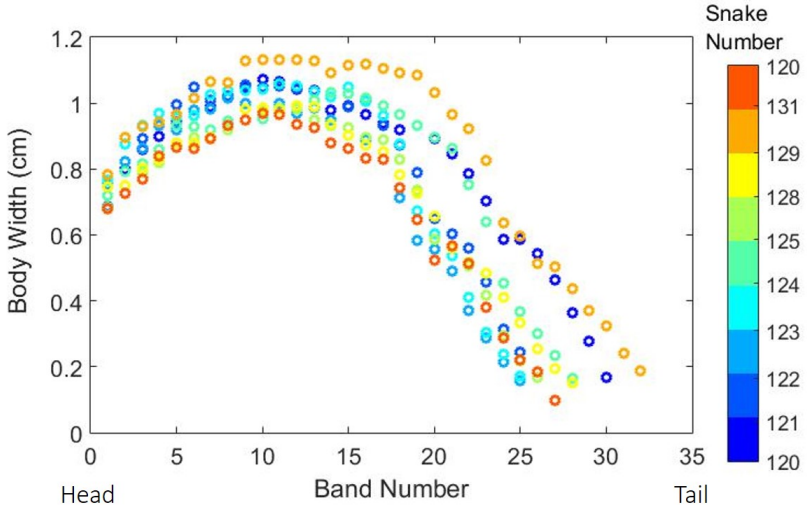


Figure A.9: Snake width at each black band. Measured from photos taken of each individual.

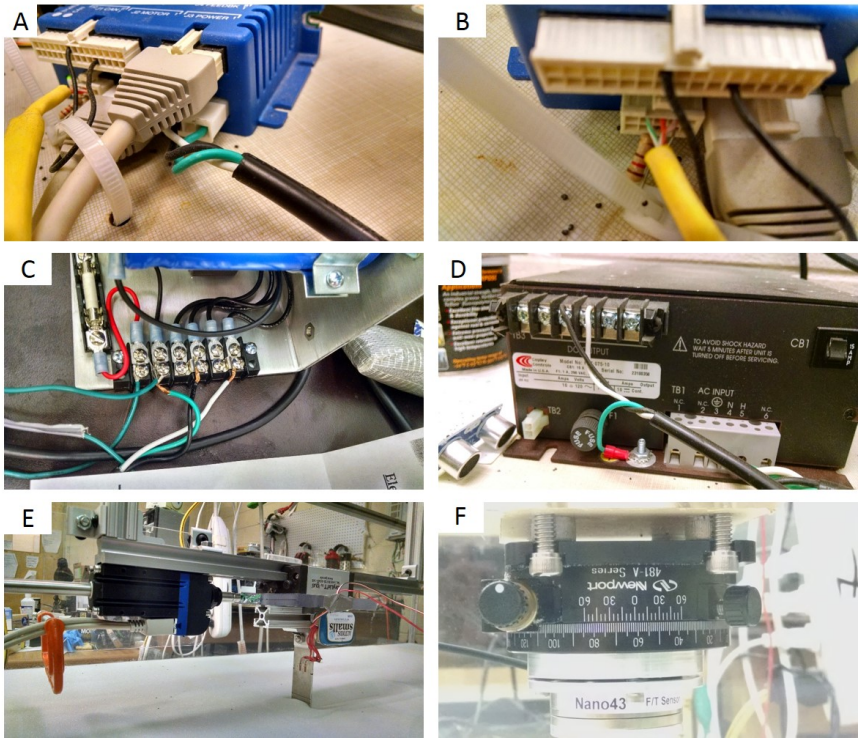


Figure A.10: Setup of Copley linear actuator for granular drag experiments. (*A,B*) Image of connections to the Copley motor controller. (*C*) Connections from the power supply to the controller. (*D*) Power input to power supply. Supplied by a three prong wall outlet. (*E*) Drag setup. Custom designed and machined connectors made out of acrylic to connect Copley motor to the Igus linear bearing and the Newport rotation stage to the linear bearing. (*F*) Closeup of rotation stage and ATI Nano43 force-torque transducer.

## REFERENCES


[1] S. Hirose, *Biologically inspired robots: snake-like locomotors and manipulators*. Oxford University Press Oxford, 1993, vol. 1093.

[2] H. Schulenburg and M.-A. Félix, "The natural biotic environment of *Caenorhabditis elegans*," *Genetics*, vol. 206, no. 1, pp. 55–86, 2017.

[3] C. Fang-Yen, M. Wyart, J. Xie, R. Kawai, T. Kodger, S. Chen, Q. Wen, and A. D. Samuel, "Biomechanical analysis of gait adaptation in the nematode *Caenorhabditis elegans*," *Proceedings of the National Academy of Sciences*, vol. 107, no. 47, pp. 20 323–20 328, 2010.

[4] J.-S. Park, D. Kim, J. H. Shin, and D. A. Weitz, "Efficient nematode swimming in a shear thinning colloidal suspension," *Soft Matter*, vol. 12, no. 6, pp. 1892–1897, 2016.

[5] T. Majmudar, E. E. Keaveny, J. Zhang, and M. J. Shelley, "Experiments and theory of undulatory locomotion in a simple structured medium," *J. Royal Soc. Interface*, rsif20110856, 2012.

[6] S. Park, H. Hwang, S.-W. Nam, F. Martinez, R. H. Austin, and W. S. Ryu, "Enhanced caenorhabditis elegans locomotion in a structured microfluidic environment," *PloS one*, vol. 3, no. 6, e2550, 2008.

[7] S. R. Lockery, K. J. Lawton, J. C. Doll, S. Faumont, S. M. Coulthard, T. R. Thiele, N. Chronis, K. E. McCormick, M. B. Goodman, and B. L. Pruitt, "Artificial dirt: Microfluidic substrates for nematode neurobiology and behavior," *J. Neurophysiol.*, vol. 99, no. 6, pp. 3136–3143, 2008.

[8] J. Tomie, D. Cairns, and S. Courtenay, "How american eels *Anguilla rostrata* construct and respire in burrows," *Aquatic Biology*, vol. 19, no. 3, pp. 287–296, 2013.

[9] J Aoyama, A Shinoda, S Sasai, M. Miller, and K Tsukamoto, "First observations of the burrows of *Anguilla japonica*," *Journal of Fish Biology*, vol. 67, no. 6, pp. 1534–1543, 2005.

[10] G. B. Gillis, "Environmental effects on undulatory locomotion in the american eel *Anguilla rostrata*: Kinematics in water and on land," *J. Exp. Biol.*, vol. 201, no. 7, pp. 949–961, 1998.

[11] B. C. Jayne, "Swimming in constricting (*Elaphe g. guttata*) and nonconstricting (*Nerodia fasciata pictiventris*) colubrid snakes," *Copeia*, pp. 195–208, 1985.

[12] ——, "Muscular mechanisms of snake locomotion: An electromyographic study of the sidewinding and concertina modes of *Crotalus cerastes*, *Nerodia fasciata* and *Elaphe obsoleta*," *J. Exp. Biol.*, vol. 140, no. 1, pp. 1–33, 1988.

[13] S. S. Sharpe, S. A. Koehler, R. M. Kuckuk, M. Serrano, P. A. Vela, J. Mendelson, and D. I. Goldman, "Locomotor benefits of being a slender and slick sand swimmer," *J. Exp. Biol.*, vol. 218, no. 3, pp. 440–450, 2015.

[14] L. M. Klauber, "The worm snakes of the genus *Leptotyphlops* in the united states and northern mexico," *Trans. San Diego Soc. Nat. Hist.*, vol. 9, no. 18, pp. 87–162, 1940.

[15] H. C. Astley and B. C. Jayne, "Effects of perch diameter and incline on the kinematics, performance and modes of arboreal locomotion of corn snakes (*Elaphe guttata*)," *J. Exp. Biol.*, vol. 210, no. 21, pp. 3862–3872, 2007.

[16] J. J. Socha, "Kinematics: Gliding flight in the paradise tree snake," *Nature*, vol. 418, no. 6898, p. 603, 2002.

[17] W. Mosauer, "On the locomotion of snakes," *Science*, vol. 76, no. 1982, pp. 583–585, 1932.

[18] J. Gray, "The mechanism of locomotion in snakes," *J. Exp. Biol.*, vol. 23, no. 2, pp. 101–120, 1946.

[19] J Gray and H. W. Lissmann, "The kinetics of locomotion of the grass-snake," *J. Exp. Biol.*, vol. 26, no. 4, pp. 354–367, 1950.

[20] B. C. Jayne, "Kinematics of terrestrial snake locomotion," *Copeia*, pp. 915–927, 1986.

[21] K. Kelley, S. Arnold, and J Gladstone, "The effects of substrate and vertebral number on locomotion in the garter snake thamnophis elegans," *Functional Ecology*, vol. 11, no. 2, pp. 189–198, 1997.

[22] R. R. Murphy, S. Tadokoro, D. Nardi, A. Jacoff, P. Fiorini, H. Choset, and A Erkmen, "Springer handbook of robotics," *ch. Search and rescue robotics*, pp. 1151–1173, 2008.

[23] R. Tyson, C. E. Jordan, and J. Hebert, "Modelling anguilliform swimming at intermediate reynolds number: A review and a novel extension of immersed boundary

method applications," *Computer Methods in Applied Mechanics and Engineering*, vol. 197, no. 25-28, pp. 2105–2118, 2008.

[24] T. McMillen, T Williams, and P Holmes, "Nonlinear muscles, passive viscoelasticity and body taper conspire to create neuromechanical phase lags in anguilliform swimmers," *PLoS computational biology*, vol. 4, no. 8, e1000157, 2008.

[25] E. D. Tytell, C.-Y. Hsu, T. L. Williams, A. H. Cohen, and L. J. Fauci, "Interactions between internal forces, body stiffness, and fluid environment in a neuromechanical model of lamprey swimming," *Proceedings of the National Academy of Sciences*, vol. 107, no. 46, pp. 19 832–19 837, 2010.

[26] E. Berger, "Friction modeling for dynamic system simulation," *Appl. Mech. Rev.*, vol. 55, no. 6, pp. 535–577, 2002.

[27] H. B. Lillywhite, *How snakes work: structure, function and behavior of the world's snakes*. Oxford University Press, 2014.

[28] H. L.W.C.C.C.L. R. Altun Z.F. and D. e. Hall, *Wormatlas*, `URLhttp://www.wormatlas.org`.

[29] P Wallén and T. Williams, "Fictive locomotion in the lamprey spinal cord in vitro compared with swimming in the intact and spinal animal.," *The Journal of Physiology*, vol. 347, no. 1, pp. 225–239, 1984.

[30] T. Zhang and D. I. Goldman, "The effectiveness of resistive force theory in granular locomotion," *Physics of Fluids*, vol. 26, no. 10, p. 101 308, 2014.

[31] H. M. Jaeger, S. R. Nagel, and R. P. Behringer, "Granular solids, liquids, and gases," *Reviews of modern physics*, vol. 68, no. 4, p. 1259, 1996.

[32] S Sponberg and R. Full, "Neuromechanical response of musculo-skeletal structures in cockroaches during rapid running on rough terrain," *J. Exp. Biol.*, vol. 211, no. 3, pp. 433–446, 2008.

[33] M. A. Daley and A. A. Biewener, "Running over rough terrain reveals limb control for intrinsic stability," *Proceedings of the National Academy of Sciences*, vol. 103, no. 42, pp. 15 681–15 686, 2006.

[34] J Gray, "The movement of sea-urchin spermatozoa," *J. Exp. Biol.*, vol. 32, no. 4, pp. 775–801, 1955.

[35] H. Berg, "Motile behavior of bacteria," 2000.

[36] J. T. Pierce-Shimomura, B. L. Chen, J. J. Mun, R. Ho, R. Sarkis, and S. L. McIntire, "Genetic analysis of crawling and swimming locomotory patterns in c. elegans," *Proceedings of the National Academy of Sciences*, pnas–0 810 359 105, 2008.

[37] S. Berri, J. H. Boyle, M. Tassieri, I. A. Hope, and N. Cohen, "Forward locomotion of the nematode c. elegans is achieved through modulation of a single gait," *HFSP journal*, vol. 3, no. 3, pp. 186–193, 2009.

[38] V. M. J. Escobedo and K. Costello, *Nasa ice-first-genomics*, URLhttps://www.nasa.gov/mission_pages/station/research/experiments/644.html.

[39] M. J. Lighthill, "Large-amplitude elongated-body theory of fish locomotion," *Proceedings of the Royal Society of London. Series B, Biological Sciences*, pp. 125–138, 1971.

[40] E. M. Purcell, "Life at low reynolds number," *American journal of physics*, vol. 45, no. 1, pp. 3–11, 1977.

[41] N. Cohen and J. H. Boyle, "Swimming at low reynolds number: A beginners guide to undulatory locomotion," *Contemporary Physics*, vol. 51, no. 2, pp. 103–123, 2010.

[42] S. J. Newman and B. C. Jayne, "Crawling without wiggling: Muscular mechanisms and kinematics of rectilinear locomotion in boa constrictors," *J. Exp. Biol.*, vol. 221, no. 4, jeb166199, 2018.

[43] H. C. Astley, C. Gong, J. Dai, M. Travers, M. M. Serrano, P. A. Vela, H. Choset, J. R. Mendelson, D. L. Hu, and D. I. Goldman, "Modulation of orthogonal body waves enables high maneuverability in sidewinding locomotion," *Proceedings of the National Academy of Sciences*, p. 201 418 965, 2015.

[44] H. Marvi and D. L. Hu, "Friction enhancement in concertina locomotion of snakes," *Journal of The Royal Society Interface*, rsif20120132, 2012.

[45] C. Gans, "Tetrapod limblessness: Evolution and functional corollaries," *American Zoologist*, vol. 15, no. 2, pp. 455–467, 1975.

[46] ——, "Locomotion of limbless vertebrates: Pattern and evolution," *Herpetologica*, vol. 42, no. 1, pp. 33–46, 1986.

[47] J Gray, "The Mechanism of Locomotion in Snakes," *J. Exp. Biol.*, vol. 23, no. 2, 101–&, 1946.

[48] W. Mosauer, "Locomotion and diurnal range of sonora occipitalis, crotalus cerastes, and crotalus atrox as seen from their tracks," *Copeia*, vol. 1933, no. 1, pp. 14–16, 1933.

[49] D. L. Hu, J. Nirody, T. Scott, and M. J. Shelley, "The mechanics of slithering locomotion," *Proceedings of the National Academy of Sciences*, vol. 106, no. 25, pp. 10 081–10 085, 2009.

[50] G. B. Gillis, "Undulatory locomotion in elongate aquatic vertebrates: Anguilliform swimming since sir james gray," *American Zoologist*, vol. 36, no. 6, pp. 656–665, 1996.

[51] J. B. GRAHAM, W. R. LOWELL, I. RUBINOFF, and J. MOTTA, "Surface and subsurface swimming of the sea snake pelamis platurus," *J. Exp. Biol.*, vol. 127, no. 1, pp. 27–44, 1987.

[52] M. Sfakiotakis, D. M. Lane, and J. B. C. Davies, "Review of fish swimming modes for aquatic locomotion," *IEEE Journal of oceanic engineering*, vol. 24, no. 2, pp. 237–252, 1999.

[53] S Bennet, T McConnell, and S. Trubatch, "Quantitative analysis of the speed of snakes as a function of peg spacing," *J. Exp. Biol.*, vol. 60, no. 1, pp. 161–165, 1974.

[54] B. R. Moon, "Testing an inference of function from structure: Snake vertebrae do the twist," *Journal of Morphology*, vol. 241, no. 3, pp. 217–225, 1999.

[55] T. Monto, *A snake skeleton in national museum of natural sciences of spain*, [Online; accessed November 11, 2018], 2016.

[56] C. Gans, "Terrestrial locomotion without limbs," *American Zoologist*, pp. 167–182, 1962.

[57] J. A. Ruben, "Some correlates of cranial and cervical morphology with predatory modes in snakes," *J. Morphol*, vol. 152, no. 1, pp. 89–99, 1977.

[58] B. C. Jayne, "Muscular mechanisms of snake locomotion: An electromyographic study of lateral undulation of the florida banded water snake (*Nerodia fasciata*) and the yellow rat snake (*Elaphe obsoleta*)," *Journal of Morphology*, vol. 197, no. 2, pp. 159–181, 1988.

[59] K. Nishikawa, A. A. Biewener, P. Aerts, A. N. Ahn, H. J. Chiel, M. A. Daley, T. L. Daniel, R. J. Full, M. E. Hale, T. L. Hedrick, *et al.*, "Neuromechanics: An integrative approach for understanding motor control," *Integrative and Comparative Biology*, vol. 47, no. 1, pp. 16–54, 2007.

[60] N. J. Cowan, J. Lee, and R. J. Full, "Task-level control of rapid wall following in the american cockroach," *J. Exp. Biol.*, vol. 209, no. 9, pp. 1617–1629, 2006.

[61] R. J. Full and D. E. Koditschek, "Templates and anchors: Neuromechanical hypotheses of legged locomotion on land," *J. Exp. Biol.*, vol. 202, no. 23, pp. 3325–3332, 1999.

[62] R. Blickhan, A. Seyfarth, H. Geyer, S. Grimmer, H. Wagner, and M. Günther, "Intelligence by mechanics," *Philosophical Transactions of the Royal Society of London A: Mathematical, Physical and Engineering Sciences*, vol. 365, no. 1850, pp. 199–220, 2007.

[63] D. L. Jindrich and R. J. Full, "Dynamic stabilization of rapid hexapedal locomotion," *J. Exp. Biol.*, vol. 205, no. 18, pp. 2803–2823, 2002.

[64] T. McGeer *et al.*, "Passive dynamic walking," *I. J. Robotic Res.*, vol. 9, no. 2, pp. 62–82, 1990.

[65] J. C. Spagna, D. I. Goldman, P.-C. Lin, D. E. Koditschek, and R. J. Full, "Distributed mechanical feedback in arthropods and robots simplifies control of rapid running on challenging terrain," *Bioinspiration & biomimetics*, vol. 2, no. 1, p. 9, 2007.

[66] J. C. Liao, "Neuromuscular control of trout swimming in a vortex street: Implications for energy economy during the karman gait," *J. Exp. Biol.*, vol. 207, no. 20, pp. 3495–3506, 2004.

[67] M. H. Dickinson, C. T. Farley, R. J. Full, M. Koehl, R. Kram, and S. Lehman, "How animals move: An integrative view," *science*, vol. 288, no. 5463, pp. 100–106, 2000.

[68] P. Liljebäck, K. Y. Pettersen, Ø. Stavdahl, and J. T. Gravdahl, "A review on modelling, implementation, and control of snake robots," *Robotics and Autonomous Systems*, vol. 60, no. 1, pp. 29–40, 2012.

[69] P. Liljeback, K. Y. Pettersen, Ø. Stavdahl, and J. T. Gravdahl, "Snake robot locomotion in environments with obstacles," *IEEE/ASME Transactions on Mechatronics*, vol. 17, no. 6, pp. 1158–1169, 2012.

[70] M. J. Travers, J Whitman, P Schiebel, D. Goldman, and H Choset, "Shape-based compliance in locomotion," in *Robotics: Science and Systems*, 2016.

[71] Y. Shan and Y. Koren, "Design and motion planning of a mechanical snake," *IEEE transactions on systems, man, and cybernetics*, vol. 23, no. 4, pp. 1091–1100, 1993.

[72] A. A. Hill, M. A. Masino, and R. L. Calabrese, "Intersegmental coordination of rhythmic motor patterns," *Journal of neurophysiology*, vol. 90, no. 2, pp. 531–538, 2003.

[73] A. D. McClellan and K. A. Sigvardt, "Features of entrainment of spinal pattern generators for locomotor activity in the lamprey spinal cord," *Journal of Neuroscience*, vol. 8, no. 1, pp. 133–145, 1988.

[74] E. Marder and D. Bucher, "Central pattern generators and the control of rhythmic movements," *Current biology*, vol. 11, no. 23, R986–R996, 2001.

[75] Q. Wen, M. D. Po, E. Hulme, S. Chen, X. Liu, S. W. Kwok, M. Gershow, A. M. Leifer, V. Butler, C. Fang-Yen, *et al.*, "Proprioceptive coupling within motor neurons drives c. elegans forward locomotion," *Neuron*, vol. 76, no. 4, pp. 750–761, 2012.

[76] J.-P. Gasc, D. Cattaert, C Chasserat, and F Clarac, "Propulsive action of a snake pushing against a single site: Its combined analysis," *Journal of morphology*, vol. 201, no. 3, pp. 315–329, 1989.

[77] B. R. Moon and C. Gans, "Kinematics, muscular activity and propulsion in gopher snakes," *J. Exp. Biol.*, vol. 201, no. 19, pp. 2669–2684, 1998.

[78] K Wieghardt, "Experiments in granular flow," *Annual Review of Fluid Mechanics*, vol. 7, no. 1, pp. 89–114, 1975.

[79] R. D. Maladen, Y. Ding, C. Li, and D. I. Goldman, "Undulatory swimming in sand: Subsurface locomotion of the sandfish lizard," *science*, vol. 325, no. 5938, pp. 314–318, 2009.

[80] Y. Ding, N. Gravish, and D. I. Goldman, "Drag induced lift in granular media," *Physical Review Letters*, vol. 106, no. 2, p. 028 001, 2011.

[81] J. Lighthill, "Flagellar hydrodynamics," *SIAM review*, vol. 18, no. 2, pp. 161–230, 1976.

[82] G. J. Berman and Z. J. Wang, "Energy-minimizing kinematics in hovering insect flight," *Journal of Fluid Mechanics*, vol. 582, pp. 153–168, 2007.

[83] B. Rodenborn, C.-H. Chen, H. L. Swinney, B. Liu, and H. Zhang, "Propulsion of microorganisms by a helical flagellum," *Proceedings of the National Academy of Sciences*, vol. 110, no. 5, E338–E347, 2013.

[84] W. Mosauer, "Adaptive convergence in the sand reptiles of the sahara and of california: A study in structure and behavior," *Copeia*, vol. 1932, no. 2, pp. 72–78, 1932.

[85] R. D. Maladen, Y. Ding, P. B. Umbanhowar, and D. I. Goldman, "Undulatory swimming in sand: Experimental and simulation studies of a robotic sandfish," *The International Journal of Robotics Research*, vol. 30, no. 7, pp. 793–805, 2011.

[86] S. S. Sharpe, Y. Ding, and D. I. Goldman, "Environmental interaction influences muscle activation strategy during sand-swimming in the sandfish lizard scincus scincus," *J. Exp. Biol.*, vol. 216, no. 2, pp. 260–274, 2013.

[87] Y. Ding, S. S. Sharpe, K. Wiesenfeld, and D. I. Goldman, "Emergence of the advancing neuromechanical phase in a resistive force dominated medium," *Proceedings of the National Academy of Sciences*, vol. 110, no. 25, pp. 10 123–10 128, 2013.

[88] K. S. Norris and J. L. Kavanau, "The burrowing of the western shovel-nosed snake, chionactis occipitalis hallowell, and the undersand environment," *Copeia*, pp. 650–664, 1966.

[89] H. Marvi, C. Gong, N. Gravish, H. Astley, M. Travers, R. L. Hatton, J. R. Mendelson, H. Choset, D. L. Hu, and D. I. Goldman, "Sidewinding with minimal slip: Snake and robot ascent of sandy slopes," *Science*, vol. 346, no. 6206, pp. 224–229, 2014.

[90] N. Mazouchova, N. Gravish, A. Savu, and D. I. Goldman, "Utilization of granular solidification during terrestrial locomotion of hatchling sea turtles," *Biology letters*, rsbl20091041, 2010.

[91] N. Mazouchova, P. B. Umbanhowar, and D. I. Goldman, "Flipper-driven terrestrial locomotion of a sea turtle-inspired robot," *Bioinspiration & biomimetics*, vol. 8, no. 2, p. 026 007, 2013.

[92] B. McInroe, H. C. Astley, C. Gong, S. M. Kawano, P. E. Schiebel, J. M. Rieser, H. Choset, R. W. Blob, and D. I. Goldman, "Tail use improves performance on soft substrates in models of early vertebrate land locomotors," *Science*, vol. 353, no. 6295, pp. 154–158, 2016.

[93] G. J. Stephens, B. Johnson-Kerner, W. Bialek, and W. S. Ryu, "Dimensionality and dynamics in the behavior of c. elegans," *PLoS computational biology*, vol. 4, no. 4, e1000028, 2008.

[94] S Hirose, *Biologically Inspired Robots: Serpentile Locomotors and Manipulators*. Oxford University Press, 1993, ISBN: 0198562616.

[95] N. Gravish, P. B. Umbanhowar, and D. I. Goldman, "Force and flow at the onset of drag in plowed granular media," *Physical Review E*, vol. 89, no. 4, p. 042 202, 2014.

[96] H Guo, J Goldsmith, I Delacruz, M Tao, Y Luo, and S. Koehler, "Semi-infinite plates dragged through granular beds," *Journal of Statistical Mechanics: Theory and Experiment*, vol. 2012, no. 07, P07013, 2012.

[97] B. Percier, S. Manneville, J. N. McElwaine, S. W. Morris, and N. Taberlet, "Lift and drag forces on an inclined plow moving over a granular surface," *Physical Review E*, vol. 84, no. 5, p. 051 302, 2011.

[98] J Gray, "Undulatory movement," *Quart. J. Microsc. Sci., NS*, vol. 94, pp. 551–578, 1953.

[99] I Albert, J. Sample, A. Morss, S Rajagopalan, A.-L. Barabási, and P Schiffer, "Granular drag on a discrete object: Shape effects on jamming," *Physical review E*, vol. 64, no. 6, p. 061 303, 2001.

[100] B. Lautrup, "Physics of continuous matter," *Exotic and Everyday Phenomena in the Macroscopic World, IOP*, 2005.

[101] T. Xu, J. Huo, S. Shao, M. Po, T. Kawano, Y. Lu, M. Wu, M. Zhen, and Q. Wen, "Descending pathway facilitates undulatory wave propagation in caenorhabditis elegans through gap junctions," *Proceedings of the National Academy of Sciences*, vol. 115, no. 19, E4493–E4502, 2018.

[102] A. A. Biewener and G. B. Gillis, "Dynamics of muscle function during locomotion: Accommodating variable conditions," *J. Exp. Biol.*, vol. 202, no. 23, pp. 3387–3396, 1999.

[103] J. W. Warren, "Notes on the behavior of chionactis occipitalis," *Herpetologica*, vol. 9, no. 3, pp. 121–124, 1953.

[104] L. M. Klauber, *Studies of reptile life in the arid southwest*. Zoological Society of San Diego, 1939.

[105] G. J. Berman, "Measuring behavior across scales," *BMC biology*, vol. 16, no. 1, p. 23, 2018.

[106] R. M. Alexander, *Principles of animal locomotion*. Princeton University Press, 2003.

[107] N. J. Cowan and E. S. Fortune, "The critical role of locomotion mechanics in decoding sensory systems," *Journal of Neuroscience*, vol. 27, no. 5, pp. 1123–1128, 2007.

[108] N. J. Cowan, M. M. Ankarali, J. P. Dyhr, M. S. Madhav, E. Roth, S. Sefati, S. Sponberg, S. A. Stamper, E. S. Fortune, and T. L. Daniel, "Feedback control as a framework for understanding tradeoffs in biology," *American Zoologist*, vol. 54, no. 2, pp. 223–237, 2014.

[109] D. I. Goldman, "Colloquium: Biophysical principles of undulatory self-propulsion in granular media," *Rev.Mod.Phys.*, vol. 86, no. 3, pp. 943–958, Jul. 2014.

[110] S Childress, A Hosoi, W. W. Schultz, and J Wang, *Natural locomotion in fluids and on surfaces: Swimming, flying, and sliding*, 2012.

[111] P Holmes, R. J. Full, D Koditschek, and J Guckenheimer, "The Dynamics of Legged Locomotion: Models, Analyses, and Challenges," *SIAM Review*, vol. 48, no. 2, pp. 207–304, Jan. 2006.

[112] E. Lauga and T. R. Powers, "The hydrodynamics of swimming microorganisms," *Reports on Progress in Physics*, vol. 72, no. 9, p. 096 601, 2009.

[113] G. Juarez, K. Lu, J. Sznitman, and P. E. Arratia, "Motility of small nematodes in wet granular media," *EPL (Europhysics Letters)*, vol. 92, no. 4, p. 44 002, 2010.

[114] C. Li, A. O. Pullin, D. W. Haldane, H. K. Lam, R. S. Fearing, and R. J. Full, "Terradynamically streamlined shapes in animals and robots enhance traversability through densely cluttered terrain," *Bioinspiration & biomimetics*, vol. 10, no. 4, p. 046 003, 2015.

[115] S Sponberg and R. J. Full, "Neuromechanical response of musculo-skeletal structures in cockroaches during rapid running on rough terrain," *J. Exp. Biol.*, vol. 211, no. 3, pp. 433–446, Feb. 2008.

[116] D. E. Koditschek, R. J. Full, and M. Buehler, "Mechanical aspects of legged locomotion control," *Arthropod structure & development*, vol. 33, no. 3, pp. 251–272, 2004.

[117] A. Ayali, A. Borgmann, A. Büschges, E. Couzin-Fuchs, S. Daun-Gruhn, and P. Holmes, "The comparative investigation of the stick insect and cockroach models in the study of insect locomotion," *Current Opinion in Insect Science*, vol. 12, pp. 1 –10, 2015, Neuroscience * Special Section: Insect conservation.

[118] K. Pearson and R Franklin, "Characteristics of leg movements and patterns of coordination in locusts walking on rough terrain," *The International Journal of Robotics Research*, vol. 3, no. 2, pp. 101–112, 1984.

[119] M. A. Daley, "Running over rough terrain: guinea fowl maintain dynamic stability despite a large unexpected change in substrate height," *J. Exp. Biol.*, vol. 209, no. 1, pp. 171–187, Jan. 2006.

[120] J. C. Spagna, D. I. Goldman, P.-C. Lin, D. E. Koditschek, and R. J. Full, "Distributed mechanical feedback in arthropods and robots simplifies control of rapid running on challenging terrain," *Bioinspiration & Biomimetics*, vol. 2, no. 1, pp. 9–18, Jan. 2007.

[121] K. Jayaram, J.-M. Mongeau, A. Mohapatra, P. Birkmeyer, R. S. Fearing, and R. J. Full, "Transition by head-on collision: Mechanically mediated manoeuvres in cockroaches and small robots," *Journal of The Royal Society Interface*, vol. 15, no. 139, p. 20 170 664, 2018.

[122] D. L. Jindrich and R. J. Full, "Dynamic stabilization of rapid hexapedal locomotion," *J. Exp. Biol.*, vol. 205, no. 18, pp. 2803–2823, Sep. 2002.

[123] R. J. Full, T. Kubow, J. Schmitt, P. Holmes, and D. Koditschek, "Quantifying dynamic stability and maneuverability in legged locomotion," *Integrative and comparative biology*, vol. 42, no. 1, pp. 149–157, 2002.

[124] J. C. Liao, "A review of fish swimming mechanics and behaviour in altered flows," *Philosophical Transactions of the Royal Society B: Biological Sciences*, vol. 362, no. 1487, pp. 1973–1993, 2007.

[125] B. R. Moon and C Gans, "Kinematics, muscular activity and propulsion in gopher snakes," *J. Exp. Biol.*, vol. 201, no. 19, pp. 2669–2684, Oct. 1998.

[126] E. M. Lifshitz, L. Pitaevskii, and V. Berestetskii, "Landau and lifshitz course of theoretical physics," *Statistical physics*, vol. 5, 1980.

[127] C. Ye, S. Ma, B. Li, and Y. Wang, "Turning and side motion of snake-like robot," in *Robotics and Automation, 2004. Proceedings. ICRA'04. 2004 IEEE International Conference on*, IEEE, vol. 5, 2004, pp. 5075–5080.

[128] J. M. Rieser, P. E. Schiebel, A. Pazouki, F. Qian, Z. Goddard, A. Zangwill, D. Negrut, and D. I. Goldman, "Collision-induced scattering of a self-propelled slithering robot," *arXiv preprint arXiv:1712.00136*, 2017.

[129] P. E. Schiebel, J. M. Rieser, A. M. Hubbard, L. Chen, and D. I. Goldman, "Collisional diffraction emerges from simple control of limbless locomotion," in *Conference on Biomimetic and Biohybrid Systems*, Springer, 2017, pp. 611–618.

[130] Z. Guo and L Mahadevan, "Limbless undulatory propulsion on land," *Proceedings of the National Academy of Sciences*, vol. 105, no. 9, pp. 3179–3184, 2008.

[131] H. Astley, J. Mendelson, and D. Goldman, "Side-impact collision: Obstacle negotiation mechanics in sidewinding snakes," in *INTEGRATIVE AND COMPARATIVE BIOLOGY*, OXFORD UNIV PRESS INC JOURNALS DEPT, 2001 EVANS RD, CARY, NC 27513 USA, vol. 57, 2017, E196–E196.

[132] D. J. Griffiths, *Introduction to electrodynamics*. Prentice Hall, 1962.

[133] S Revzen and J. M. Guckenheimer, "Finding the dimension of slow dynamics in a rhythmic system," *Journal of The Royal Society Interface*, vol. 9, no. 70, pp. 957–971, Mar. 2012.

[134] T McGeer, "Passive Dynamic Walking," *International Journal of Robotics Research*, vol. 9, no. 2, pp. 62–82, Apr. 1990.

[135] U Saranli, M Buehler, and D. E. Koditschek, "RHex: A simple and highly mobile hexapod robot," *International Journal of Robotics Research*, vol. 20, no. 7, pp. 616–631, Jul. 2001.

[136] M. C. Marchetti, J. F. Joanny, S Ramaswamy, T. B. Liverpool, J Prost, M Rao, and R. A. Simha, "Hydrodynamics of soft active matter," *Reviews of Modern Physics*, vol. 85, no. 3, p. 1143, 2013.

[137] K. Drescher, J. Dunkel, L. H. Cisneros, S. Ganguly, and R. E. Goldstein, "Fluid dynamics and noise in bacterial cell–cell and cell–surface scattering," *Proceedings of the National Academy of Sciences*, vol. 108, no. 27, pp. 10 940–10 945, 2011.

[138] V Kantsler, J Dunkel, and M Polin, "Ciliary contact interactions dominate surface scattering of swimming eukaryotes," in *Proceedings of the National Academy of Sciences*, 2013, pp. 1–9.

[139] T Zhang and D. I. Goldman, "Erratum: "The effectiveness of resistive force theory in granular locomotion" [Phys. Fluids 26, 101308 (2014)]," *Physics of Fluids*, vol. 26, no. 10, p. 101 308, Oct. 2014.

[140] T. Zhang, "Modeling and control of locomotion in complex environments," PhD thesis, Georgia Institute of Technology, 2016.

[141] D. Rollinson, Y. Bilgen, B. Brown, F. Enner, S. Ford, C. Layton, J. Rembisz, M. Schwerin, A. Willig, P. Velagapudi, *et al.*, "Design and architecture of a series elastic snake robot," in *Intelligent Robots and Systems (IROS 2014), 2014 IEEE/RSJ International Conference on*, IEEE, 2014, pp. 4630–4636.

[142] G. V. Lauder and E. D. Tytell, "Hydrodynamics of undulatory propulsion," *Fish physiology*, vol. 23, pp. 425–468, 2005.

[143] Project Chrono, *Chrono: An Open Source Framework for the Physics-Based Simulation of Dynamic Systems*, `http://projectchrono.org`.

[144] G. Bartolotti, *Corn snake adult*, [Online; accessed December 10, 2018], 2016.

[145] I. red list of threatened species, *Panterhophis guttatus range*, [Online; accessed December 10, 2018], 2016.

[146] E. Grunwald and M. Dye, *Panterhophis guttatus range*, [Online; accessed December 10, 2018], 2008.

[147] E. B. Daeschler, N. H. Shubin, and F. A. Jenkins Jr, "A devonian tetrapod-like fish and the evolution of the tetrapod body plan," *Nature*, vol. 440, no. 7085, p. 757, 2006.

[148] R. L. Hatton, Y. Ding, H. Choset, and D. I. Goldman, "Geometric visualization of self-propulsion in a complex medium," *Physical review letters*, vol. 110, no. 7, p. 078 101, 2013.

[149] R. D. Maladen, Y. Ding, P. B. Umbanhowar, A. Kamor, and D. I. Goldman, "Mechanical models of sandfish locomotion reveal principles of high performance subsurface sand-swimming," *Journal of The Royal Society Interface*, vol. 8, no. 62, pp. 1332–1345, 2011.

[150] F Qian and D. I. Goldman, "The dynamics of legged locomotion in heterogeneous terrain: universality in scattering and sensitivity to initial conditions.," *Robotics: Science and Systems*, pp. 1–9, 2015.

[151] R. R. Murphy, S Tadokoro, D Nardi, A Jacoff, P Fiorini, H Choset, and A. M. Erkmen, "Search and rescue robotics," in *Springer Handbook of Robotics*, B Siciliano and O Khatib, Eds. Berlin, Heidelberg: Springer Berlin Heidelberg, 2008, pp. 1151–1173, ISBN: 978-3-540-30301-5.

[152] R. J. Full and D. E. Koditschek, "Templates and anchors: neuromechanical hypotheses of legged locomotion on land," *J. Exp. Biol.*, 1999.

[153] J Aguilar, T Zhang, F Qian, M Kingsbury, B McInroe, N Mazouchova, C Li, R Maladen, C Gong, M Travers, R. L. Hatton, H Choset, P. B. Umbanhowar, and D. I. Goldman, "A review on locomotion robophysics: the study of movement at the intersection of robotics, soft matter and dynamical systems," *Reports on Progress in Physics*, pp. 1–35, Sep. 2016.

[154] C. Gong, D. I. Goldman, and H. Choset, "Simplifying gait design via shape basis optimization.," in *Robotics: Science and Systems*, 2016.

[155] C. Li, S. T. Hsieh, and D. I. Goldman, "Multi-functional foot use during running in the zebra-tailed lizard (callisaurus draconoides)," *J. Exp. Biol.*, jeb–061 937, 2012.

[156] L. J. Vitt and R. D. Ohmart, "Ecology and reproduction of lower colorado river lizards: I. callisaurus draconoides (iguanidae)," *Herpetologica*, pp. 214–222, 1977.

[157] W. H. Karasov and R. A. Anderson, "Correlates of average daily metabolism of field-active zebra-tailed lizards (callisaurus draconoides)," *Physiological zoology*, vol. 71, no. 1, pp. 93–105, 1998.

[158] W. L. Korff and M. J. McHenry, "Environmental differences in substrate mechanics do not affect sprinting performance in sand lizards (uma scoparia and callisaurus draconoides)," *J. Exp. Biol.*, vol. 214, no. 1, pp. 122–130, 2011.

[159] D. J. Irschick and B. C. Jayne, "Comparative three-dimensional kinematics of the hindlimb for high-speed bipedal and quadrupedal locomotion of lizards," *J. Exp. Biol.*, vol. 202, no. 9, pp. 1047–1065, 1999.

[160] D. J. Irschick and B. C. Jayne, "A field study of the effects of incline on the escape locomotion of a bipedal lizard, *Callisaurus draconoides*," *Physiological and Biochemical Zoology*, vol. 72, no. 1, pp. 44–56, 1999.

[161] R. C. Snyder, "Quadrupedal and bipedal locomotion of lizards," *Copeia*, vol. 1952, no. 2, pp. 64–70, 1952.

[162] ——, "Adaptations for bipedal locomotion of lizards," *American Zoologist*, pp. 191–203, 1962.

[163] T Kohlsdorf and A. Biewener, "Negotiating obstacles: Running kinematics of the lizard sceloporus malachiticus," *Journal of Zoology*, vol. 270, no. 2, pp. 359–371, 2006.

[164] J. P. Olberding, L. D. McBrayer, and T. E. Higham, "Performance and three-dimensional kinematics of bipedal lizards during obstacle negotiation," *J. Exp. Biol.*, vol. 215, no. 2, pp. 247–255, 2012.

[165] R. J. Full, T. Kubow, J. Schmitt, P. Holmes, and D. Koditschek, "Quantifying dynamic stability and maneuverability in legged locomotion1," *Integrative and Comparative Biology*, vol. 42, no. 1, pp. 149–157, 2002. eprint: /oup/backfile/content_public/journal/icb/42/1/10.1093/icb/42.1.149/2/i1540-7063-042-01-0149.pdf.

[166] S. Revzen, D. E. Koditschek, and R. J. Full, "Towards testable neuromechanical control architectures for running," in *Progress in Motor Control*, Springer, 2009, pp. 25–55.

[167] P Liljeback, K. Y. Pettersen, Ø Stavdahl, and J. T. Gravdahl, "Snake Robot Locomotion in Environments With Obstacles," *IEEE/ASME Transactions on Mechatronics*, vol. 17, no. 6, pp. 1158–1169,

[168] A. J. Ijspeert, "Central pattern generators for locomotion control in animals and robots: A review," *Neural networks*, vol. 21, no. 4, pp. 642–653, 2008.

[169] H. Askari and K. Kamrin, "Intrusion rheology in grains and other flowable materials," *Nature materials*, vol. 15, no. 12, p. 1274, 2016.

[170] J. Aguilar and D. I. Goldman, "Robophysical study of jumping dynamics on granular media," *Nature Physics*, vol. 12, no. 3, p. 278, 2016.